



UNIVERSITÀ
degli STUDI
di CATANIA



UNIVERSITÀ
DEGLI STUDI
DI PALERMO

DOTTORATO DI RICERCA IN
SCIENZA DEI MATERIALI E NANOTECNOLOGIE
XXXII CICLO

ANGELO ARMANO

CHARGE TRANSFER PROCESSES BETWEEN
GRAPHENE AND SMALL MOLECULES
OR CARBON NANOPARTICLES

TUTOR

Prof. S. Agnello (UniPA)

Co-TUTOR

Dr. F. Giannazzo (CNR-IMM)

COORDINATORE

Prof.ssa M. G. Grimaldi (UniCT)

TESI PER IL CONSEGUIMENTO DEL TITOLO DI DOTTORE DI RICERCA

· 10 | 2019 ·

CONTENTS

INTRODUCTION	1
1 GRAPHENE	3
1.1 CARBON	4
1.2 ALLOTROPES OF CARBON	6
1.2.1 Bulk Materials	7
1.2.2 Nano Materials	7
1.3 ELECTRONIC STRUCTURE OF GRAPHENE	8
1.3.1 Tight Binding Method	9
1.3.2 Energy Bands	11
1.3.3 Charge Carrier Density	14
1.4 OPTICAL PROPERTIES	17
1.4.1 Light Absorption	17
1.4.2 Light Emission	19
1.5 VIBRATIONAL PROPERTIES	20
1.5.1 Normal Modes and Phonon Dispersion	21
1.5.2 Raman scattering processes	23
1.6 INFLUENCING FACTORS ON RAMAN SCATTERING	25
1.6.1 Light Energy and Power	25
1.6.2 Number of Layers	26
1.6.3 Defects and Disorder	28
1.6.4 Strain	31
1.6.5 Doping	33
1.7 TRANSPORT PROPERTIES	36
1.8 SYNTHESIS METHODS	37
1.8.1 Top Down	37
1.8.2 Bottom Up	39
2 CHARGE TRANSFER PROCESSES	41
2.1 PRINCIPLES OF ADSORPTION	41
2.1.1 Physisorption	42
2.1.2 Chemisorption	43
2.2 ADSORPTION ON GRAPHENE	44
2.2.1 Physisorption on Graphene	44
2.2.2 Chemisorption on Graphene	47
2.2.3 Adsorption Kinetics	51
2.3 CHARGE EXCHANGE WITH NANOPARTICLES	53

2.4	CARBON NANOPARTICLES	55
3	BASIC CONCEPTS OF METHODS	57
3.1	RAMAN SPECTROSCOPY	58
3.1.1	Classical Description	59
3.1.2	Quantum Description	60
3.1.3	Selection Rules and Exclusion Principle	62
3.2	PHOTOLUMINESCENCE SPECTROSCOPY	63
3.2.1	Principles of Photoluminescence	63
3.2.2	Quenching of the Emission	67
3.3	ATOMIC FORCE MICROSCOPY	68
3.3.1	Principles of AFM	68
3.3.2	Amplitude Modulation AFM	70
4	MATERIALS AND METHODS	74
4.1	SYNTHESIS OF MATERIALS	74
4.1.1	Graphene	74
4.1.2	Carbon Dots	75
4.2	RAMAN SPECTROSCOPY	76
4.3	ATOMIC FORCE MICROSCOPY	77
4.4	THERMAL PROCESSING	78
5	EXPERIMENTAL RESULTS	80
5.1	INTERACTION WITH MOLECULES	80
5.1.1	Characterization of Substrates	80
5.1.2	Characterization of Graphene	81
5.1.3	Influence of substrate on doping by O ₂	84
5.1.4	Hydroxylated vs Methylated SiO ₂	99
5.1.5	Folded graphene	103
5.1.6	Comparison with other gases	107
5.1.7	Doping Removal by Water	107
5.1.8	Strain modification	110
5.1.9	Model for Graphene-Molecules Interaction	112
5.2	INTERACTION WITH NANOPARTICLES	115
5.2.1	Characterization of Deposited CDs	115
5.2.2	Emission of CDs in Solid-Phase	117
5.2.3	CDs-Graphene Interaction	119
5.2.4	Model for Graphene-Nanoparticles Interaction	123
6	CONCLUSIONS	125
	BIBLIOGRAPHY	127
	CURRICULUM VITÆ	140

INTRODUCTION

Two dimensional materials constitute a novel class of nanomaterials whose scientific interest is motivated by the intriguing properties arising from their low-dimension structure. In fact, as in the case of zero-dimensional and mono-dimensional materials, such as quantum dot and carbon nanotubes, the reduced dimensionality gives rise to peculiar properties compared to their three-dimension counterparts. Among two dimensional materials, graphene plays a key role in nanoscience, since it has been the first member of this class to be discovered and its applications are now based on almost fifteen years of basic research. Composed by carbon atoms only, it is very stable and cheap compared to other two dimensional materials, and it is one of the few whose sheet thickness is constituted by only a single layer of atoms. As previously stated, the two dimensional structure of carbon atoms gives rise to unexpected properties in comparison to those found in graphite and diamond. In fact, extraordinary electrical mobility and thermal conductivity make graphene attractive for the design of nanosize p-n junctions or transparent capacitive layers. Furthermore, in spite of a strong structural stability, graphene is very sensitive to surrounding species because the electronic clouds which are relevant for conduction phenomena are exposed to the surface. This kind of interaction can be profitably used both in order to modify the features of graphene and as mark feature for sensing. Therefore, to determine which species can interact with graphene and to finely control the modification occurring in the latter are mandatory steps in order to implement this phenomena in practicable applications of graphene.

In this Thesis, the interactions between graphene and two kind of species are explored in their own aspects at first, and then combined together in order to clarify the processes which are at the basis of the observed phenomena. In particular, the subject of the study is graphene synthesized by chemical vapor deposition and transferred on various oxide substrates. The first interacting species to be investigated are small molecules, such as nitrogen, carbon dioxide, water and oxygen, for which the interaction with graphene is carried out by means of thermal treatment in controlled atmosphere. Herein, oxygen is the most significant case since it is able to induce a considerable p-doping in graphene. Thence, the reported study aims to clarify several basic features of the doping process: dependence on temperature, time kinetics, and influence of the substrate surface (both by comparing different substrates and by considering graphene with no direct contact with the substrate). Furthermore, the study is deepened by evaluating the correlation with structural modification of graphene and the kinetic of doping removal performed by water. On the other hand, carbon dots are the second interacting species that is investigated, that is a peculiar kind of carbon nanoparticles which features extraordinary optical emission properties. In this case, graphene and carbon dots are assembled in a solid phase composite material where the mutual influence between them reveals the presence of a photoinduced electron transfer from carbon dots to graphene. All the investigation is carried out by using several experimental

techniques, such as micro-Raman and micro-photoluminescence spectroscopy and atomic force microscopy, in order to reveal the electronic and morphological features of the samples.

The Thesis is organized according to the following structure:

CHAPTER 1 briefly reviews the chemistry of carbon on which the different carbon-based nanomaterials are based. Thereafter, by focusing the discussion on graphene, its fundamental physical properties (electronic, vibrational, transport) are deeply discussed, by taking care to highlight their connection with the optical properties of the material, especially for what concerns Raman spectroscopy.

CHAPTER 2 provides the basics about those interaction processes by which graphene experiences charge transfer phenomena. In particular, Sec. 2.1 and Sec. 2.2 concern the interaction with molecules, usually mediated by adsorption, whereas Sec. 2.3 presents the recent literature about charge transfer between graphene and nanoparticles. Finally, the key issues of the specific carbon nanoparticles used in this Thesis are reported in Sec. 2.4, where their photocycle and their interaction with surroundings species are briefly described.

CHAPTER 3 presents the fundamentals of the main experimental techniques used in this Thesis, namely Raman spectroscopy, photoluminescence spectroscopy, and atomic force microscopy.

CHAPTER 4 provides information about the synthesis of the samples of graphene and carbon nanoparticles used in this Thesis. In addition, main technical information about the instrumentation used for spectroscopy and microscopy is reported, as well as the design of the apparatus used for thermal processing.

CHAPTER 5 reports a basic characterization of the graphene samples and the results of the experiments performed on them. In particular, the chapter is divided in two sections: the first one concerns the interaction between graphene and molecules (Sec. 5.1), and the second one concerns the interaction with carbon nanoparticles (Sec. 5.2). At the end of both sections, an interpretative model is proposed in order to systematize the results previously discussed.

CHAPTER 6 concludes the Thesis by summarizing the main results and by suggesting some future perspective for this research.

Most of the results of this Thesis have been already published on various scientific journals. In addition to the regular citation in the general bibliography, a list of the published contents is included in the of PhD activities reported at the end of the Thesis.

1 | GRAPHENE

FIRST observed in 2004 [1], graphene has rapidly established a key role in the branch of material science which concerns the investigation of nanomaterials [2]. Its outstanding electrical and thermal transport performances, wide optical transparency, high mechanical resistance combined with structural flexibility make graphene an interesting material for several applications [3–5]. Some remarkable examples are solar cells and flexible capacitive systems [3, 6–9], field effect, radio-frequency, and vertical THz transistors [10–12], and volatile memories [13]. Besides, the discovery of graphene represented a real turning point also for basic sciences, having unveiled the existence of two-dimensional materials. Therefore the discovery of graphene represents a turning point in these application and also a stimulus for the research on nanomaterials for having unveiled the possibility to isolate and stably observe two-dimensional materials.

According to the IUPAC, graphene is defined as a single layer of graphite which is one of the main macroscopic allotropes of carbon [14]. As depicted in Fig. 1a, graphene can be described as a polycyclic aromatic hydrocarbon molecule of quasi infinite extension [14]. In particular, graphene is ideally composed by only carbon atoms arranged in a *honeycomb* structure, that is an hexagonal lattice extending in a single sheet of atoms. Therefore, the key feature of this material consists in a two-dimensional structure which, as described below, is at the basis of the extraordinary properties of graphene.

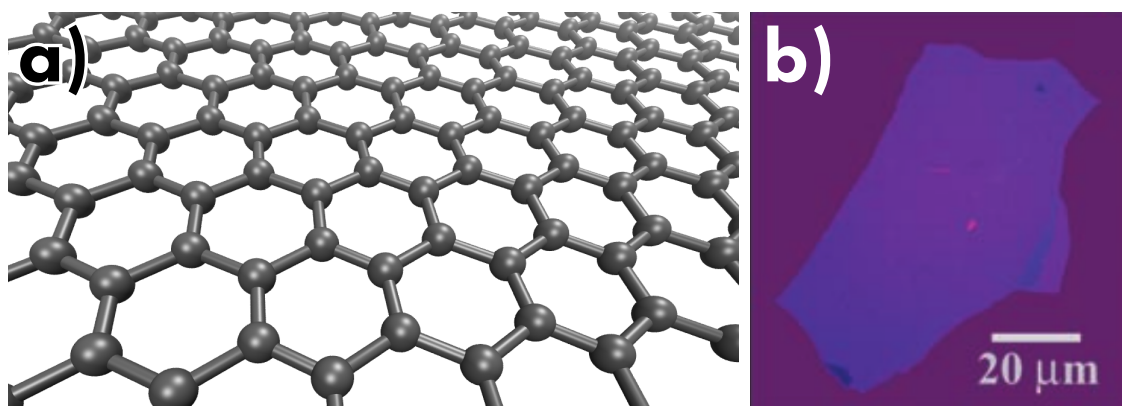


Figure 1: (a) Ball and stick model of a portion of graphene sheet where the carbon atoms are arranged in an hexagonal lattice. (b) Image of graphene captured by optical microscopy, reported from [1].

Since its planar extension can be very large compared to its nanometric thickness (the lateral size of graphene can easily overcome the thickness by more than three orders of magnitude, as shown in Fig. 1b), graphene cannot be properly considered neither a large molecule, nor a bulk material. As well as the other two-dimensional materials, graphene falls into the large family of nanomaterials, though. Even if the nomenclature of nano-size world is not yet well defined, *nanomaterials* are said those materials in which at least one external or internal dimension is on the scale of nanometer [15, 16]. In addition to this fundamental property, nanomaterials are

classified according to various factors: constituent elements, characteristic dimensionality, and elementary or composite structure [15–17]. For the aims of this discussion, it is important to highlight some of these classes, to which graphene belongs:

CARBON-BASED NANOMATERIALS concerning materials almost entirely composed by carbon or in which this element plays a key role in the definition of their properties. Some notable examples are *fullerenes*, carbon *nanotubes*, and carbon *nanoparticles* [17, 18].

LOW-DIMENSIONAL MATERIALS concerning materials which the nanometric scale implies a reduced dimensionality (that is the presence of at least one dimension which is much smaller to the other ones), which gives rise to some peculiar properties. Therefore, as depicted in Fig. 2, beyond a classic three-dimensional material, two-, one-, and zero-dimensional nanomaterials can be found [15, 16].

For the latter class, it is important to note that the limited dimensionality of the materials is not just a fancy feature, but a fundamental aspect which implies peculiar behaviors and properties for the nanomaterials which are unknown for the macroscopic case [19]. Basing on the cited ex-

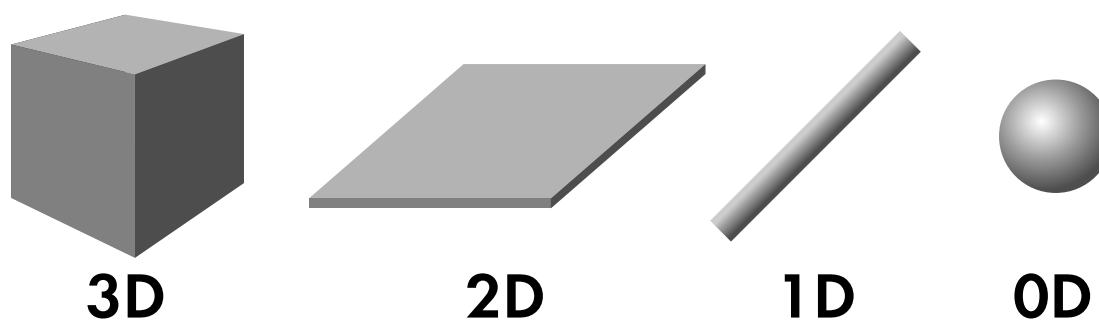


Figure 2: Representative depiction of three-dimensional (3D), two-dimensional (2D), one-dimensional (1D), and zero-dimensional (0D) structures.

amples, every possible low-dimensional system is well represented by some carbon-based nanomaterials. The capability of carbon to assemble itself in so different structures derives from the different number and structure of possible bonds which feature this element. Therefore, the investigation of carbon electronic structure is the starting point to understand structure and properties of carbon based nanomaterials, and in particular, of graphene.

1.1 CARBON

Carbon is one of the most abundant elements on Earth and, since it is at the basis of organic compounds, the known biology is based on it [20]. Its *luck* is due to a peculiar propensity to allotropy. In fact, both in bulk material, and in molecular structures, carbon shows a peculiar variability in bonding (from two to four bonds with other atoms can subsist, of both single, double or triple order) which determines many possible compounds and molecular species based on it [21, 22]. Carbon is the sixth chemical element of the periodic table characterized by atomic number 6, and its electronic configuration is thereby with four electrons available to form covalent chemical bonds. The electronic configuration of carbon at the ground state, whose energy distribution is reported in Fig. 3a, is $(1s^2)2s^2 2p^2$ [23]. The valence electrons are thereby placed in

the $2s$ orbitals and in the degenerate $2p$ orbitals. Since only these electrons can be shared with other atomic species, a maximum of four electrons are theoretically available to form covalent chemical bonds [24]. By also considering the excited state obtained by promoting one electron from $2s$ atomic orbital to the last free $2p$ orbital (Fig. 3b), only two or four electrons seem to be available for bonds. However, this prediction proves wrong, by contrasting the experimental evidences both in bond number and in incorrect orientations. Therefore, the bare atomic orbitals obtained for hydrogen result inadequate for a valid description of carbon bonds.

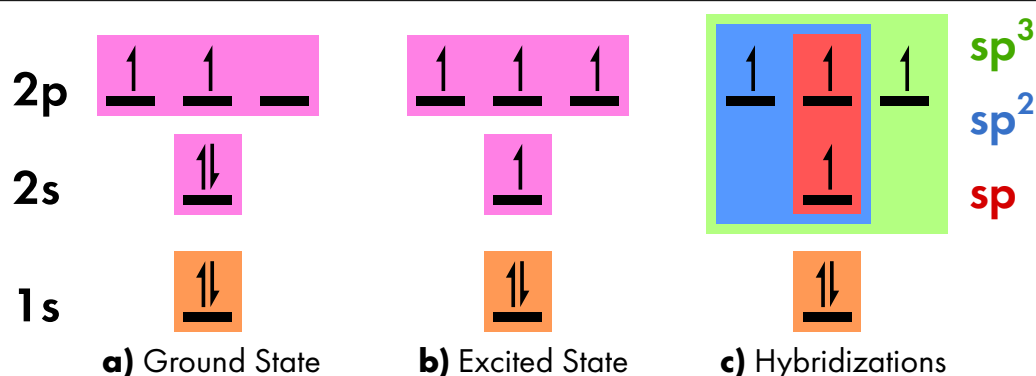


Figure 3: Electronic configuration diagram vs energy for carbon atom in its (a) ground state and (b) excited state. For the latter, the three possible hybridization types are marked: sp (red), sp^2 (blue), and sp^3 (green) in panel (c).

A better description is obtained by considering the presence of *hybrid* orbitals for the valence electrons of carbon [18, 22]. These orbitals are defined as the combination of several simple atomic orbitals allowed by the slight energy difference between them [24, 25]. As depicted in Fig. 3c, three possible schemes are compatible with the electronic configuration of carbon [23, 24]:

sp HYBRIDIZATION which involves the $2s$ orbital and a single $2p$ orbital (Fig. 4a). The two hybrid orbitals are placed at intermediate energy (Fig. 4b), are characterized by asymmetric lobes (due to the $2p$ contribution), and aligned on a single axis, thus assuming a linear geometry (Fig. 4c). In the formation of molecular bonds, the sp orbitals contribute to the formation of a triple bond together with the two remaining $2p$ orbitals, as in the ethyne molecule. In this case, the two carbon atoms share the electron of one sp orbital to form a σ bond and the electrons of both the remaining $2p$ orbitals to form two π bonds (Fig. 4d).

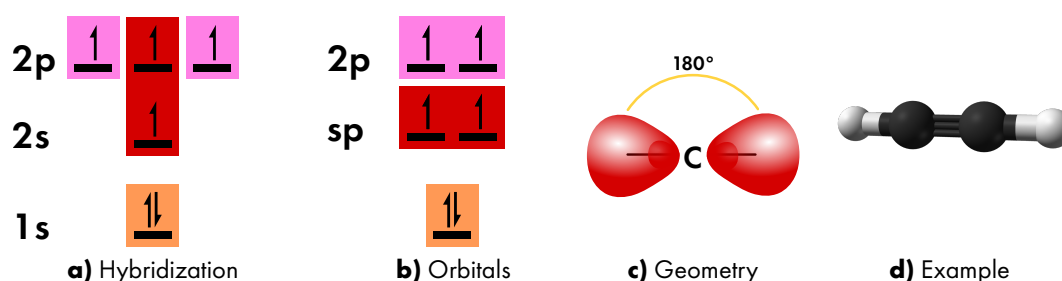


Figure 4: (a) sp hybridization scheme and (b) resulting electronic configuration with hybrid orbitals. (c) Geometry of sp orbitals, and (d) example of such hybridization in ethyne molecule.

sp^2 HYBRIDIZATION which involves the $2s$ orbital and two $2p$ orbitals (Fig. 5a). As in the previous case, the three hybrid orbitals are placed at intermediate energy (Fig. 5b), but are characterized by asymmetric lobes (due to the $2p$ contribution) arranged along three different axes, thus assuming a planar triangular geometry (Fig. 5c). In the formation of molecular bonds, the sp^2 orbitals contribute to the formation of a double bond together with the only remaining $2p$ orbital, as in the ethene molecule. In this case, the two carbon atoms share one electron of one sp^2 orbital so as to form a σ bond and the electron of the remaining $2p$ orbital for the formation of a π bond (Fig. 5d). A notable case is the benzene molecule whereby the three π bonds give rise to a delocalized orbital all around the carbon hexagon. Such a feature is relevant for electron transport in carbon systems.

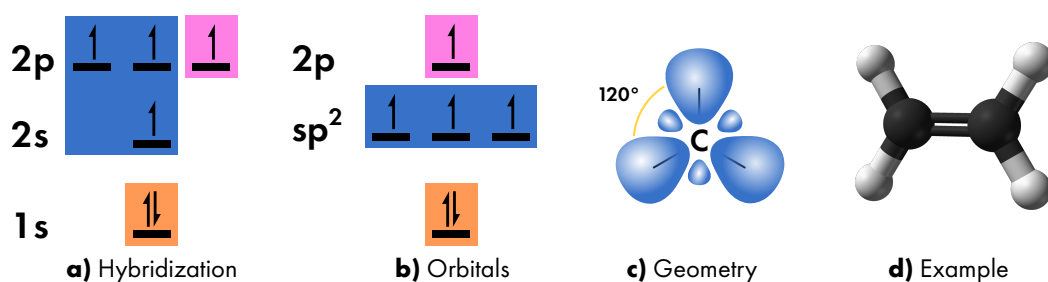


Figure 5: (a) sp^2 hybridization scheme and (b) resulting electronic configuration with hybrid orbitals. (c) Geometry of sp^2 orbitals, and (d) example of such hybridization in ethene molecule.

sp^3 HYBRIDIZATION which involves the $2s$ orbital and all of the $2p$ orbitals (Fig. 6a). As in the previous case, the three hybrid orbitals are placed at intermediate energy (Fig. 6b), are characterized by asymmetric lobes (due to the $2p$ contribution), but are now arranged along four different axes, thus assuming a tetrahedral geometry (Fig. 6c). In the formation of molecular bonds, the sp^3 orbitals contribute to the formation of single bonds, as in the ethane molecule. In this case, the two carbon atoms share only the electron of one sp^3 orbital so as to form a σ bond (Fig. 6d).

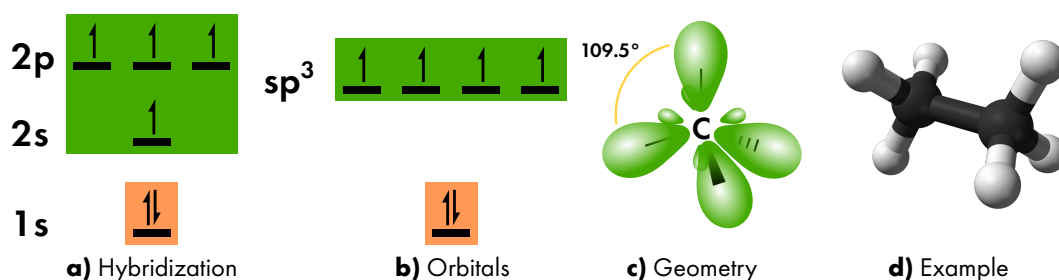


Figure 6: (a) sp^3 hybridization scheme and (b) resulting electronic configuration with hybrid orbitals. (c) Geometry of sp^3 orbitals, and (d) example of such hybridization in ethane molecule.

1.2 ALLOTROPES OF CARBON

Between the discussed hybridization schemes, only sp^2 and sp^3 contribute to the various structures of carbon materials. Nevertheless, the possibility to assume two bond schemes is sufficient

to determine the presence of carbon allotropes. In this section, the macroscopic allotropes of carbon are briefly discussed as case study of carbon and introduction to the more various case of nanomaterials, by emphasizing the role of carbon orbital hybridization in the definition of the various structures.

1.2.1 BULK MATERIALS

Diamond and graphite are the two main forms assumed by carbon in the macroscopic scale [21, 22]. As depicted in Fig. 7, diamond is composed by carbon atoms featuring sp^3 hybridization and, according to the bond geometry of this hybridization, the carbon atoms are arranged in a three-dimensional tetrahedral lattice (Fig. 7a). On the other hand, graphite is composed by carbon atoms in sp^2 hybridization, which are arranged in various two-dimensional hexagonal lattices, the latter stacked one upon the other by weak van der Waals interactions (Fig. 7b). From this perspective, graphite is nothing more than a quasi-infinite stacking of graphene layers [2].

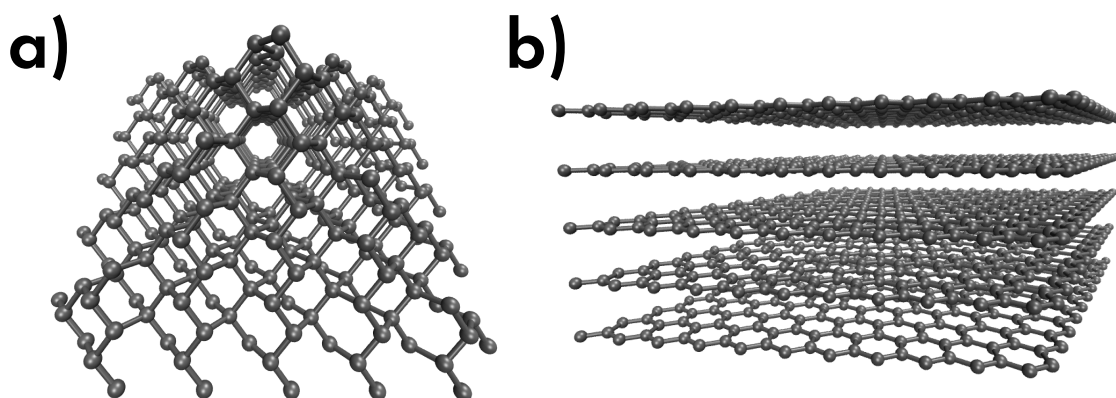


Figure 7: Exemplary ball and stick model of (a) diamond and (b) graphite.

It is impressive that, in spite of the same composition (namely only constituted by carbon), these two materials show diametrically opposed properties which result exclusively from the different hybridization of carbon atoms and the consequent different structure which it gives rise. Diamond has very high hardness, whereas graphite is quite fragile because of the weak bond between the single layers of which it is made. Besides, graphite is an electrical conductor, whereas diamond, featured by a bandgap equal to 5.5 eV is an insulator. As a consequence, the diamond is transparent at the visible light and the graphite has a flat absorption spectrum which makes it black.

1.2.2 NANO MATERIALS

Heading down to the nanoscale world, many other carbon based structures can be found, whose properties are related not only to the various hybridization, but also to the limitation of space dimension. As previously noted, the main carbon based nanomaterials are, in order of discovery, fullerene (Fig. 8a), carbon nanotubes (Fig. 8b), and graphene (Fig. 8c). Fullerene is a

0D carbon system constituted by a single shell of carbon atoms arranged in a sphere-like surface according to a truncate polyhedral structure. For example, the atomic structure of the most abundant kind of fullerene, namely C_{60} , corresponds to a truncated icosahedron [26]. In general, the various types of fullerene are obtained on varying the mixed contribution of sp^2 and sp^3 hybrid orbitals, with a further amount of the first one with increasing of fullerene size [2]. In particular, by considering an ever larger fullerene, its surface approaches a planar geometry. Finally, as the diameter approaches infinity, a perfect 2D system surface is obtained which actually corresponds to graphene.

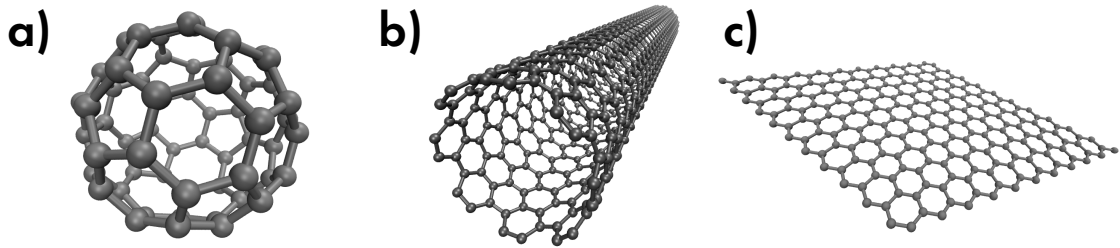


Figure 8: Ball and stick models of (a) fullerene, (b) carbon nanotubes, and (c) graphene.

As mentioned in the previous section, graphene is a single layer of graphite sheet, and only sp^2 hybridization is featured [2]. In the case of fullerene, the contribution of sp^3 hybridization limits the delocalization of electrons on the entire surface [26]. On the contrary, the complete predominance of sp^2 hybridization in graphene allows the formation of continuous delocalized molecular orbital deriving by π bonds, similar to the case of benzene previously reported [27, 28]. As discussed in the following section, this feature is the key for the peculiar electronic behavior of graphene.

Finally, carbon nanotubes can be figured in the midway between fullerene and graphene. In this case, the carbon atoms are arranged on a cylindrical surface, with length infinitely larger than the diameter [2, 29]. As for fullerene, carbon nanotubes are characterized by a mixed contribution of sp^2 and sp^3 hybrid orbitals which determines their electronic properties ranging from semiconductor to metal [29]. On the other hand, as in the case of graphene, because of the large contribution of sp^2 hybridization, delocalized orbitals can also occur, depending on the specific structure of the carbon nanotube [29]. In conclusion, the particular structure assumed by carbon atoms in the various nanomaterials strongly affects the distribution of electron orbitals and the electronic behavior of carbon nanomaterial.

1.3 ELECTRONIC STRUCTURE OF GRAPHENE

The band structure of graphene can be derived by various methods, such as Density Functional Theory [30], pseudo-potential [31], and tight binding method [32–34]. The latter method, in spite of its simplicity, provides a useful description of the contribution of π and σ orbitals in the electronic structure, and in particular in the electron transport in the material. Accordingly, the following discussion is focused on this method only.

1.3.1 TIGHT BINDING METHOD

A simple way to reconstruct the total wavefunction of a poly-atomic system (both for molecules and solids) is to use a Linear Combination of Atomic Orbitals (LCAO) of each single atom [23, 35]. Herein, the tight binding approximation consists in the assumption that the influence of each atom on the other is small, and therefore the atomic orbitals of free atoms can be used for their total energy determination [23, 35].

In accordance with the Bloch's theorem, the wavefunction of an electron Φ subjected to a periodic potential (as in the case of crystals) is independent from translations along the lattice vectors \mathbf{a}_i , and must thereby be expressed in form of *Bloch's function*, that is as product of a planewave of wavevector k and a lattice-periodic function:

$$\psi(\mathbf{k}, \mathbf{r}) = e^{i\mathbf{k}\cdot\mathbf{r}}\varphi(\mathbf{r}), \text{ with } \varphi(\mathbf{r}) = \varphi(\mathbf{r} - \mathbf{R}) \quad (1)$$

where \mathbf{R} marks the position of the atom [23]. In a crystal with n atoms in its unit cell, n Bloch functions can be used as eigenstate basis and the wavefunction of the i -th atom is given by

$$\Phi_i(\mathbf{k}, \mathbf{r}) = \frac{1}{\sqrt{N}} \sum_{\mathbf{R}} e^{i\mathbf{k}\cdot\mathbf{R}} \varphi_i(\mathbf{r} - \mathbf{R}) \quad (i = 1, \dots, n), \quad (2)$$

where the summation is taken over the positions of the atom \mathbf{R} in the unit cell, for the ($N \sim 10^{24}$) unit cells of the crystal, and φ_i are the atomic orbitals of the i -th state. Therefore, any wavefunction can be expressed in terms of such set of functions:

$$\Psi_i(\mathbf{k}, \mathbf{r}) = \sum_{j=1}^n c_{ij}(\mathbf{k}) \Phi_j(\mathbf{k}, \mathbf{r}), \quad (3)$$

where c_{ij} are the coefficients of vector decomposition. Given the Hamiltonian \mathcal{H} of the solid system, the solution of the Schrödinger's equation for the wavefunction Ψ_i

$$\mathcal{H}\Psi_i = E\Psi_i, \quad (4)$$

is given by the i -th eigenvalue of Hamiltonian $E_i(\mathbf{k})$ ($i = 1, \dots, n$) for a given \mathbf{k} . Its value can be written as

$$E_i(\mathbf{k}) = \frac{\langle \Psi_i | \mathcal{H} | \Psi_i \rangle}{\langle \Psi_i | \Psi_i \rangle} = \frac{\int \Psi_i^* \mathcal{H} \Psi_i d\mathbf{r}}{\int \Psi_i^* \Psi_i d\mathbf{r}}. \quad (5)$$

Substituting the Eq. 3 in Eq. 5 the following equation is obtained:

$$E_i(\mathbf{k}) = \frac{\sum_{j,k=1}^n c_{ij}^* c_{ik} \langle \Phi_j | \mathcal{H} | \Phi_k \rangle}{\sum_{j,k=1}^n c_{ij}^* c_{ik} \langle \Phi_j | \Phi_k \rangle} = \frac{\sum_{j,k=1}^n c_{ij}^* c_{ik} \mathcal{H}_{jk}}{\sum_{j,k=1}^n c_{ij}^* c_{ik} \mathcal{S}_{jk}}, \quad (6)$$

where the integrals over the Bloch's orbitals \mathcal{H} and \mathcal{S} are called *transfer integral* and *overlap integral* matrices, respectively, and their elements are defined as

$$\mathcal{H}_{jk} = \langle \Phi_j | \mathcal{H} | \Phi_k \rangle, \quad \mathcal{S}_{jk} = \langle \Phi_j | \Phi_k \rangle \quad (j, k = 1, \dots, n). \quad (7)$$

The coefficients c_{ij}^* are thereby optimized to minimize the eigenvalues of energy $E_i(\mathbf{k})$. In particular, by imposing the local minimum condition in the partial derivatives

$$\frac{\partial E_i(\mathbf{k})}{\partial c_{ij}^*} = \frac{\sum_{k=1}^n c_{ik} \mathcal{H}_{jk}}{\sum_{j,k=1}^n c_{ij}^* c_{ik} \mathcal{S}_{jk}} - \frac{\sum_{j,k=1}^n c_{ij}^* c_{ik} \mathcal{H}_{jk}}{\left(\sum_{j,k=1}^n c_{ij}^* c_{ik} \mathcal{S}_{jk} \right)^2} \sum_{k=1}^n c_{ik} \mathcal{S}_{jk} = 0 \quad (8)$$

the following equation is derived:

$$\sum_{k=1}^n \mathcal{H}_{jk} c_{ik} = E_i(\mathbf{k}) \sum_{k=1}^n \mathcal{S}_{jk} c_{ik}. \quad (9)$$

By defining the column vector of coefficients C_i , the Eq. 9 can be expressed in matrix format as

$$\mathcal{H} C_i = E_i(\mathbf{k}) \mathcal{S} C_i, \quad \text{with} \quad C_i = \begin{bmatrix} c_{i1} \\ \vdots \\ c_{in} \end{bmatrix}, \quad (10)$$

and transposing the right hand side to the left, the following equation is obtained:

$$[\mathcal{H} - E_i(\mathbf{k}) \mathcal{S}] C_i = 0. \quad (11)$$

This matrix equation has nontrivial solution ($C_i \neq 0$) if the *secular equation* is satisfied, that is if the determinant of $\mathcal{H} - E_i(\mathbf{k}) \mathcal{S}$ is null:

$$|\mathcal{H} - E_i(\mathbf{k}) \mathcal{S}| = 0. \quad (12)$$

The secular equation here reported is an equation of degree n , whose solutions give the n eigenvalues of energy, that is the energy dispersion relations (or energy bands) $E_i(\mathbf{k})$. Therefore, the procedure to derive these bands in tight binding methods is as follow [33]:

- 1| Specify the lattice vectors \mathbf{a}_i and the unit cell. Specify the coordinates of the atoms in the unit cell and select n atomic orbitals which are considered for the calculation.
- 2| Specify the reciprocal lattice vectors \mathbf{b}_i and the Brillouin zone. In the latter, select the high symmetry points and \mathbf{k} points along the high symmetry axes.
- 3| For the \mathbf{k} points, calculate the transfer integrals and the overlap integrals.
- 4| Substitute the latter in the secular equation to obtain the energy bands $E_i(\mathbf{k})$.

1.3.2 ENERGY BANDS

In order to describe the electronic structure of graphene, the first aspect to consider is the crystalline structure of the material. As previously discussed, graphene is composed by carbon atoms arranged in an hexagonal structure. As shown in Fig. 9, this structure is equivalent to the composition of two hexagonal Bravais lattices, marked by A and B [23, 34]. The position of each carbon atom in the space can be decomposed in terms of an opportune basis as $\mathbf{R} = m\mathbf{a}_1 + n\mathbf{a}_2$ where m and n are two integers, and \mathbf{a}_1 and \mathbf{a}_2 are the two lattice vectors defined as

$$\mathbf{a}_1 = a \left(\frac{3}{2}, \frac{\sqrt{3}}{2} \right), \quad \mathbf{a}_2 = a \left(\frac{3}{2}, -\frac{\sqrt{3}}{2} \right) \quad (13)$$

in terms of their (x, y) coordinates, where $a = 1.42 \text{ \AA}$ is the lattice constant of graphene expressed in terms of the C-C bond length. These vectors also define the primitive cell of graphene lattice which, because of the composition of the two sub-lattices, includes two carbon atoms [34]. In addition, with reference to each carbon atom, the positions of first-nearest neighbors (belonging to the other sub-lattice) are given by the vectors

$$\delta_1 = a \left(\frac{1}{2}, \frac{\sqrt{3}}{2} \right) \quad \delta_2 = a \left(\frac{1}{2}, -\frac{\sqrt{3}}{2} \right) \quad \delta_3 = a(-1, 0), \quad (14)$$

whereas the six second-nearest neighbors (belonging to the same sub-lattice) are placed at

$$\delta'_{\pm 1} = \pm \mathbf{a}_1, \quad \delta'_{\pm 2} = \pm \mathbf{a}_2, \quad \delta'_{\pm 3} = \pm(\mathbf{a}_2 - \mathbf{a}_1) \quad [34]. \quad (15)$$

The vectors \mathbf{b}_1 and \mathbf{b}_2 describing the reciprocal lattice of graphene, defined as $\mathbf{a}_i \mathbf{b}_j = 2\pi \delta_{ij}$ are

$$\mathbf{b}_1 = \frac{2\pi}{3a} (1, \sqrt{3}), \quad \mathbf{b}_2 = \frac{2\pi}{3a} (1, -\sqrt{3}) \quad [23]. \quad (16)$$

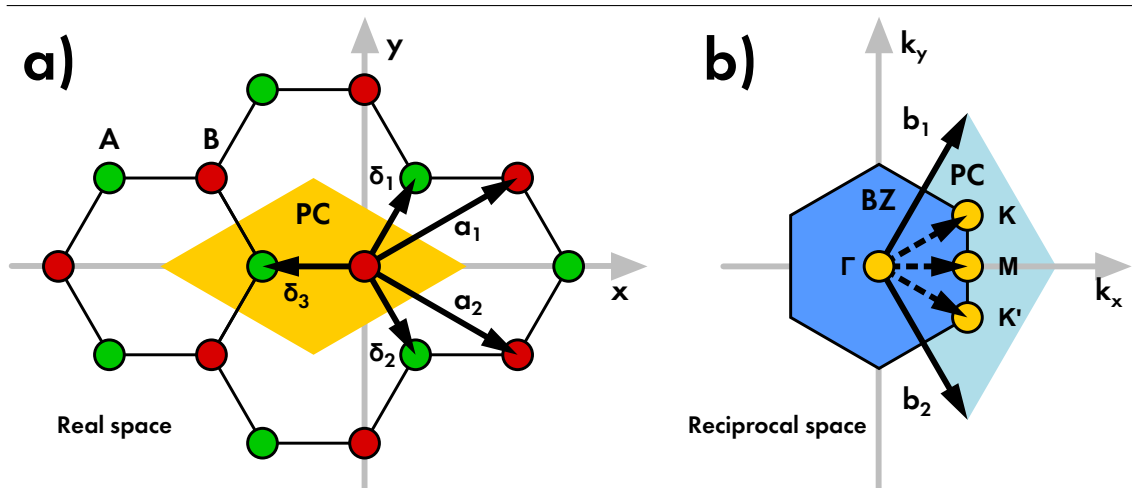


Figure 9: (a) Hexagonal structure of graphene in the real space. The atoms are distinguished in accordance to the two sub-lattices A (green) and B (red) to which they belong. Primitive vectors (\mathbf{a}_1 and \mathbf{a}_2) and first near-neighbor vectors (δ_1 , δ_2 and δ_3) are marked and primitive cell (PC) is highlighted. (b) Reciprocal lattice of graphene. Primitive vectors (\mathbf{b}_1 and \mathbf{b}_2), and high symmetry points Γ , K , K' , and M (yellow) are marked. The PC and the first Brillouin zone (BZ) are highlighted. Adapted from Ref.[34].

The most important region in the reciprocal space is the first Brillouin zone, since the remaining space is a periodical copy of this basic zone. In particular, the notable points of Brillouin zone are the high symmetry points Γ , \mathbf{K} , \mathbf{K}' , and \mathbf{M} , which are placed at the center of the first Brillouin zone, at its corners and at the center of its sides, respectively. These points are given in terms of (k_x, k_y) coordinates by

$$\begin{aligned} \Gamma &= (0, 0), & \mathbf{K} &= \left(\frac{2\pi}{3a'}, \frac{2\pi}{3\sqrt{3}a} \right), \\ \mathbf{M} &= \left(\frac{2\pi}{3a'}, 0 \right), & \mathbf{K}' &= \left(\frac{2\pi}{3a'}, -\frac{2\pi}{3\sqrt{3}a} \right) \end{aligned} \quad [34]. \quad (17)$$

Due to the periodicity of atoms in a crystal lattice, the entire discussion of the electronic structure can be restricted to the couple of atoms included in the unit cell. Since different bands can be derived by considering the π or the σ orbitals of both carbon atoms, the Bloch's function for electrons in the unit cell of graphene is given by:

$$\Phi_j = \frac{1}{\sqrt{2}} \sum_{\mathbf{R}_\alpha} e^{i\mathbf{k} \cdot \mathbf{R}_\alpha} \varphi_j(\mathbf{r} - \mathbf{R}_\alpha), \quad (\alpha = A, B), \quad (18)$$

where the summation is taken over the position \mathbf{R}_α for the A and B carbon atoms. As discussed in the Sec. 1.1, the π molecular orbital between carbon atoms of graphene is obtained by the combination of the remaining $2p_z$ orbitals. In this case, the Eq. 18 can be written as

$$\Psi_\pi = \frac{1}{\sqrt{2}} \left(e^{i\mathbf{k} \cdot \mathbf{R}_A} \varphi_A(\mathbf{r} - \mathbf{R}_A) + e^{i\mathbf{k} \cdot \mathbf{R}_B} \varphi_B(\mathbf{r} - \mathbf{R}_B) \right), \quad (19)$$

where $\varphi_{A,B} = 2p_z$, $\mathbf{R}_A = \delta_3$, and $\mathbf{R}_B = \mathbf{0}$. In accordance with the tight binding approximation, only the contributions from terms up to nearest-neighbors are considered in order to easily calculate the transfer and overlap matrix elements. By substituting Eq. 19 in Eq. 7, the diagonal elements of \mathcal{H}_{AA} atom is given by:

$$\begin{aligned} \mathcal{H}_{AA} &= \frac{1}{N} \sum_{\mathbf{R}_A} \sum_{\mathbf{R}'_A} e^{i\mathbf{k}(\mathbf{R}'_A - \mathbf{R}_A)} \langle \varphi_A(\mathbf{r} - \mathbf{R}_A) | \mathcal{H} | \varphi_A(\mathbf{r} - \mathbf{R}'_A) \rangle = \\ &= \underbrace{\frac{1}{N} \sum_{\mathbf{R}_A = \mathbf{R}'_A} \varepsilon_{2p_z}}_{\text{same atom}} + \underbrace{\frac{1}{N} \sum_{\mathbf{R}_A = \mathbf{R}'_A \pm \delta_3} e^{\pm i\mathbf{k} \cdot \delta_3} \langle \varphi_A(\mathbf{r} - \mathbf{R}_A) | \mathcal{H} | \varphi_A(\mathbf{r} - \mathbf{R}'_A) \rangle}_{\text{first nearest-neighbors}} + \dots = \\ &= \varepsilon_{2p_z} + \dots \end{aligned} \quad (20)$$

where, for the sake of simplicity, the small contribution of first nearest-neighbors is neglected since the highest contribution arises from the same atom terms. Similarly, the second diagonal term of B atom is given by $\mathcal{H}_{AA} = \varepsilon_{2p_z}$. On the contrary, the highest contribution for the calcu-

lation of the off-diagonal element \mathcal{H}_{AB} arises from nearest-neighbor placed at $\mathbf{R}_B = \delta_{1,2,3}$, the elements can be written as

$$\begin{aligned}\mathcal{H}_{AB} &= \frac{1}{N} \sum_{\mathbf{R}_A} \sum_{\mathbf{R}_B} e^{ik(\mathbf{R}_B - \mathbf{R}_A)} \langle \varphi_A(\mathbf{r} - \mathbf{R}_A) | \mathcal{H} | \varphi_A(\mathbf{r} - \mathbf{R}_B) \rangle = \\ &= t(e^{ik \cdot \delta_1} + e^{ik \cdot \delta_2} + e^{ik \cdot \delta_3}) = t \left[2e^{i\frac{k_x}{2}a} \cos\left(\frac{k_y \sqrt{3}}{2}a\right) + e^{ik_x a} \right] = tf(\mathbf{k}),\end{aligned}\quad (21)$$

where $t = \langle \varphi_A(\mathbf{r} - \mathbf{R}_A) | \mathcal{H} | \varphi_A(\mathbf{r} - \mathbf{R}_B) \rangle$ and the function $f(\mathbf{k})$ is the sum of the phase factors. Similarly, the further off-diagonal element is given by $\mathcal{H}_{BA} = \mathcal{H}_{AB}^* = tf^*(\mathbf{k})$. On the other hand, by using similar arguments, the elements of overlap matrix are given by:

$$\mathcal{S}_{AA} = \mathcal{S}_{BB} = 1, \quad \mathcal{S}_{AB} = sf(\mathbf{k}), \quad \mathcal{S}_{BA} = sf^*(\mathbf{k}), \quad (22)$$

where $s = \langle \varphi_A(\mathbf{r} - \mathbf{R}_A) | \mathcal{S} | \varphi_A(\mathbf{r} - \mathbf{R}_B) \rangle$. Therefore, the secular equation takes the form

$$\begin{aligned}|\mathcal{H} - E\pi\mathcal{S}| &= \begin{vmatrix} \mathcal{H}_{AA} - E\pi\mathcal{S}_{AA} & \mathcal{H}_{AB} - E\pi\mathcal{S}_{AB} \\ \mathcal{H}_{BA} - E\pi\mathcal{S}_{BA} & \mathcal{H}_{BB} - E\pi\mathcal{S}_{BB} \end{vmatrix} = \\ &= \begin{vmatrix} \varepsilon_{2p_z} & (t - E\pi s)f(\mathbf{k}) \\ (t - E\pi s)f^*(\mathbf{k}) & \varepsilon_{2p_z} \end{vmatrix} = 0,\end{aligned}\quad (23)$$

thus obtaining the energy dispersion relation in the form

$$E_{\pi}^{\pm} = \frac{\varepsilon_{2p_z} \pm t\sqrt{|f(\mathbf{k})|}}{1 \pm s\sqrt{|f(\mathbf{k})|}} \approx \varepsilon_{2p_z} \pm t\sqrt{|f(\mathbf{k})|} - s|f(\mathbf{k})| + \dots, \quad (24)$$

where the values for the choice of + or - sign correspond to the energy bands of π and π^* molecular orbital, that is valence and conduction band respectively, and the modulus of the complex function $f(\mathbf{k})$ is given by

$$\begin{aligned}|f(\mathbf{k})| &= 3 + 4 \cos\left(\frac{\sqrt{3}}{2}k_y a\right) \cos\left(\frac{3}{2}k_y a\right) + 2 \cos\left(\sqrt{3}k_y a\right) = \\ &= 1 + 4 \cos\left(\frac{\sqrt{3}}{2}k_y a\right) \cos\left(\frac{3}{2}k_y a\right) + 4 \cos^2\left(\frac{\sqrt{3}}{2}k_y a\right).\end{aligned}\quad (25)$$

The parameters t and s are not uniquely identified, but their values are typically given in the range $t = -(2.8-3.033)$ eV and $s = 0.07-0.129$ eV in order to fit theoretical or experimental data [34]. In addition, the energy for wavevector null $E(\mathbf{0}) = \varepsilon_{2p_z}$ is usually chosen null, but its experimental value corresponds to the work function of graphene with no charge doping equal to $\varphi_{Gr} = -4.6$ eV [36].

A representation of the energy dispersion relations of Eq. 24 is plotted in Fig. 10 for finite values of t and s from Ref. [34]. Some important features of graphene energy bands can be highlighted. For $s \approx 0$, the conduction and the valence bands are asymmetric and thus the electron-hole symmetry is broken. As a result of the symmetry between the A and B sublattices (that is these lattices are composed by the same atomic species), the two bands are not completely separated,

but they are in contact at the K and K' points of Brillouin zone. In particular, the expansion of the full band structure of Eq. 24 close to the K and K' points is isotropic and it is given by

$$E_{\pm}(\mathbf{k}) \approx \pm \hbar v_F |\mathbf{k}| + O[(k/K)^2] = \frac{3}{2} ta |\mathbf{k}|, \quad (26)$$

where $v_F = 3ta/2\hbar \sim 10^6$ m/s is the *Fermi velocity* [34]. At the K and K' points the dispersion relation thereby follows a linear relation, thus resembling the form of an ultrarelativistic particle described by the Dirac equation for effective massless particle [34, 37, 38]. Therefore, the energy bands of graphene at the K and K' points are commonly said *Dirac cones*. Besides, a maximum

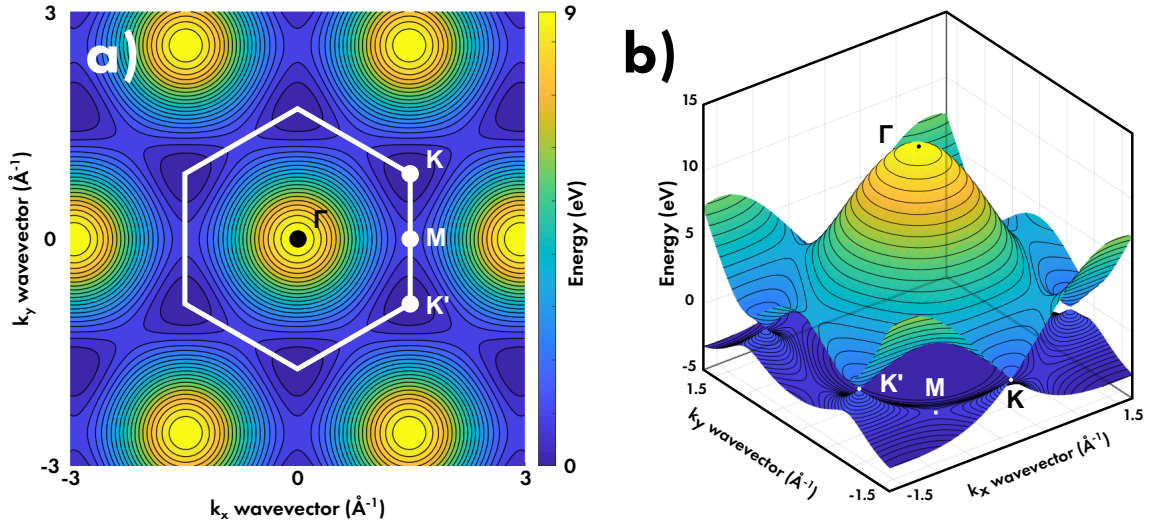


Figure 10: (a) 2D, and (b) 3D surface plots of graphene energy bands for finite values of coefficients in Eq. 24 equal to $t = 2.7$ eV and $s = 0.2t$ and $\varepsilon_{2p_z} = 0$. The high symmetry point Γ , K , K' , and M in the first Brillouin zone (white hexagon) are marked by labels

and a saddle point are determined at the Γ and M , respectively, where in addition a bandgap of ~ 20 eV and ~ 6 eV are found. Due to this feature, graphene is a semiconductor with null bandgap, hence it falls under the category of semimetals. Finally, since the electronic density n is related to the Fermi momentum k_F by the relation $n = k_F^2/\pi$, a relation with Fermi energy can be established in the form [34]

$$E_F = \hbar v_F \sqrt{\pi n}. \quad (27)$$

Since the vibrational spectroscopic features of graphene are closely related to the value of E_F , the Eq. 27 finds wide use in the estimation and in the control of graphene p- or n- type doping [37].

1.3.3 CHARGE CARRIER DENSITY

The dispersion relation $E(\mathbf{k})$ obtained in Eq. 24 provides the information of what energy is allowed for the states in conduction or valence bands at given wave vector \mathbf{k} . However, in order to achieve a complete description of electronic behavior of graphene it is necessary to answer to the following questions [23]:

- how many states exist for a given energy?
- what is the probability of occupation of these states?

Concerning the latter question, due to the fermionic nature of electrons, the probability that a conduction electron of graphene occupies a state at given energy is described by the *Fermi-Dirac distribution* given by

$$f(E) = \frac{1}{1 + e^{\left(\frac{E-E_F}{k_B T}\right)}}, \quad (28)$$

where E_F is the Fermi energy of the system, k_B is the Boltzmann constant, and T is the statistic temperature of the system [39]. This distribution is a step-like function which indicates that the occupation of energy levels placed below E_F has even probability, whereas the occupation probability fades for energy levels placed above E_F . The smoothness of $f(E)$ decreases for ever lower T , up to assume a full step shape.

On the other hand, the way in which the states are distributed on energy, that is their degeneracy, is described by the *density of states* $g(E)$ [23, 39]. Despite an analytic derivation of graphene density of states is possible by assuming $s = 0$ in Eq. 24, only a qualitative discussion is here reported, by taking care to highlight the most relevant aspects concerning graphene: the derivative of dispersion relation $E(\mathbf{k})$, and the reduced dimensionality of the system.

By considering the density of states at a given energy $g(E)$, the number of states at energy between E and $E + dE$ is expressed by $g(E)dE$. This quantity can be obtained by integrating $g(\mathbf{k})d^3\mathbf{k}$, that is the number of states with wavevector between \mathbf{k} and $\mathbf{k} + d\mathbf{k}$ over the entire \mathbf{k} -space [23]

$$g(E)dE = \int g(\mathbf{k})d^3\mathbf{k}. \quad (29)$$

As previously noted, the dimension of the \mathbf{k} -space is equal to the dimension n of real space, and therefore, a hypersurface defined in this space is characterized by dimension $n - 1$. By labelling the electronic states by their wave vector, and by considering the possible states of a system at a given energy E_0 , a corresponding hypersurface $S_k(E_0)$ is selected in the \mathbf{k} -space [23, 39]. The integrand of Eq. 29 can be evaluated as

$$g(\mathbf{k})d^3\mathbf{k} = 2 \frac{\text{volume of } \mathbf{k}\text{-space occupied by states at energy } E_0}{\text{volume of } \mathbf{k}\text{-space occupied by a single state}} = 2 \frac{\delta(E_0 - E(\mathbf{k}))d^3\mathbf{k}}{u_{\mathbf{k}}}, \quad (30)$$

where the factor 2 is due to the spin degeneracy, and thus the Eq. 29 becomes

$$g(E)dE = 2 \int \frac{\delta(E_0 - E(\mathbf{k}))}{u_{\mathbf{k}}} d^3\mathbf{k}. \quad (31)$$

This volume integral can be expressed as a surface integral over the isoenergy surface $S_k(E_0)$. In particular, the volume element $d^3\mathbf{k}$ can be written as $d^2S d\mathbf{k}_{\perp}$. The vector \mathbf{k}_{\perp} is perpendicular to

the surface $S_k(E_0)$, and proportional to the gradient of energy $|\nabla_{\mathbf{k}}E|$. Thence its differential is $dk_{\perp} = 1/|\nabla_{\mathbf{k}}E|dE$, and the Eq. 31 can be given by

$$g(E) = 2 \int_{S_k(E)} \frac{d^2S dk_{\perp}}{u_{\mathbf{k}}} = 2 \int_{S_k(E)} \frac{d^2S}{u_{\mathbf{k}}} \frac{1}{|\nabla_{\mathbf{k}}E(\mathbf{k})|}. \quad (32)$$

In this equation, it is easy to note that, for specific value of \mathbf{k} in which $\nabla_{\mathbf{k}}E(\mathbf{k}) = 0$, that is minima, maxima and saddle points of $E(\mathbf{k})$ the density of states $g(E)$ diverges, giving rise to the so-called *van Hove singularities* [23]. On this basis, for a free gas of electrons of a n -dimensional system, the number of states up to energy $E_F = \hbar^2 k_F^2 / 2m$ is given by the integral

$$N(E_F) = \frac{2}{u_{\mathbf{k}}} \int_0^{k_F} d^n \mathbf{k}. \quad (33)$$

By considering the dependence on the modulus of the wave vector $|\mathbf{k}| = k$ only, the surface element in the second member of Eq. 33 is proportional to the surface of a $(n - 1)$ -sphere

$$d^n \mathbf{k} = \begin{cases} 4\pi k^2 dk, & \text{3D system} & 2\pi k dk, & \text{2D system} \\ dk, & \text{1D system} & \delta(k) dk, & \text{oD system,} \end{cases} \quad (34)$$

The density of states is thereby obtained through the derivative of the solution of Eq. 33 for the various volume elements of Eq. 34. In general, the dependencies on energy obtained for $g(E)$ are given by

$$g(E) = \begin{cases} \propto \sqrt{E}, & \text{3D system} & \propto E^0, & \text{2D system} \\ \propto \frac{1}{\sqrt{E}}, & \text{1D system} & \propto \delta(E), & \text{oD system,} \end{cases} \quad (35)$$

and therefore no general dependence of density of states on energy should be guessed for 2D systems, as for example electrons in graphene.

On the basis of these arguments, it is possible to comment the density of states of graphene reported in Fig. 11. Since the 2D nature of the system no general trend on energy is determined. However, two van Hove singularities are determined by the saddle point for $E(\mathbf{k})$ at the M point (Fig. 10). As mentioned in the discussion of the energy bands, the symmetry between electrons and holes is broken for $s \neq 0$. Such an aspect involves the density of states too, where the density of states for holes is enhanced by the symmetry break. Finally, for ideal graphene the density of states vanishes for $E = \varepsilon_{2p_z}$, whereas for doped graphene non-null contributions can be introduced [40].

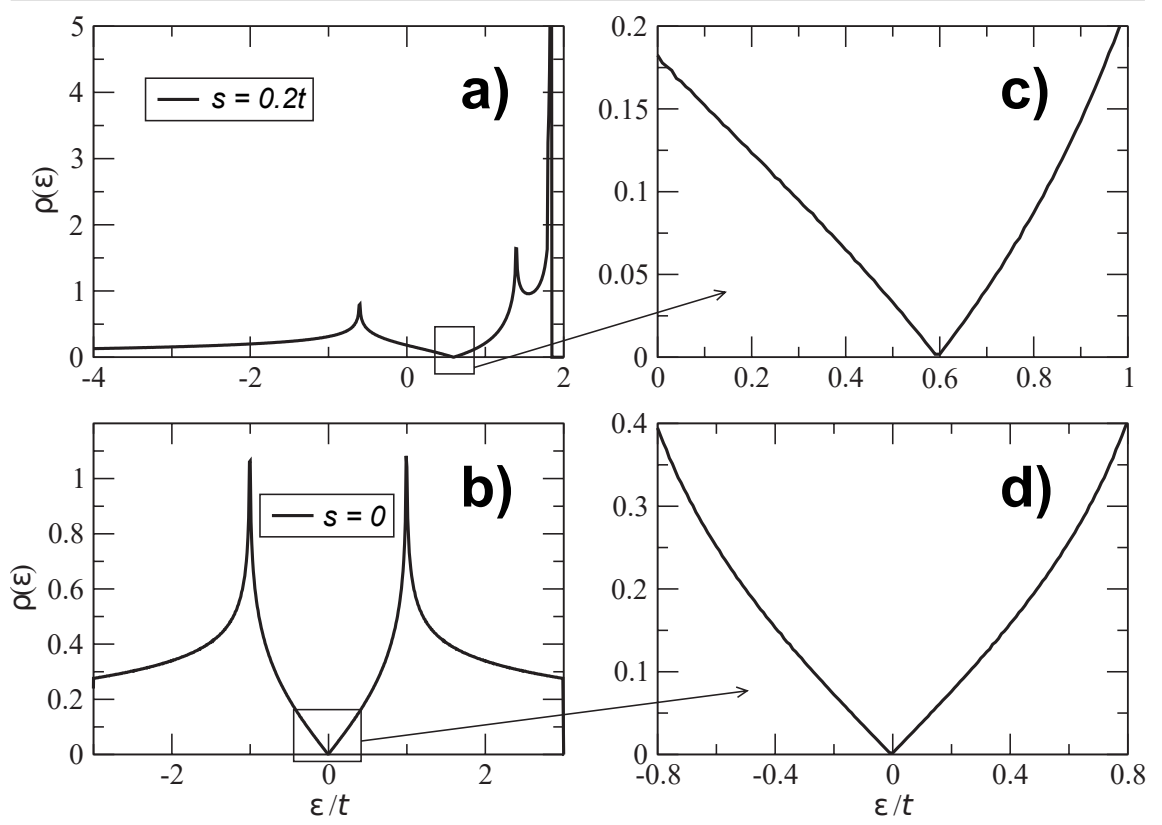


Figure 11: Density of states of graphene calculated by assuming (a) $s \neq 0$, and (b) $s = 0$ in Eq. 24. (c,d) Detailed plot of energy near to ε_{2p_z} . Figure adapted from Ref. [34].

1.4 OPTICAL PROPERTIES

On the basis of the electronic structure, it is possible to properly interpret the optical properties of graphene, thus relating information obtained by various spectroscopies to the electronic structure of graphene. In this section, the optical absorption and the light emission of graphene are briefly described. Since its relevance in the investigation of graphene properties, inelastic light scattering processes, that is Raman scattering, will be discussed in Chp. 3.

1.4.1 LIGHT ABSORPTION

Because of the zero bandgap between valence and conduction bands, graphene absorbs light in a wide range of the electromagnetic spectrum, that is in the far-infrared (FIR), mid-infrared (MIR), near-infrared (NIR), visible, and ultraviolet (UV) spectroscopic region, as illustrated in Fig. 12 [41]. For undoped graphene, the theoretical optical conductivity is found to be independent of frequency and equal to

$$\sigma(\omega) = \frac{\pi e^2}{2h}, \quad (36)$$

where e is the electron charge, and h is the Planck's constant, and the optical absorbance is thereby given by

$$A(\omega) = \frac{4\pi}{c}\sigma(\omega) = \pi\alpha \approx 2.29\%, \quad (37)$$

where c is the speed of light. The optical absorption of graphene is thereby proportional to the fine structure constant α , and equal to about 2.3% of incident light [42, 43]. It is impressive that such an absorption is caused by a single layer of carbon atoms, but since almost all of the light is transmitted, graphene can be still considered a good candidate to be used as transparent conductive layer [3]. However, a simple *white* absorption is nearly restricted to the NIR-visible region because of two critical factors: the Fermi level determined by doping (by which graphene is actually almost always affected, even if unintentionally) and the singularities in the density of states [3, 41, 43]. Due to the large bandgap at the Γ point of the first Brillouin zone, the optical

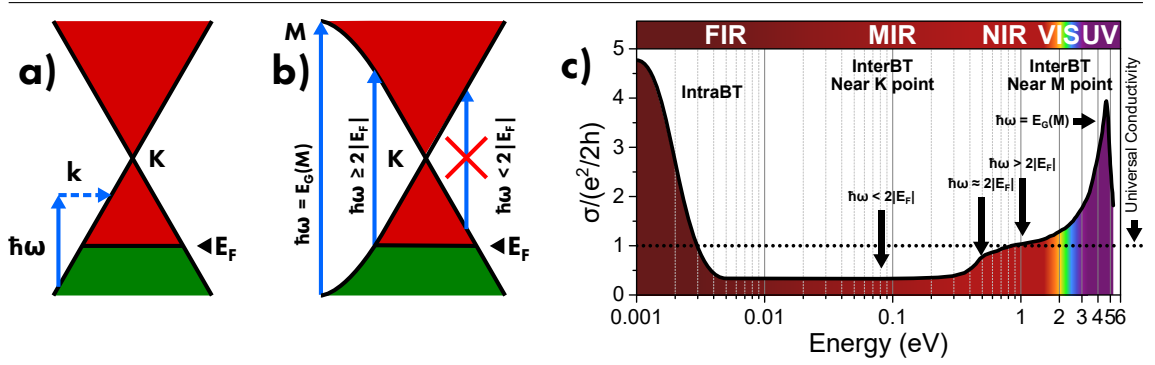


Figure 12: (a) Diagram of intraband light absorption transitions at the K point of graphene Brillouin zone showing the absorption of photons at various energies ($\hbar\omega$, continuous arrows) assisted by phonon/defect scattering (k , dashed arrows). (b) Diagram of interband light absorption transitions at the K and M points showing the absorption of photons at various energies ($\hbar\omega$) for allowed and forbidden transitions. (c) Light absorption of graphene in the far-infrared (FIR), mid-infrared (MIR), near-infrared (NIR), visible (VIS) regions due to intraband and interband transitions at the K point. The effect of non-null graphene Fermi Energy determines the enhancement of absorption in the FIR region and the quenching in the MIR region due to oscillator strength sum rule and Pauli blocking, respectively. Finally, the absorption band in VIS-UV region due to the transition at M point is also reported. Adapted from Refs. [44–46].

phenomena in graphene are related to electron placed near the K and the M points, depending on the amount of energy involved. In particular, at low energy, intraband transitions are activated, whereas interband transitions arise at higher energy [41].

In the FIR region, the optical absorption of graphene is due to intraband indirect transitions, whose diagram is shown in Fig. 12a. In this case, both the start and the final electronic states are placed in the valence band, and a phonons or defect assisted scattering of electrons is required in order to satisfy the momentum conservation. These transitions occur both for free carriers and collective charge carriers (plasmons) [41]. In this case, concerning free carriers, the optical response is described by sheet conductivity obtained in Drude model:

$$\sigma(\omega) = \frac{\sigma_0}{1 + i\omega\tau}, \quad (38)$$

where σ_0 is the conductivity and τ is the electron scattering time. From this quantity the Drude weight $D = \pi\sigma_0/\tau$ is derived, the latter corresponding to the integrated oscillator strength of

free carrier absorption. For the massless electrons of graphene, the Drude weight is given by $D = e^2 v_F \sqrt{\pi n}$, thus relating the intensity of the optical absorption to the charge carrier density n [41]. Concerning plasmons, the absorption is favored by the low effective electron mass in graphene and by the high doping levels attainable in graphene. In this case, an absorption band is found at a specific plasmonic resonance frequency $\omega_p \sim 10^2 \text{ cm}^{-1}$, which value can be tuned by the charge carrier density according to a proportionality relation given by $\omega_p \propto n^{1/4}$ [41, 47].

On the other hand, the optical absorption from MIR and NIR region is related to interband transitions (shown in Fig. 12b) in which the electrons are promoted by the valence band to the conduction band [41]. Contrary to the previous case, also direct transitions are allowed, and the specific weight of direct and indirect transitions depends on light energy: direct processes dominate the low energy transitions ($\hbar\omega \approx 0.1\text{--}2 \text{ eV}$), whereas indirect processes prevail in the case of high energy transition ($\hbar\omega \geq 3 \text{ eV}$) [48]. As in the case of intraband transitions, the features of interband transitions are closely dependent on the doping state of graphene. In fact, as suggested by the diagram shown in Fig. 12b, the lack of electrons in valence band due to p-doping induces Pauli blocking of optical transition at energy lower than $2|E_F|$ [41, 46], and hence the absorption of graphene can be tuned by the doping. For graphene with chemical potential close to its Fermi energy, the sheet conductivity is given by

$$\sigma(\omega) = \frac{\pi e^2}{4h} \left[\tanh\left(\frac{\hbar\omega + 2E_F}{4k_B T}\right) + \tanh\left(\frac{\hbar\omega - 2E_F}{4k_B T}\right) \right], \quad (39)$$

where T is the temperature and k_B is the Boltzmann constant, characterized by a step-trend smoothed by temperature [41]. Therefore, as shown in Fig. 12c, the increase of charge doping induces the formation of an absorption edge, below which no absorption is found, and therefore, as effect of oscillator strength sum rule, the absorbing oscillators lost in the MIR region are transferred to the low energy oscillators in the FIR region [44]. Further specific examples of doping-dependent interband transitions in graphene will be discussed in the following sections.

Finally, in the visible-NUV region, the absorption spectrum of graphene significantly deviates by the universal value $\pi\alpha$, by featuring the broad asymmetric band at about $\hbar\omega_0 = 4.62 \text{ eV}$ shown in Fig. 12c [41]. Such a feature is determined by transitions near the M point, that is the saddle-point of the Brillouin zone, where the density of states features a logarithmic divergence proportional to $-\log|1 - \omega/\omega_0|$. In addition, a many-body effect – that is electron-electron or electron-hole interactions – is involved in this process, thus determining the asymmetry of the considered band [41].

1.4.2 LIGHT EMISSION

Since the lack of bandgap into the band structure of pristine graphene, the photocycle of photoexcited graphene usually ends in non-radiative recombination [41]. In fact, as illustrated in Fig. 13a, the electron-hole pairs generated by interband transition thermalize by rapidly relaxing towards low energy states. In particular, during the relaxation path, electron and holes differentiate their momenta, and hence the radiative recombination is prevented by the lack of momentum conservation. Therefore, the photoluminescence of graphene cannot be revealed in steady state

conditions, but only by means of ultrafast spectroscopy. The emission of thermalized electron-hole pairs features a wide emission profile (Fig. 13b), and decays in various time scales: fast 5–20 fs decay for direct recombination, and slow 100–250 fs and 1 ps decay for phonon assisted recombination [48]. Concerning doped graphene, the probability of radiative recombination of non-thermalized electron-hole pairs is dramatically enhanced. In fact, considering an electron-hole pair excited at energy $\hbar\omega \geq 2|E_F|$, once the electron relaxes at energy lower than $|E_F|$, it will easily find a hole with equal momentum wherewith recombine, as depicted in Fig. 13c. The emission spectrum of doped graphene is shown in Fig. 13d, whose emission peak, placed at $2|E_F|$, is tuned by the doping level.

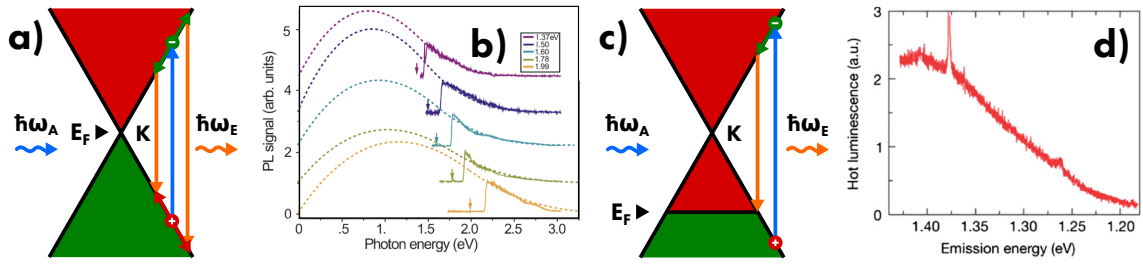


Figure 13: (a) Diagram and (b) spectra of photoluminescence thermalized electrons in graphene. (c) Diagram and (d) spectra of photoluminescence non-thermalized electrons in graphene. Adapted from Refs. [41, 48].

1.5 VIBRATIONAL PROPERTIES

The modification of some graphene properties (obviously structural, but also electronic) is reflected in some deviation from the ideal lattice, and it follows that even the vibrations of lattice change. Therefore, the investigation of graphene cannot ignore the use of some vibrational spectroscopies. As discussed in the previous section, the information provided by IR spectroscopy is mainly related to intraband or interband electronic transitions. For such a reason, Raman spectroscopy is almost exclusively used in order to investigate vibrational properties of graphene.

Raman spectroscopy has emerged as one of the most powerful methods in the investigation of graphene. On the one hand, Raman spectroscopy is an easy technique, is practicable at relatively low costs, no invasiveness, and in various experimental conditions. On the other hand, despite its simple structure, graphene features a very rich Raman spectrum, composed by several well defined bands. As shown in Fig. 14, several bands of graphene are shared with other carbon-based materials but characterized by different features due to the strong sensitivity of Raman spectra to different structures. Concerning graphene, the main Raman bands which are related to one-phonon scattering processes are labeled as G ($\sim 1580 \text{ cm}^{-1}$), and the defect-assisted D ($\sim 1350 \text{ cm}^{-1}$), and D' ($\sim 1620 \text{ cm}^{-1}$). These bands are accompanied by those related to the respective two-phonons processes, 2D ($\sim 2680 \text{ cm}^{-1}$), 2D' ($\sim 3250 \text{ cm}^{-1}$) and some composite bands, D+D' ($\sim 1580 \text{ cm}^{-1}$), and D+D'' ($\sim 2450 \text{ cm}^{-1}$). Thanks to the richness and clarity of the Raman spectrum of graphene, it is possible to use it as fingerprint, and a lot of information can be extracted by whatever anomaly in the band position or intensity [49, 50].

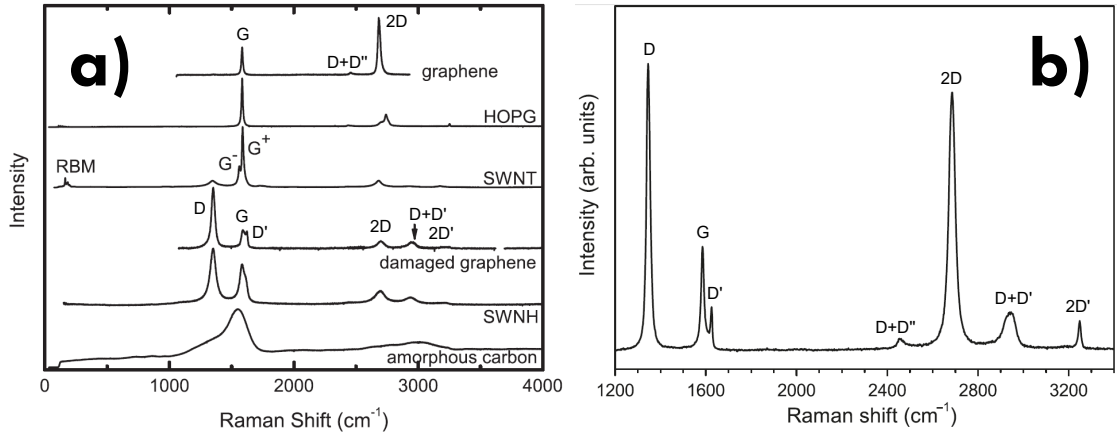


Figure 14: (a) Raman spectra of (top to bottom) monolayer graphene, highly oriented pyrolytic graphite (HOPG), single-wall carbon nanotube (SWNT), single-wall carbon nanohorns (SWNH) and hydrogenated amorphous carbon. The label for the main bands are reported. Adapted from Ref. [49]. (b) Raman spectra of defected monolayer graphene. Adapted from Ref. [50]

In this section, the vibrational properties of graphene are reported with regard to the normal modes and the phonon dispersion which belong to its lattice. These elements will be progressively related to the Raman active modes and to the Raman scattering processes which cause the typical spectrum of graphene. Finally, the relation between spectroscopic features and the properties of interest for this thesis, that is doping and strain, are reported. The theoretical and practical aspects of inelastic light scattering at the basis of Raman spectroscopy will be discussed in a dedicated section of Chp. 3.

1.5.1 NORMAL MODES AND PHONON DISPERSION

The vibrational properties of a material are fundamentally related to the symmetry of the crystalline lattice which constitutes it. In fact, the symmetry is involved in the definition of the main vibrational features, such as phonon dispersion and normal modes. Concerning the latter, they determine every possible vibrations of the lattice. The honeycomb lattice of graphene discussed in Sec. 1.3 is characterized by a symmetry which belongs to the space group $P6/mmm$. The quantized vibrations of graphene, that is the phonons, are labeled by their wavevector q , with modulus q . The latter cannot assume arbitrary values, but is limited to values belonging to the first Brillouine zone of the reciprocal lattice shown in Fig. 9.

The energy, and thus the frequency of phonons in graphene can be given by a force constant model by means of which, in all similar to the case of electrons discussed in Sec. 1.3.2, the dispersion relation between frequency and wavevector and a density of states are obtained [49]. The calculated *branches* are shown in Fig. 15a and labeled in accordance to the kind of motion to which carbon atoms are subjected. In order of decreasing energy, the branches are distinguished as: three optical (O) and three acoustic (A) by involving or not a variation in charge momentum. Among them, one longitudinal (L) and two transverse (T) are distinguished according to whether the atom motion occurs along or perpendicular to the direction of the wavevector. In addition,

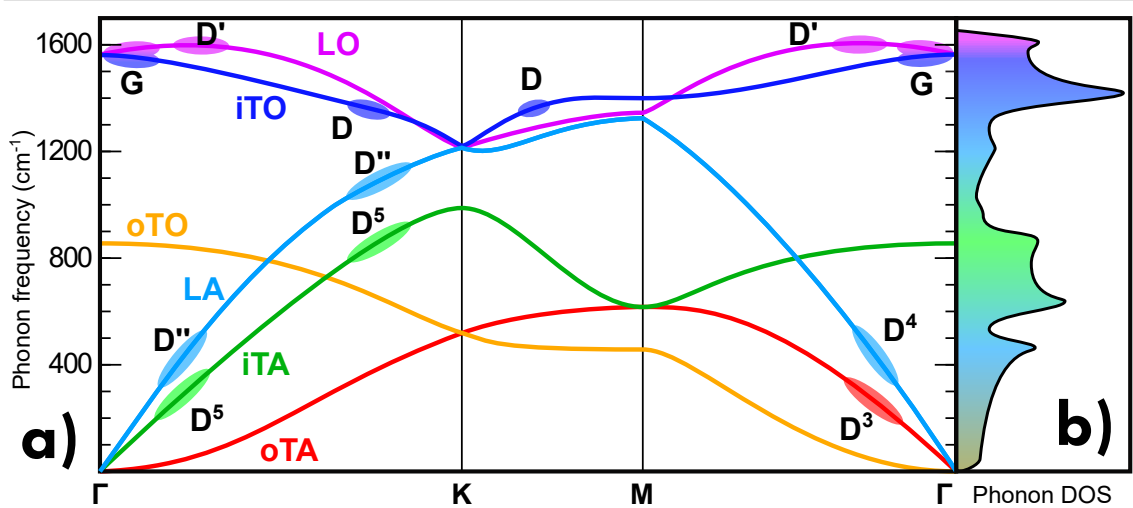


Figure 15: (a) Phonon dispersion relation of graphene along the direction connecting the high-symmetry points Γ , K , and M . Phonon branches are labeled in accordance with their type of atomic displacement. The contribution to Raman scattering is indicated, as well as the corresponding range of phonon wavevector. (b) Phonon density of states (DOS) of graphene. The contribution of Raman mode at different phonon frequency is indicated by color. Adapted from Refs. [51, 52].

for transverse branches only, in-plane (i) or out-of plane (o) are distinguished according to whether the atom motion is in or out of the graphene plane [49].

A key feature is shown by the iTO and LO phonon branches where the so-called *Kohn anomaly* can be observed, that is the presence of cusps at the Γ and K points (Fig. 15a). Such a feature is typically found in metals, due to the relevant electron-phonon coupling, and is thereby a sign of the semimetallic nature of graphene [53–55]. In particular, the motion of nuclei in metals is screened by the electrons, which can be described as a dielectric medium. It is shown that the derivative of phonons frequency is related to the derivative of this dielectric function. As a consequence, any singularity in the dielectric function is reflected to the phonon dispersion. The singularity and thereby the Kohn anomaly may occur for $q = k_1 - k_2$, where k_1 and k_2 are both on the Fermi surface. In graphene, the Fermi level is at $k = K$, and since $K' = 2K$, two Kohn anomalies occur, for $q = \Gamma = 0$ and $q = K$. Finally, the weight of various branches is indicated by the phonon density of states shown in Fig. 15b, thus allowing the assignment of phonon branches to spectroscopic bands [49].

The most relevant vibrational contributions come from phonons near to the Γ and K points. The atom displacement of these modes in graphene is illustrated in Fig. 16. At the Γ point ($q \approx 0$), the wavevector features a symmetry belonging to the point group D_{6h} , to which six normal modes belong: A_{2u} , B_{2g} , E_{1u} , and E_{2g} , with double degeneration for the last two modes. Between them, only the two E_{2g} modes are Raman active modes (Fig. 16a). Besides, at the K point ($q \neq 0$), the wavevector features a symmetry belonging to the point group D_{3h} , to which six normal modes correspond: A'_1 , A'_2 , E' , and E'' with double degeneration for the last two modes (Fig. 16b). In this case, all of these modes are Raman active, albeit they feature different intensity [50].

On the basis of this information, it is possible to assign the Raman bands of graphene to specific phonon branches and atom displacement. Concerning phonons near to the Γ point, the G band corresponds to the two degenerate E_{2g} modes for phonons in the iTO branch. By removing this degeneracy, the G band is splitted in two bands, G^+ and G^- , as in the case of carbon nanotubes

or strained graphene. Moreover, the D' , $2D'$ bands correspond to the two E_{2g} modes for phonons in the LO branch. Concerning phonons near to the K point, the D and $2D$ bands correspond to the A'_1 mode for phonons in the iTO branch, whereas the D'' band corresponds to the mode E' in the LA branch. Finally, the other minor Raman bands (rarely measurable due to their very low signal intensity) D^3 , D^4 , and D^5 correspond to the modes E'' , E' , and A'_2 for phonons in the oTA , LA, and iTA branches, respectively [50].

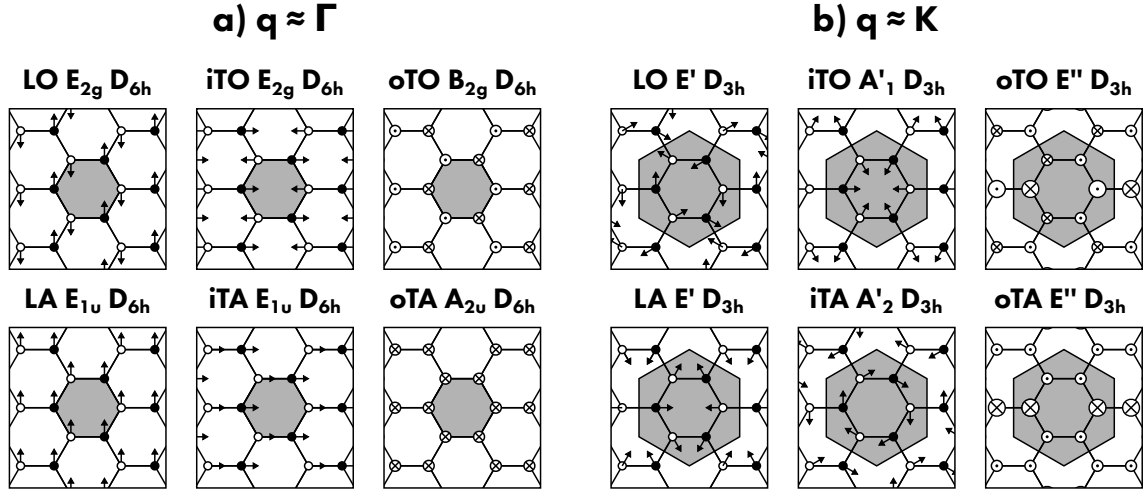


Figure 16: Phonon modes of single-layer graphene at wavevector equal to (a) $q \approx \Gamma$ and (b) $q \approx K$. Each mode is indicated by the symmetry of wavevector, the space group label in Mulliken notation, and by the type of the corresponding atom displacement, Adapted from Refs. [50].

1.5.2 RAMAN SCATTERING PROCESSES

Numerous types of Raman scattering processes occur in graphene. With reference to the types discussed in Chp. 3, graphene features both resonant and non-resonant scattering, as well as one-phonon, two-phonon, and defect-assisted scattering. In addition, intravalley or intervalley scattering occur whether the light-generated electron-hole pair is scattered by a low-wavevector (low- q , for $q \approx \Gamma$) or high-wavevector (high- q , for $q \approx K$), and thus involving electronic states in a single or two Dirac cones, respectively. As illustrated in Fig. 17, the main Raman bands of graphene originate from the following processes [56]:

G BAND: belongs to a single-phonon process, in which a non-resonant electron-hole pair is scattered by a low-wavevector phonon in iTO branch corresponding to the two E_{2g} vibrational modes (Fig. 17a).

D' BAND: belongs to an intravalley defect-assisted single-phonon process, in which a resonant electron-hole pair is scattered by a low- q phonon in LO branch corresponding to the two E' vibrational modes and by a defect (Fig. 17b,c).

$2D'$ BAND: intravalley two-phonon process, in which a resonant electron-hole pair is scattered by two equal low- q phonons in LO branch corresponding to the two E' vibrational modes (Fig. 17d).

D BAND: intervalley defect-assisted one-phonon process, in which a resonant electron-hole pair is scattered by a high- q phonon in iTO branch corresponding to the A'_1 vibrational mode and by a defect (Fig. 17e).

2D BAND: intervalley two-phonon process, in which a resonant electron-hole pair is scattered by two equal high- q phonons in iTO branch corresponding to the A'_1 vibrational mode (Fig. 17f,g).

D+D' BAND: intervalley defect-assisted two-phonon process, in which a resonant electron-hole pair is scattered by two different wavevector phonons, the one at low- q in iTO branch corresponding to the two E' vibrational modes and the other at high- q in the LO branch corresponding to the A'_1 vibrational mode, and by a defect (Fig. 17h).

D+D'' BAND: intervalley defect-assisted two-phonon process, in which a resonant electron-hole pair is scattered by two different wavevector phonons both at high- q value, the one in the iTO corresponding to the two E' vibrational modes and the other in the LA branch corresponding to the E' vibrational mode (Fig. 17f,g).

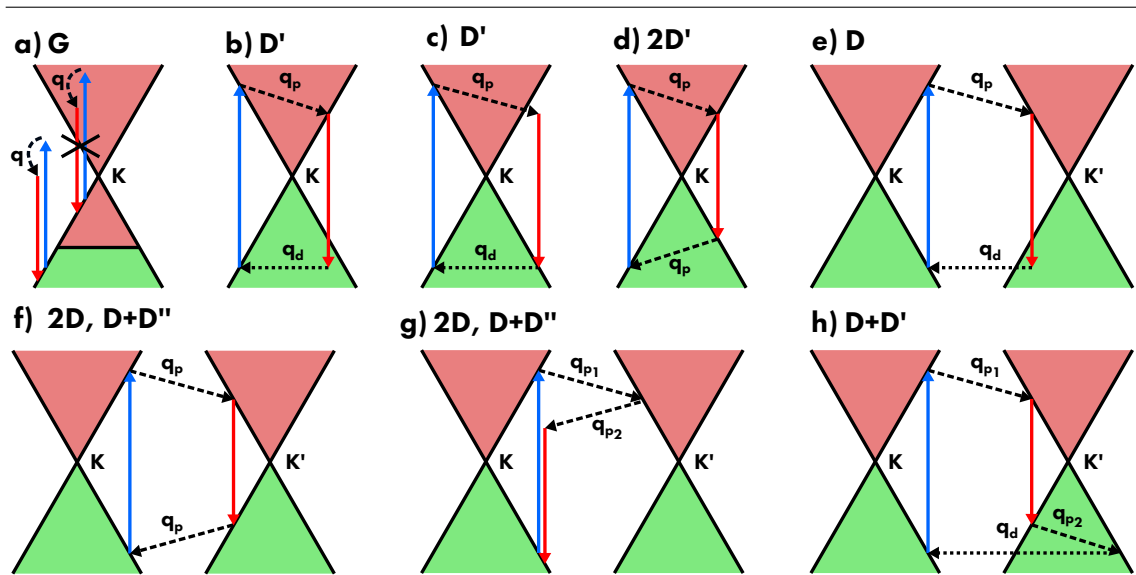


Figure 17: Raman scattering processes in graphene which determine the (a) G band, (b,c) D' band, (d) 2D' band, (e) D band, (f,g) 2D and D+D'' bands, and (h) D+D' band. The light induced electron-hole pair generation and the following recombination are indicated by blue and red arrows, respectively, whereas the phonon (q_p) and the defect (q_d) scattering are indicated by dashed and dotted arrows, respectively. Adapted from Ref. [56].

Only a small portion of all the possible Raman processes are reported in Fig. 17. For example, in the case of D' mode, two scattering processes can occur as shown in Fig. 17b,c, where the two processes differ only in whether scattering (phonon or defect) is in resonance with the electronic states, respectively. This aspect occurs for all of the defect assisted scattering processes above reported. Moreover, the intervalley processes are distinguished in *outer* (not shown) and *inner* (Fig. 17f for 2D mode) depending on the crossing or not of Dirac cones [49, 56].

1.6 INFLUENCING FACTORS ON RAMAN SCATTERING

The specific features of the reported Raman bands are closely dependent on various factors, under whose influence the appearance of Raman spectrum of graphene can vary significantly. Therefore, the monitoring of the Raman spectrum is an important way to obtain information about several properties of graphene, both of morphological and electronic nature. Herein, the most influencing factors are discussed.

1.6.1 LIGHT ENERGY AND POWER

The first influence on the Raman spectrum of graphene to be considered is the dependence of G and 2D peak positions on the features of light used to induce Raman scattering (usually laser sources). Concerning the dependence on the energy, every Raman bands of graphene, except the G band, feature a dispersion of its peak position on using different excitation laser energies, as well as a significant dependence of band intensity [57, 58]. Such a feature can be explained by taking into account the resonant nature of the scattering processes related to these bands [37, 56]. As illustrated in Fig. 18, the variation of laser energy modulates the resonance with the electronic bands of graphene occurring in the scattering processes. For higher energy, the electron-hole pair at k further away from the K point is generated, and hence a different wavevector is necessary for the resonant scattering process. In accordance with the phonon dispersion relation shown in Fig. 15, an higher mode frequency is expected. Near the K point, both the electron and phonon dispersion relations can be approximated by the linear relations $E(k) = \hbar v_F k$ and $E(q) = \hbar v_{ph} q$, respectively, where $v_F = \hbar^{-1} \partial E(k) / \partial k$ and $v_{ph} = \hbar^{-1} \partial E(q) / \partial q$. By the scheme reported in Fig. 18a it is shown that the laser energy can be expressed as, $E_L = 2v_F k$, whereas the energy of single phonon is equal to $E_{ph} = v_{ph} q$, and the wavevector of the scattered phonon is given by $q = k \pm k' \approx 2k$ [49]. Therefore, for the 2D mode in which two phonon scatterings occur, the energy is given by

$$E_{2D} = 2 \frac{v_{ph}}{v_F} E_L, \quad (40)$$

and thereby featuring a linear dispersion with the laser energy reported in Fig. 18b. Finally, be ν_L the laser frequency, the intensity of G band is proportional to ν_L^4 , as usual for Raman scattering. On the contrary, since all the other bands arise from a resonant process, their intensity is fixed. Therefore, the relative intensity between the G band and any other band varies significantly with the laser energy, as shown in Fig. 18c [49, 50].

On the other hand, G and 2D peak position features a significant dispersion with respect to the power of incident light which is related to thermal effects [59, 60]. In fact, the lattice bonds of graphene are softened with the increase of temperature and both G and 2D bands feature a significant redshift and a similar effect can be induced during the Raman measurement. [59, 61]. According to what discussed in the previous sections, a fraction of the incident light is absorbed by graphene and then dissipated by lattice vibration. As depicted in Fig. 18d, the light fraction absorbed increases with laser power thus heating graphene in a well defined region beneath the

laser spot. Consequently, the C–C bond distance increases as effect of thermal expansion thus inducing a redshift in peak position of Raman bands (Fig. 18e) [59, 61]. Some authors have profitably exploited the evolution of G and 2D peak positions with respect to laser power in order to evaluate the thermal conductivity for both suspended and supported graphene. The highest values are obtained for suspended graphene at ambient temperature, for which the thermal conductivity reaches extremely high values: $\kappa \sim 4840\text{--}5300$ W/mK [59], $\kappa \sim 1450\text{--}3600$ W/mK [62], $\kappa \sim 1700\text{--}3200$ W/mK [63]. Besides, the thermal conductivity decreases for higher temperature ($\kappa \sim 920\text{--}1900$ W/mK [62]) and for supported graphene ($\kappa \sim 50\text{--}1020$ W/mK [61]) as effect of the decrease of phonon mean free path [64].

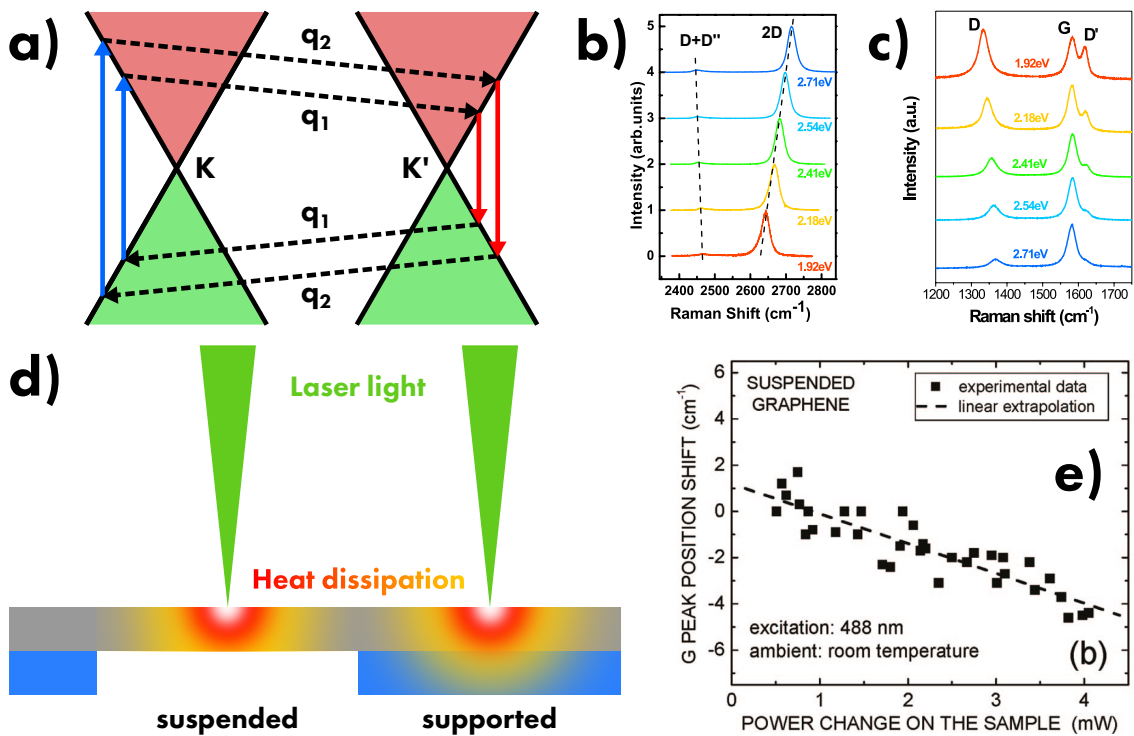


Figure 18: (a) Scheme of laser energy influence on scattering process for 2D mode (b) Peak position dispersion of D+D'' and 2D bands for various laser energies. (c) Intensity change of G band for increasing laser energy, whereas the other resonant bands do not shown any enhancement. Adapted from Refs. [49, 57]. (d) Heat dissipation for suspended and supported graphene. (e) Shift of G peak position as effect of laser power. Reprinted from Ref. [59].

1.6.2 NUMBER OF LAYERS

Since graphene (single-layer system) and the graphite (infinite-layer system) feature a considerably different Raman spectrum, a progressive evolution of the intralayer vibrations is expected for a multi-layer system with arbitrary number of graphene layers. This spectroscopic feature is due to the coupling between the some layers which do not behave as single system, but separately. Therefore, some peculiar new bands related to the relative motion between sheets (that is interlayer vibrations) appear for multi-layer graphene.

Concerning intralayer vibrations, the increasing of the number of layers (evidenced by the increase of optical contrast shown in Fig. 19a), induces the enhancing of G band integrated intensity, as effect of the increase of the number of absorbing atoms (Fig. 19b,c) [37, 65–67]. Besides, 2D

band features a remarkable broadening on increasing the number of layer, thus reporting an ever large full width at half-maximum (FWHM) and an ever lower intensity ratio I_{2D}/I_G (Fig. 19d) [37, 65–68]. The reason of this spectroscopic evolution lies in the splitting of energy bands occurring in multi-layer graphene [37]. In particular, by considering a two-layer graphene, the vertical stacking of graphene sheets splits the conduction and the valence bands in a upper (u) and a lower (l) bands in proximity of the K and K' points because of interlayer coupling, as illustrated in Fig. 19e [37]. Therefore, the scattering process reported in Fig. 17 is converted to four possible

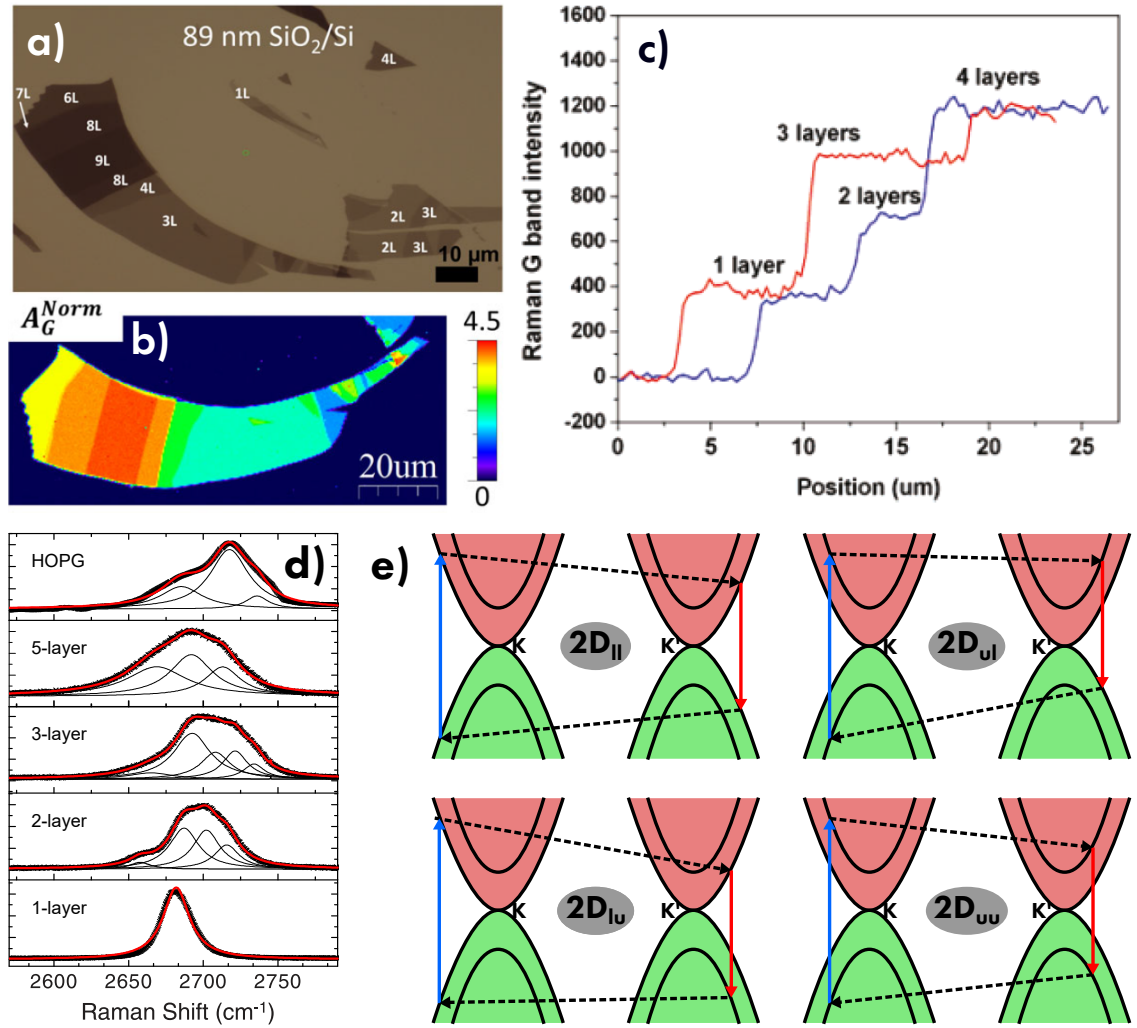


Figure 19: Evolution of (a) optical contrast and (b,c) G band intensity of graphene by increasing the number of layers. Adapted from Refs. [65, 66]. (d) Lorentzian component of 2D band for single-layer graphene, multi-layer graphene and HOPG characterized by various numbers of layer. Reprinted from Ref. [68]. (e) Splitting of conduction and valence band of two-layer graphene where four 2D scattering processes are possible. Adapted from Ref. [37].

processes, hence causing the splitting of 2D band in four close subbands ($2D_{II}$, $2D_{III}$, $2D_{IV}$, and $2D_{V}$), as shown in Fig. 19d. For a n -layer graphene, n^2 scattering processes occurs for 2D band, but their different contributions to the final shape of 2D band cannot be evaluated because of strong energy overlap. For this reason, just more than five layers are enough to get the 2D band almost indistinguishable from the case of graphite [69, 70]. Therefore, by considering the simultaneous increase of G band intensity and the broadening of 2D band with the number of layers, the peak amplitude ratio between 2D and G bands (I_{2D}/I_G) is a easy parameter to rapidly evaluate

the presence of a single-layer graphene. In fact, this is the only case in which $I_{2D}/I_G \geq 1$, whereas G band becomes dominating for every multi-layer graphene. Finally, it is important to notice that the specific stacking of graphene layer influences the splitting of electronic bands and hence the shape of 2D band [37].

In addition, interlayer coupling vanishes for specific alignments, thus obtaining two overlapped and independent graphene sheets. As shown in Fig. 20a, folded graphene features a reduction in Fermi velocity v_F which, according to Eq. 26, modifies the slope of the electronic bands at K point, and thus phonon at higher wavevectors are necessary for the scattering cycle of 2D band [71]. The relation between Fermi energy and 2D frequency shift is thereby given by

$$\frac{dv_F}{v_F} = - \frac{\hbar v_F}{[E_L - \hbar(\omega_{2D}/2)]} \frac{d\omega_{2D}}{dq} d\omega_{2D}, \quad (41)$$

where E_L is the energy of laser, and ω_{2D} is the frequency of the 2D band, which increases on decreasing the Fermi velocity (Fig. 20b) [71].

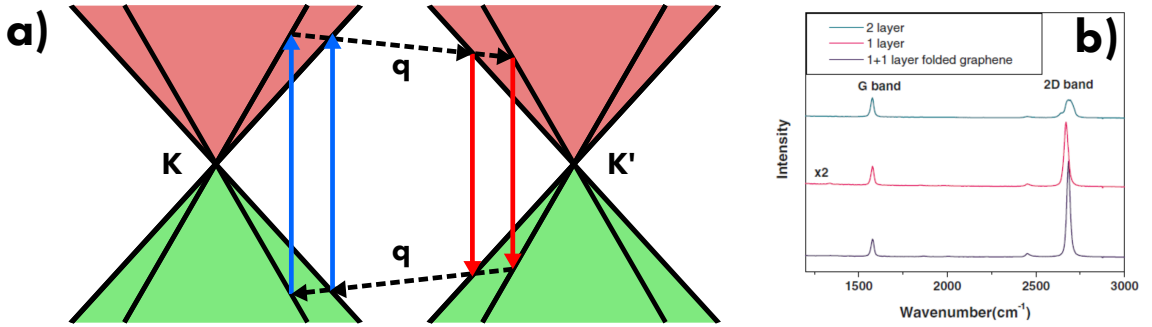


Figure 20: (a) Scheme of Fermi velocity influence on scattering process for 2D mode. The slope decrease is related to graphene folding. (b) Raman spectra of folded graphene compared to single and double-layer graphene. Adapted from Ref. [71].

Concerning interlayer vibrations, the main modes which arise from the relative motion between the graphene sheets are: the shear vibrational mode (C) which corresponds to a low-frequency E_{2g} mode located between 30–44 cm^{-1} depending on the number of layers, and the layer-breathing modes (LBMs) located between 80–300 cm^{-1} [50, 56].

1.6.3 DEFECTS AND DISORDER

Another factor to be considered is the lack of structural integrity, which obviously affects the vibration of a crystal lattice, and therefore, the Raman spectrum of graphene shows pronounced variation due to the presence of defects and disorder of the material.

Concerning the internal region of graphene flakes, various kind of defects can affect the structure of graphene. As shown in Fig. 21a-f, some of them are characterized by the lack of carbon atoms and by the consequent position rearrangement for the remaining atoms [72]. Such defects are typically related to domain-boundary region of graphene, where different crystalline seeds with arbitrary orientation are forced to realize a crystalline continuity [73, 74]. In other

cases, dangling bonds of a vacancy are saturated by other species. In particular, F (fluorinated graphene) and N (N-doped graphene) induced during graphene synthesis [75–79] and implanted metals such as Pt, Pd and Ni are most notable atomic species [80–84]. Besides =O along –OH, –CO and –COOH are typical moieties of graphene oxide (Fig. 21g) [85].

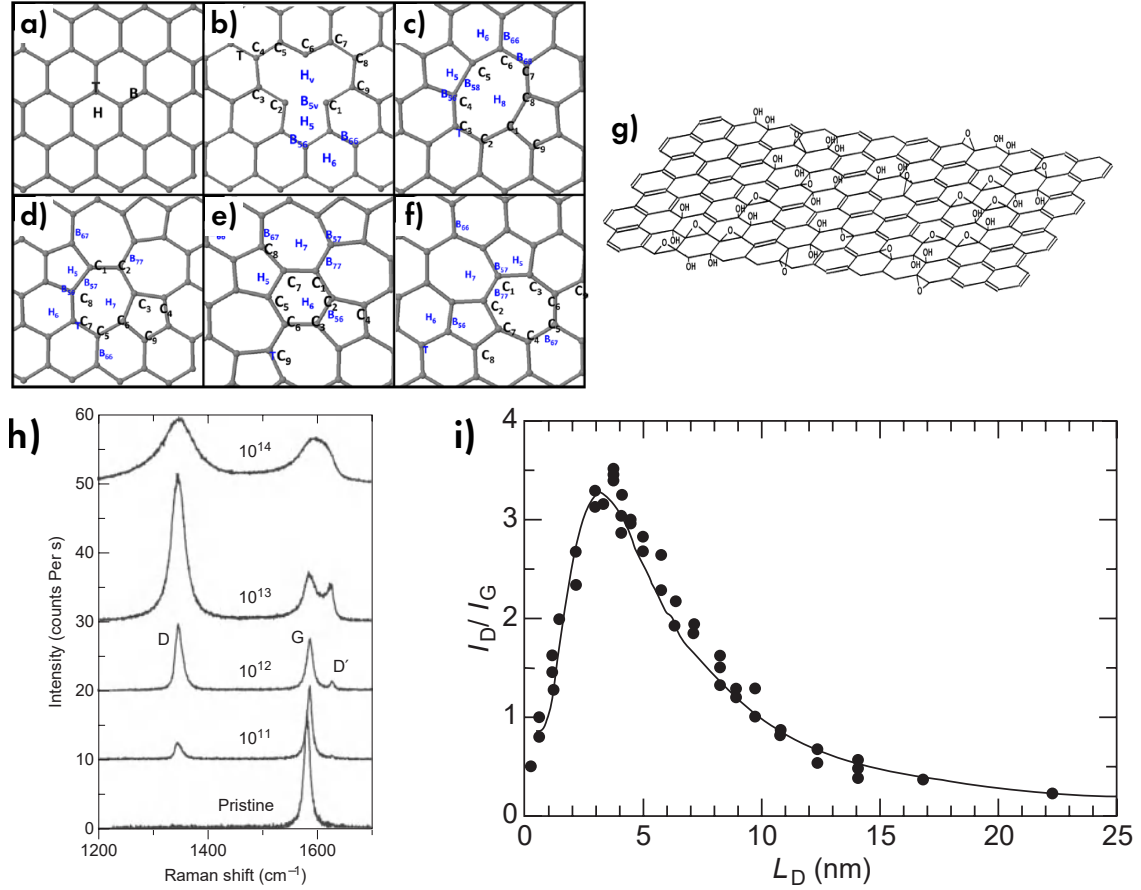


Figure 21: Typical defects in graphene: (a) pristine graphene, (b) monovacancy defect, (c) double-vacancy defect, (d) 555-777 defect, (e) 5555-6-7777 defect, and (f) Stone-Wales defect. Adapted from Ref. [72]. (g) Representative model of graphene oxide. Adapted from Ref. [86]. (h) Raman spectrum of graphene subjected to ion bombardment at various irradiation doses (10^{11} , 10^{12} , ... Ar ions cm^{-2}). (i) Relative intensity between D and G bands (I_D/I_G) on increasing the interdefect distance L_D . Adapted from Ref. [87].

As previously discussed, D and D' band are the main defect-related Raman band of graphene, and their intensity varies considerably with the defect concentration [56, 87, 88]. In fact, as shown in Fig. 21h,i, the generation of defects by ions bombardment on a pristine sample induces the appearance of D band. Moreover, it can be noticed that the increase of D band intensity reaches its maximum, and then decreases at ever higher concentration (evaluated in terms of interdefect distance L_D). Such a nonmonotonic behavior is related to the overlap efficiency between the defect sites. At low defect concentration, D band is active for undamaged zones in proximity of defect and ever more regions can be involved by increasing the defects. Although, at high concentration, the defect starts to compete one each other, and D band is no more enhanced. Finally, at very high concentration, the defects limitate the extension of D-active regions, and D band features a drastically reduced intensity and broadened bandwidth [50, 87, 88]. In addition, since the electron-phonon and the electron-defect scattering events are competitive, the same is

true for the respective Raman bands, and thereby 2D band intensity is reduced by the increase of defects in graphene structure [89].

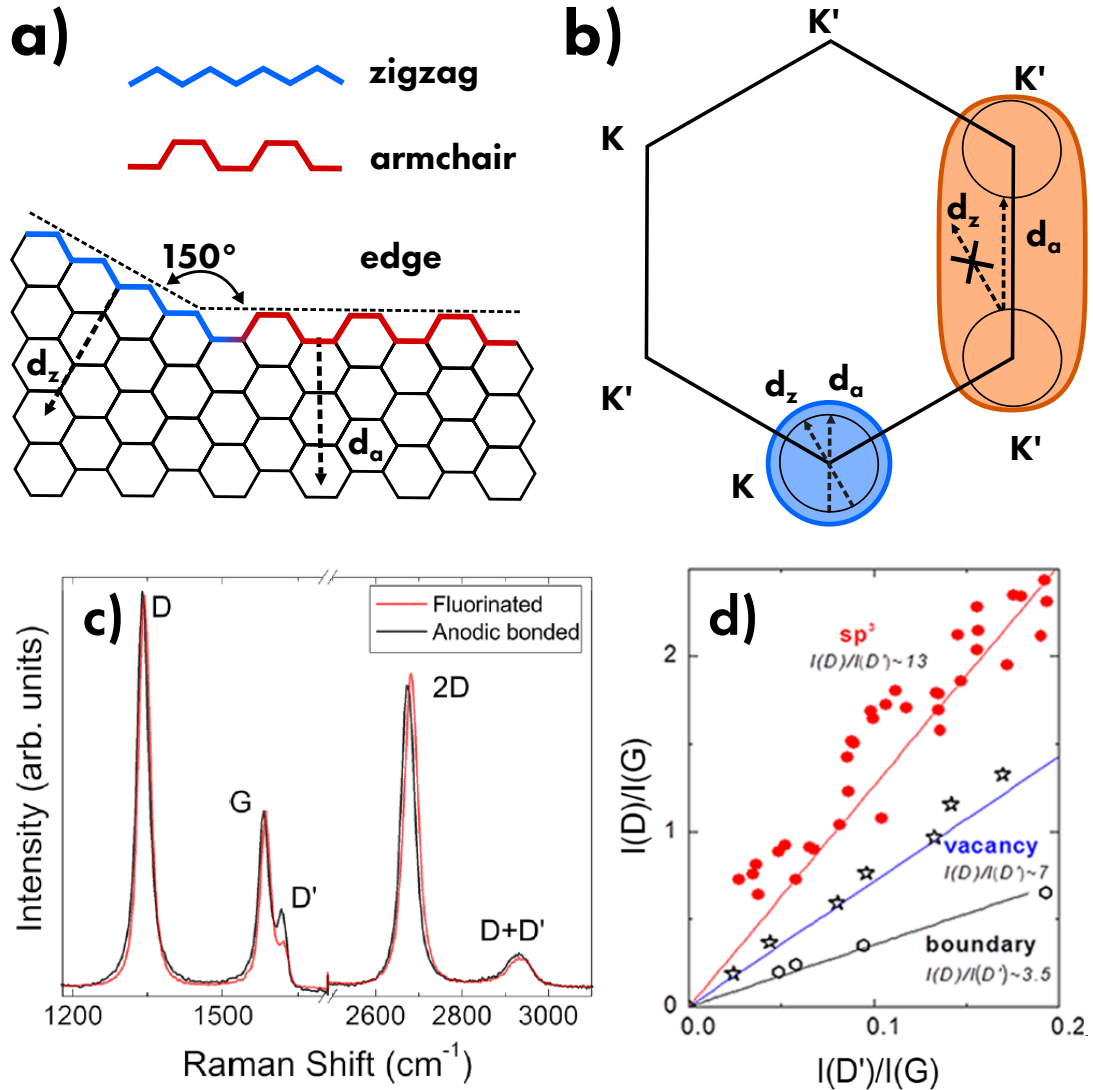


Figure 22: (a) Different edge structures for graphene: zigzag (blue) and armchair (red), and their respective momenta transferred to scattered electrons (d_z and d_a). (b) Wavevector change by scattering at different types of edge, and consequent contribution to Raman scattering bands. Adapted from Ref. [49]. (c) Raman spectra of defective graphene produced by fluorination (saturated defects) and anodic bonding (unsaturated defects). (d) Linear dependence between the $I_D/I_{D'}$ ratio for graphene featuring different types of defects. Adapted from Ref. [90].

As previously mentioned, D and D' bands are the only bands which include an electron-defect scattering event, and both of them can thereby be used as markers of defects and disorder in graphene structure. Since these two bands are characterized by different scattering processes, their features are not a trivial duplicate. Therefore, conspicuous information about graphene structure can be obtained by comparing their spectroscopic features. As shown in Fig. 15, D and D' bands arise from phonons at different wavevector values: low value for D', and high value for the D band. Therefore, as shown in Fig. 17, D band arises from an intervalley scattering process, whereas D' from an intravalley one. Such a feature implies a different contribution for scattering from edge defects at the border of graphene flakes. In fact, as depicted in Fig. 22, when an electron collides with the edge of a flake it is scattered backward, perpendicularly to the edge interface,

and thus the direction of the momentum depends on the type of graphene edge: zigzag (d_z) and armchair (d_a) [49, 91, 92]. As a consequence, both kinds of edge allow intravalley defect scattering which gives rise to D' band, whereas only the armchair boundary allows the intervalley defect scattering related to D band, thus allowing to determine the edge structure on the basis of D band intensity [91, 92]. Both computational and experimental investigation showed the close relation between the intensity of D' band and the specific nature of defects [90, 93], whereas the intensity of D band is mainly due to defect concentration [87, 88]. Therefore, the intensity ratio $I_D/I_{D'}$ can be used as control parameter of defect structure. In particular, D' band intensity increase by inducing vacancy defects, where the $I_D/I_{D'}$ ratio is found maximum. On the contrary the D' band fades in the case of defect saturated by other species, thus enhancing the $I_D/I_{D'}$ ratio as shown in Fig. 22 [90, 93].

1.6.4 STRAIN

Another morphological factor which influences the Raman spectrum of graphene is the mechanical strain to which the material can be subjected. In fact, the application of compressive or tensile strain modifies the volume of graphene and thereby induces a lattice deformation: deviation from a perfect planar geometry in the case of compression, and stretching of lattice in the case of tension. For example, the effect of strain can be observed in the linear dispersion of G and 2D bands shown in Fig. 23.

By modeling the atom bonds of the lattice as a harmonic oscillator, the equation which describes the atom motion is given by

$$M\ddot{u} + ku = 0, \quad (42)$$

where M is the mass of carbon atoms, u is the atom displacement and k is the bond elastic constant characteristic for the system, and whose solution is

$$u(t) = A \cos(\omega_0 t), \quad (43)$$

where A is the oscillation amplitude, and $\omega_0 = \sqrt{k/M}$ is the oscillation frequency. The strain of a material is typically described in the linear displacement regime, that is by applying an external force linearly proportional to the atom displacement $F_e = \lambda u$. Therefore, the Eq. 42 becomes:

$$M\ddot{u} + ku - \lambda u = M\ddot{u} + (k - \lambda)u = 0, \quad (44)$$

whose solution for $k - \lambda > 0$ is

$$u(t) = A \cos(\omega_1 t), \quad \omega_1 = \sqrt{(k - \lambda)/M}. \quad (45)$$

and thereby the effect of strain is only the modification of the oscillation frequency. More generally, the equation describing the strain applied on a material can be expressed as

$$M\ddot{u}_i + ku_i + \sum_{klm} K_{iklm} \varepsilon_{lm} u_k = 0, \quad (46)$$

where ε_{lm} are the elements of the second rank tensor of strain and $K_{iklm} = \partial K_{ik} / \partial \varepsilon_{lm}$ are the elements of the fourth rank tensor which gives the change in the elastic constant element K_{ik} between the displacements u_i and u_k due to ε_{lm} . The strain tensor in its diagonal form has elements ε_{ll} and ε_{tt} , which take into account the longitudinal (l) or transverse (t) orientation between strain and phonon propagating direction [49]. By considering the symmetry of the vibrational mode E_{2g} , the solution of Eq. 46 for G band (which splits in the G^+ and G^-) in the case of uniaxial strain is given by

$$\frac{\partial \omega}{\omega_{G^\pm}^0} = \gamma_G (\varepsilon_{ll} + \varepsilon_{tt}) \pm \frac{1}{2} \beta_G (\varepsilon_{ll} - \varepsilon_{tt}) = -\frac{1}{\omega_{G^\pm}^0} \frac{\partial \omega}{\varepsilon_h} \varepsilon_h - \frac{1}{\omega_{G^\pm}^0} \frac{\partial \omega}{\varepsilon_s} \varepsilon_s, \quad (47)$$

thus obtaining the dispersion of G band peak by applying strain [94]. In Eq. 47, $\omega_{G^\pm}^0 = \omega_G$ is the mode frequency for unstrained graphene, the Grüneisen parameter γ_G describes the G frequency shift due to hydrostatic strain $\varepsilon_h = \varepsilon_{ll} + \varepsilon_{tt}$, and the parameter β_G describes the G frequency shift due to shear strain $\varepsilon_s = \varepsilon_{ll} - \varepsilon_{tt}$ [49]. In the case of biaxial strain $\varepsilon_{ll} = \varepsilon_{tt}$, and thence the Eq. 47 reduces to

$$\frac{\partial \omega}{\omega_G^0} = -2\varepsilon \gamma_G \quad [94]. \quad (48)$$

On the other hand, by considering the symmetry of the vibrational mode A'_1 , the solution of Eq. 46 for 2D band in the case of both uniaxial and biaxial strain is given by

$$\frac{\partial \omega}{\omega_{2D}^0} = -4\varepsilon \gamma_{2D} \quad [94]. \quad (49)$$

A linear dispersion of peak frequency by strain is thereby obtained for both G and 2D bands, in agreement with the data reported in Fig. 23. However, such linear relation is largely limited to tensile strain and for compressive strain lower than 0.4%, whereas non-linear behavior starts for further compression [94, 95]. Moreover, unexpected behavior are found for graphene flakes affected by domain-boundary [74].

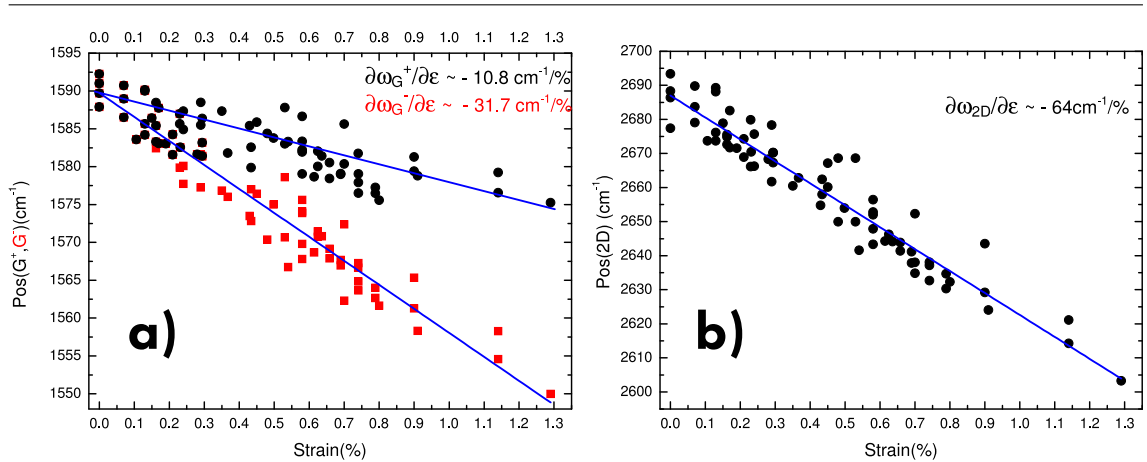


Figure 23: Modification of peak frequency of (a) G, and (b) 2D bands as effect of uniaxial strain. In the former panel, the splitting of G band in G^+ and G^- bands can be observed. Adapted from Ref. [94].

1.6.5 DOPING

Finally, one of the most relevant influence factors is the charge doping (that is the variation in the population of electronic states of the material) especially as regards G and the 2D band features. As previously mentioned, iTO and LO phonon modes feature a strong coupling with electrons, as attested by the presence of the Kohn anomaly at Γ and K points for these branches. On the basis of this coupling, phonons and electrons renormalize their energy as effect of a mutual interaction, which manifests itself in the phonon decay in virtual electron-hole pair (Fig. 24a) [49, 89]. The phonon dependence on the electron-phonon interaction can be evaluated by using second-order perturbation theory [49]. For a vibrational mode λ , the phonon frequency is written as

$$\hbar\omega_\lambda = \hbar\omega_\lambda^0 + \hbar\omega_\lambda^I = \hbar\omega_\lambda^0 + \hbar\Delta\omega_\lambda, \quad (50)$$

where ω_λ^0 is the unperturbed phonon frequency, and $\omega_\lambda^I = \Delta\omega_\lambda$ is the frequency variation given by the second order perturbation term which provides the phonon frequency shift. The latter quantity and the phonon bandwidth Γ_λ (due to finite phonon lifetime) are given by

$$\hbar\Delta\omega_\lambda = \text{Re}\{\Pi(E_F)\} \quad (51)$$

$$\Gamma_\lambda = \text{Im}\{\Pi(E_F)\}, \quad (52)$$

that is the real and imaginary parts of photon self-energy Π equal to

$$\Pi(E_F) = 2 \sum_{\mathbf{k}} \frac{|\langle eh(\mathbf{k})|H_{int}|\omega_\lambda\rangle|^2}{\hbar\omega_\lambda^0 - E + i\Gamma_\lambda} \cdot \left(f(E_h(\mathbf{k}) - E_F) - f(E_e(\mathbf{k}) - E_F) \right), \quad (53)$$

where $\langle eh(\mathbf{k})|H_{int}|\omega_\lambda\rangle$ is the matrix element for creating an electron-hole pair at momentum

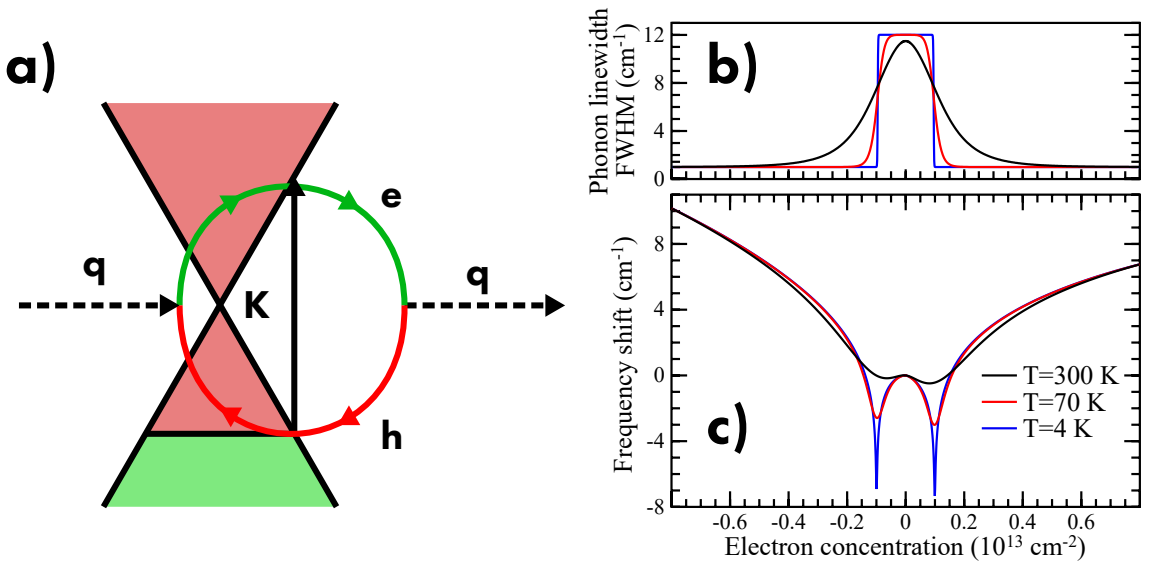


Figure 24: (a) Interaction between phonon and virtual electron-hole pair. Modification of (b) bandwidth (c) peak frequency for G band on varying the doping. Adapted from Ref. [53].

k by means of phonon ω_λ , $E_h(\mathbf{k})$ and $E_e(\mathbf{k})$ are the hole and electron energies, and Γ_λ is the decay induced bandwidth [37, 49]. Therefore, both the phonon frequency and bandwidth depend on Fermi energy E_F .

The calculated curve for G phonon frequency and bandwidth on varying Fermi energy via doping concentration are shown in Fig. 24b,c. By increasing doping, since the phonon cannot decay in an electron-hole pair at energy lower than $2|E_F|$, the lifetime of the phonon increases and the bandwidth fades (Fig. 24a). Besides, the phonon frequency is softened for $|E_F| \leq \hbar\omega_G^0/2$, whereas is stiffened for higher energy. For low doping, the modification of ω_G is nearly linear and symmetric under p and n-doping. On the contrary, high p-doping induces an ever greater stiffening, while a further softening is found for high n-doping [49, 53, 89, 96]. This behavior is in accordance with experimental data reported in Fig. 25. Concerning 2D phonon, its frequency is

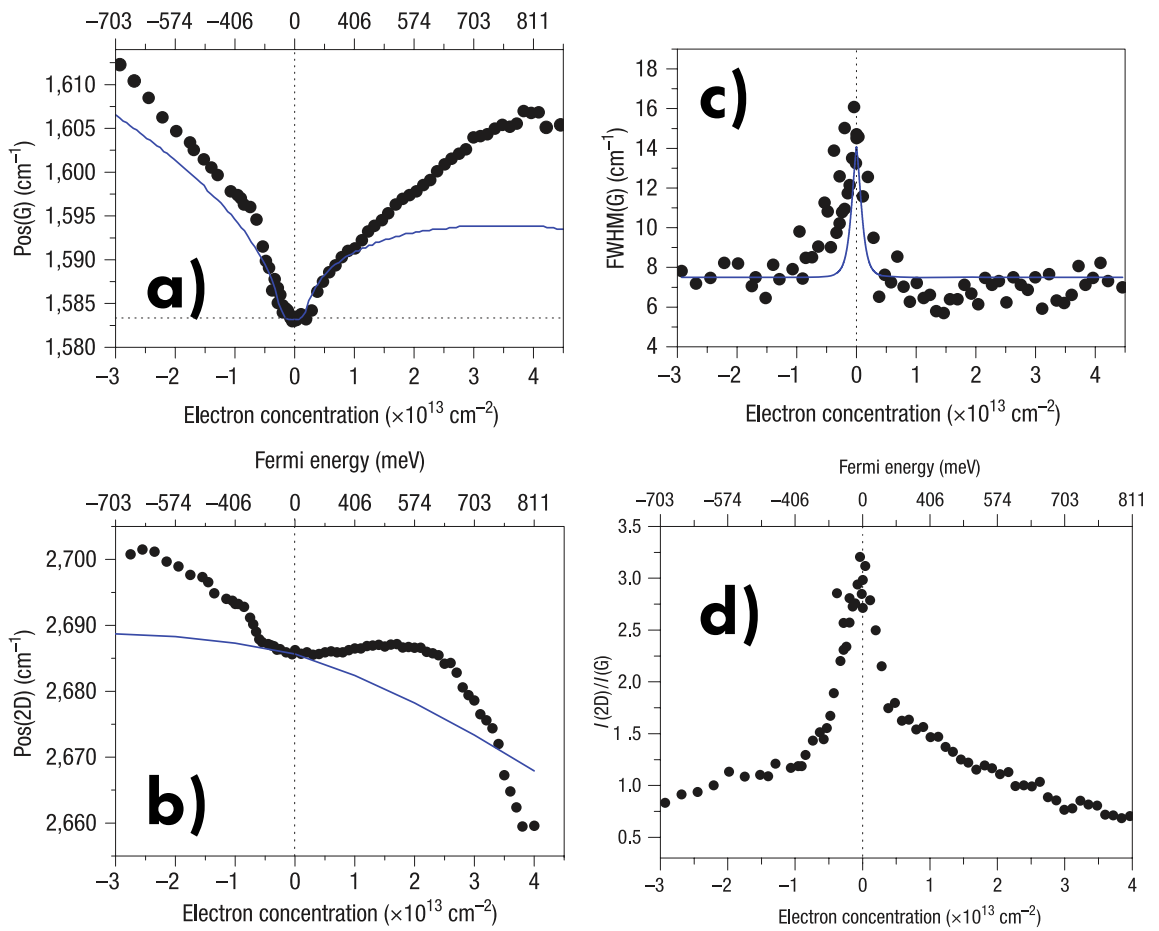


Figure 25: Modification of peak frequency of (a) G band and (b) 2D band, (c) G bandwidth, and (d) ratio between G and 2D integrated intensity for graphene doped by gate voltage application. Adapted from Ref. [96].

affected by doping similarly to the case of G phonon, albeit with different ranges of linearity. In particular, the 2D frequency varies almost linearly at low doping, but softens significantly even at moderate n-doping (Fig. 25) [89, 96].

Finally, a further quantity sensitive to doping is the integrated intensity of Raman bands, as shown in Fig. 25. In particular, whether the intensity of G band does not depend on doping, the

intensity of 2D band is clearly reduced by the increase of doping, both of p- and n-type. In fact, under the assumption of a fully resonant process, the intensity of 2D band can be written as

$$I_{2D} \propto \left(\frac{\gamma_K}{\gamma_{e-ph} + \gamma_D + \gamma_{ee}} \right)^2, \quad (54)$$

where γ_{e-ph} is the electron-phonon scattering rate, γ_D is the electron-defect scattering rate, and γ_{ee} is the electron-electron scattering rate [89, 96]. Between those terms, only γ_{ee} depends on Fermi energy, by scaling linearly with it, and I_{2D} decreases on the increase of doping. Therefore, the relative intensity between G and 2D bands I_{2D}/I_G is used to monitor the doping. The intrinsic value for undoped graphene has been evaluated to be $I_{2D}/I_G = 12-17$, but this prediction agrees only for suspended graphene, since in the case of substrate-supported graphene, the interference effects must be included [89, 97, 98]. Considering a typical substrate composed by 285 nm of amorphous SiO₂ grown on a Si wafer, the interference effects reduce the value down to $I_{2D}/I_G \approx 5$. Nevertheless, lower values are typically found in experiments, as effect of unintentional p-doping induced by the interaction with the substrate surface charges [89, 99–101].

Despite the peak frequency shifts of G and 2D bands mark the actual doping in graphene samples, such an evaluation can be distorted by concurrent occurrence of other effects on these bands, such as folding or strain in graphene sheet. Nevertheless, according to the recent literature, the different contribution σ of the various effects can be partially disentangled by using a method developed by the author of Refs. [102–104]. Herein, the shifts of G and 2D band are analyzed by using a *G-2D map* obtained by plotting the peak position of 2D band vs that of G band (see Fig. 26a), and each given spectrum is represented by a single point on this map. Therefrom, the contributions of doping and strain are evaluated by decomposing the position of this point against two main axes which are traced according to the single dependence on doping (different for p or n type) and strain (both tensile and compressive). The intersection between these

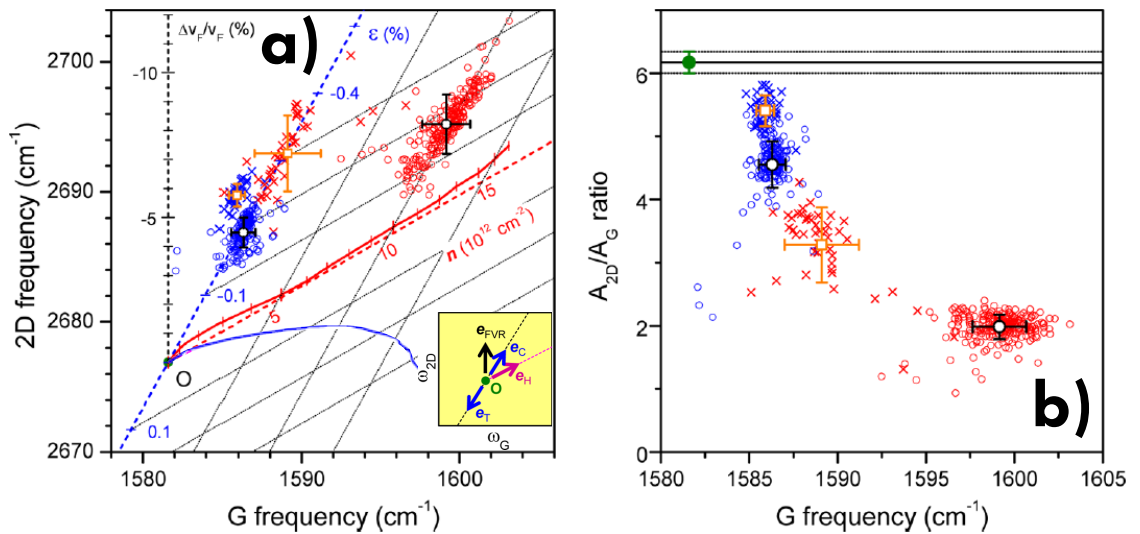


Figure 26: (a) G-2D map of graphene in various doping and strain configurations. Each point corresponds to a given G and 2D peak position extracted from a given spectrum. The map is described by three independent axes: doping (n) by distinguishing between p (red) or n (blue) doping, strain (ϵ), and Fermi velocity variation ($\Delta v_F/v_F$, black) (b) doping influence on I_{2D}/I_G . Adapted from Refs. [102, 103].

axes corresponds to the *ideal* unstrained and undoped configuration of graphene. Thence, every points at the right side of strain axis can be decomposed against these axes evaluating the different contribution of doping and strain. Besides, the points placed at the left of the strain axis require a further axis, namely the Fermi velocity axis, since neither doping or strain can describe this zone of the map. Compared to the easy evaluation of doping obtained by the I_{2D}/I_G ratio, the reported procedure gives some advantages and disadvantages. In fact, I_{2D}/I_G depends only by doping and its evaluation is not affected by other phenomena. On the other hand, the G-2D map provides a more accurate evaluation of doping levels, and in some cases it allows to better discriminate between p or n-doping. Nevertheless, the simultaneous occurrence of strain, doping and Fermi velocity variation cannot be disentangled. Therefore, this method requires that at least one of these parameters keep (or it is assumed to be) unmodified [102, 103].

1.7 TRANSPORT PROPERTIES

One of the reasons of the great interest in the implementation of graphene in microelectronic devices lies in its promising performances in both electrical and thermal transport phenomena. The key aspects concerning these properties are briefly described in the following.

According to the description of its band structure, graphene is a semimetal, that is a zero-gap semiconductor. The most appreciated electrical property of graphene is its very high charge mobility, which features values between $5 \times 10^4 \text{ cm}^2(\text{Vs})^{-1}$ (at 300 K) and $20 \times 10^4 \text{ cm}^2(\text{Vs})^{-1}$ (at 4 K), much higher than those reported for silicon and copper [105]. The mobility is related to the other electrical quantities by the relation $\sigma = qN\mu = 1/\rho$, where q is the charge, σ is the electric conductivity, that is the inverse of the electrical resistivity ρ , N the charge carrier concentration, and μ the carrier mobility [105]. Among these parameters, charge carrier concentration is the most manageable, since it can be driven by varying the top-gate voltage V_g applied to a graphene sheet included in a field effect transistor [1, 96, 106]. In particular, the electrical conductivity of graphene reported in Fig. 27a features a linear dependence on gate voltage with an ambipolar behavior due to the capability of conduction of both electrons and holes in graphene. Its numerical value changes from a maximum of $60 \text{ m}\Omega^{-1}$ up to the minimum of about $\sigma_{\min} \approx 4e^2/h \approx 2.5 \text{ m}\Omega^{-1}$ in correspondence of the charge neutrality point (NCP), that is when the Fermi level is placed at the Dirac point $E_F = E(\mathbf{K})$. Therefore, the manipulation of the intrinsic doping of graphene can be unambiguously monitored by the voltage shift of NCP [1, 50, 105]. Furthermore, the values of the physical quantities above reported feature an important dependence on both charge doping and temperature. As shown in Fig. 27b, the resistivity of graphene features a peak in correspondence of the NCP, and its height is determined by temperature in the range of $\text{k}\Omega$. On the contrary, consistent electron or hole doping reduces the resistivity down to few $100 \text{ }\Omega$ [1, 37]. Besides, in the case of hole doping obtained by charged-impurity (revealed by the shift of the NCP voltage) the charge mobility decreases from $1.32 \times 10^4 \text{ cm}^2(\text{Vs})^{-1}$ to $0.081 \times 10^4 \text{ cm}^2(\text{Vs})^{-1}$ (Fig. 27a) [50, 107].

Similar to other metallic materials, both lattice and charge carriers contribute to the thermal transport of graphene. By considering the Wiedemann-Franz law which relates the temperature

to the electronic thermal and electrical conductivity $\kappa_e = LT\sigma$ (where $L = 2.44 \times 10^{-8} \text{V}^2\text{K}^{-2}$ is the Lorentz number) a high thermal conductivity is expected for suspended graphene, which in fact shows impressive values between 2000 and 5000 $\text{W}(\text{mK})^{-1}$, thus outstanding both metals such as copper, and other notable nanomaterials such as carbon nanotubes [105, 107, 108]. However, the transfer of graphene on a support substrate as for example SiO_2 drastically reduces its thermal conductivity down to 300–400 $\text{W}(\text{mK})^{-1}$ as effect of phonon coupling [64, 108–110].

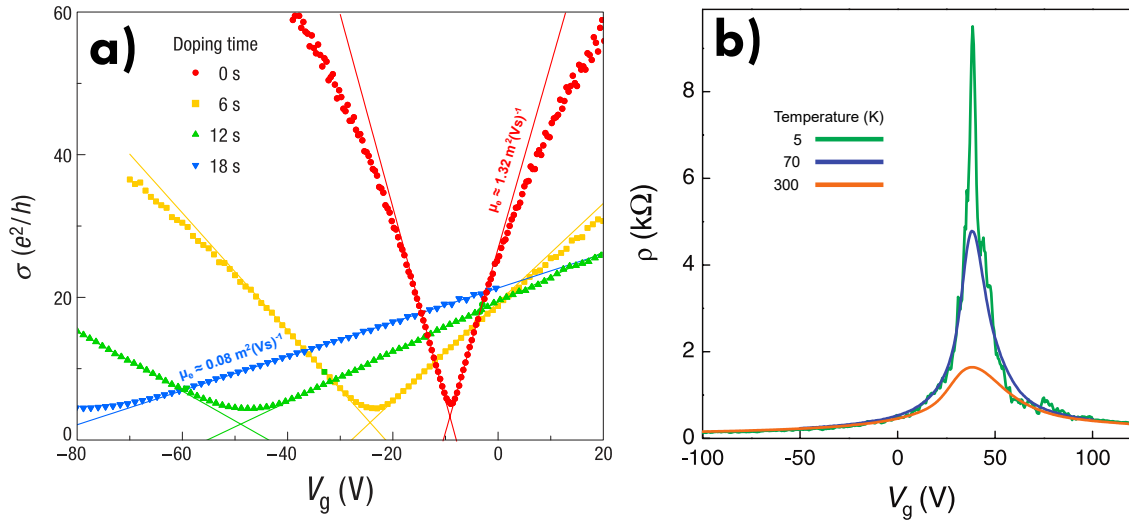


Figure 27: (a) Conductivity σ versus gate voltage V_g of graphene with different doping concentration. (b) Dependence of few layer graphene resistivity ρ on gate voltage V_g for different temperatures. Adapted from Ref. [1, 106].

1.8 SYNTHESIS METHODS

Since the first isolation of graphene carried out by Novoselov and Geim in 2004 [1], a plethora of production methods have been developed, by exploiting a large variety of physical or chemical phenomena. Currently, these methods show different and complementary characteristics, but none of them can comply all the possible requirements, for example large extension, large production, defect-free structure, functionalization, cleanliness from impurities, low costs. Therefore, case by case the choice between them is driven by evaluating which method is better suitable for a specific application. In general, the methods developed until now can be grouped in two categories depending on the direction of the manufacturing process: *bottom up* methods, which start from molecular precursor that are assembled together to build up objects of higher hierarchical level, and *top down* methods, in which macroscopic materials are reduced to their nanometric constituting elements or used as raw material, as in the case of graphite and waste plastic for graphene, respectively [18, 111, 112]. Some of the most common synthesis methods of graphene are described in the following.

1.8.1 TOP DOWN

MECHANICAL EXFOLIATION based on the separation of single graphene sheets which constitute graphite, and thanks to its simplicity this method was used for the discovery of

graphene [1]. On its favor, it produces the highest quality graphene thanks to the high purity of graphite, and it is a relatively easy procedure since the vertical stacking of graphene sheets is assured only by weak van der Waals interactions. For this reason this technique can be extended to other van der Waals heterostructures, such as transition metal dichalcogenide (MoS_2 , MoSe_2 , TiSe_2 , WSe_2). However, this method is limited by two main factors: small amount of product and exiguous extension of graphene flakes (the latter factor bypassable by using of HOPG as raw material) [37]. In detail, the direct manipulation of top graphene sheet on the graphite can be performed both by scotch tape and by tips originally produced for scanning probe microscopy [37, 111].

LIQUID-PHASE EXFOLIATION in this case the exfoliation procedure is performed in liquid-phase, and the separation of the graphene sheets is obtained by sonication [37, 111, 112]. This procedure is preferable to mechanical exfoliation since in comparison it produces a large quantity of graphene flakes with larger lateral size. By contrast, the most critical issue consists in the damaging of the internal structure of graphene flakes in which some defects can be induced. However, some investigations have shown that this undesired effect can be avoided by putting in solution some specific chemicals, such as surfactants [113] or intercalating molecules [114]. In this way it is possible to facilitate the exfoliation and thus requires weaker sonication [37, 112].

ELECTROCHEMICAL EXFOLIATION performed in liquid-phase as the previous method, but based on the use of a graphite source (usually HOPG) as electrodes in an electrolyte solution. In this case the produced graphene features low defect concentration because the sheets separation is induced by the electrochemical reaction rather than by mechanical waves, thus assuring the production of a high quality graphene [112].

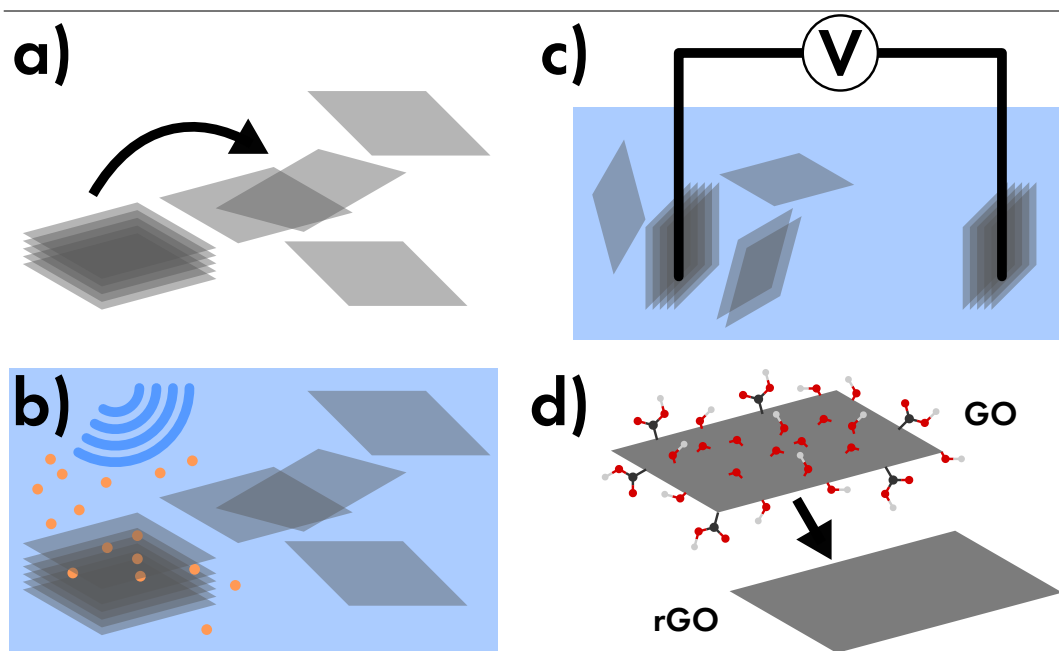


Figure 28: Graphene produced by (a) mechanical exfoliation, (b) liquid-phase exfoliation, (c) electrochemical exfoliation, and (d) reduced graphene oxide (rGO) obtained from graphene oxide (GO).

GRAPHENE OXIDE REDUCTION uses graphene oxide (GO) as main precursor. GO is usually obtained by many methods, such as from the exfoliation of graphite oxide (*Hummer's method*) which follows a top down strategy [115], or by using glucose as source (*Tang-Lau method*) according to a bottom up strategy [116]. Concerning the first case, the exfoliation of graphite oxide is easier than that of native graphite, thus featuring notable advantages with its respect [112]. Both chemical or thermal approaches can be exploited for the reduction of GO (Fig. 28d) and the quality of graphene is determined by the degree of reduction actually reached, usually never complete [117, 118]. Some authors usually call this material *graphene* but it should be referred as *reduced graphene oxide* (rGO) because of its peculiar properties. In fact, rGO significantly differs from *actual* graphene, and it is thereby preferred for applications which take profit from the presence of functional groups onto graphene (optical and liquid application), rather than in those in which a high purity level is mandatory (solid state microelectronic) [85, 86].

1.8.2 BOTTOM UP

CHEMICAL VAPOR DEPOSITION (CVD) is one of the most common methods for the production of graphene for microelectronic application both because the excellent features of the produced graphene and because it makes use of technologies well established in microelectronics industry. In particular, a mixture of molecular hydrogen and small hydrocarbon as carbon source (methane, ethane) are used to grow layer by layer the largest high-quality graphene flakes onto various substrates made by transition metals (Cu, Ni, Pt, Pd) [8]. Moreover, by varying precursors, it is possible to include specific dopants element in graphene such as boron, nitrogen or oxygen in order to obtain B-doped, N-doped, or O-doped graphene. Thereafter, graphene is covered by a protective layer usually made by polymers such as poly(methyl methacrylate) and then transferred onto other substrates by using thermal release tape. Unfortunately, precisely this step constitutes the weakness of CVD methods, since some residues of the protective layer keep onto graphene even after dedicated cleaning bath [37, 111, 119]. Finally, plasma-enhanced CVD has proved an excellent method to grow vertical graphene nanosheets, that is a special graphene morphology which features peculiar transport properties of interest for microelectronics [120–122].

THERMAL ANNEALING basing on CVD method, produces graphene by using a couple or a multiple stack of an amorphous carbon layer deposited onto a metal layer (Ni, Co and Cu are the most common choices). The annealing dissolves the amorphous carbon into the metal layer, and thus obtaining the segregation of a thin carbon layer, that is graphene, onto the surface of the metal (Fig. 29b) [111, 123, 124]

SOLVOTHERMAL in its turn similar to CVD method, produces graphene by means of the reaction between some chemicals in liquid phase (Fig. 29c). Some reaction are based on the pyrolysis or the thermal decomposition of carbon based precursors [111, 125, 126]. Besides, other methods use also precursor species containing nitrogen, such as in the case of the reaction between CCl_4 and Li_3N , which produces N-doped graphene flakes [123, 127].

EPITAXIAL GROWTH based on the synthesis of graphene by the thermal decomposition of the surface of SiC. In addition to the very high-quality structure of graphene obtained by this technique, the real advantage is the growth of graphene directly on a semiconductor. In this way it is possible to obtain the same quality of CVD, but avoiding the transfer step and problems related to it [112, 128–131].

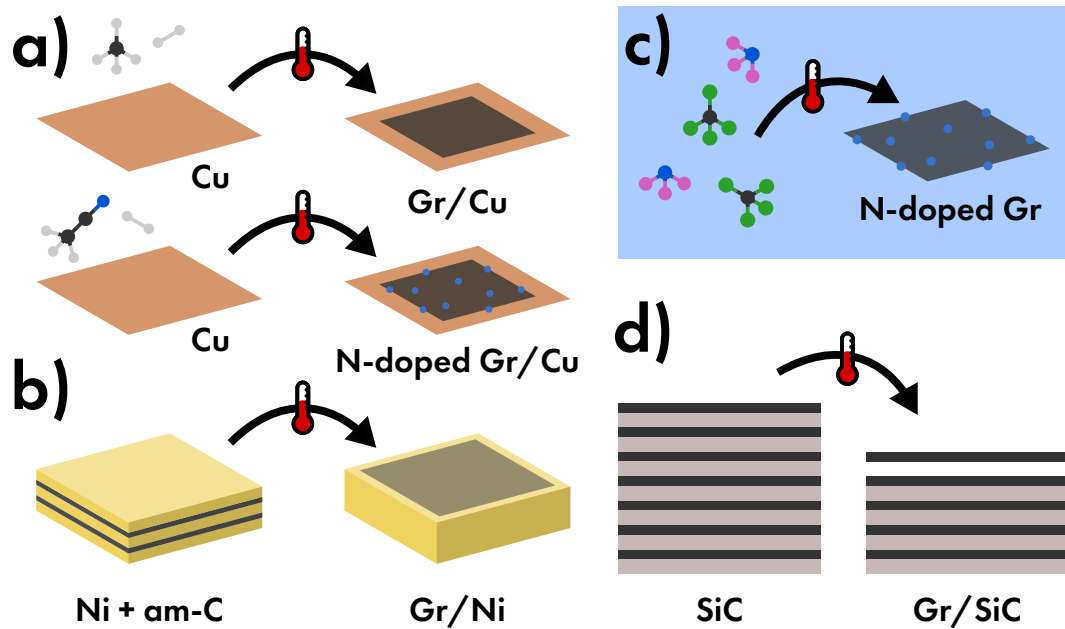


Figure 29: Graphene (Gr) or nitrogen doped graphene (N-doped Gr) produced by (a) chemical vapor deposition, (b) thermal annealing of amorphous carbon (am-C) (c) solvothermal synthesis, and (d) epitaxial growth on SiC.

2 | CHARGE TRANSFER PROCESSES

SINCE its two-dimensional structure, graphene actually coincides with its own surface, and therefore surface effects dominate the interaction with the environment. The interaction between the graphene and other species, such as molecules or nanoparticles, is one of the most investigated phenomena involving graphene because of its impact in various applications. Herein, a key role is played by charge transfer processes whereby the electronic properties of graphene can be significantly modified. Due to the different nature of molecules and nanoparticles, these two species feature different charge transfer mechanisms. Concerning simple molecules, charge transfer is mainly related to adsorption phenomena which put in relation the electronic structures of graphene and adsorbates. In addition, the adsorption can be followed by further processes, such as red-ox reactions where graphene acts as a catalyst substrate so as to allow the reaction of adsorbates through the provision of charges. Besides, in the case of nanoparticles, charge transfer occurs through the energy matching between electronic states of graphene and nanoparticles. The latter can occur thanks to the close contact between the surface orbitals of the nanoparticles and the π orbitals of graphene, but the transfer is available only for a favorable energy alignment of involved states. Therefore, the discussion of charge transfer processes between graphene and molecules or nanoparticles has to be reported separately, even whether both of them are based on the strong sensitivity of graphene to the environment. These aspects are reviewed in this chapter since they constitute one of the main topics of the present Thesis.

2.1 PRINCIPLES OF ADSORPTION

When one part of a system is found in solid phase, its participation to interaction processes with other species gains peculiar characteristics. For example, the bulk structure of the solid phase imposes some conditions to the other phase such as motion limitation, as well as introduces some concepts typical of solid state such as the electronic band structure. Therefore, it is necessary to describe the solid-gas or solid-liquid interaction in terms of *adsorption*, that is the interaction between the molecules and the surface of the solid phase [132, 133]. It is useful to distinguish two types of adsorption [132, 134]:

PHYSISORPTION where molecules and surface interact by means of weak van der Waals forces (dispersion-repulsion) and electrostatic interaction (polarization, dipole and quadrupole interaction) which describes effects of induced polarization between them. This interaction is not selective, does not feature directional character, is significant only at relatively low temperature, does not require activation, is fast and totally reversible, can involve several layers of adsorbates, and does not allow charge transfer distinct from polarization effects;

CHEMISORPTION where molecules and surface interacts by means of stronger interaction, up to the formation of chemical bond between them. This interaction is highly selective, is strongly directional, requires activation, may be slow and irreversible, can involve only one layer of adsorbates, and does allow charge transfer during the bond formation.

Similar to other interactions, adsorption can be described by a potential energy dependent on the distance between surface and adsorbate. As shown in Fig. 30, in the total adsorption interaction between a surface (S) and a molecular species (X_2), the effects of chemisorption and physisorption occur in different energy and distance scale ranges. In particular, the chemisorption potential features a deep minimum ($E_{CS} \geq 0.5-1 \text{ eV} = 50-100 \text{ kJ/mol}$) at close distance ($d_{CS} = 1-3 \text{ \AA}$) which corresponds to the formation of a chemical bond ($S-X_2$), whereas the physisorption potential features a shallow minimum ($E_{PS} \geq 10-500 \text{ meV} = 1-50 \text{ kJ/mol}$) at longer distance ($d_{PS} = 3-10 \text{ \AA}$) which corresponds to the formation of a weak structure ($S \cdots X_2$).

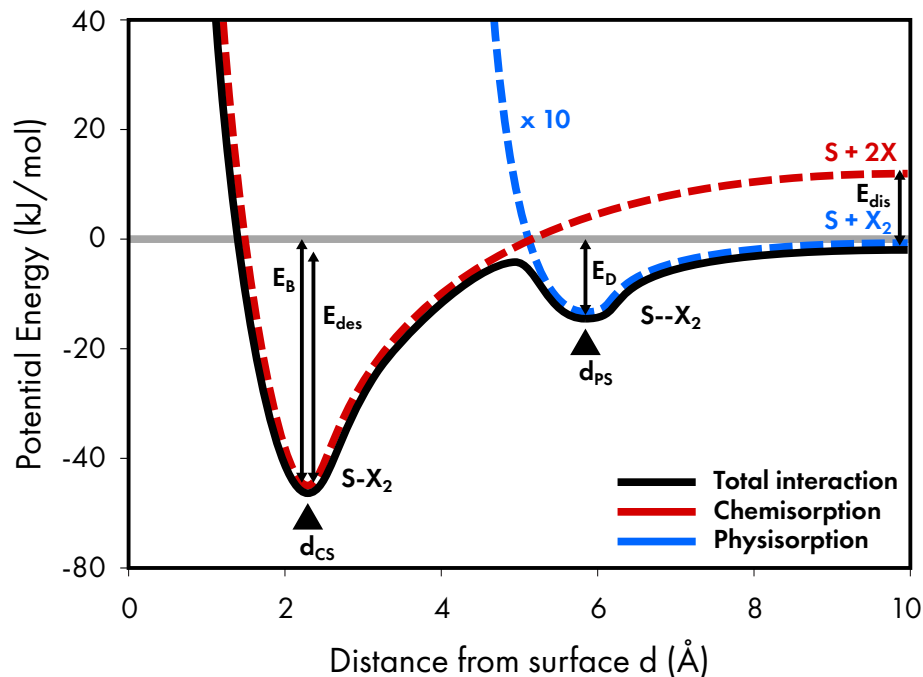


Figure 30: Adsorption potential energy between a surface (S) and a molecular moiety (X_2) including both chemisorption (red line) and physisorption (azure line) interactions. The two interactions feature their characteristic potential well depth E_B and E_D (not in scale), and their characteristic lengths d_{CS} and d_{PS} . Adapted from Ref. [132].

2.1.1 PHYSISORPTION

When a molecule approaches a surface, their electrons experience a mutual influence due to a series of weak intermolecular forces collectively named *van der Waals forces*:

KEESOM FORCE including the electrostatic interaction between permanent charges, and multipoles (that is dipoles, quadrupoles...);

DEBYE FORCE including the mutual attraction between a permanent multipole and an induced multipole (polarization effect);

LONDON FORCE including the mutual attraction between an instantaneous multipole and an induced multipole (dispersion effect).

In addition to these forces, a short-range repulsive potential due to Pauli repulsion has to be considered, which decays exponentially far from the atom or molecule, and prevents the overlap of occupied wavefunctions [132, 133].

Van der Waals bond, is significantly weaker than both ionic and covalent bonds, and since it does not involve any preferential orbital, it has no directional character. The potential which describes the intermolecular forces is thereby given by the sum of repulsive Pauli V_R and attractive van der Waals V_{vdW} terms [132, 133]:

$$V(d) = V_R(d) + V_{vdW}(d) = C_R e^{-d/a} - \frac{C_{vdW}}{d^n}, \quad (55)$$

where C_R and a give the weight and the characteristic length of Pauli repulsion, C_{vdW} is the van der Waals constant related to the polarizability of molecules, and d is the intermolecular distance. Besides, the power n depends on the type of interacting objects: $n = 6$ for intermolecular or interatomic interaction or $n = 3$ if a surface is involved [132, 133]. Therefore, van der Waals interaction is characterized by a shorter range interaction compared to charge-charge electrostatic interaction. The potential of Eq. 55 features a minimum at an equilibrium distance, and therefore a stable structure can arise by this kind of interaction.

2.1.2 CHEMISORPTION

Chemisorption involves forces much stronger than those ones occurring in physisorption, and the properties of adsorbates feature a larger modification due to the mixing with the wavefunction of substrate surface [133]. When a substrate features surface electron not involved in valence bonds, a significant interaction occurs between the wavefunctions of surface and adsorbate molecules, strong enough to induce the formation of chemical bonds among them. For that reason, chemisorption occurs especially for metal substrates. As a consequence, the molecular orbitals of the adsorbate are modified, as depicted in Fig. 31. In particular, in the case of adsorption on non-transition metals, their energy levels shift towards lower values and broaden, coherently

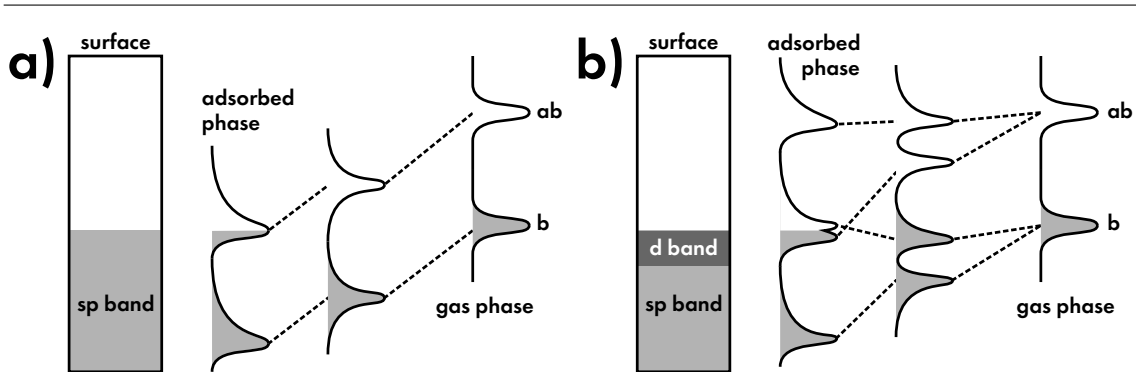


Figure 31: Modification of electronic states of adsorbate as a consequence of adsorption on the surface of (a) non-transition metal (whose band structure features only sp band) and (b) transition metal (whose band structure features both sp and d bands). Adapted from Refs. [132, 133].

to bound and hence more stable configuration. Besides, in the case of transition metals, the interaction with d orbitals induces an additional splitting in the adsorbate orbitals, giving rise to specific bonding and antibonding chemisorption energy levels. In both cases, the resulting alignment of the energy levels of surface and adsorbate determines the evolution of intermolecular and intramolecular interactions. In fact, whether the antibonding orbitals of adsorbate are placed below the Fermi energy of substrate, the intermolecular bond between adsorbate and substrate will be strengthened, while the intramolecular bonds in the adsorbate will be weakened. The latter process is on the basis of *dissociative adsorption* in which the surface acts as catalyst for specific reactions [133]. By considering the case of the dissociation of a diatomic molecule depicted in Fig. 32, due to the weakening of specific bonds, the energy barrier for the realization of the *activated complex* (AC) which leads to the dissociation of the molecule can be reduced by adsorption. Thence, the alternative reaction path features lower energy barrier at the *transient state* (TS), and thus the dissociation will proceed more easily for the adsorbed molecules compared to those in the gas phase [133].

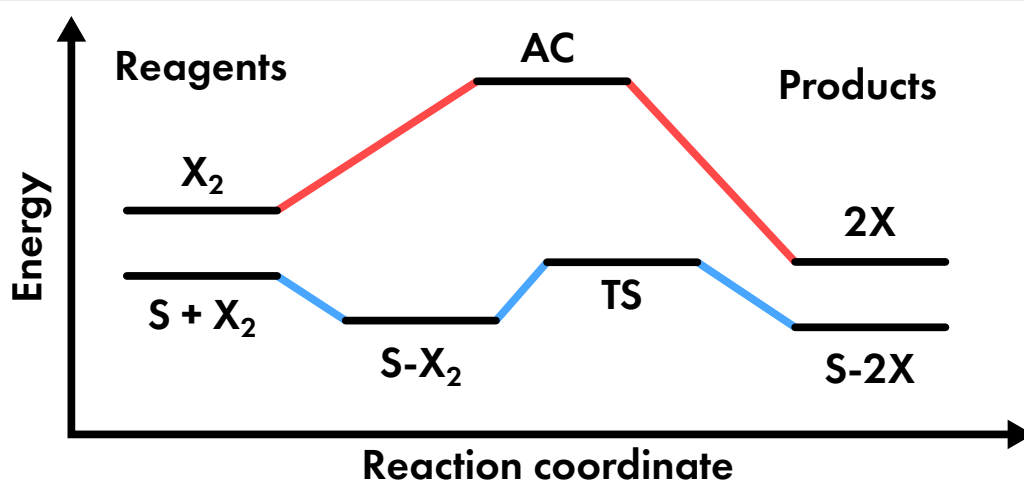


Figure 32: Reaction path of dissociation reaction for diatomic molecule in the case of free molecule (red lines) featuring a large energy barrier for the realization of the activated complex (AC), and in the case of adsorbed molecule (blue lines) which features a lower barrier for the realization of transient state (TS). Adapted from Ref. [133].

2.2 ADSORPTION ON GRAPHENE

2.2.1 PHYSISORPTION ON GRAPHENE

Graphite is the most obvious case in which graphene interacts by means of van der Waals forces. In fact, as mentioned in the previous chapter, this type of interaction occurs between the π orbitals of graphene sheets, so as to determine a vertical stacking. The weakness of this interaction is the reason of the easy exfoliation of graphite. Similarly, a large class of molecules containing delocalized orbitals of aromatic moieties can adsorb onto graphene, giving rise to specific modification of graphene [46, 135–137]. However, the typical counterparts of graphene in physisorption are the substrates on which the graphene is deposited, and the small molecules.

Concerning the substrate, the most relevant case is the interaction with oxides. In fact, aiming to use graphene as metal layer in nano-size metal-oxide-semiconductor field-effect transistor (MOSFET), it has to be stacked onto a oxide layer used as insulating layer. In particular, amorphous silica (SiO_2), alumina (Al_2O_3), and hafnia (HfO_2) are the usual oxides in this application. The former is used also as prototype system thanks to the enhancement of graphene Raman signal for this oxide, whereas the latter two are used for the investigation of specific features more application-oriented. Despite the performance of a device is strongly dependent on the macroscopic bulk properties of the insulating substrate (bandgap, electron affinity, dielectric constant), also the microscopic properties of its surface determine a relevant influence on graphene. In particular, graphene features a *mean modification* which originates from *local influences* related to the specific surface groups of the substrate on which it is adsorbed. As shown in Fig. 33, the typical surface groups or vacancies of SiO_2 are [99, 138]:

SILANOL GROUP namely a silicon atom bound to an hydroxyl group ($\text{Si}-\text{OH}$), which can be found in isolated, vicinal and geminal configuration (Fig. 33a,b,c);

SILOXANE GROUP namely two silicon atoms connected by an oxygen atom ($\text{Si}-\text{O}-\text{Si}$) in bridge position (Fig. 33d);

DANGLING BONDS namely a hydrogen (V'_H) or oxygen (V'_O) vacancies, which determine unsaturated bonds for oxygen ($\text{Si}-\text{O}^*$) and silicon (Si^*) atoms, respectively (Fig. 33e,f).

Each of those groups induces different modifications on graphene related to their characteristic adsorption, and moreover, the same group can give rise to different interactions according to its orientation. In fact, since the geometry of surface groups is strictly imposed by the bonds with the rest of the substrate and by mutual interaction between groups, they are not totally free to rearrange their geometry during the adsorption onto graphene [99–101].

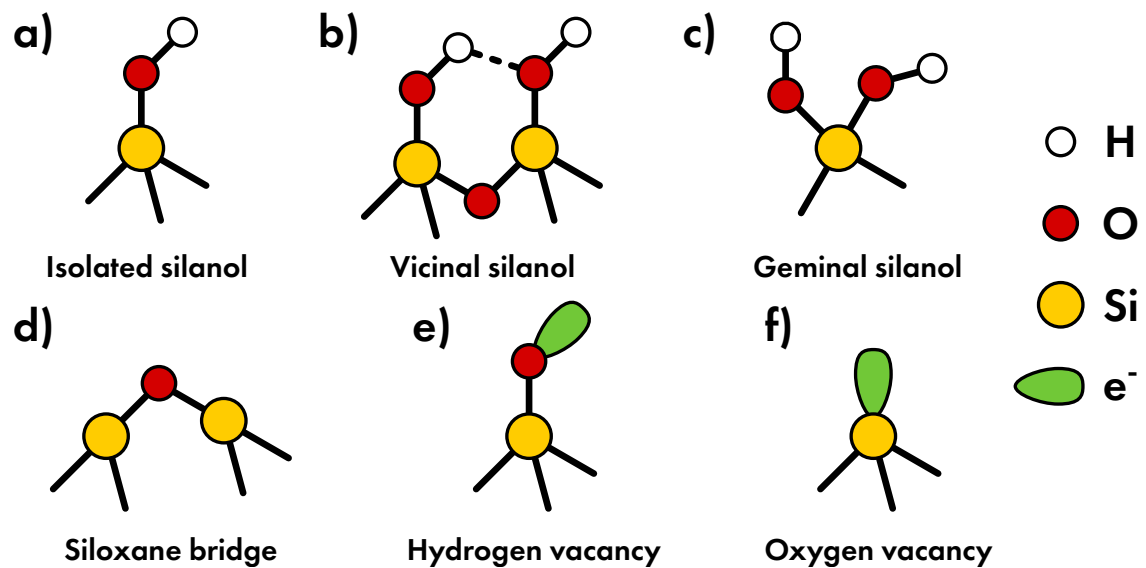


Figure 33: Surface groups of SiO_2 : silanol groups in (a) isolated, (b) vicinal, and (c) geminal configuration, (d) siloxane group. Surface vacancies of SiO_2 : (e) hydrogen, and (f) oxygen vacancies.

Charge mobility and sheet resistivity are the main properties of graphene which are affected by the interaction with the substrate, and both of them are related to charge doping, that is the modification of charge carrier concentration. In fact, it has been found that the adsorption of the substrate surface functional groups on graphene causes readjustment of electron population, thus determining the shift of Fermi energy and the appearance of electron or hole doping [99–101]. In addition, it can be noted that the interstitial space between SiO₂ and graphene transferred on it is not empty, but full of water molecules. In fact, in connection with the concentration of silanol groups, the surface of SiO₂ can feature a consistent interaction with water by establishing hydrogen bonds with silanol groups. Therefore, it is expected that part of the modification of graphene induced by the substrate is mediated by the water buffer layer, and only minoritarily carried out directly by the substrate [139–141]. Some works have shown how the modulation of the hydrophilic character of the SiO₂ surface can actually control the properties of graphene. This modulation can be achieved in various ways: by performing O₂ plasma treatment, so as to remove the adsorbed water molecules; by performing high temperature annealing (1000°C) in order to convert hydrophilic silanol groups in hydrophobic siloxane groups; by substituting hydroxyl groups with apolar groups such as methyl groups [142–144]. In particular, this surface modification allows to remove the unintended doping and the hysteresis effects related to the presence of interstitial molecules or trap-sites in the graphene-substrate interface. Therefore, as shown in Fig. 34, the fine methylation of the substrate by hexamethyldisilazane (HMDS) allows to fix this hysteresis, along to the fine determination of charge doping.

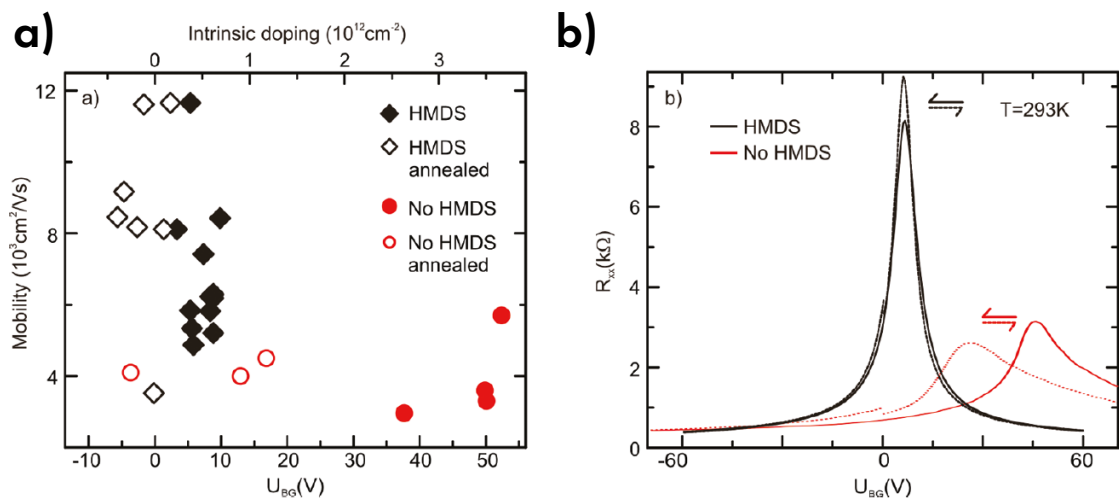


Figure 34: (a) Mobility versus charge neutrality point and (b) sheet resistivity versus gate voltage of graphene for hydrophilic (red) and hydrophobic (black) substrate obtained by HMDS. Adapted from Ref. [143].

Finally, it has been revealed that the electric properties of graphene can be affected by the physisorption of small atmospheric molecules too. As shown in Fig. 35, the exposure at ambient temperature of graphene to H₂O, NO₂, NH₃ and CO in gas phase significantly modifies the sheet resistivity of graphene, as well the charge doping can be finely tuned to the opportune level [145].

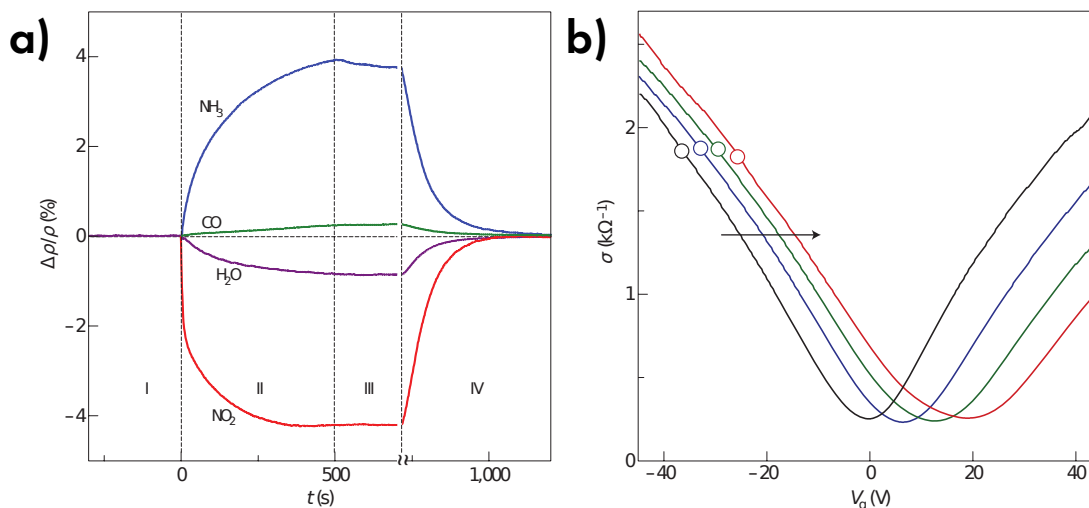


Figure 35: (a) Relative sheet resistivity of graphene exposed to H_2O , NO_2 , NH_3 and CO in gas phase. (b) Shift of charge neutrality point as effect of doping by NO_2 molecules. Adapted from Ref. [145].

2.2.2 CHEMISORPTION ON GRAPHENE

The adsorption of small molecules on graphene can also be pursued by activating chemisorption with the assistance of temperature. In such a way it is possible to obtain more stable bonds than by physisorption and therefore more defined modification of graphene properties are expected. To this aim, thermal treatments in controlled atmosphere have proven to be an effective and affordable method to modify the electronic properties of graphene [146]. In this respect, some key aspects have been pointed out by the recent literature: one of the most relevant modifications is the p-doping obtained by exposure to oxygen as revealed by the evolution of the Raman spectrum of graphene, whereas other gases induce little or no effect (Fig. 36a). In fact, the evolution of the G peak position shows the occurrence of a reversible charge doping which fades after a following exposure to an inert atmosphere (Fig. 36b) [147–149]. The doping removal is mainly ascribed to the interaction with water since the exposure to ambient humidity conditions causes the removal of doping up to the complete recovery of pristine properties, whereas doping keeps stable by storing graphene in a dried environment or even by further treatment in vacuum [147, 150]. Moreover, as revealed by *ex-situ* measurements, the induced doping is strongly dependent on the treatment temperature, whereby ever higher temperatures induce a higher doping up to a saturation level (Fig. 36c) [151]. Regarding the structure of graphene, this kind of doping can be easily attained at relatively low temperature (up to 300°C) with no mark of damage, whereas higher temperature induces defects and the destruction of the sample [151–153]. Besides, the changes of strain revealed by the G-2D map shown in Fig. 36d, is ascribed to the modification of the adhesion between graphene and substrate due to thermal stress [102, 149, 154]. However, the actual correlation between the strain evolution and the doping process is not yet clear.

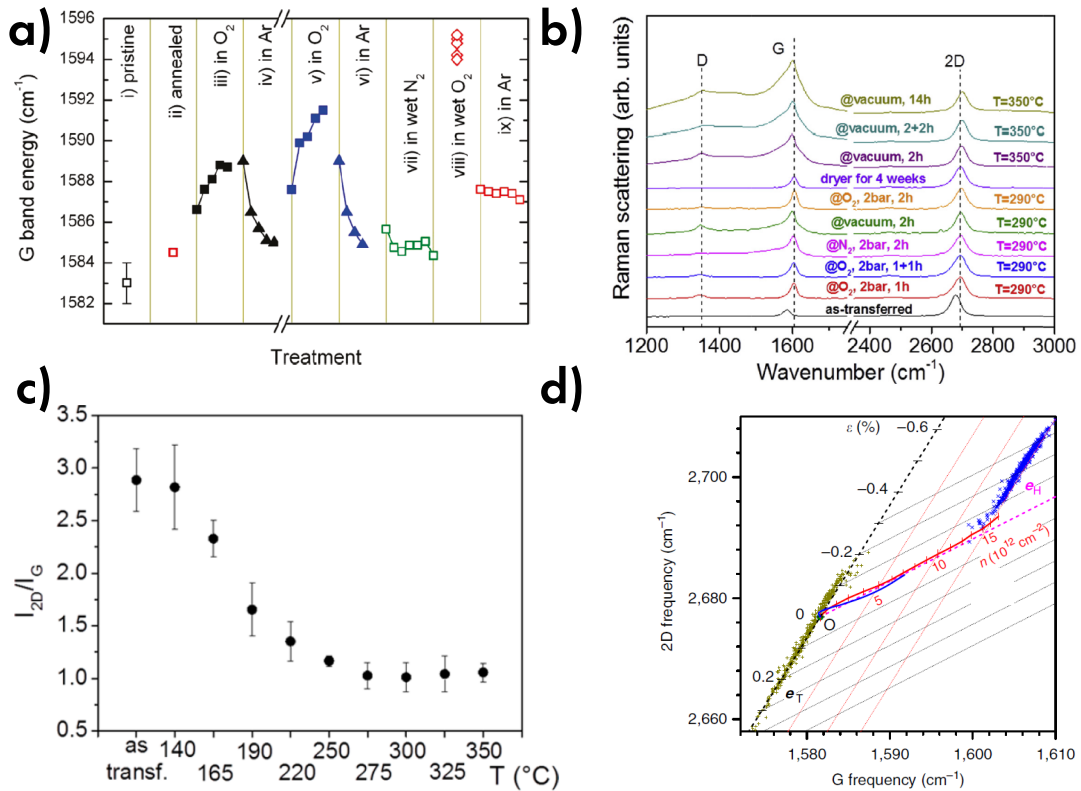


Figure 36: (a) Evolution of G band peak position as effect of thermal treatment in different atmospheres, adapted from Ref. [147]. (b) Raman spectra of graphene treated in various atmospheres, adapted from Ref. [149]. (c) Evolution of I_{2D}/I_G ratio as result of doping induced by oxygen, adapted from Ref. [151] (d) Evolution of G-2D peak position correlation as result of doping induced by thermal treatment, adapted from Ref. [102].

A detailed study of doping removal on a single graphene flake previously doped by thermal treatment (Fig. 37a,b) has shown that the interaction between graphene and molecules giving doping takes place in the interstitial space between the graphene and the substrate (Fig. 37c,d) [155]. In particular, the radial doping removal from the edges of the flake towards its center has been found by evaluating the local evolution of the peak position of G band, as reported in Fig. 37e. This effect has been ascribed to the diffusion of water between graphene and substrate which can be identified cause the loss of doping. On the contrary, a hypothetical interaction with the water on the top face of graphene would have induced an homogeneous modification [155]. This hypothesis leads to some important issues:

- the presence of the substrate is necessary for the occurrence of doping, certainly by defining a *protected* space where the intermediate adsorption stage between the graphene and the molecules can keep stable, and maybe because of some specific properties of the substrate surface which favor the process;
- despite the charge carriers induced by doping in the π or π^* orbitals of graphene (for p or n doping, respectively) are exposed to both the top and bottom faces of graphene, the doping loss requires the diffusion beneath the bottom face. Therefore, the charge carriers are probably kept stable by the products of the doping reaction located beneath graphene and the alteration of such products by the interaction with water would break the stability of doping, thus causing its loss.

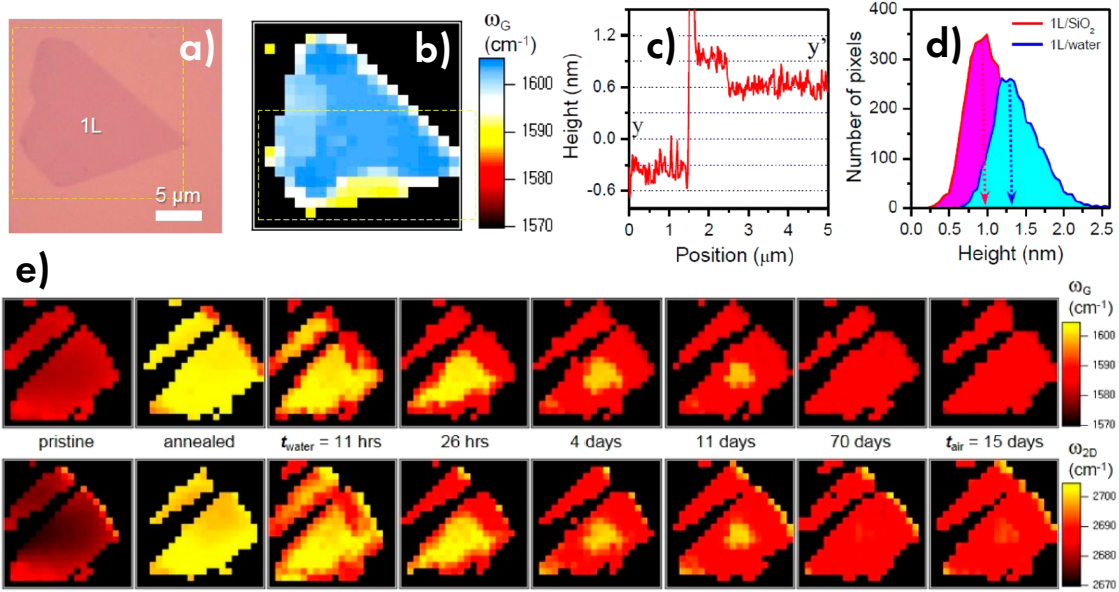


Figure 37: Single graphene flake shown by (a) optical microscopy and by (b) Raman imaging based on the peak amplitude of the graphene G band (the color scale is based on the G peak position). (c) Morphological section profile acquired by AFM and (d) height distribution extracted by an entire micrograph revealing the size of the interstitial space between the graphene and the substrate. (e) Raman imaging reporting the evolution of G and 2D peak position in p-doped graphene flake as effect of a following immersion in water. The radial removal of doping is highlighted. Adapted from Ref. [155].

As previously mentioned, chemisorption can induce the weakening of internal bonds in adsorbates, up to induce their dissociation. In addition, the obtained products can give rise to further *post-adsorption processes*. As shown in Fig. 38, the most effective interaction is found in correspondence of graphene defective sites, that is atom vacancies [156], substitutional doping, both from transition metals [80–84] and non-metals atoms [157–159]. However, it has been revealed that the chemisorption can fairly occur even onto an undamaged graphene sheet [160]. Furthermore, the chemisorption efficiency onto these regions can be enhanced whether they were formerly *specialized*. This applies to the supporting substrate, whose surface groups are adsorbed

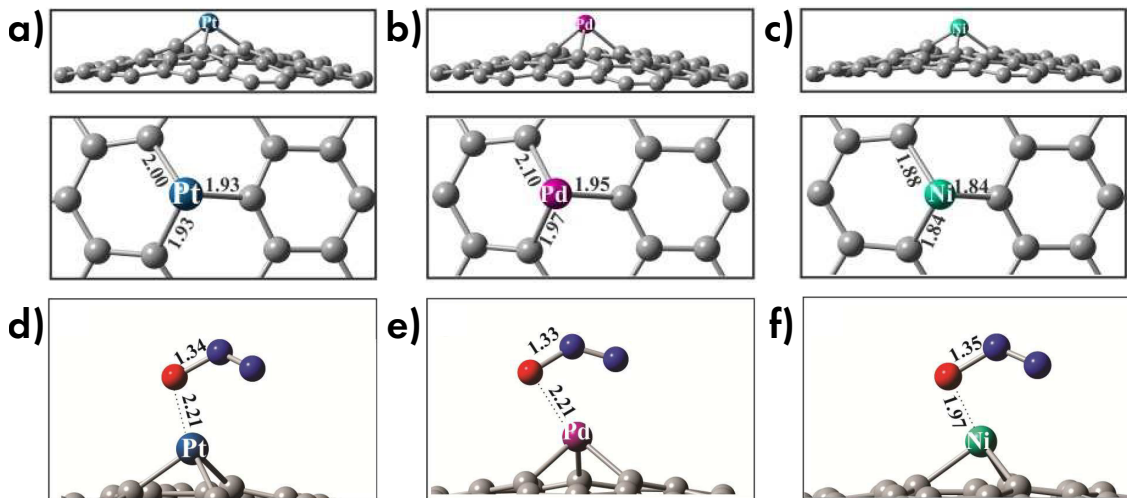
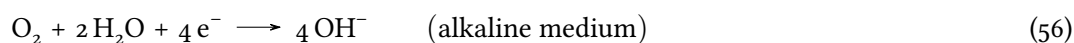


Figure 38: Defect sites in graphene doped by transition metal atoms (a) Pt, (b) Pd, (c) Ni, shown in side and top view. (d,e,f) Optimized geometry for N_2O molecule adsorbed on three different defect sites. Adapted from Ref. [82].

on graphene, and therefore can locally affect the electronic properties of graphene, as revealed in some works by computational investigation [161–164]. Reduction–oxidation reactions (red-ox) are typical post-adsorption processes involving the graphene [83, 84, 165–169]. In particular, these processes can concern a plethora of small molecules, such as H_2O , CO_2 , CO , N_2O , NO_2 , and O_2 , and hence they suggest a possible use of graphene for gas sensing application or in the degradation of pollutants [81–83, 156, 162]. For the purpose of this Thesis, it is important to discuss more extensively the reduction reaction of molecular oxygen. Whether by means of different processes, this reaction takes place in both alkaline and acidic conditions, and the reduction can occur through two possible pathways [83, 165, 170]. The direct four-electron pathways, which involve the dissociative adsorption of oxygen, are given by



or as an alternative two consecutive two-electron pathways given by



in the case of alkaline medium, and by



in the case of acidic medium. Whether both pathways can in principle occur, the four-electron pathways (56) and (57) are expected to dominating the time kinetics of the reaction since they proceed slower than the two-electron pathways (58) and (59) [165, 170].

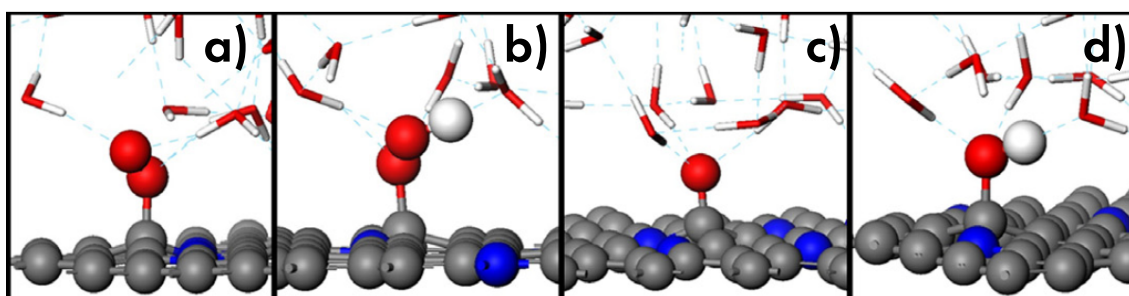


Figure 39: Oxygen reduction transition states in the two-electron pathway for graphene adsorbed oxygen: (a) adsorbed configuration, (b) result of reaction 58a, (c) oxygen dissociation, (d) reaction of the remaining oxygen. Adapted from Ref. [83].

Concerning chemisorbed molecules (Fig. 39), the reduction is promoted by the possible weakening of intramolecular bonds, and therefore the effective pathways result slightly modified, by featuring reduced energy barriers between the transition states [83]. In the case of a metal adsorption substrate its role will be twofold: as just mentioned it will promote the oxygen reduc-

tion by the adsorption induced effect, and most importantly, it will provide the required electrons to assuring the charge balance in the red-ox reaction. A similar contribution could be expected in the case of adsorption onto graphene, which they would feature a charge doping consistent with the required charge transfer: p-doping by promoting adsorbate reduction and n-doping by promoting adsorbate oxidation [171–174].

2.2.3 ADSORPTION KINETICS

The evaluation of the kinetics of a process, that is its dependence on time, is one of the most representative features to be studied. In fact, alongside the trivial evaluation of the range of time necessary to the completion of the process, the specific dependence on time provides information about the phenomena on which the process is based. Therefore, the investigation of a time kinetics aims to evaluate which kinetics model fit to the best the experimental evidences [175]. In the case of adsorption on a surface, it is important to note that the comprehensive process includes four consecutive stages as depicted in Fig. 40:

- 1| **EXTERNAL DIFFUSION:** transport of adsorbate from its bulk solution towards the surface;
- 2| **INTERNAL DIFFUSION:** transport of adsorbate towards the adsorption sites of the surface;
- 3| **PROPER ADSORPTION:** the actual adsorption process that sees the formation of the bond between adsorbate and surface.

Most importantly, the slowest stage determines the total kinetics observed in the experiments. Since external diffusion is extremely fast, the kinetics is usually contended by internal diffusion (henceforth simply named diffusion) and the adsorption [175, 176].

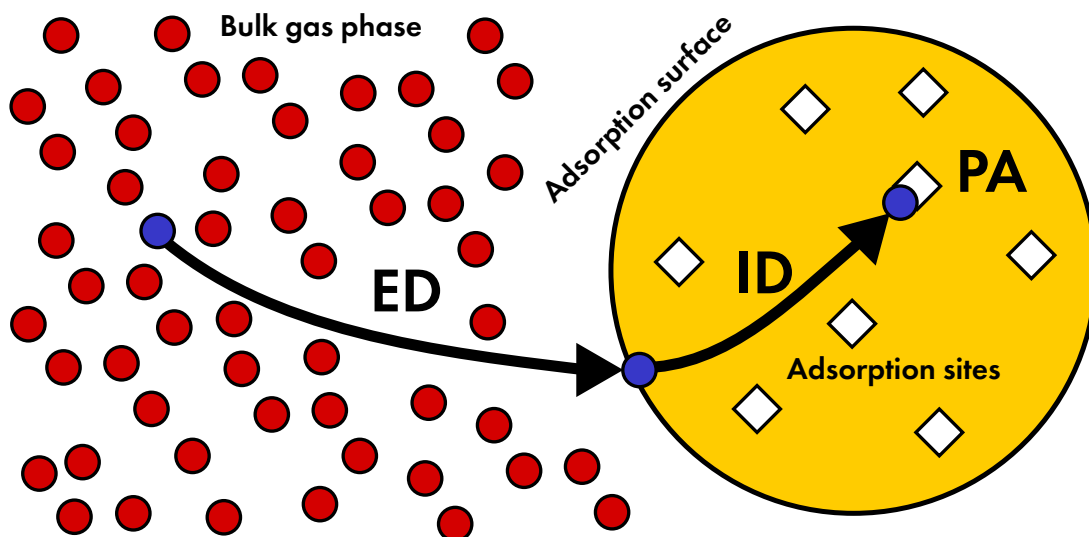


Figure 40: Consecutive stages of an adsorption process between a molecular adsorbate (red and blue circles) and an adsorption surface (yellow circle): external diffusion (ED), internal diffusion (ID) and finally the proper adsorption (PA) on adsorption sites (white diamonds).

Diffusion models are based on the assumption that the adsorbate diffusion towards the adsorption sites is the slowest stage, and therefore the rate limiting one. By indicating as Q the amount of adsorbed species, and as Q_{max} the saturation level, the most notable kinetics models are:

CRANK MODEL describing the homogeneous and isotropic diffusion of adsorbate species that in the case of a spherical adsorbent is given by

$$Q(t) = Q_{max} \left[1 - \left(\frac{6}{\pi^2} \right) \sum_{n=1}^{\infty} \left(\frac{1}{n} \cdot \exp(-D_s n^2 \pi^2 t / R^2) \right) \right], \quad (60)$$

where R^2 is the sphere radius, and D_s the diffusion constant. In addition, the simplified versions for short and long times are commonly used:

$$Q(t) = Q_{max} \left[\frac{6}{\sqrt{\pi}} (-D_s t / R^2)^{1/2} - 3 \right] \quad (\text{short times}) \quad (61)$$

$$Q(t) = Q_{max} \left[1 - \left(\frac{6}{\pi^2} \right) \exp(-D_s n^2 \pi^2 t / R^2) \right] \quad (\text{long times}). \quad (62)$$

WEBER-MORRIS MODEL describing the intraparticle diffusion according to the rate equation

$$Q(t) = k_{id} t^{1/2} + C, \quad (63)$$

where k_{id} is the intraparticle diffusion rate constant, and C is related to the boundary layer thickness.

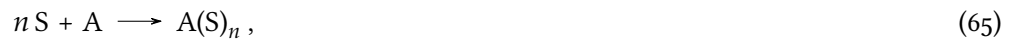
BANGHAM MODEL describing the pore diffusion given by the relation

$$Q(t) = k_{pd} t^{\vartheta}, \quad (64)$$

where k_{pd} is the pore diffusion rate constant, and ϑ is given by generalizing the exponent of the Weber-Morris model

On the other hand, the reaction models are based on the assumption that the reaction between adsorbate species and adsorption sites which follows the diffusion step is the slowest stage, and therefore the rate limiting one. By indicating k_a the adsorption rate, k_d the desorption rate, the most remarkable kinetics models are:

PSEUDO n TH-ORDER MODEL which describes the irreversible adsorption



occurring in n localized sites, involving no interaction between the adsorbed moieties, assuming that the maximum adsorption is achieved by saturating a single-layer of adsorbates. In this case, the kinetics is governed by a power law rate equation

$$\frac{dQ}{dt} = kQ^n, \quad (66)$$

whose exponent n is equal to the number of sites involved in the single adsorption event, and whose solutions are given by

$$Q(t) = Q_{max}(1 - e^{-k_a t}) \quad (n = 1) \quad (67)$$

$$Q(t) = Q_{max} \left[1 - \left(\frac{1}{1 + k_a Q_{max}^{n-1}} \right)^{-\frac{1}{n-1}} \right] \quad (n > 1) \quad (68)$$

LANGMUIR MODEL which makes the same assumption as the previous model, but desorption is now available



and the time evolution is described by

$$Q(t) = Q_{max} \left(\frac{k_a}{k_a + k_d} \right) \cdot (1 - e^{-(k_a + k_d)t}) \quad (70)$$

ELOVICH MODEL which makes the same assumption of a pseudo n th-order model, but multi-layer of adsorbates can be formed, whether by requiring higher adsorption energy



In this case, the time evolution is given by the relation

$$Q(t) = \frac{1}{\beta} \ln(\alpha \beta t), \quad (72)$$

where α is the bare rate constant of adsorption, and β is a factor related to the modification of the adsorption energy $E_a = E_{a0} + RT\beta Q$ on increasing of adsorption layers. The total rate is therefore given by $k_a = \alpha \exp(\beta Q)$.

In the following, these models will be further considered to critically interpret the obtained experimental results.

2.3 CHARGE EXCHANGE WITH NANOPARTICLES

When graphene is coupled with optically active materials, different kinds of charge transfer process can occur such as photoinduced electron transfer (PET) [177, 178]. According to the scheme reported in Fig. 41a, PET involves a *donor* and an *acceptor* species, and the electron transfer between them is activated by the light stimulation of the donor, as discussed in Chp. 3. Provided that the excited state of the donor features an electron at an higher energy compared to the unoccupied level of the acceptor, the electron transfer can occur between them. Therefore, the proper energy alignment between the donor and acceptor energy levels is mandatory to allow the electron migration. In this respect, many works have shown that graphene can be

profitably used in this kind of process. In various systems graphene acts as electron acceptor whereas both molecules [179, 180] and nanoparticles were exploited as donor. Concerning the latter case, the most relevant materials are quantum dots (QDs) transition-metal dichalcogenide nanoparticles [181], oxides nanoparticles such as ZnO [182–184] and TiO₂ [185–187], and carbon-based nanoparticles [177, 187, 188]. The designation of the donor/acceptor roles here reported originates from the mutual energy alignment of empty electron states, evaluated in terms of different quantities: work function for metals (such as graphene), electron affinity (for semiconductors) and redox potential (for various kinds of nanoparticles). In particular, the work function of graphene evaluates its Fermi level and is usually placed below the energy of the surface empty states of some nanoparticles. Therefore, the electron promoted to these states by light excitation can migrate towards the graphene, since the latter dispose of empty states at equal or below energy.

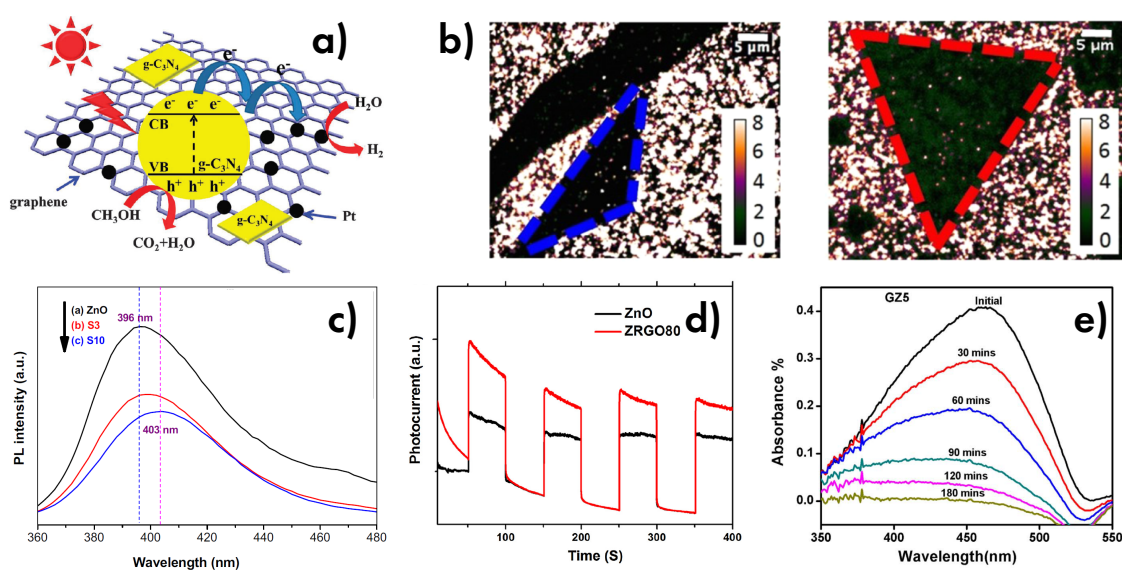


Figure 41: (a) Energy scheme of charge transfer mechanism between optically active nanoparticles and graphene. (b) Emission quenching of CdSe nanoparticles deposited onto graphene (left) and MoS₂ (right) in compared to nanoparticles deposited onto an insulating substrate. (c) Emission quenching of ZnO nanoparticles in contact with graphene, adapted from Ref. [183]. (d) Photocurrent in a ZnO/graphene nanocomposite, adapted from Ref. [184]. (e) Photodegradation of methyl orange by ZnO/graphene nanocomposite, adapted from Ref. [182].

Quenching of photoluminescence is one of the most easily observable physical quantity which marks the PET between nanoparticles and graphene. In particular, the quenching is attributed to the separation of the electron-hole pair induced by PET which prevents their radiative recombination. Moreover, this separation can take place both in solid and liquid phase, as reported by the emission quenching for CdSe nanoparticles deposited onto graphene or MoS₂ shown in Fig. 41b and for ZnO nanoparticles in contact with reduced graphene oxide shown in Fig. 41c, respectively. In addition, the electron transfer can be characterized by the measurement of the photocurrent generated in the graphene because of the injected electrons (Fig. 41d) and by the evaluation of photocatalytic properties. In the latter case, the charge transfer from the nanoparticles towards graphene is evaluated by the decrease of the emission intensity of a third molecule. In fact, the photodegradation of such a molecule is enhanced by the diffusion on graphene surface of the electrons originated in the nanoparticles by photoexcitation, since graphene features a larger spe-

cific surface area compared to nanoparticles. Therefore, the interest in these processes is both for a basic research point of view aiming to clarify interactions occurring between graphene and nanoparticles, and for an application research in order to exploit composite nanomaterials in optoelectronic devices [177, 178, 189].

2.4 CARBON NANOPARTICLES

Carbon Dots (CDs) are a large family of optically active carbon nanoparticles well known for their excellent emission properties in the visible spectrum. Various types of CDs have been synthesized by both top-down and bottom-up methods, thus obtaining fundamental differences in size, elemental composition, structure, surface passivation. As a result, the various types of CDs show very different spectroscopic features which in some cases are related to completely different photoemission mechanisms [190]. CDs shows many characteristics of QDs, as well as further remarkable advantages: tunable properties, easy synthesis methods, cheap precursors, and low toxicity [190]. Therefore, a CD-graphene composite system looks promising for applications based on carbon nanomaterials which require low-costs and biocompatibility. For the purpose of this thesis, a peculiar kind of nitrogen-doped CDs was used. Such CDs are obtained by bottom-up synthesis (more details are provided in Chp. 4) and feature a quasi-spherical shape with typical size of about 1–10 nm (Fig. 42a) and are formed by two main parts: a *core* constituted by a nanocrystal of carbon and nitrogen atoms arranged in a β - C_3N_4 lattice (Fig. 42b), and a *surface* passivated by carboxyl ($-\text{COOH}$), hydroxyl ($-\text{OH}$), and amide ($-\text{CONH}_2$) functional groups (Fig. 42c) [191, 192]. According to the most accepted model, both these two parts are in-

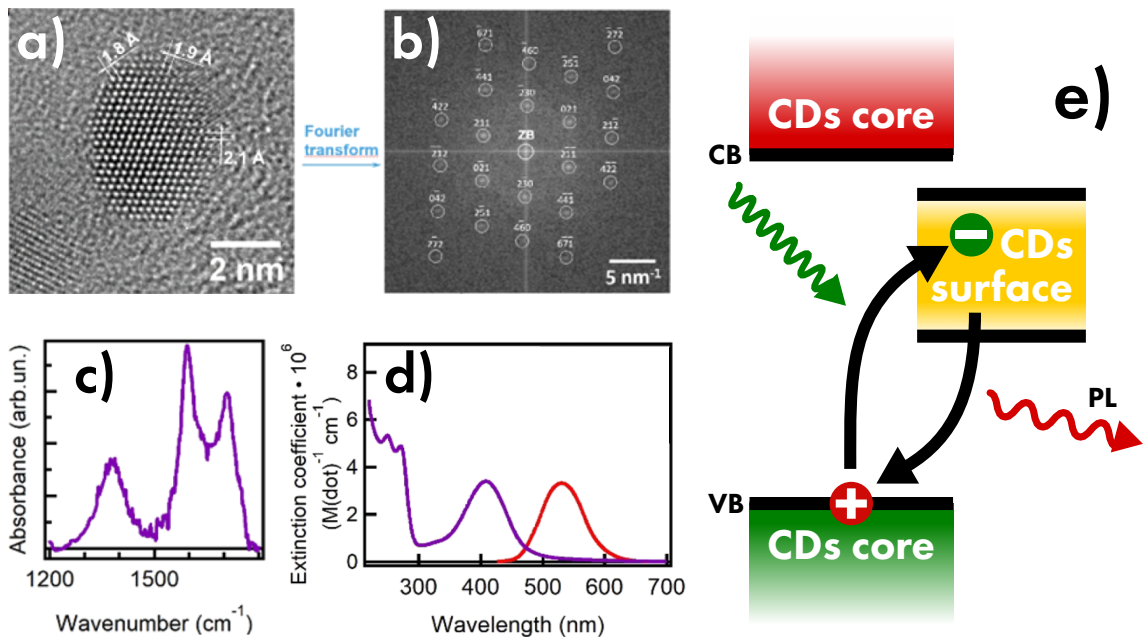


Figure 42: (a) HR-TEM image of CDs and (b) its Fourier transform, attesting the β - C_3N_4 core lattice. (c) IR absorption spectrum of CDs related to the amide and carboxyl surface groups. (d) Absorption and emission spectra (the latter excited at 440 nm) of CDs. Figures adapted from Ref [191]. (e) Energy levels scheme of CD photocycle, involving the core valence band and the surface states.

volved in the emission mechanism of CDs. As depicted in Fig. 42e, optical absorption originates an electron-hole pair attributed to a transition between the valence band of the core and the unoccupied states exposed to the surface. Then, the radiative recombination of the electron-hole pair gives rise to the fluorescence [193]. It is evident that the electron-transfer towards surface occurring in the photocycle of these CDs implies a strong sensitivity of the following photoluminescence to the environment. In fact, the charge exposed at the surface can interact with the surrounding species even by means of short-range processes. In this regard, the most renowned cases concern various types of charge transfer processes involving ions [194, 195], molecules [193, 196], and nanomaterials [197, 198]. The propensity of CDs to act as electron donor reported in these results suggests that the energy of the surface levels CDs is higher of those characterizing the other common interacting species. For such a reason, CDs are a promising choice to be used as a graphene sensitizer.

3 | BASIC CONCEPTS OF METHODS

THE main contribution to the experimental approach at the basis of this Thesis is given by two spectroscopic techniques: Raman spectroscopy and photoluminescence spectroscopy. Both of them are based on the interaction between radiation and matter, which can be opportunely exploited to extract information about the investigated system.

All the spectroscopies are based on the transition involving real or virtual states respectively induced by the absorption, emission or scattering of an electromagnetic radiation. As depicted in Fig. 43, a given material features several energy levels which are subdivided in different energy range-scales according to the type of corresponding state. In particular, the electronic states are characterized by the largest energy distance, and the UV-VIS radiation (1.24–12.4 eV) is necessary for transitions between these states. Moreover, each electronic energy level is constituted by various close sub-levels related to specific vibrational states of the material. The energy differences between these states are several orders of magnitude smaller compared to those featuring the electronic states. Therefore, IR radiation (1.24 meV–1.24 eV) is sufficient to induce vibrational transitions. In its turn, the vibrational energy levels are constituted by further sub-levels related to rotational states. In this case, the energy differences are even smaller and the transitions are activated by microwave radiation (1.24 μ eV–1.24 meV). Therefore, the study of the different electronic, vibrational and rotational structures of a given material necessitates of different spectroscopic techniques. In this Thesis, photoluminescence spectroscopy performed in UV-VIS range was used to investigate the emission properties of optically active materials. On the other hand, Raman spectroscopy was used to provide information about the structure of the materials which

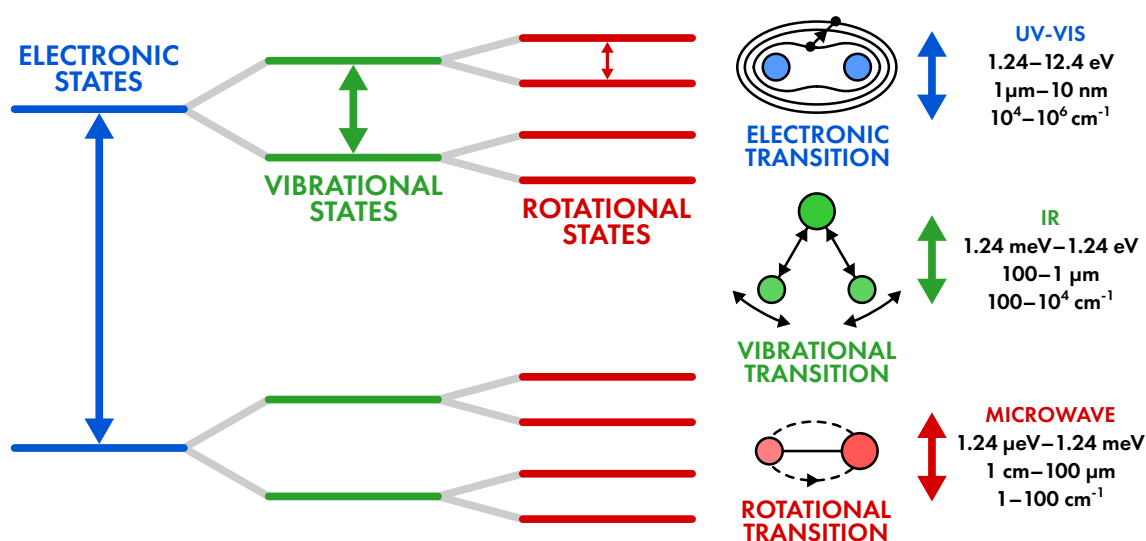


Figure 43: Representative diagram of the electronic, vibrational and rotational energy levels in molecules highlighting their hierarchical relation (left). Processes activated for different kinds of transitions and their typical spectroscopic values of the radiation (right).

in some cases is also related to their electronic properties. In addition, because of the nano-size of graphene and nanoparticles, Atomic Force Microscopy was used in order to evaluate the morphology of samples. In the following sections, the theory of the techniques above cited is discussed, by pointing out their main aspects.

3.1 RAMAN SPECTROSCOPY

Raman spectroscopy is one of the most common techniques for the investigation of structural properties of materials. Similar to the case of IR spectroscopy, Raman spectroscopy arises from light induced transitions between vibrational states, but the analogies between these two techniques ends here. On the other hand, unlike the IR spectroscopy, Raman spectroscopy is not based on transitions caused by light absorption, but on a different process which involves light scattering. In particular, the physical quantity measured by IR spectroscopy is the attenuation as a function of the wavelength of a light beam after it had traveled through a material described by the Lamber-Beer law [199]

$$I = I_0 e^{-\varepsilon(\lambda)cd}, \quad A = \ln\left(\frac{I_0}{I}\right) = \varepsilon(\lambda)cd, \quad (73)$$

where I_0 is the original intensity of the light beam, ε is the molar extinction coefficient, λ is the wavelength of the incident radiation, c is the molar concentration (mol/L), d is the traveled thickness, and A is the absorbance. By contrast, the variation between the incident and the scattered photon energy as effect of the interaction with matter is evaluated in Raman spectroscopy. In particular, scattered light consists of two contributions [199, 200]:

RAYLEIGH SCATTERING concerning most of the scattered photons which feature no variation in their energy after the interaction with matter, that means

$$h\nu = h\nu_0, \quad (74)$$

where ν_0 is the frequency of the incident photon and ν that one of the scattered photon;

RAMAN SCATTERING concerning a very small fraction of the scattered photons (10^{-5} of those involved in Rayleigh scattering) which feature a variation in their energy given by

$$h\nu = h\nu_0 \pm h\Delta\nu, \quad (75)$$

where $h\Delta\nu = \Delta E$ is the energy difference between two vibrational states. By the interaction with the material, the scattered photon can thereby leave or acquire energy giving rise to *Stokes* and *anti-Stokes* lines, respectively.

To avoid terminology misunderstanding, it is important to note that IR and Raman spectra are commonly expressed in terms of wavenumber $\tilde{\nu}$ defined as

$$\tilde{\nu} = \frac{1}{\lambda} = \frac{\nu}{c}, \quad (76)$$

which is the inverse of the wavelength, and thus it is given in cm^{-1} . Notwithstanding, the wavenumber is commonly named *frequency* when discussed in both IR and Raman spectra [199, 200].

3.1.1 CLASSICAL DESCRIPTION

Some key issues of Raman scattering can be derived by using a classical description of the interaction between radiation and matter. In this respect, the incident radiation is described by an electromagnetic plane wave given by [200, 201]

$$E = E_0 \sin 2\pi\nu_0 t, \quad (77)$$

where E_0 and ν are the amplitude and frequency of the electric field, respectively. Therefore, an electric dipole moment is induced in the irradiated sample with the same oscillation:

$$P = \alpha E = \alpha E_0 \sin 2\pi\nu_0 t, \quad (78)$$

where α is the polarizability. Such quantity is a characteristic of the materials and depends on the position of nuclei. For small atom displacement ($q \approx 0$ from the equilibrium position q_0) the polarizability can be written as

$$\alpha = \alpha_0 + \left(\frac{\partial \alpha}{\partial q} \right)_0 q + \dots, \quad (79)$$

where α_0 is the polarizability at the equilibrium position. Whether the material undergoes to lattice vibration, the atom displacement in the harmonic approximation is given by

$$q = q_0 \sin 2\pi\nu_m t, \quad (80)$$

where ν_m is the vibration frequency of a specific normal mode identified by the label m . In this case the polarizability can be written as

$$\alpha = \alpha_0 + \left(\frac{\partial \alpha}{\partial q} \right)_0 q_0 \sin 2\pi\nu_m t + \dots, \quad (81)$$

thereby rewriting the dipole momentum as

$$\begin{aligned} P &= \alpha_0 E_0 \sin 2\pi\nu t + \left(\frac{\partial \alpha}{\partial q} \right)_0 q_0 E_0 \sin 2\pi\nu_m t \cdot \sin 2\pi\nu_0 t \\ &= \alpha_0 E_0 \sin 2\pi\nu t + \frac{1}{2} \left(\frac{\partial \alpha}{\partial q} \right)_0 q_0 E_0 \left[\cos(2\pi \underbrace{(\nu_0 + \nu_m)}_{\text{anti-Stokes}} t) + \cos(2\pi \underbrace{(\nu_0 - \nu_m)}_{\text{Stokes}} t) \right]. \end{aligned} \quad (82)$$

Therefore, as shown in Fig. 44, the polarization oscillates through the modulation of three components and gives rise to a radiation constituted by: one contribution from Rayleigh scattering at frequency $\nu = \nu_0$ and two contributions from Raman scattering at frequency $\nu_0 \pm \nu_m$ for Stokes (– sign) and anti-Stokes (+ sign), respectively [200, 201].

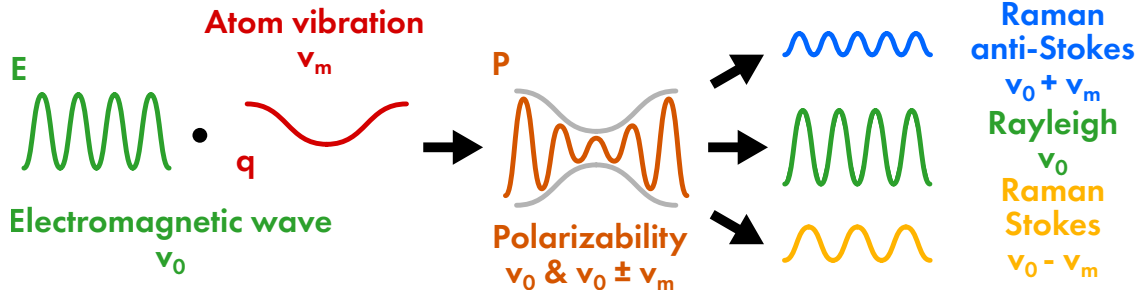


Figure 44: Composition of the electromagnetic radiation (green) and atomic vibration (red) oscillation frequency, ν_0 and ν_m , respectively, in the oscillation modes of polarizability (orange). The latter gives rise to Rayleigh scattering (green) at the same frequency of the incident radiation, and to Stokes (yellow) and anti-Stokes (azure) lines of Raman scattering at frequency $\nu_0 \pm \nu_m$. Adapted from Ref. [201].

Furthermore, by evaluating the intensity of the light emitted by the oscillating dipole, we obtain the relation

$$I = \frac{16\pi^4\nu^4}{c^2}|P|^2 = \frac{16\pi^4}{3c^2}E_0^2 \left\{ \nu_0^4 \alpha_0^2 \cos^2 2\pi\nu_0 t + (\nu_0 + \nu_m)^4 \left[\left(\frac{\partial \alpha}{\partial q} \right)_0 \frac{q_0}{2} \right]^2 \cos^2(2\pi(\nu_0 + \nu_m)t) \right. \\ \left. + (\nu_0 - \nu_m)^4 \left[\left(\frac{\partial \alpha}{\partial q} \right)_0 \frac{q_0}{2} \right]^2 \cos^2(2\pi(\nu_0 - \nu_m)t) \right\} + \text{cross terms} \quad (83)$$

by neglecting the contribution of cross terms. Two important issues are pointed out in this equation:

- the intensity of both Rayleigh and Raman lines is proportional to the fourth power of frequency. Therefore, despite Raman scattering occurs independently of the frequency of incident light, UV-VIS light sources are commonly used instead of IR sources in order to obtain a more intense spectrum. However, whether in such a way it is possible to acquire more intense Raman spectra, a competitive photoluminescence can occur when the material is optically active, thus overpowering a much weaker Raman signal.
- the ratio between the Stokes and anti-Stokes lines is given by

$$\frac{I_{\text{Stokes}}}{I_{\text{anti-Stokes}}} = \left(\frac{\nu_0 - \nu_m}{\nu_0 + \nu_m} \right)^4 < 1, \quad (84)$$

thus evaluating a higher intensity for anti-Stokes lines compared to the Stokes ones, in contrast with the experimental evidence [200].

3.1.2 QUANTUM DESCRIPTION

Classical and quantum mechanical descriptions of light scattering are very similar, despite they differ in some fundamental issues. By the quantum approach, the interacting material is quantum mechanically treated, whereas the electromagnetic radiation is classically treated in terms of an incident plane wave. In particular, Raman scattering is described as a transition between an initial $|i\rangle$ and a final $|f\rangle$ state assumed at defined energy $\hbar\omega_i$ and $\hbar\omega_f$, respectively [201]:

$$|i\rangle = \psi_i e^{-i\omega_i t}, \quad |f\rangle = \psi_f e^{-i\omega_f t}, \quad (85)$$

through intermediate states $|r\rangle$ with an undefined energy $\hbar\omega_r$ with non-null width $2\Gamma_r$:

$$|i\rangle = \psi_r e^{-i(\omega_r t - \Gamma_r)} . \quad (86)$$

The transition between these states is obtained by means of first-order perturbation theory, and is described by the transition dipole momentum, whose component along the spatial coordinates $Q, \sigma = x, y, z$ is given by

$$(p_Q^{(1)})_{fi} = \frac{1}{2\hbar} \sum_{r \neq i, f} \left[\frac{\langle f | \hat{p}_Q | r \rangle \langle r | \hat{p}_\sigma | i \rangle}{\omega_{ri} - \omega - i\Gamma_r} + \frac{\langle f | \hat{p}_\sigma | r \rangle \langle r | \hat{p}_Q | i \rangle}{\omega_{rf} - \omega - i\Gamma_r} \right] \tilde{E}_{\sigma_0} e^{-i\omega_s t} + \text{complex conjugate}, \quad (87)$$

where $\hbar\omega_{ab} = \hbar(\omega_a - \omega_b)$ is the energy difference between two given states a and b , ω_s is the angular frequency of the scattered light, and \tilde{E}_{σ_0} is the complex component of the electromagnetic radiation along the σ direction. Therefore, since transition polarizability $(\alpha_{Q\sigma})_{fi}$ is related to the transition dipole momentum by

$$(p_Q^{(1)})_{fi} = \frac{1}{2} (\alpha_{Q\sigma})_{fi} [\tilde{E}_{\sigma_0}(\omega) e^{-i\omega_s t} + \tilde{E}_{\sigma_0}^*(\omega) e^{i\omega_s t}], \quad (88)$$

its components are given by

$$(\alpha_{Q\sigma})_{fi} = \frac{1}{\hbar} \sum_{r \neq i, f} \left[\frac{\langle f | \hat{p}_Q | r \rangle \langle r | \hat{p}_\sigma | i \rangle}{\omega_{ri} - \omega - i\Gamma_r} + \frac{\langle f | \hat{p}_\sigma | r \rangle \langle r | \hat{p}_Q | i \rangle}{\omega_{rf} - \omega - i\Gamma_r} \right]. \quad (89)$$

By this equation, the influence of radiation frequency on the intensity of scattered light can be evaluated. In fact, according to the energy level diagram shown in Fig. 45, when $\omega \ll \omega_{ri}$ for all $|r\rangle$ states (Fig. 45a), no well-defined energy level corresponds to the transition, thus involving a *virtual state* which is not a stationary solution of Schrödinger equation of the system. Therefore,

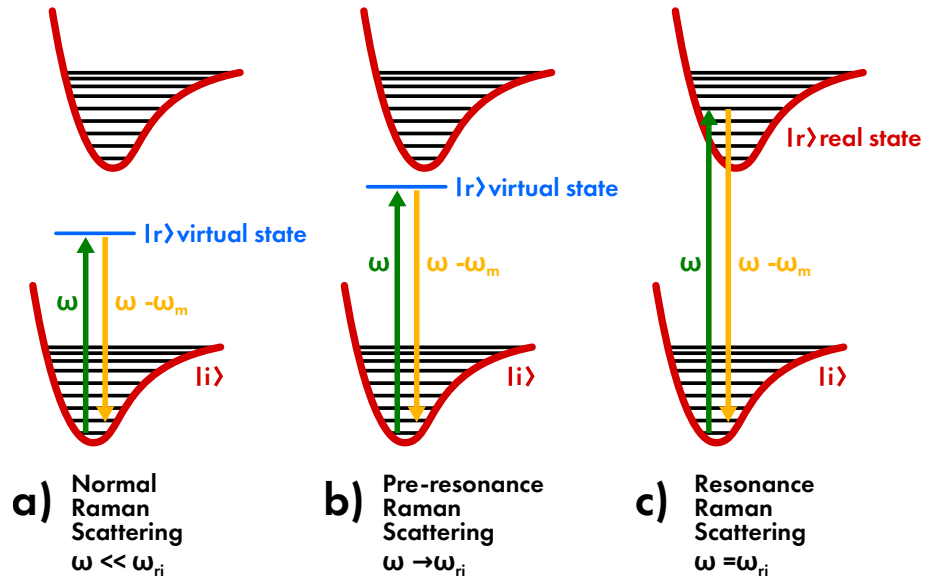


Figure 45: Raman scattering processes in (a) non-resonant transition towards a virtual state far away from electronic levels, (b) pre-resonant transition towards a virtual state near an excited electronic level (c) resonant transition towards a real state in the excited electronic level. Adapted from Ref.[201].

in this case the scattering process involves a virtual transition whose probability is relatively low. Besides, in the pre-resonance regime ($\omega \rightarrow \omega_{ri}$) (Fig. 45c), that is when the energy of the intermediate states $|r\rangle$ is close to real energy levels, the denominators of Eq. 89 decrease, thus enhancing the intensity of scattered radiation. The highest intensity is reached at full resonance $\omega = \omega_{ri}$ (Fig. 45c) when the transition involves discrete and real vibrational levels belonging to a higher electronic state. Therefore, the spectra acquired in full resonance regime are characterized by an intensity enhanced by a factor 10^3 – 10^5 (with obvious measurement advantages), and moreover, they get an intrinsic relation to the electronic structure of the sample [200, 201].

3.1.3 SELECTION RULES AND EXCLUSION PRINCIPLE

Both classical and quantum descriptions of the induced dipole momentum provide important insights on the Raman scattering availability. In fact, by Eq. 82, the Raman lines arise only when

$$\left(\frac{\partial \alpha}{\partial q}\right)_0 \neq 0, \quad (90)$$

thus deriving the classical selection rule of Raman scattering, that is: a vibrational mode is Raman active when the polarizability features a stationary point of inflection at $q = 0$ [199, 200]. More generally, polarizability is not necessarily an isotropic quantity. Therefore, the relation between the induced polarization and the electric field is given by the polarizability tensor α through the equation $\mathbf{P} = \alpha \cdot \mathbf{E}$, which implies

$$\begin{cases} P_x &= \alpha_{xx}E_x + \alpha_{xy}E_y + \alpha_{xz}E_z \\ P_y &= \alpha_{yx}E_x + \alpha_{yy}E_y + \alpha_{yz}E_z \\ P_z &= \alpha_{zx}E_x + \alpha_{zy}E_y + \alpha_{zz}E_z \end{cases}, \quad (91)$$

and since α is usually a symmetric tensor: $\alpha_{ij} = \alpha_{ji}$ for $i \neq j$. Consequently, a vibrational mode is *Raman-active* whether at least one of these components follows the Eq. 90. This selection rule can be easily understood by visualizing the spatial evolution of polarizability due to a vibrational motion, as shown in Fig. 46 for the CO_2 and H_2O molecules, the *polarizability ellipsoid* obtained by plotting $1/\sqrt{\alpha_{ii}}$. By comparing the various vibrational modes, the ones which feature a symmetric variation of the ellipsoid are Raman-inactive, since $(\partial \alpha_{ii}/\partial q) = 0$ at $q = 0$ (Fig. 46b,c,e,f). On the contrary, the modes in which the ellipsoid varies asymmetrically are Raman-active, since $(\partial \alpha_{ii}/\partial q) \neq 0$ at $q = 0$ (Fig. 46a,d,e) [200, 201].

In respect to the symmetry, this results can be discussed in terms of the Eq. 89, where the integrals

$$\langle f | \hat{p}_e | r \rangle \langle r | \hat{p}_\sigma | i \rangle = \langle f | \hat{p}_e \hat{p}_\sigma | i \rangle \propto \int \psi_f(q) \rho \sigma \psi_i(q) dq \neq 0 \quad (92)$$

are non-null only whether the product $\psi_f(q) \rho \sigma \psi_i(q)$ contains the totally symmetric representation. Therefore, the vibration is Raman active if the component of the polarizability belongs to the same symmetry species as that of the vibration [200, 201]. A similar argument can be used to evaluate the IR-activity of a vibrational mode. In this case, an equation similar to the Eq. 92

can be derived, but involving only one coordinate in the integrals, and therefore IR and Raman active modes features different symmetry, as shown in Fig. 46. This condition, called the *mutual exclusion principle*, can be resumed as: for any molecules having a centre of symmetry, the vibrations symmetric with respect to the center of symmetry are Raman-active, whereas those that are antisymmetric are IR-active. As a consequence IR and Raman active modes are mutually exclusive for such molecule [200, 201].

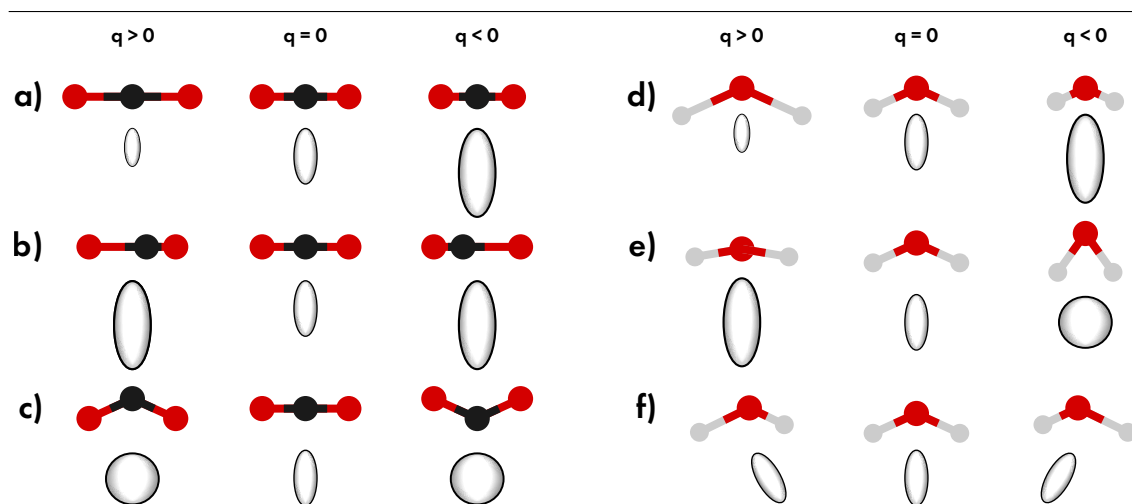


Figure 46: Evolution of polarizability ellipse as effect of vibrational motion for three different normal modes in (a,b,c) CO_2 and (d,e,f) H_2O molecules. Adapted from Ref. [200].

3.2 PHOTOLUMINESCENCE SPECTROSCOPY

The electronic structure of optically active materials is commonly investigated by means of optical absorption and emission processes involving electronic states. In fact, these two phenomena allow to evaluate fundamental quantities for a certain material, such as the energy distribution of orbitals for molecules or the eventual energy bandgap of solids. In addition, intramolecular electronic transitions are dramatically influenced by external agents, which can both enhance or quench the efficiency of specific radiative processes. Therefore, optical spectroscopy provides information about intermolecular phenomena such as solvation, complex formation, collisions, and so on [202].

3.2.1 PRINCIPLES OF PHOTOLUMINESCENCE

As previously mentioned, the absorption of UV-VIS light by a material induces an electronic transition between two states. According to the *Jablonski diagram* depicted in Fig. 47, absorption mostly involves the transitions among singlet electronic states, labeled by S_0 , S_1 , and so on, featuring a very fast characteristic time (10^{-15}s) [202, 203]. The absorption between different states is characterized by a vibrational fine structure due to electron-phonon coupling. By considering, as an example, the transition $S_0 \rightarrow S_2$, absorption can occur from any populated vibrational

substate of the S_0 electronic state to any vibrational substates of the S_2 state, although not all with the same efficiency [202, 203]. Then, through *internal conversion*, that is the non-radiative transition $S_2 \rightarrow S_1$, and then through vibrational relaxation, the systems relaxates to the vibrational ground state of the S_1 state. Therefrom, two different radiative recombination paths can occur [202, 203]:

FLUORESCENCE which corresponds to the transition $S_1 \rightarrow S_0$ and whose time-scale is related to life-time of the S_1 state (10^{-9} – 10^{-7} s);

PHOSPHORESCENCE which corresponds to much slower spin-forbidden transition $T_1 \rightarrow S_0$ (10^{-6} – 10 s) occurring after *intersystem crossing* from the singlet S_1 state to the triplet T_1 state (10^{-10} – 10^{-8} s).

Alternatively, the system continues the internal conversion from any excited state towards the S_0 state, thus relaxing with no light emission.

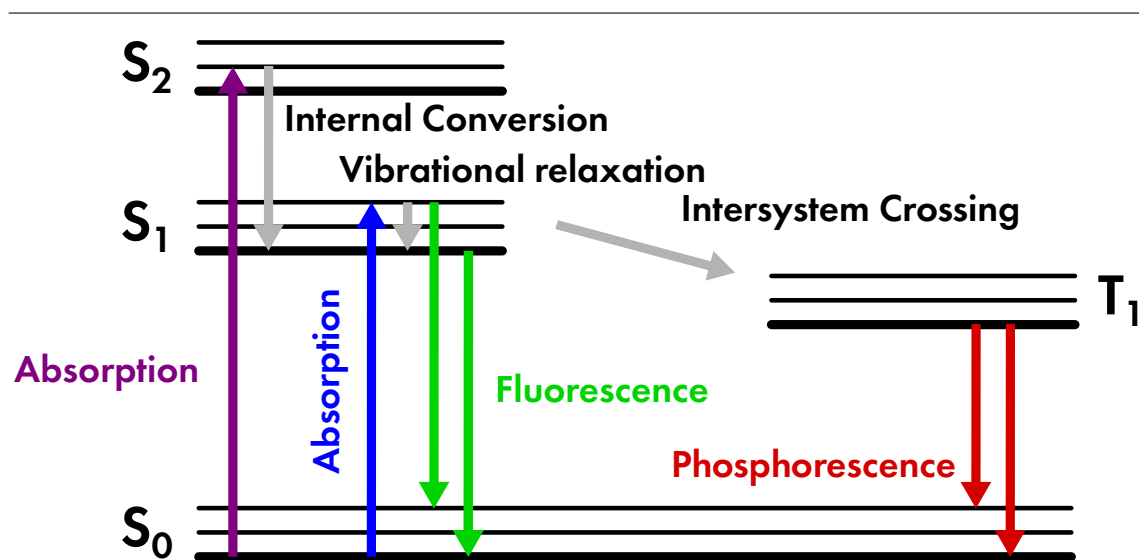


Figure 47: Jablonski diagram of the typical photocycle of a molecule constituted by: light absorption (violet and blue), internal conversion and vibrational relaxation towards the ground vibrational level of the excited (grey), fluorescence (green), and phosphorescence (red). Adapted from Ref. [202].

As general characteristics, an emission spectrum extends for a wide wavelength range, the peak position is shifted with respect to the absorption spectrum of the same species (Fig. 48a), and it can feature the presence of vibrational fine structure (Fig. 48b). The total energy decrease of the emission with respect to the absorption, called *Stokes shift* is due to non-radiative relaxation occurring between the transitions related to absorption and emission and involves the electron-phonon coupling. The other features can be explained in connection with the vibrational structure of the considered species. In fact, as previously mentioned, the electronic states usually feature a wide energy spread which includes the energy spectrum of the vibrational sub-states, and the latter are fully involved in the transitions between electronic states. According to time dependent perturbation theory, a transition between states is caused by the interaction between matter and electromagnetic field by means of the addition of a small

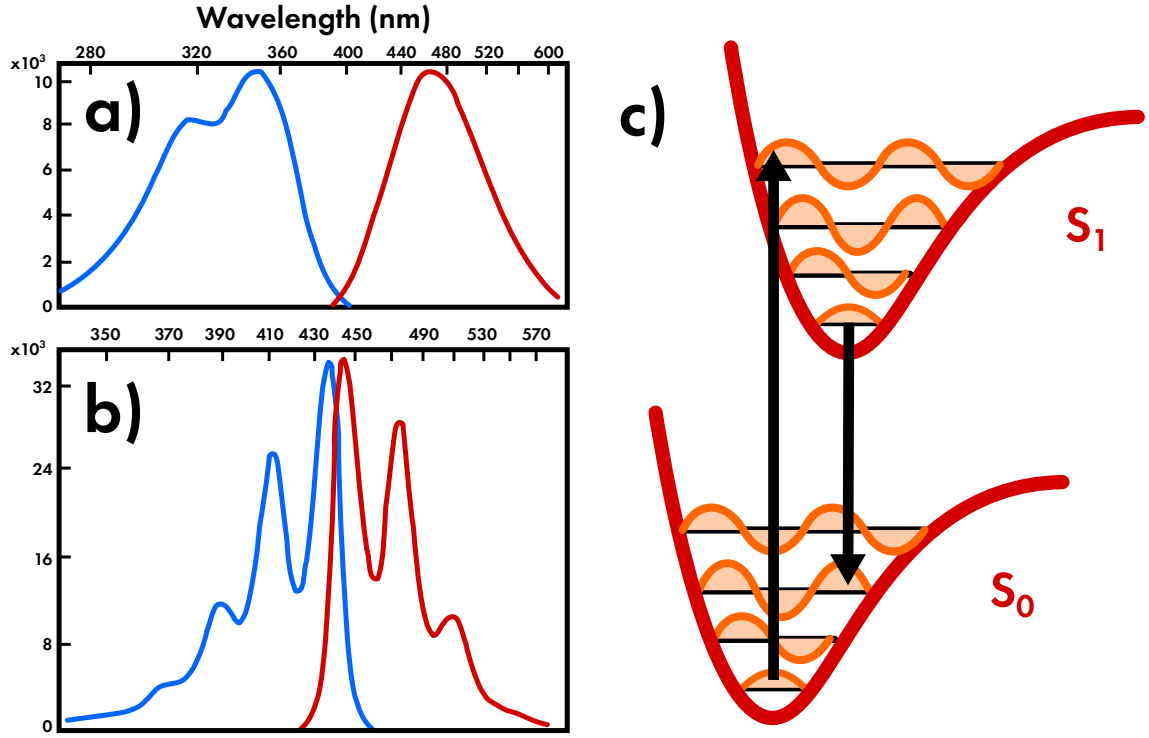


Figure 48: (a,b) Representative absorption (blue line) and fluorescence (red line) spectra of two molecules featuring the Stokes shift between absorption and emission peak wavelength, and the eventual presence of distinct vibronic structures. (c) Involvement of various vibrational levels in the fluorescence process. Transition between vibrational levels of S_0 and S_1 states are favored by the Franck-Condon factor, that is the overlap of vibrational contribution to the wavefunctions. Adapted from Refs. [202, 203].

perturbative term \mathcal{V} to the original Hamiltonian describing the system \mathcal{H} , such that the overall Hamiltonian is given by [203, 204]

$$\mathcal{H}(t) = \mathcal{H}_0 + \mathcal{V}(t), \quad \text{where } \mathcal{V} \ll \mathcal{H}_0. \quad (93)$$

By considering the interaction with a single monochromatic electromagnetic wave $\mathbf{E} = \hat{\mathbf{z}}E_0 \cos \omega t$, the additive term can be expressed by using the electric dipole approximation as

$$\mathcal{V}(t) = \mathbf{E} \cdot \boldsymbol{\mu} = -e\mathbf{E} \cdot \mathbf{z} = -eE_0 \sin \omega t, \quad (94)$$

where $\boldsymbol{\mu} = e\mathbf{z}$ is the electric dipole moment of the system. Given two states $|i\rangle$ and $|f\rangle$ whose energy separation is $E_f - E_i = \hbar\omega_0$, the probability of the electronic transition between these states due to the electromagnetic radiation is derived by the time dependent perturbation theory in the case of sinusoidal perturbation:

$$P_{i \rightarrow f} = \left(\frac{|\mu_{if}|E_0}{\hbar} \right)^2 \frac{\sin^2[(\omega_0 - \omega)t/2]}{(\omega_0 - \omega)^2} = \frac{2u}{\epsilon_0 \hbar} |\mu_{if}|^2 \frac{\sin^2[(\omega_0 - \omega)t/2]}{(\omega_0 - \omega)^2}, \quad (95)$$

where $u = \varepsilon_0 E_0^2/2$ is the energy density of the electromagnetic wave and μ_{if} is the element of the transition dipole moment given by

$$\mu_{if} = \langle f | \mathcal{V} | i \rangle = \langle f | \boldsymbol{\mu} | i \rangle = \int \Psi_f^* \boldsymbol{\mu} \Psi_i. \quad (96)$$

where ψ_f and ψ_i are the final and initial states of the overall molecule. Thence, by extending the discussion to an incoherent polychromatic radiation, the system interacts with electromagnetic radiation at a whole range of frequencies. In this case, we substitute u with $\varrho(\omega)d\omega$, where $\varrho(\omega)$ is the energy density of the radiation in the frequency range $d\omega$, and the Eq. 95 has to be integrated with respect all the possible frequencies:

$$P_{i \rightarrow f} = \frac{2}{\varepsilon_0 \hbar} |\mu_{if}|^2 \int_0^\infty \varrho(\omega) \frac{\sin^2[(\omega_0 - \omega)t/2]}{(\omega_0 - \omega)^2} d\omega = \frac{\pi}{\varepsilon_0 \hbar^2} |\mu_{if}|^2 \varrho(\omega_0) t. \quad (97)$$

Finally, the transition rate is obtained by the time derivative of the probability of transition

$$R_{i \rightarrow f} = \frac{\pi}{3\varepsilon_0 \hbar^2} |\mu_{if}|^2 \varrho(\omega_0), \quad (98)$$

where the factor $1/3$ is added by average of the transition dipole moment over all polarizations and all incident directions.

It is important to note that the same probability rate is obtained for a reverse transition from the $|f\rangle$ to the $|i\rangle$ state: $P_{i \rightarrow f} = P_{f \rightarrow i}$. These two transition are referred to the *stimulate absorption* and *stimulate emission*, respectively. In the first case, the system in its ground state interacts with the radiation and it reaches an excited state by gaining the required energy through the absorption of the radiation. In the second case the systems is already in its excited state, and the interaction with the radiation causes the return to the ground states by loosing the exceeding energy by emitting radiation. The latter process is involved in differs from the *spontaneous emission* responsible of the photoluminescence. In this case the transition downward does not involve any applied electromagnetic field, but gives rise only because of the *zero point radiation*.

As shown, the transition probability is strictly connected to the element of the electric dipole moment connecting the two states. For a molecular system, such a quantity should be evaluated by considering the electronic and the nuclear contribution to the electric dipole moment

$$\boldsymbol{\mu} = \boldsymbol{\mu}_e + \boldsymbol{\mu}_N = -e \sum_i \mathbf{r}_i + e \sum_\alpha Z_\alpha \mathbf{R}_\alpha, \quad (99)$$

where e is the electron charge, eZ_α is the charge of the electron. However, since the period of nuclear vibration (10^{-10} – 10^{-12} s) is much slower than the characteristic time of absorption, the nuclei of the molecule can be considered as *frozen* during the transition between electronic states [203, 204]. This consideration is at the basis of the *Born-Oppenheimer approximation*, which allows to factorize the total wavefunction in two terms: the electronic one φ_i and the nuclear one χ_a . Therefore, by labeling the states $\Psi_{ia} = \varphi_i \chi_a$ and $\Psi_{fb} = \varphi_f \chi_b$ as $|ia\rangle$ and $|fb\rangle$, respectively, we obtain

$$|\mu_{if}|^2 = |\langle fb | \boldsymbol{\mu} | ia \rangle|^2 = |\langle a | b \rangle|^2 \cdot |\langle f | \boldsymbol{\mu}_e | i \rangle|^2 = |\langle a | b \rangle|^2 \cdot |\mu_{fi}^e|^2. \quad (100)$$

In this equation, the second factor takes into account the dipole transition moment between the two electronic states, whereas the first factor is the *Franck-Condon* factor which evaluates the overlap between the vibrational level of ground and excited electronic states [203, 204]. Therefore, the absorption involves also those excited vibrational levels of the excited state which features a significant overlap to the ground vibrational level of the ground electronic state. In conclusion, the factor $|\mu_{fi}^e|^2$ determines the transition probability through selection rules, whereas the factor $|\langle a|b \rangle|^2$ establishes the shape of absorption or emission bands according to the vibrational substructure.

3.2.2 QUENCHING OF THE EMISSION

As seen in the previous section, not all the possible relaxation paths of a photocycle give rise to photoluminescence. That is the case of internal conversion, intersystem crossing and vibrational relaxation, whereby the excited system loses progressively its energy, and until it reaches the ground state. Moreover, a quenching of the fluorescence can be caused by the intervention of external species, which activate further non-radiative relaxation. In the latter case, quenching involves a *donor* (D) that is the optically active species which is excited by an external electromagnetic field, and an *acceptor* (A) species (sometimes optically active too) to which the excitation is transferred. The energy acquired by photoexcitation in the donor species can be transferred to the acceptor through the following processes [202]:

RESONANCE ENERGY TRANSFER whereby the transfer occurs by long-distance dipole-dipole interaction (about 1–10 nm) which by enabling the exchange of the excitation between donor and acceptor, that is: $D^* + A \longrightarrow D + A^*$ (Fig. 49a), where D^* and A^* represent the donor and the acceptor species in their excited state. To this aim, the overlap of the emission spectrum of the donor and the absorption spectrum of the acceptor is required.

DEXTER ENERGY TRANSFER whereby an electron excited to the LUMO^a state of the donor and an electron in HOMO^b state of the acceptor are mutually exchanged: $D^* + A \longrightarrow D + A^*$ (Fig. 49b). This is a short range exchange interaction (between 1–10 Å) which requires the overlap of donor and acceptor wavefunctions.

PHOTOINDUCED ELECTRON TRANSFER as in the previous case, this is a short range interaction which requires the overlap of donor and acceptor wavefunctions. By contrast, both donor and acceptor can donate electron, accordingly to the reciprocal energy alignment of their HOMO and LUMO levels. In the case of *reductive* electron transfer, the photoexcited species acts as electron acceptor: $D^* + A \longrightarrow D^- + A^+$ (Fig. 49c), whereas in the case of *oxidative* electron transfer, the photoexcited species acts as electron donor: $D^* + A \longrightarrow D^+ + A^-$ (Fig. 49d).

a lowest unoccupied molecular orbital

b highest occupied molecular orbital

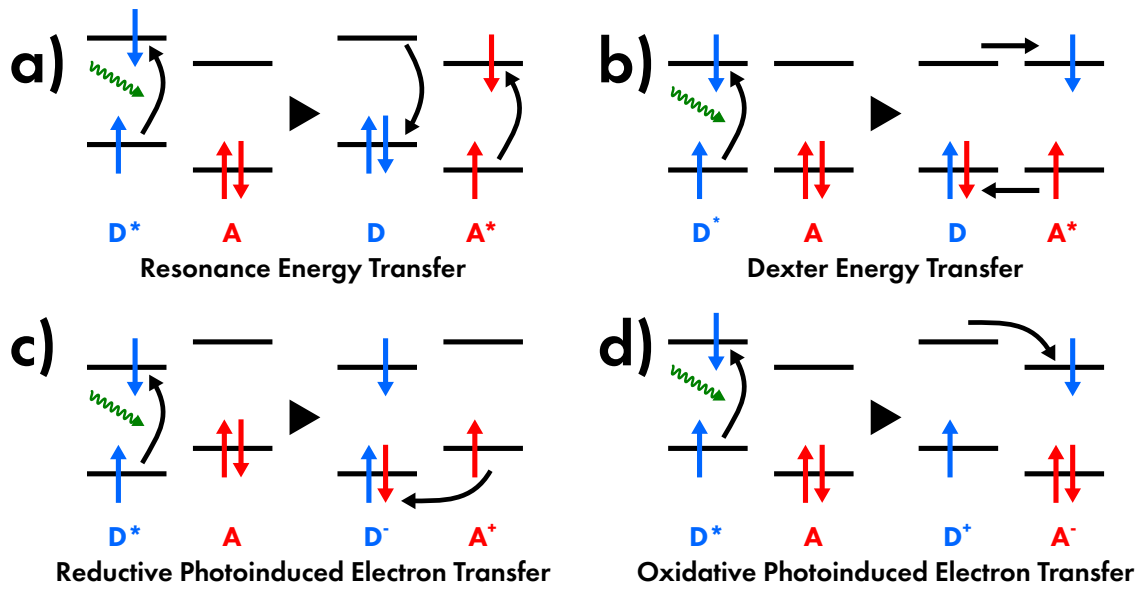


Figure 49: Mechanisms of fluorescence quenching: (a) resonance energy transfer, (b) Dexter energy transfer, (c) reductive photoinduced electron transfer, and (d) oxidative photoinduced electron transfer. Adapted from Ref. [202].

3.3 ATOMIC FORCE MICROSCOPY

Scanning probe microscopy (SPM) is a class of imaging techniques especially suitable to investigate surfaces of materials and especially 2D materials where the surface matches the entire material. In SPM techniques, the image acquisition is performed by scanning the sample surface by means of a physical probe. The motion of this probe is characterized by an interaction parameter which depends on the distance from the surface. By imposing constant such parameter, the probe is lifted or lowered according to the surface morphology, thus reconstructing the profile of the sample surface [205, 206]. Among such techniques, Atomic Force Microscopy (AFM) is one of the most renowned and diffused for its wide capability and its simplicity. Theoretical principles of this technique are briefly discussed in the following sections.

3.3.1 PRINCIPLES OF AFM

Concerning AFM, several atomic interactions are exploited, basing on short or long range probe-surface interaction and different probes design are required for specific cases. As depicted in Fig. 50a,b, a probe is commonly constituted by the following parts [205, 206]:

SUBSTRATE whereby the probe is connected to the instrumentation and by which the probe motion is controlled;

CANTILEVER which constitutes the vibrating element of the probe and is characterized by specific elastic properties;

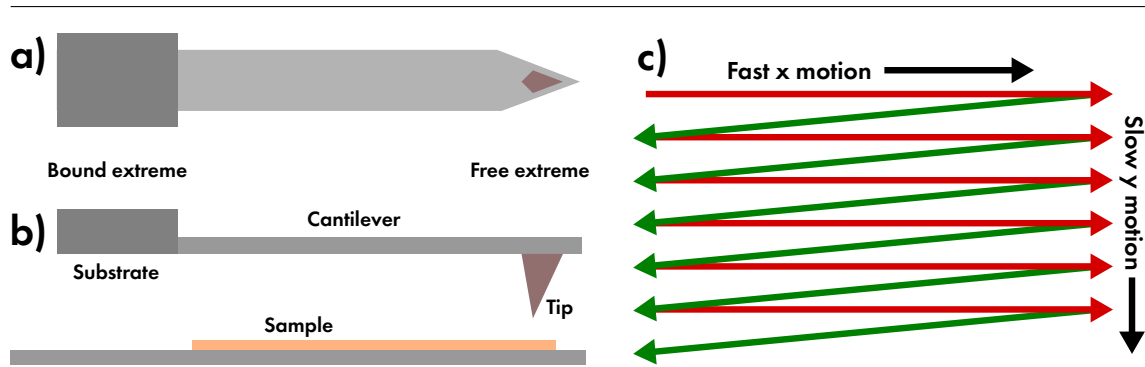


Figure 50: Representative depiction of an AFM probe and its main parts in (a) bottom view and (b) side view. (c) Motion scheme of AFM probe during the measurement. The composite motion along the x and y axes gives rise to the trace (red) and retrace (green) profiles.

TIP which features a pyramidal shape, whose apex scans the sample surface, and whose size is one of the main factors which determine the maximum image resolution.

The probe scans the surface along two directions. The first one is orthogonal to the surface (along the z axis) and this motion reconstructs the profile of the surface. On the other hand, the second direction is parallel to the surface and allows the scanning of a specific region of the sample. As shown in Fig. 50c, the latter motion is in its turn constituted by two components: a fast motion along the scan axis (x) and a slow motion along the perpendicular axis (y) [205, 206]. The combination of these two movements returns two images: the *trace image*, where the motion corresponds to the left-right scanning, and the *retrace image*, which corresponds to the right-left scanning. The similarity of these two images is a mandatory requirement in order to assure a satisfying scanning quality [205, 206].

During the AFM scanning, several types of tip-surface interaction occur. These interactions are distinguished by their attractive or repulsive nature, and in addition by their conservative or dissipative behavior. In particular, they are [205, 206]:

VAN DER WAALS FORCES already mentioned in Chp. 2, which are mainly attractive and related to the dipole-dipole interactions. Despite they are usually conservative because of their electrostatic nature, they can induce energy dissipation whether the probe modifies the surface morphology;

CONTACT FORCES short range repulsive interaction related to the overlap between the wavefunction of surface and tip electrons prevented by Pauli exclusion principle;

CAPILLARY FORCES attractive occurring between the probe tip and the thin water film which covers the surface of the sample during ambient measurements. The eventual formation and breaking of water meniscus causes energy dissipation;

ADHESION FORCES that is a restoring forces due to unintended chemical bonds between tip and surface. Such bonds are broken when the probe tip gets away from the surface, and the potential energy acquired by the sample surface is dissipated as thermal energy.

3.3.2 AMPLITUDE MODULATION AFM

Among the various image acquisition modes available in AFM, *Amplitude Modulation AFM* mode (AM-AFM) is one of the most suitable in ambient measurement. In this mode, the probe undergoes to a periodic oscillation controlled by means of a piezoelectric crystal linked to the probe substrate. In particular, an oscillating electric tension is applied to the piezoelectric in order to induce a periodic response of the cantilever. The actual oscillation amplitude of cantilever is determined by its specific resonance condition [205, 206].

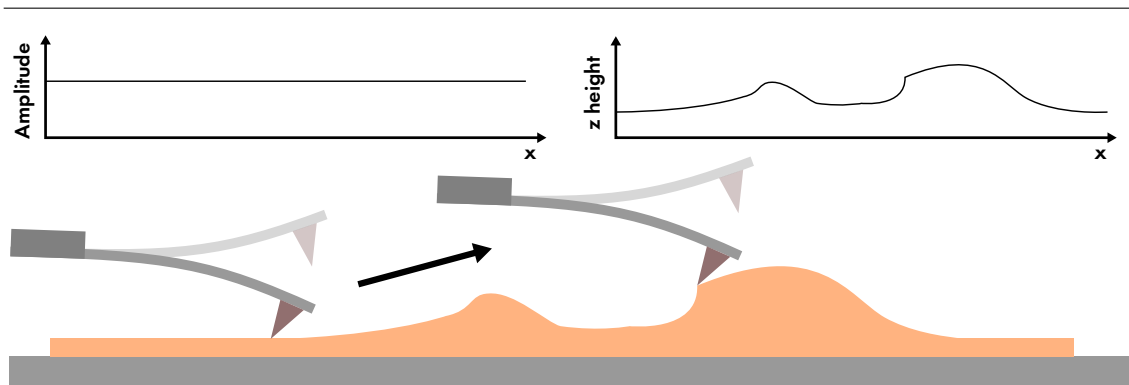


Figure 51: Profile scanning and height evaluation during an amplitude modulation AFM measurement.

The oscillation amplitude is the key parameter of AM-AFM measurement. When the probe is far away from the surface, the cantilever oscillation features an initial amplitude. Thereafter, as the cantilever approaches the surface, tip and surface start to mutually interact and the cantilever oscillation amplitude decreases. The engage of the surface takes place when the amplitude features a specific value, called *set-point amplitude* A_{sp} . Such an amplitude is identified as interaction parameter and is modified during the scanning motion. The vertical motion of the probe will be thereby varied by a feedback system in order to restore the set-point value, thus reconstructing the surface profile [205, 206].

Different acquisition modes can be performed by AM-AFM, but all the AFM images reported in the experimental section of this thesis were acquired in a single mode, namely *Intermittent Contact Mode* (also called *tapping mode*). By using this mode, the set-point amplitude is kept constant and the tip is mainly influenced by the short range repulsion forces due to the direct contact with the surface. Despite the instrumental sensitivity increases with the set-point amplitude this approach can significantly modify the real morphology of the surface because of the high energy occurring in large oscillations and, in extreme cases, it may induce severe damage to both the sample and the probe tip. Therefore, a compromise has to be established between measurement precision and measurement fidelity. Finally, since the relative strength of these forces, no restrictions on measurement ambient air are recommended.

The composite shape of probes and the various interactions previously mentioned complicate the description of tip motion during the AFM measurement, and relevant approximations are thereby required. By limiting the description to the fundamental oscillation mode, the cantilever can be thought as an harmonic oscillator which is driven by a sinusoidal force $F_0 \cos \omega t$,

is damped by a viscous medium, and undergoes an external force due to tip-surface interaction $F_{ts}(d)$ [205, 206]. In this model, the equation of motion of the cantilever is given by

$$m\ddot{z} = -kz - \frac{m\omega_0}{Q}\dot{z} + F_0 \cos \omega t + F_{ts}(d), \quad (101)$$

where m is the actual probe mass, k is the elastic constant of recovery force, ω_0 is the natural frequency of cantilever, and Q is the quality factor. To fully understand the dynamic of the cantilever described by the Eq. 101, it is useful to consider two simplified cases:

- If the tip-surface force is constant and null $F_{ts}(d) = 0$, the Eq. 101 can be analytically solved, and in the case of weak damping the solution gets the form

$$z(t) = B \exp\left(-\frac{\omega_0}{2Q}t\right) \cos(\omega_r t - \beta) + A \cos(\omega_r t - \varphi), \quad (102)$$

where $\omega_r = \omega_0 \sqrt{1 - 1/4Q^2}$, B and β are determined by the initial conditions and include eventual integration constants. On the other hand, the amplitude A is given by

$$A(\omega) = \frac{F_0/m}{\sqrt{(\omega_0^2 - \omega^2) + (\omega\omega_0/Q)^2}}, \quad (103)$$

and the phase φ is

$$\tan(\varphi) = \frac{\omega\omega_0/Q}{\omega_0^2 - \omega^2}, \quad (104)$$

with $Q = \omega_0/\Gamma$, where Γ is the full width at half maximum of the amplitude curve. Therefore, the solution of Eq. 102 features two terms: a transient solution describing a damped oscillator, and a stationary solution due to the driving force. The typical trend of amplitude and phase on varying the driving frequency are shown in Fig. 52.

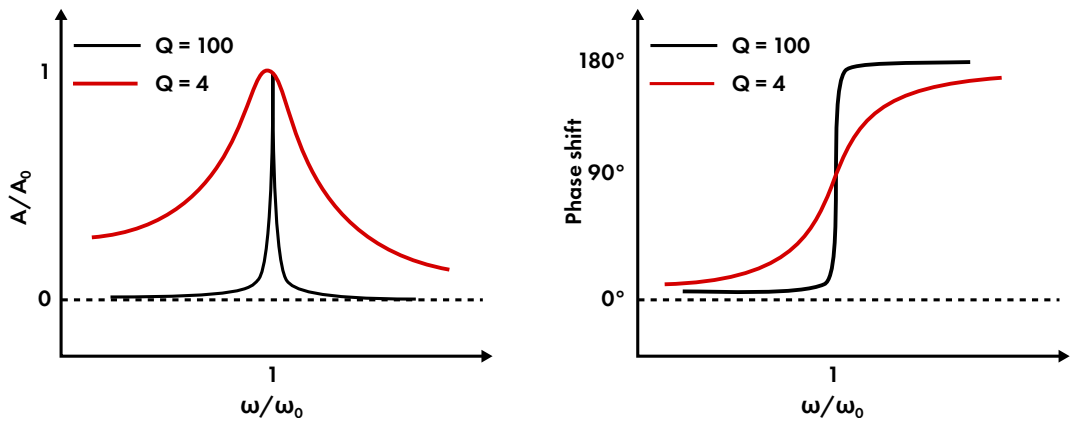


Figure 52: Typical response of amplitude and phase of cantilever oscillation as a function of the frequency of the driving force.

- In many cases of interest, for small oscillation of the cantilever with respect to its equilibrium position, the tip-surface force $F_{ts}(d)$ can be approximated as linearly dependent of the tip-surface distance, and it can be expressed as

$$F_{ts}(z) = F_{ts}(0) + \left(\frac{dF_{ts}}{dz} \right)_0 z = F_{ts}(0) - k_{ts}z. \quad (105)$$

By this approximation, the tip-surface interaction is thereby characterized by an elastic constant $k_{ts} = -(\frac{dF_{ts}}{dz})_0$, thus modifying only the proper oscillation frequency of probe ω_0 which becomes

$$\omega_1 = \omega_0 + \Delta\omega \quad \text{where} \quad \Delta\omega = \frac{\omega_0 k_{ts}}{2k}. \quad (106)$$

By assuming that when the probe is far away from the surface it oscillates at its own resonance frequency ω_0 , as reported in Fig. 53 once it engages the surface the resonance frequency changes:

- in the case of van der Waals interactions the force is attractive and then $k_{ts} = -(\frac{dF_{ts}}{dz})_0 < 0$, so the maximum amplitude shifts towards lower frequency;
- in the case of contact interactions the force is repulsive and then $k_{ts} = -(\frac{dF_{ts}}{dz})_0 > 0$, so the maximum amplitude shifts towards higher frequency.

If the cantilever keeps oscillating at frequency ω_0 , it will feature a reduced oscillation amplitude. Overall, this phenomenon is at the basis of the feedback system which modifies the probe-surface distance to keep a specific amplitude value. It is important to note that the variation of amplitude depends on the derivative of amplitude peak curve, since a sharper curve will provide a significant amplitude variation. In particular, the amplitude peak curve sharpness is governed by the quality factor of the probe (see Fig. 52), and therefore the probe has to be designed in order to maximize quality factor in order to sharpen the amplitude peak curve and to obtain a better instrumental response [205, 206].

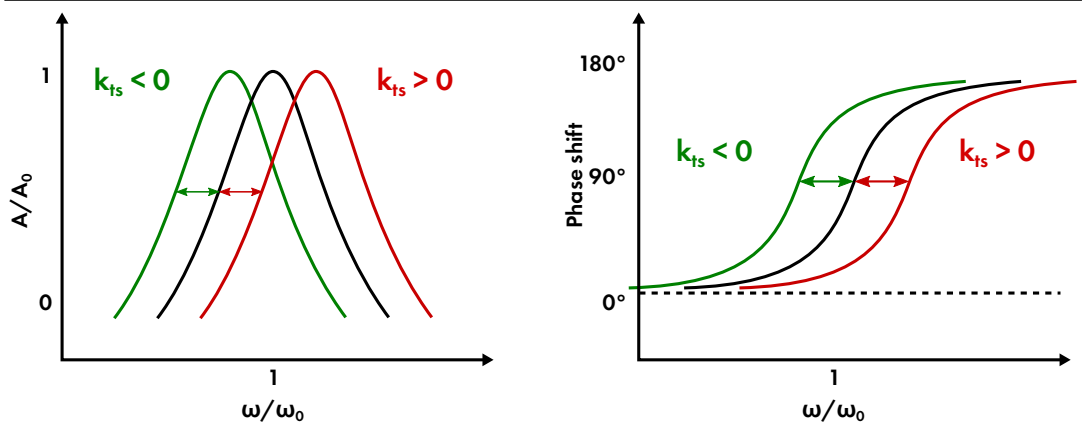


Figure 53: Modification of amplitude and phase response as effect of attractive (green) and repulsive (red) tip-surface interactions.

According to the description above reported, by scanning two different materials having the same height, the measured profile should feature no interface structure and it is not possible to distinguish among them by the morphological AFM image. On the other hand, by considering the impact of the tip-surface dissipation effects, the oscillation phase features a non-trivial evolution [205, 206]. In fact, by performing an energy balance where the energy transferred from the driving force to the probe E_{exc} is equal to

$$E_{\text{exc}} = E_{\text{med}} + E_{\text{dis}}, \quad (107)$$

where E_{med} is the dissipation due to the damping by the given medium in which the measurement is carried out, and E_{dis} is the dissipation due to the tip-surface interaction. By considering the stationary solution for the probe oscillation $z = z_0 + A \cos(\omega t - \varphi)$, it is possible to evaluate the work corresponding to the terms E_{exc} and E_{med} in an oscillation period

$$E_{\text{exc}} = \oint F_0 \cos(\omega t) \frac{dz}{dt} dt = \frac{\pi k A_0 A(\omega) \sin \varphi}{Q} \quad (108)$$

$$E_{\text{med}} = \oint \left(\frac{m\omega_0}{Q} \right) \frac{dz}{dt} dt = \frac{\pi k A^2 \omega}{Q \omega_0}, \quad (109)$$

and thus it can be obtained

$$E_{\text{dis}} = \frac{\pi k A^2}{Q} \left(\frac{A_0}{A} \sin \varphi - \frac{\omega}{\omega_0} \right). \quad (110)$$

In this way, the relation between oscillation phase and dissipated energy is revealed. Therefore, two materials featuring different energy dissipations will be distinguished by different phase values. This effect is at the basis of the *phase image*, which provides fundamental information about the composition of different materials in the investigated surface [205, 206]. An exemplary case of this procedure is reported in Fig. 54 where the scan of two different materials having the same surface height can be revealed only by the phase.

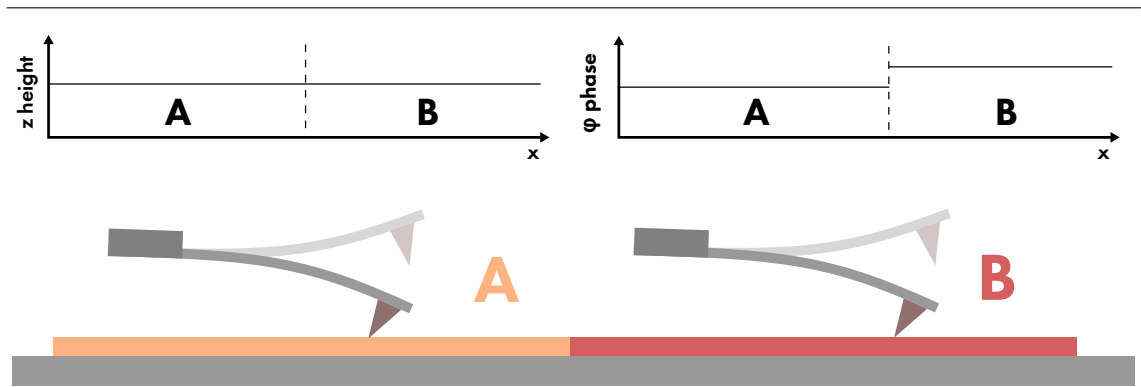


Figure 54: Profile scanning (z) and phase evaluation (φ) during an amplitude modulation AFM measurement. In particular, different phase value for two materials (A and B) is shown.

4 | MATERIALS AND METHODS

IN this chapter, major details of the materials and experimental methods used in this thesis are summarized. In particular, the synthesis procedures of graphene and carbon nanoparticles are illustrated, whereas their basic characterization is reported in Chp. 5. Finally, main details of the instrumentation used for Raman and photoluminescence measurements and for AFM imaging are reported, as well as the setup used for thermal processing experiments.

4.1 SYNTHESIS OF MATERIALS

4.1.1 GRAPHENE

Commercial single-layer graphene (Gr) produced by Graphenea Inc. was used for all the experiments reported in this Thesis [207]. According to the manufacturing specifications, graphene was grown on a copper foil (Cu) by means of Chemical Vapor Deposition (CVD), at a temperature of 1000°C by using CH₄ (methane) as carbon precursor [119, 208]. The transfer of graphene on the final substrates depicted in Fig. 55 was performed in collaboration with Dr. Filippo Giannazzo and Dr. Emanuela Schilirò (CNR-IMM)^a. First, a thin film of Poly(methyl methacrylate) (PMMA) was deposited by spin coating onto the top surface of the Gr/Cu foil. Then a thermal release tape (TRT) was laminated on PMMA. The copper foil was etched by immersion in salt bath by using (NH₄)₂S₂O₈ (ammonium persulfate) or FeCl₃ (ferric chloride), and by a cleaning in deionized

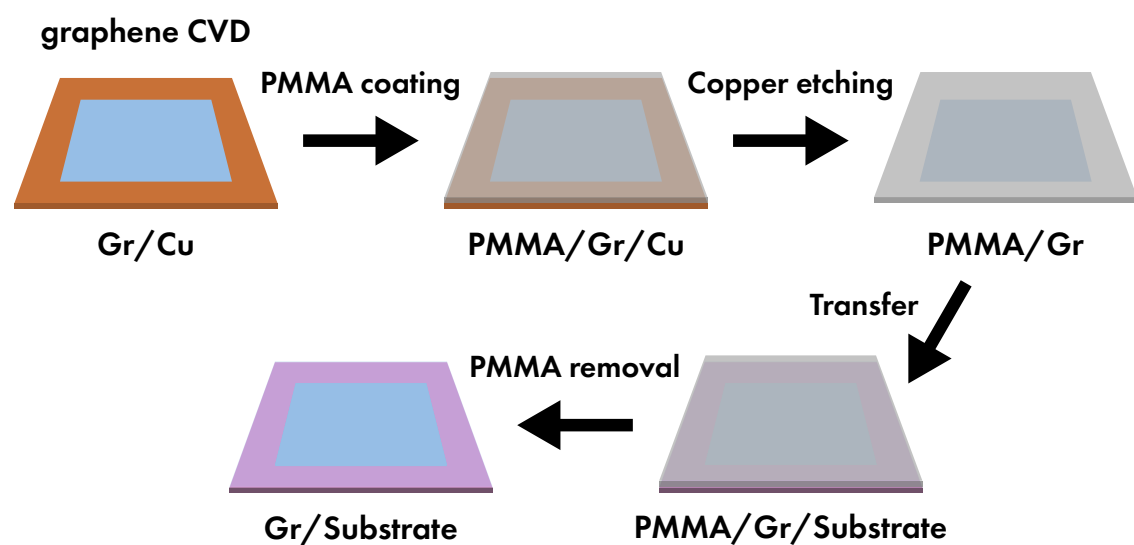


Figure 55: Scheme of the transfer procedure of graphene from the copper foil where it is grown to the final substrate.

^a National Research Council - Institute for Microelectronics and Microsystems, Strada VIII 5, 9511, Catania, Italy.

water. The remaining TRT/PMMA/Gr stack was transferred to the various substrates by thermo-compression printing, thus causing the release of TRT. Finally, the sample was cleaned from PMMA by acetone bath, thus obtaining the Gr/substrate stack. In particular, the three substrates were constituted by a silicon wafer on which different surface thin films were grown:

- amorphous SiO_2 was thermally grown on the top surface of silicon wafer until reaching a 300 nm thick layer. In addition, a further hydrophobic substrate was obtained by substituting the hydroxyl groups of SiO_2 surface by methyl groups by means of hexamethyldisilazane (HMDS). The HMDS has been applied by means of a spin-coating equipment, using a double step of spin speed: 100 RPM for 2 min and 1000 RPM for 1 min.
- amorphous Al_2O_3 was grown by thermal atomic layer deposition at 250°C using $\text{Al}_2(\text{CH}_3)_6$ (tri-methyl aluminium) and water as aluminium and oxygen precursors, respectively, until reaching a 40 nm thick layer.
- amorphous HfO_2 was deposited by plasma enhanced atomic layer deposition at 250°C by using $[(\text{CH}_3)_2\text{N}]_4\text{Hf}$ (tetrakis-dimethylamino hafnium) as hafnium precursor and O_2 -plasma as oxygen source until reaching a 50 nm thick layer.

The three kinds of samples obtained by using these substrates are thereby labeled as Gr/ SiO_2 /Si, Gr/ Al_2O_3 /Si, and Gr/ HfO_2 /Si. In the following chapters, for the sake of simplicity, in some occasions a simplified version of the previous labels is used: Gr/ SiO_2 , Gr/ Al_2O_3 , and Gr/ HfO_2 , respectively. In addition, graphene transferred onto the hydrophilic and hydrophobic SiO_2 /Si substrate is labeled Gr/h- SiO_2 and Gr/m- SiO_2 , respectively

4.1.2 CARBON DOTS

Carbon dots (CDs) were synthesized in collaboration with Prof. Fabrizio Messina and Dr. Alice Sciortino (UniPA)^b. In particular, as discussed in Chp. 2, the CDs exploited for this Thesis consisted in nitrogen-doped carbon nanoparticles with typical size of about 1–10 nm constituted by a $\beta\text{-C}_3\text{N}_4$ core, namely carbon-nitride in the peculiar β phase, and by a surface passivated by various functional groups: carboxyl ($-\text{COOH}$) and amide ($-\text{CONH}_2$) [191, 192]. In particular, CDs were obtained through a bottom-up technique by using citric acid monohydrate as carbon precursor and urea as nitrogen precursor, both dissolved in water. They both underwent to a carbonization process performed by microwave irradiation until the complete evaporation of water occurred [191, 192]. From the resulting CDs powder, two different solutions were prepared. The first one was prepared dissolving the as synthesized powder in ethanol, in a concentration of 0.1 g/l [192]. The second solution was prepared dissolving the same powder in water, in a concentration of 0.1 g/l, and then separating the most luminescent fraction by means of size exclusion chromatography [191]. The study of CDs was performed exclusively in solid phase, after having deposited 1 μl of CDs dispersion onto a target substrate: Gr/ SiO_2 /Si or bare SiO_2 /Si. The deposition was performed by drop-casting technique in fume hood so as to accelerate the drying of the solvents, and thus preventing the unintended aggregation of nanoparticles.

^b University of Palermo, Department of Physics and Chemistry - Emilio Segrè, Via Archirafi 36, 90123 Palermo, Italy.

4.2 RAMAN SPECTROSCOPY

Two different instruments were used for the Raman spectroscopy measurements: *Bruker SENTERRA Spectrometer*, and *Horiba LabRam HR-Evolution Spectrometer*. Despite they differ in some technical specifics, both instruments share the main elements depicted in Fig. 56: a laser source (even more than one) at fixed power and wavelength, a series of neutral density filters to modulate the power of the light reaching the sample, a microscopy system which allows to resolve in a microscopic scale the sample zone involved in the measurement, a pinhole which allows to measure in confocal mode, thus enhancing both the vertical and the lateral space resolutions, a diffraction grating for the energy dispersion of the scattered light, a motorized stage for the fine positioning of the sample.

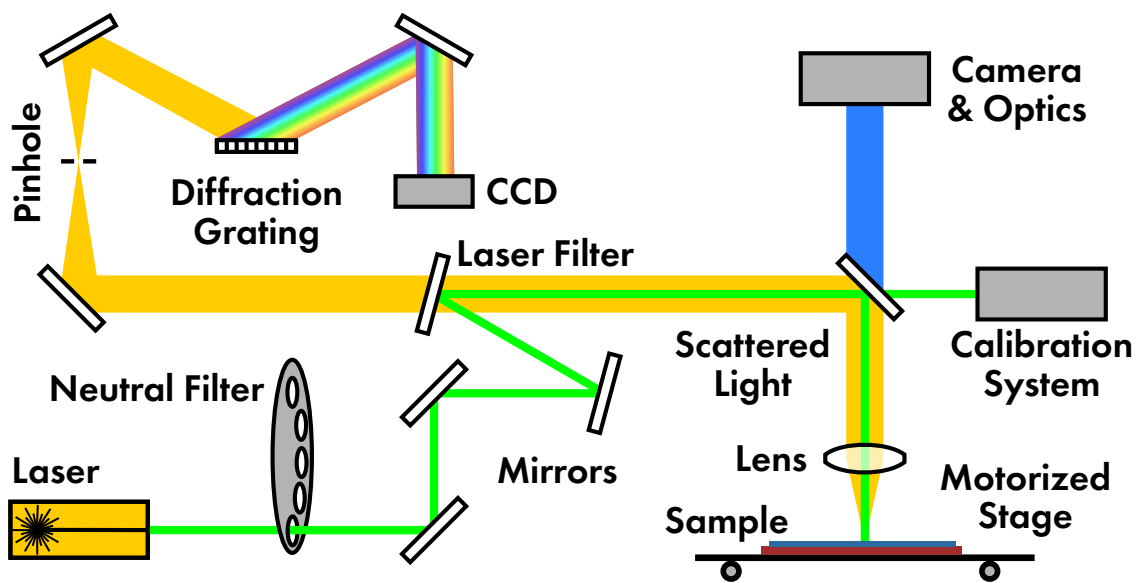


Figure 56: Scheme of the internal elements of a typical Raman spectrometer.

Given a sample, the Raman spectrum is acquired by the following procedure:

The laser light goes into the optical system and by controlling its power by a chosen neutral filter. The light reaches the sample thanks to a series of mirrors, and it is focused in a well defined spot on the surface by a microscope lens. There, some of the light is scattered and collected by the microscope. The Raman scattering is guided towards the spectrometer, whereas the Rayleigh scattering is stopped by an opportune filter. In this stage, the scattered light goes through a pinhole in order to select the portion of light coming only from the focal plane. Finally, the light spectrum is obtained by diffraction grating and acquired by a CCD. Successively, during the data analysis, all the spectra are calibrated again (a first calibration is performed just before the measurement) by aligning them to the silicon band located at 520.7 cm^{-1} , whose presence is due to the wafer [209, 210].

In particular, the following parameters were used for the measurements, by taking care to adapt the laser power to avoid any sample modification:

BRUKER SENTERRA SPECTROMETER used for μ -Raman and μ -PL spectroscopy at 532 nm (2.33 eV) excitation laser performed by using a confocal optical microscopy system with $50\times$ optical magnification, a best spectral resolution equal to 9 cm^{-1} , and a data pitch equal to 0.5 cm^{-1} . μ -Raman measurements were performed at nominal power of 5 mW on a target area equal to $4\times 4\text{ }\mu\text{m}^2$ for Gr/SiO₂ and Gr/Al₂O₃, and $4\times 15\text{ }\mu\text{m}^2$ for Gr/HfO₂. μ -PL measurements were performed at nominal power of 2 mW on a target area equal to $4\times 4\text{ }\mu\text{m}^2$.

HORIBA LABRAM HR-EVOLUTION SPECTROMETER used for Raman Spectroscopy at 633 nm (1.96 eV) excitation laser performed by using a confocal optical microscopy system with $100\times$ optical magnification, a best spectral resolution equal to 7 cm^{-1} , and a data pitch equal to 1 cm^{-1} . All the measurements were performed at nominal power equal to 5 mW on a target area of $1\times 1\text{ }\mu\text{m}^2$.

4.3 ATOMIC FORCE MICROSCOPY

Two different instruments were used for the AM-AFM imaging: *Bruker FastScan Bio Microscope*, and *Veeco MultiMode Microscope*. Both microscopes are mainly constituted by the elements depicted in Fig. 57: a probe whose oscillations are controlled by a piezoelectric, a diode laser and a photodiode used for the monitoring of probe tip oscillation, a piezoelectric scanner whose xy motion is set by the user, whereas the z motion is driven by a lock in amplifier and a Proportional-Integral-Derivative (PID).

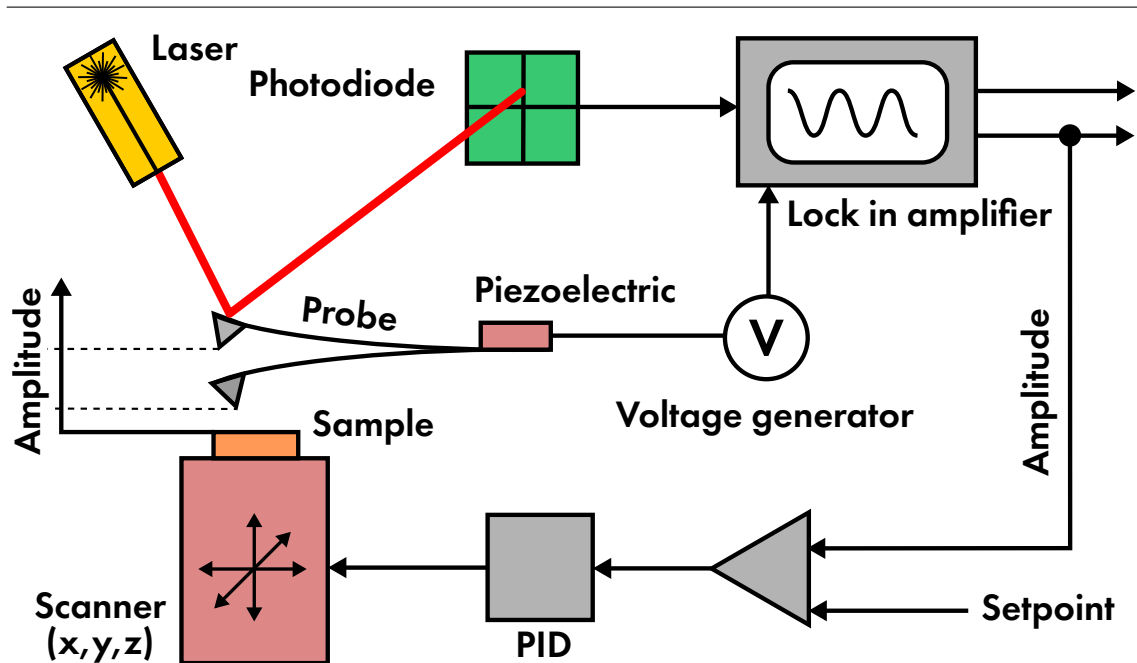


Figure 57: Scheme of the elements of a typical atomic force microscope for amplitude modulation measurements.

The images are obtained by the following procedure:

First, the oscillation of the probe is calibrated by selecting a well defined resonance peak in the amplitude-frequency curve. Then, in order to monitor the motion of

the probe, a laser is carefully pointed on the top surface of the tip and therefore reflected towards a photodiode. In such a way the oscillation of the tip are translated in a electrical signal. Thus, the signal is enhanced by a lock-in amplifier and the actual oscillation amplitude is compared to setpoint value. The latter stage is done by the PID, which thereby transmits a feedback signal to the sample scanner. In fact, after the initial engage between tip and sample surface, the scanner modifies the tip-surface distance accordingly to the feedback of the PID. Finally, the image of the surface is obtained by collecting the values of the various relevant quantities (tip-surface distance, oscillation amplitude, oscillation phase) during the scanning of the sample along x and y directions. In addition, the software Gwyddion v. 2.52 and Bruker NanoScope Analysis were used for the post-measurement correction and the extraction of quantitative information.

In particular, the measurements were performed by the following instrumentation:

BRUKER FASTSCAN BIO MICROSCOPE equipped with Bruker FastScan A probes with tip radius approximately equal to 5 nm. AFM images were acquired by using tapping mode on different micrometric scales, up to $5 \times 5 \mu\text{m}^2$ of area.

VEECO MULTIMODE MICROSCOPE equipped with Nanosensors and Bruker probes. These latter were characterized by a tip radius approximately equal to 5 nm. Even in this case, AFM images were acquired by using tapping mode on different micrometric scales, up to $2 \times 2 \mu\text{m}^2$ of area.

4.4 THERMAL PROCESSING

Thermal treatments in controlled atmosphere were conspicuously used in order to modify the materials described in the previous sections. In every experiments the typical procedure consisted in: the sample was exposed to a given gas, at a given temperature, and for time. Successively, measurements were carried out *ex-situ* at ambient conditions. As depicted in Fig. 58, the apparatus was constituted by the following parts:

- two reaction chambers, the first one was made by stainless steel of about 100 ml volume and was used for treatments at high temperature, and the second one was made by a blind PTFE tube of about 50 ml volume and was used for treatments at ambient temperature;
- a vacuum pump used to empty the first reaction chamber and the other connections. The treatments were performed in two pressure regimes: *ultra high vacuum* (10^{-5} mbar) in the case of treatment in vacuum, and *high vacuum* ($3 \cdot 10^{-1}$ mbar) for the pre-vacuum preceding the gas injection.
- pure gases used in order to perform thermal treatments in selective gas: oxygen (O_2), nitrogen (N_2), and carbon dioxide (CO_2) with 20 parts per million of impurity. Treatments in gas atmosphere were performed at 2 bar of pressure;

- a muffle oven used to heat the first reaction chamber to the desired temperature, in the range 150–400°C;
- a Parr reactor model 4651 of about 250 ml volume containing a gas phase of helium and a liquid phase of water was used as water evaporator after heating at 150°C.

In addition, two cooling procedures were used at the end of the thermal treatment:

FAST COOLING performed by rapidly quenching the temperature of the sample up to the ambient temperature within about 60 seconds.

SLOW COOLING performed by slowly decreasing the temperature of the sample up to the ambient temperature within about 6 hours.

Finally, some peculiar procedures used for the thermal processing of graphene reported in the following chapter are specifically described in the following:

STANDARD TREATMENT performed at 300°C, 2 hours of gas exposure, and at pressure equal to 2 bar whether a specific atmosphere is chosen, or alternatively in ultra high vacuum, and completed by a fast cooling.

VARYING TEMPERATURE performed in oxygen atmosphere only at standard pressure of 2 bar, 2 hours of gas exposure, in a wide range of temperature from 150°C up to 400°C by incremental steps of 25°C, and completed by a fast cooling.

VARYING TIME performed in oxygen atmosphere only at standard pressure of 2 bar, at temperature equal to 300°C, in a time range of gas exposure between 5 minutes and 2 hours, reached by different time incremental steps, and completed by a fast cooling.

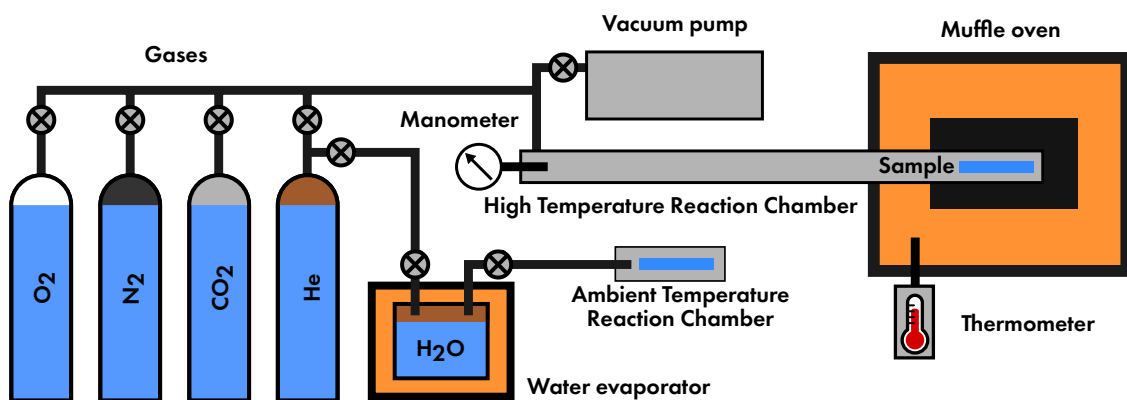


Figure 58: Scheme of the apparatus utilized for the thermal treatments in controlled atmosphere.

5 | EXPERIMENTAL RESULTS

THE content of this chapter concerns the results of the experimental investigation of graphene interaction with other species. The general aim of the study is the attempt to clarify those processes of interaction influencing the charge distribution in graphene energy levels in order to advance the knowledge for potential applications of graphene in electronic and optoelectronic devices. In particular, the chapter is subdivided in two sections: the first one concerns the interaction with small molecules and the second one concerns the interaction with carbon nanoparticles.

5.1 INTERACTION WITH MOLECULES

5.1.1 CHARACTERIZATION OF SUBSTRATES

As discussed in Chp. 4, the graphene samples studied in this Thesis were transferred on different substrates, namely SiO_2/Si , $\text{Al}_2\text{O}_3/\text{Si}$, and HfO_2/Si . The substrates utilized as support of graphene were firstly characterized in terms of the morphological and chemical properties to evaluate their influence on the structural and electronic features of graphene. The AFM images shown in Fig. 59 report the morphological characterization of the substrate surface. Herein, by

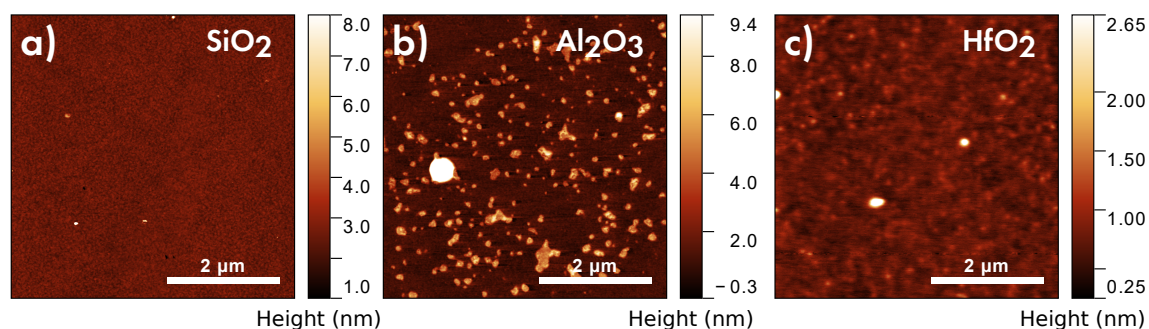


Figure 59: Image acquired by Atomic Force Microscopy of the substrate utilized in this thesis: (a) SiO_2 , (b) Al_2O_3 , (c) HfO_2 . Adapted from Ref. [211].

taking care to discard the incidental clusters of residual PMMA (that is avoiding all white spots in Fig. 59), a value of surface roughness equal to 0.22(1) nm, 0.31(1) nm, and 0.13(2) nm was obtained for SiO_2 , Al_2O_3 , and HfO_2 surfaces, respectively (Fig. 60a) [211]. On the other hand, the water affinity of surface moieties was evaluated in terms of the contact angle of a water drop deposited on the various substrates^a. Such a quantity resulted equal to 60(2)°, 74(1)°, and 87(2)°, for SiO_2 , Al_2O_3 , and HfO_2 surfaces, respectively (Fig. 60b) [211]. Therefore, different morphological and chemical features of the three substrates here reported can be exploited to compare the behavior of supported graphene in contact with different surfaces.

^a Stella Lo Verso of STMicroelectronics, Stradale Primosole 50, I-95121 Catania, is acknowledged for these measurements.

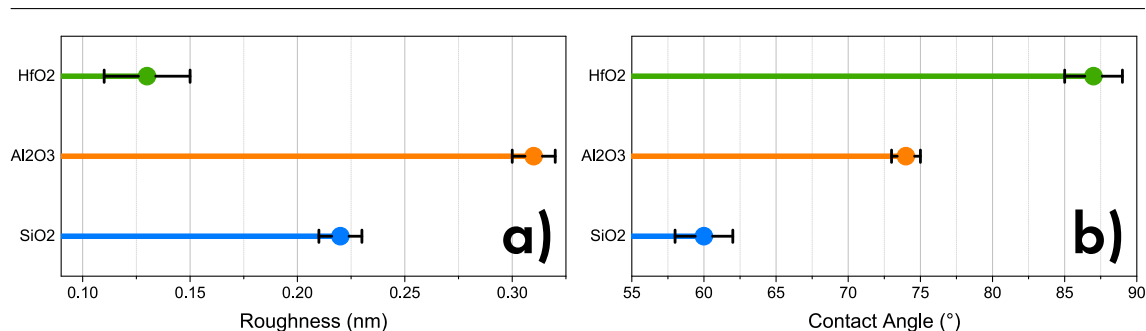


Figure 60: Comparison of (a) surface roughness and (b) water affinity of SiO₂, Al₂O₃, and HfO₂ substrates.

5.1.2 CHARACTERIZATION OF GRAPHENE

As discussed in Chp. 4, after the synthesis by chemical vapor deposition (CVD), graphene (Gr) was transferred on various final substrates, thus obtaining the three samples Gr/SiO₂/Si, Gr/Al₂O₃/Si, and Gr/HfO₂/Si according to the stack depicted in Fig. 61a. Despite the synthesis by CVD is renowned for the production of large area graphene with very low defect concentration, the transfer can affect its structural integrity. Therefore, some cracks and wrinkles (folded graphene) can be induced during this process, as shown in the images acquired by optical microscopy of graphene on the oxide substrates reported in Fig. 61b,c,d for the three samples. The overall surface of Gr/substrate stack features thereby both Gr and substrate surface regions. However, the transfer seems to affect the structural integrity of graphene only at the macroscopic scale. In fact, as shown by AFM images reported in Fig. 62, graphene features undamaged flakes without internal cracks. In addition, some residual PMMA clusters are found on the surface of the sample, having resisted the acetone bath. Such residues are found in various ways: as small numerous clusters on the surface of SiO₂ (Fig. 62a), as large well isolated clusters on the surface of Gr (Fig. 62b), and as

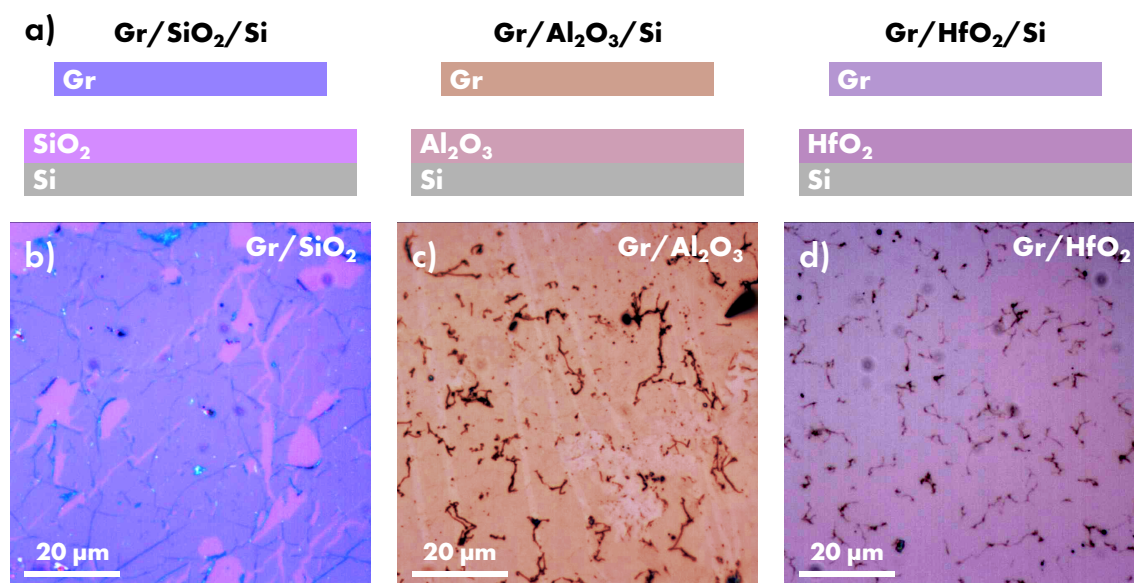


Figure 61: (a) Scheme of layer stacking which constitutes the three samples. Image acquired by optical microscopy of (b) Gr/SiO₂, (c) Gr/Al₂O₃, and (d) Gr/HfO₂ samples.

a wide thin layer spread on large region of the sample (Fig. 62c) [212]. Furthermore, graphene features a mean roughness equal to 0.27(5) nm, by considering only regions free of PMMA residues.

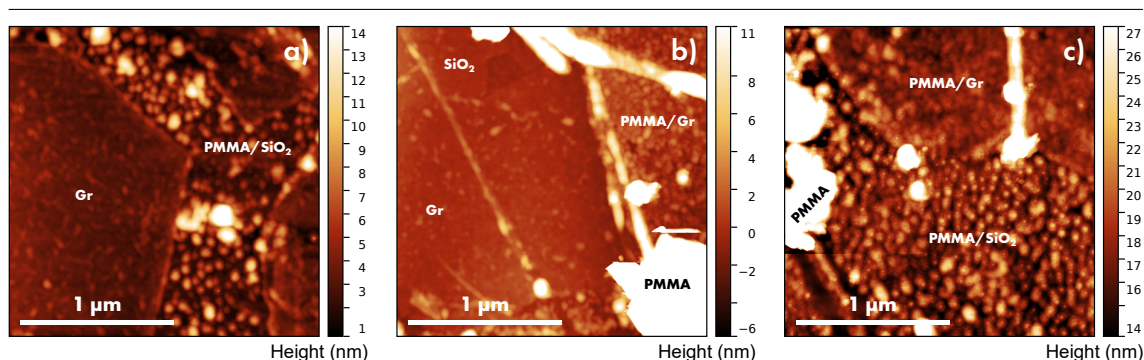


Figure 62: Image acquired by Atomic Force Microscopy of Gr on the SiO₂/Sisubstrate. Different morphology of PMMA residues are found: (a) small and (b) large clusters, or (c) thick layer on the surface of the sample. Adapted from Ref. [213].

Raman spectroscopy provided the largest part of information concerning graphene. The typical Raman spectra of native Gr/SiO₂, Gr/Al₂O₃, and Gr/HfO₂ are shown in Fig. 63, and all spectra report the main features of graphene, that is the D, G and 2D bands. The following quantities were extracted from each of those spectra: G and 2D band peak position ($\bar{\nu}_G$ and $\bar{\nu}_{2D}$), their full width at half maximum (FWHM) (Γ_G and Γ_{2D}) and the ratio of their peak amplitude ($I_{2D}/I_G = R$) [56]. The average values of these quantities arising from a sampling constituted by a number of measurements between 20 and 80 taken in different points of the sample and their uncertainty (expressed in terms of one standard deviation) are reported in Tab. 1. Every spectrum features the typical G and 2D bands with a ratio R higher than 1, thus indicating the presence of a single-layer Gr. Furthermore, the spectra suggest that the fraction of carbon atoms in sp² hybridization

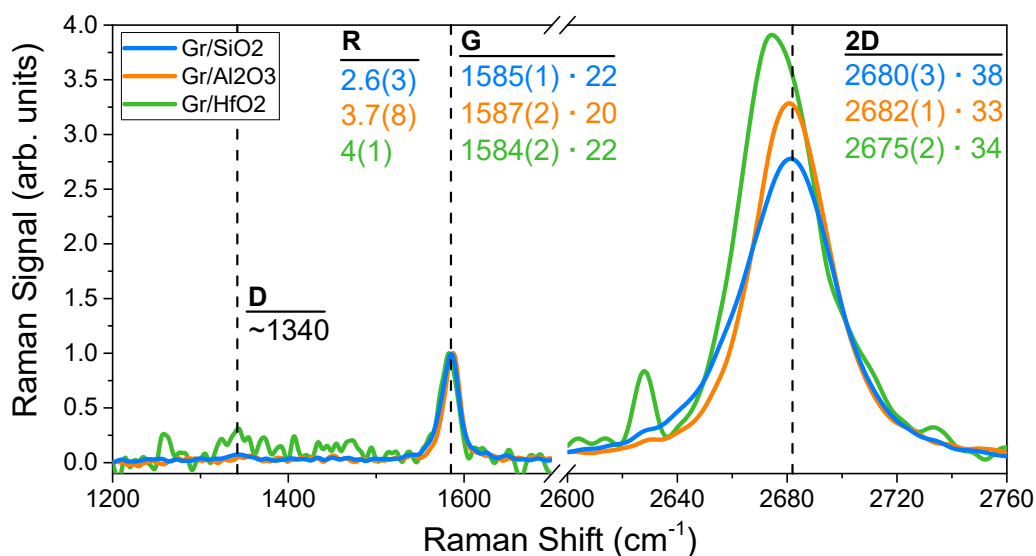


Figure 63: Raman spectra normalized at G peak amplitude of Gr/SiO₂, Gr/Al₂O₃, and Gr/HfO₂. Dashed lines mark the peak position of D, G, and 2D bands for Gr/SiO₂ sample. For each sample, amplitude ratio R, peak positions and FWHM are reported. Adapted from Refs. [211, 212]

prevails on the contribution of defects concentration, since the very low intensity of D band ($\sim 1340\text{ cm}^{-1}$). Besides, the different signal/noise ratio observed on varying the substrate (clearly comparable in the spectral region between 1200 and 1700 cm^{-1}) is related to the strong influence of the oxide layer. In fact, as reported in literature, the thickness and dielectric constant of the latter affect significantly the Raman signal intensity of Gr [97].

Sample	$\bar{\nu}_G\text{ (cm}^{-1}\text{)}$	$\bar{\nu}_{2D}\text{ (cm}^{-1}\text{)}$	$\Gamma_G\text{ (cm}^{-1}\text{)}$	$\Gamma_{2D}\text{ (cm}^{-1}\text{)}$	R
Gr/SiO ₂	1585(1)	2680(3)	22(3)	38(3)	2.6(3)
Gr/Al ₂ O ₃	1587(2)	2682(1)	20(3)	33(2)	3.7(8)
Gr/HfO ₂	1584(2)	2675(2)	22(3)	34(5)	4(1)

Table 1: Raman spectroscopic features of Gr/SiO₂, Gr/Al₂O₃, and Gr/HfO₂ [211].

Most importantly, as shown in Fig. 64a, the correlation between G and 2D peak positions allows to obtain a clearer distinction of the three samples. In fact, three different point clouds are found, and each of them describes a different and well-defined average configuration with its own spread on strain and doping values. From a qualitative point of view, it is easy to note that both Gr/Al₂O₃ and Gr/HfO₂ point clouds show different *orientations* compared to Gr/SiO₂, thus suggesting a different heterogeneity in strain and doping configurations. In particular, their point clouds show a narrower distribution along the strain axis, and a broader distribution along the doping axis, indicating a more ordered structure, and a more heterogeneous electronic structure. On the other hand, from a quantitative point of view, each sample features a doping below the minimum level of sensitivity of this technique (10^{12} cm^{-2} charge carriers concentration), and

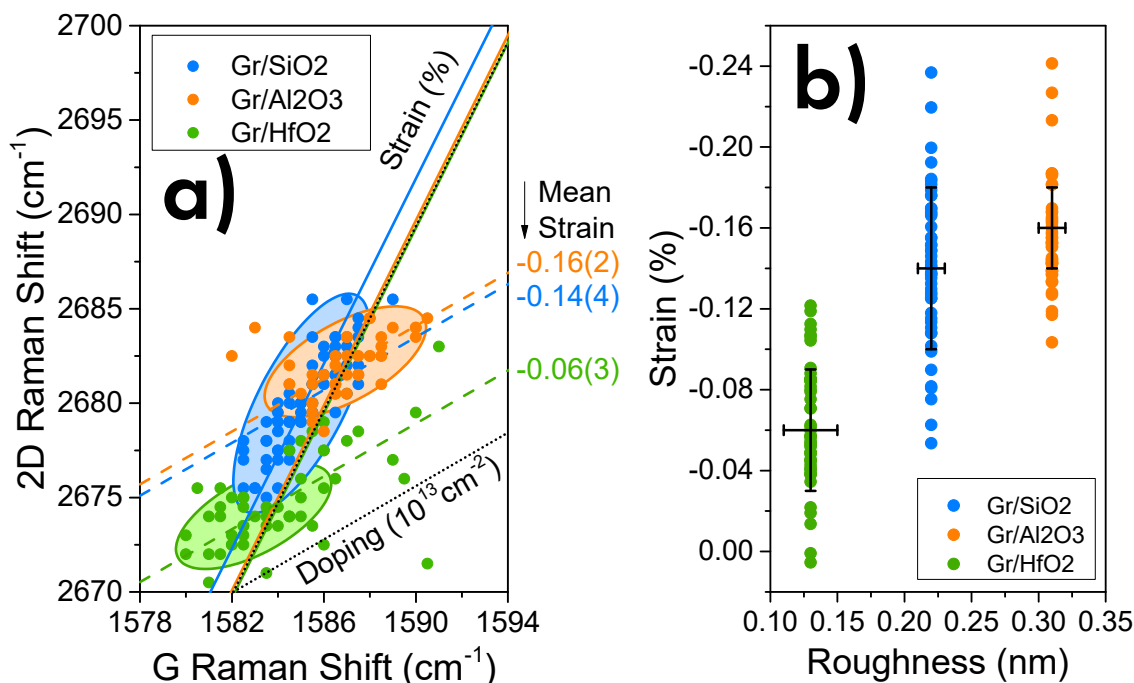


Figure 64: (a) Correlation map between G and 2D peak position of Gr/SiO₂, Gr/Al₂O₃, and Gr/HfO₂. Qualitative ellipses highlight the three point clouds. Dotted lines mark strain and doping axes. For each cloud, dashed lines and continuous lines mark the average strain and doping, respectively. The extracted values of strain are also reported. (b) Correlation between the graphene strain evaluated by G-2D map and the substrate roughness evaluated by AFM. In all the panels, the uncertainty value for the last digit is reported in parenthesis. Adapted from Refs. [211, 212].

therefore a quantitative estimation is possible only for strain. In this case, the dashed lines of Fig. 64a indicate a strain equal to $\varepsilon = -0.14(4) \%$, $\varepsilon = -0.16(2) \%$, and $\varepsilon = -0.06(3) \%$, for Gr/SiO₂, Gr/Al₂O₃, and Gr/HfO₂ respectively. The close connection between the roughness of Gr and the morphology of the substrate has already been shown in literature [214, 215]. In particular, the surface covered by Gr features a reduced roughness, interpreted as a smoothing effect similar to the case of a foil laying on a non-flat surface. In addition, the study reported in Sec. 5.1.8 will show the relation between the roughness of Gr opportunely estimated by AFM and its strain evaluated by Raman spectroscopy [212]. Based on these findings, the strain of graphene and the substrate roughness are assumed correlated, revealing a relation of proportionality between them, as shown in Fig. 64b. These results indicate that some structural features of native Gr depend on how Gr lies down on the substrate after the transfer process: the higher the roughness of the substrate and the higher the strain of Gr [211].

5.1.3 INFLUENCE OF SUBSTRATE ON DOPING BY O₂

As previously reported in literature, the exposure of Gr to oxygen molecules at opportune temperature and pressure induces a doping effect [147, 148, 150–153]. This modification of the electronic state was mainly investigated for SiO₂/Si substrate. Herewith, a deepening of the process and a comparison with other substrates was carried out in order to generalize the results and also to understand the basic physical features underneath the doping process.

In order to discern the doping effect of O₂ from the pure thermal effect, we compare the results of thermal treatments in O₂, and in N₂, since on the basis of previous experiments, these two atmospheres correspond to a reactive and an inert atmosphere, respectively [149]. Typical spectra of Gr/SiO₂ thermally treated in *standard conditions* (at 300°C, 2 bar for 2 h) are reported in Fig. 65a and compared with the spectrum of the native sample of Fig. 63.

Concerning the O₂ treatment, no modification for D band occurs, thus confirming that this thermal treatment preserves the *sp*² structure of graphene. Besides, the spectrum shows a significant blueshift of both G and 2D bands. This feature, in addition to the strong decrease of R ratio, suggests the occurrence of doping in graphene, according to the discussion of Chp. 1 [212]. Similar modifications are found also for the N₂ treatment, even if by minor magnitude. Most importantly, a further broad spectroscopic feature appears in the region between 1200 and 1700 cm⁻¹, very similar to the D and G unresolved peaks of amorphous carbon (am-C) [216–218]. Despite the appearance of this spectroscopic contribution is well reported in literature as effect of thermal treatment of supported graphene, it was variously interpreted as related to the formation of defects in graphene structure or to the presence of amorphous carbon as product of degradation and dehydrogenation of PMMA residual on the sample surface [149, 218–221]. To discern between these two hypothesis, a multi-peak analysis of that region was performed. As shown in Fig. 65b, the whole region can be described by four bands which feature two distinct ranges of width. The two narrowest can be attributed to the Raman signal of graphene (the amplitude of the so extracted G band is used for the normalization of Fig. 65a) which does not appear relevantly changed from the native sample except by a slight increase of D band [218–220, 222]. On the other hand, the two broadest bands can be attributed to the proper Raman signal of amorphous carbon.

This analysis is in accordance with the hypothesis by which the broad band belongs to am-C. On the basis of this conclusion, the appearance of this band is thereby related to the carbonization of the PMMA residues found over the surface of graphene. Besides, the complete absence of this band in the case of O₂ treatment can be justified by the reaction between the oxygen molecules and the PMMA or the am-C, with a probable transfer in gas phase of the products.

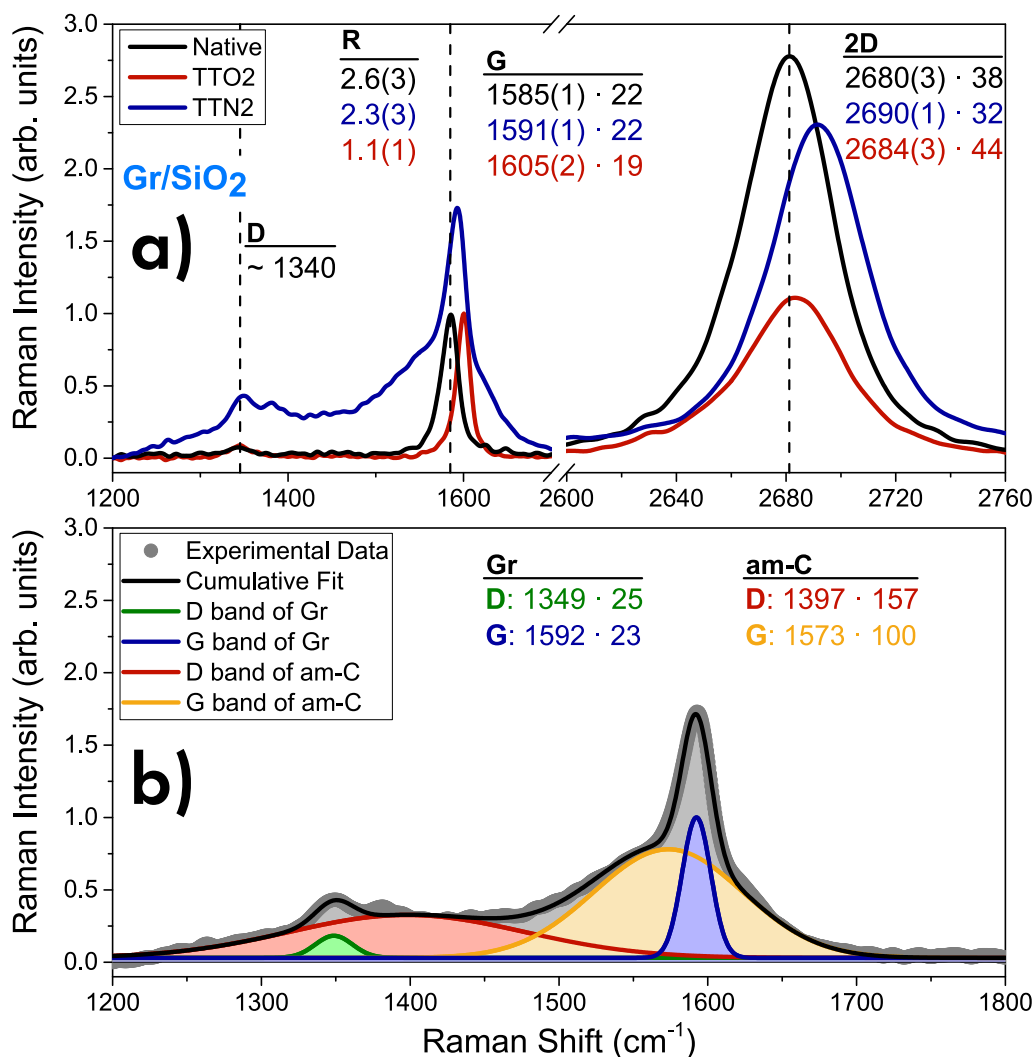


Figure 65: (a) Raman spectra normalized at G peak amplitude of native (black line), thermally treated in O₂ (TTO₂), and thermally treated in N₂ (TTN₂) Gr/SiO₂. For the latter, the normalization of the spectrum is done according to the analysis reported in the next panel. Dashed lines mark the peak position of D, G, and 2D bands for Gr/SiO₂ sample. The mean values of amplitude ratio R, peak positions and FWHM are reported. The uncertainty value for their last digit is reported in parenthesis. Adapted from Ref. [212]. (b) Multi-peak analysis of Gr/SiO₂ thermally treated in N₂ reported in the previous panel. The mean values of peak positions and FWHM are reported.

A similar analysis conducted for Gr/Al₂O₃ and Gr/HfO₂ (spectra are reported in Fig. 66 after the subtraction of the am-C bands) reveals same evolution already discussed for Gr/SiO₂, with the blueshift of G and 2D band and the change of the amplitude ratio. In particular, the absence of D band is particularly clear for Gr/Al₂O₃ (Fig. 66a), whereas the low signal-noise ratio featuring the spectrum of Gr/HfO₂ does not allow to detect the D band, thus making difficult to draw the same conclusion. However, a large occurrence of defect sites can be excluded by the peak amplitude ratio I_D/I_G which, even if hard to estimate, is certainly lower than 0.3 [56].

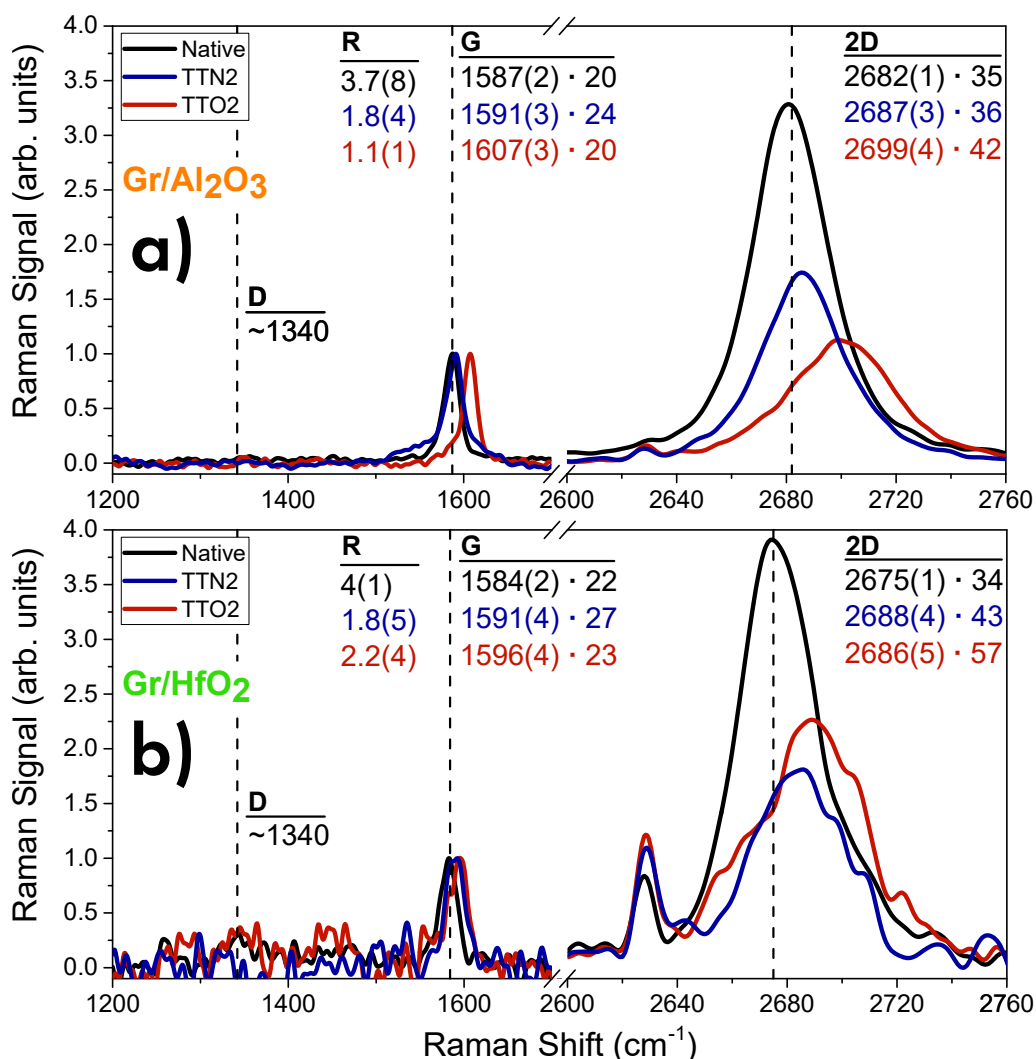


Figure 66: Raman spectra normalized at G peak amplitude of native (black line), thermally treated in O₂ (TTO₂), and thermally treated in N₂ (TTN₂) (a) Gr/Al₂O₃, and (b) Gr/HfO₂. Dashed lines mark the peak position of D, G, and 2D bands for Gr/SiO₂ sample. For each sample, amplitude ratio R, peak positions and FWHM are reported. The uncertainty value for their last digit is reported in parenthesis. Adapted from Ref. [211].

As previously mentioned, the correlation between G and 2D peak frequencies provides fundamental information about doping and strain of graphene. As shown in Fig. 67a,b, the point clouds of both Gr/SiO₂ and Gr/Al₂O₃ thermally treated samples are clearly shifted compared to the native ones and similarly *dense*. On the contrary, in the case of Gr/HfO₂ (Fig. 67c), the same treatments in N₂ and O₂ atmospheres cause more heterogeneous results. In fact, despite a similar trend of shifts is recognizable, both the point clouds are largely spread on the graph, indicating a non-homogeneous effect of both strain and doping.

Concerning the N₂ treatment, the shape of point clouds is approximately similar to the native ones. In addition, a slight increase of doping is found for Gr/SiO₂ (at the limit of the sensitivity of this technique), reaching the value of $D = 0.2(6) \times 10^{13} \text{ cm}^{-2}$ and an increase of compressive

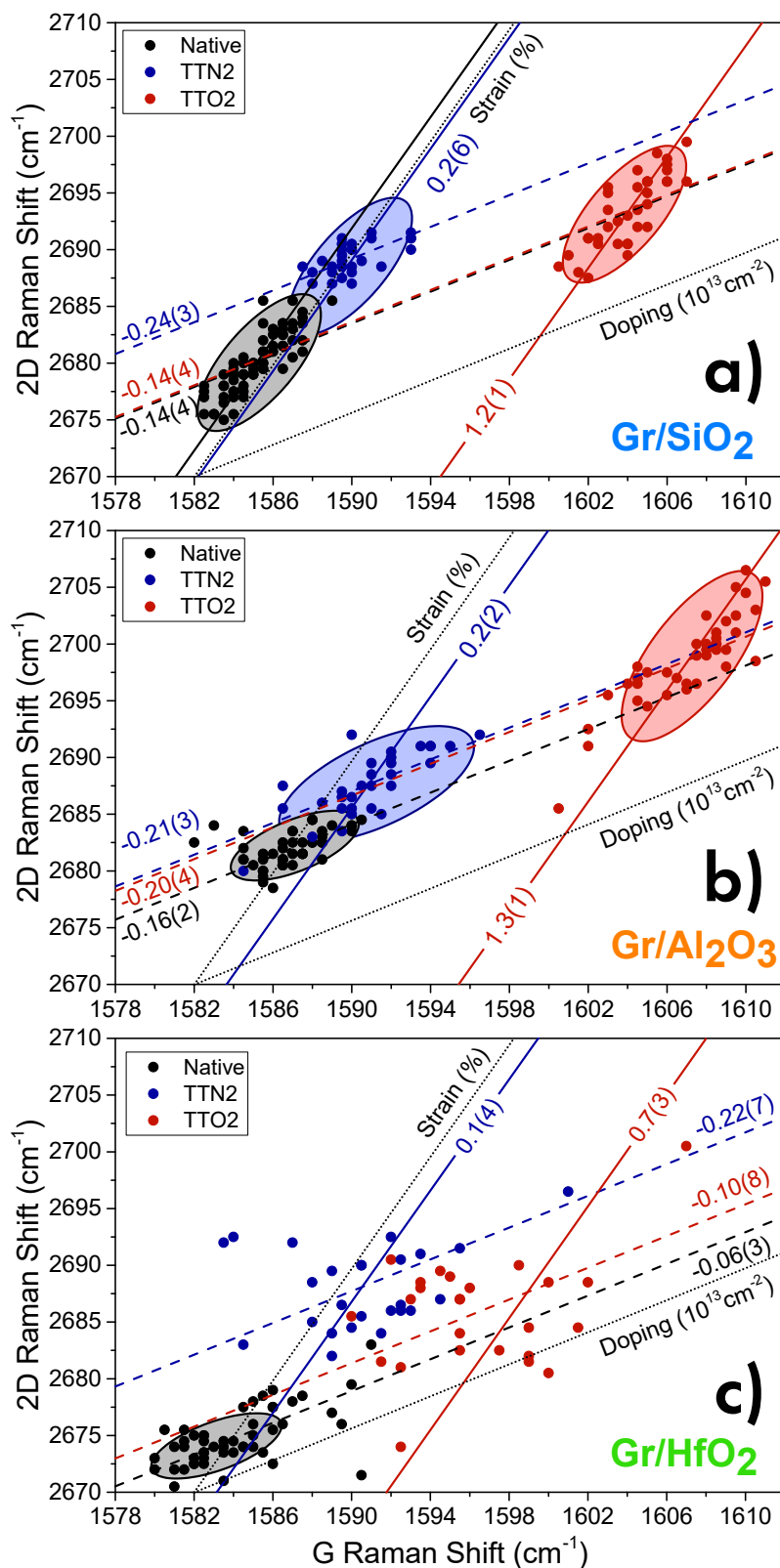


Figure 67: G-2D correlation map of native (black), and treated samples at $T = 300^\circ\text{C}$, for 2 hours, at pressure of 2 bar of oxygen (red, TTO₂) and nitrogen (blue, TTN₂) atmosphere for (a) Gr/SiO₂, (b) Gr/Al₂O₃, and (c) Gr/HfO₂. Qualitative ellipses highlight the dense point clouds. Dotted lines mark strain and doping axes. For each sample, dashed lines and continuous lines mark the average strain and doping, respectively. The extracted values of strain and doping are also reported. The uncertainty value for their last digit is reported in parenthesis. Adapted from Refs. [211, 212].

strain up to $\varepsilon = -0.24(3)\%$ [212]. These values are similar to those found for Gr/Al₂O₃, which features $D = 0.2(2) \times 10^{13} \text{cm}^{-2}$ and $\varepsilon = -0.21(3)\%$, in addition to the increase of spread along the doping axis [211]. Besides, despite of the larger spread of point cloud, similar mean values are obtained for Gr/HfO₂: $D = 0.1(4) \times 10^{13} \text{cm}^{-2}$ and $\varepsilon = -0.22(7)\%$.

More remarkable changes occur as effect of O₂ treatment. As reported in Fig. 67, the point cloud of Gr/SiO₂ is uniformly shifted to values of significant doping equal to $D = 1.2(1) \times 10^{13} \text{cm}^{-2}$ with no relevant modification of strain which maintains the native value of $\varepsilon = -0.14(4)\%$. Concerning the Gr/Al₂O₃, a similar evolution is found for doping, which increases up to $D = 1.3(1) \times 10^{13} \text{cm}^{-2}$ in contrast with previous investigations [149]. A different evolution is found for strain, which increases up to $\varepsilon = -0.20(4)\%$, comparable to N₂ treatments. In addition, compared to the native cloud, Gr/Al₂O₃ treated by O₂ is affected by a larger spread along strain axis than along doping axis, as well as a higher Γ_{2D} (Fig. 68e), thus suggesting that the O₂ doping process involves the modification of the Gr structure towards a more disordered configuration, more similar to typical Gr/SiO₂. Moreover, it can be suggested that the decrease in doping spread and Γ_G is due to the doping process itself, which constrains the charge carrier concentration to a specific level, more strictly determined than for the native (unintentional) doping. On the other hand, for Gr/HfO₂, the cloud features a very large spread, related to a strong structural and electronic heterogene-

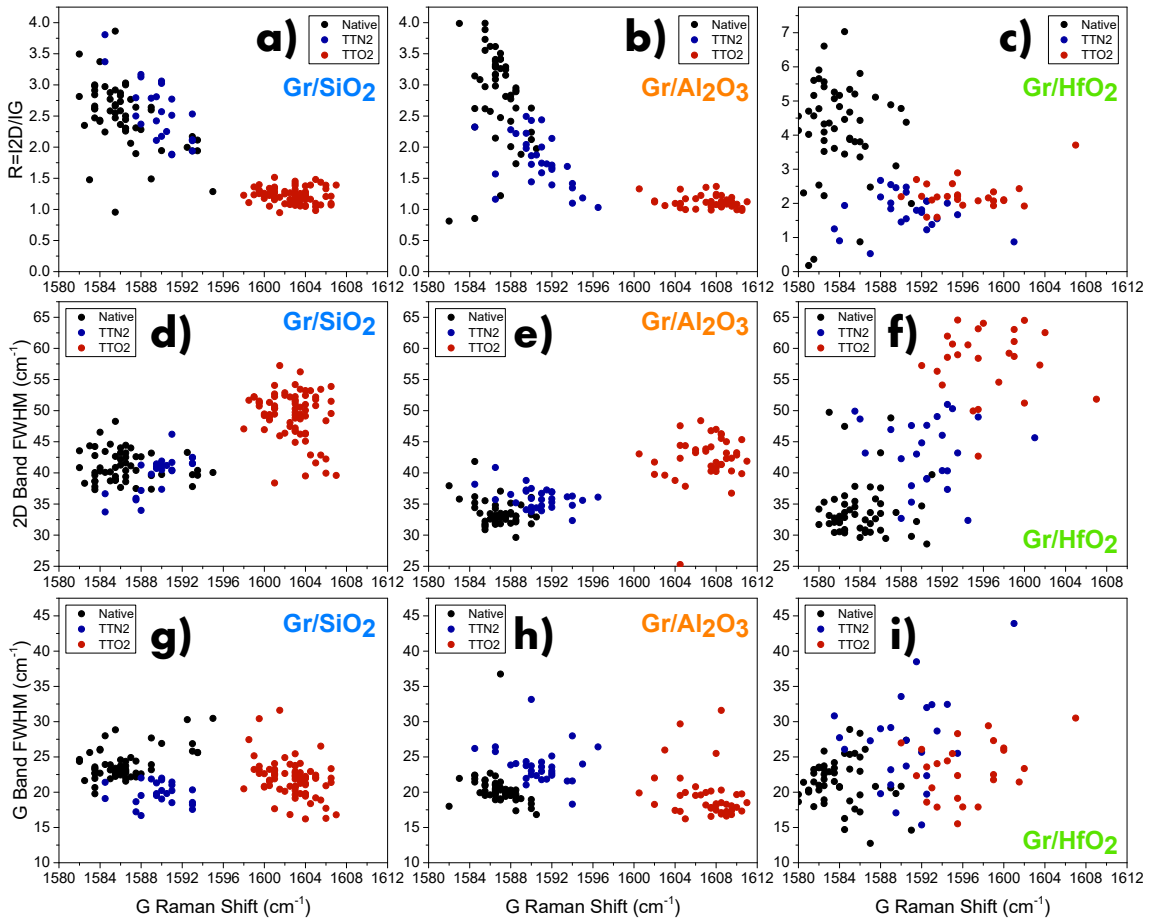


Figure 68: Correlation between (a,b,c) 2D-G bands peak intensity ratio R, (d,e,f) 2D FWHM, (g,h,i) G FWHM, and the peak position of G band of native (black), thermally treated in O₂ (red, TTO₂), and thermally treated in N₂ (blue, TTN₂) Gr/SiO₂, Gr/Al₂O₃, and Gr/HfO₂, respectively. Adapted from Refs. [151, 211, 212].

ity. In this case, a doping level equal to $D = 0.7(3) \times 10^{13} \text{cm}^{-2}$ is estimated, on average lower than the other two samples. Finally, the strain reaches the value $\varepsilon = -0.10(8)\%$, lower than N_2 treatments [211]. Furthermore, we can note three main effects of treatment in O_2 : it heavily modifies the ratio R by drastically reducing it (Fig. 68a–c); the G and 2D peak positions blueshift significantly, and the FWHM of G and 2D band result modified (Fig. 68d–i). In particular, the evolution of R and Γ_G are in accordance with a doping effect, despite the larger reduction of Γ_G expected cannot be observed due to instrumental limitation.

Some works in literature exploited different treatment parameters (temperature, gas pressure and exposure time) in order to provide more information about the nature of doping process. The most relevant cases have already been discussed in Chp. 2. In previous investigation concerning Gr/SiO₂, Lee et al. showed the occurrence and the time evolution of doping in graphene and proved the connection to the intercalation of small molecules (O_2 , H_2O) in the interstitial space between graphene and substrate [155]. Further investigation of Piazza et al. exploited the dependence on treatment time and temperature of doping to extract information about this process [151]. In particular, the dependence on temperature was used to report a first estimation of temperature distribution of *stable doping states*, whereas the dependence on time was used to evaluate the time range in which the doping occurs. On the other hand, no effect of gas pressure were observed in the explored range (0.5–10 bar) [151]. Therefore the effect of substrate substitution treatment temperature and time is evaluated in the following section in order to more clarify the role of substrate in the doping process.

DOPING VS TEMPERATURE

The dependence of doping on treatment temperature was investigated by performing a series of thermal treatments on a given sample, with duration of 2 hours each and increasing the temperature by steps of 25°C up to 400°C and then evaluating *ex-situ* the doping by Raman spectroscopy. In particular, the experiment was performed for Gr/Al₂O₃ and Gr/HfO₂, whereas the data for Gr/SiO₂ are reported from Ref. [151]. As shown in Fig. 69, a progressive increase of doping is revealed for every sample by the shift of point clouds along the doping axes and by the decrease of the ratio R reported in Fig. 70. Concerning the strain, a slight increase of compressive strain is found for Gr/Al₂O₃ and Gr/HfO₂, contrary to what is reported for Gr/SiO₂ where a strong decrease of strain was revealed at maximum doping levels [151]. Furthermore, in agreement to what reported in the previous section, a broadening of strain values distribution is revealed on the increase of doping for Gr/Al₂O₃, and Gr/HfO₂. In particular, it is possible to observe the progressive evolution of strain spread thanks to the gradual increase of doping by temperature, as well as the heterogeneity which characterizes this change. Concerning the latter aspect, as reported in Fig. 70e,f, Gr/Al₂O₃, and Gr/HfO₂ feature the increase of Γ_{2D} against $\bar{\nu}_G$, that is against doping. Since Γ_{2D} is related to strain spread and therefore to the structural disorder of graphene, this result strengthens the idea of a correlation between doping process and structural reassessment of Gr structure. Most importantly, Γ_{2D} reaches the maximum values at intermediate temperature, thus indicating that the condition of the largest structural disorder characterizes the state of intermediate doping. On the contrary, this evolution does not occur in Gr/SiO₂, which maintains the same strain spread and Γ_{2D} for the entire explored range of doping.

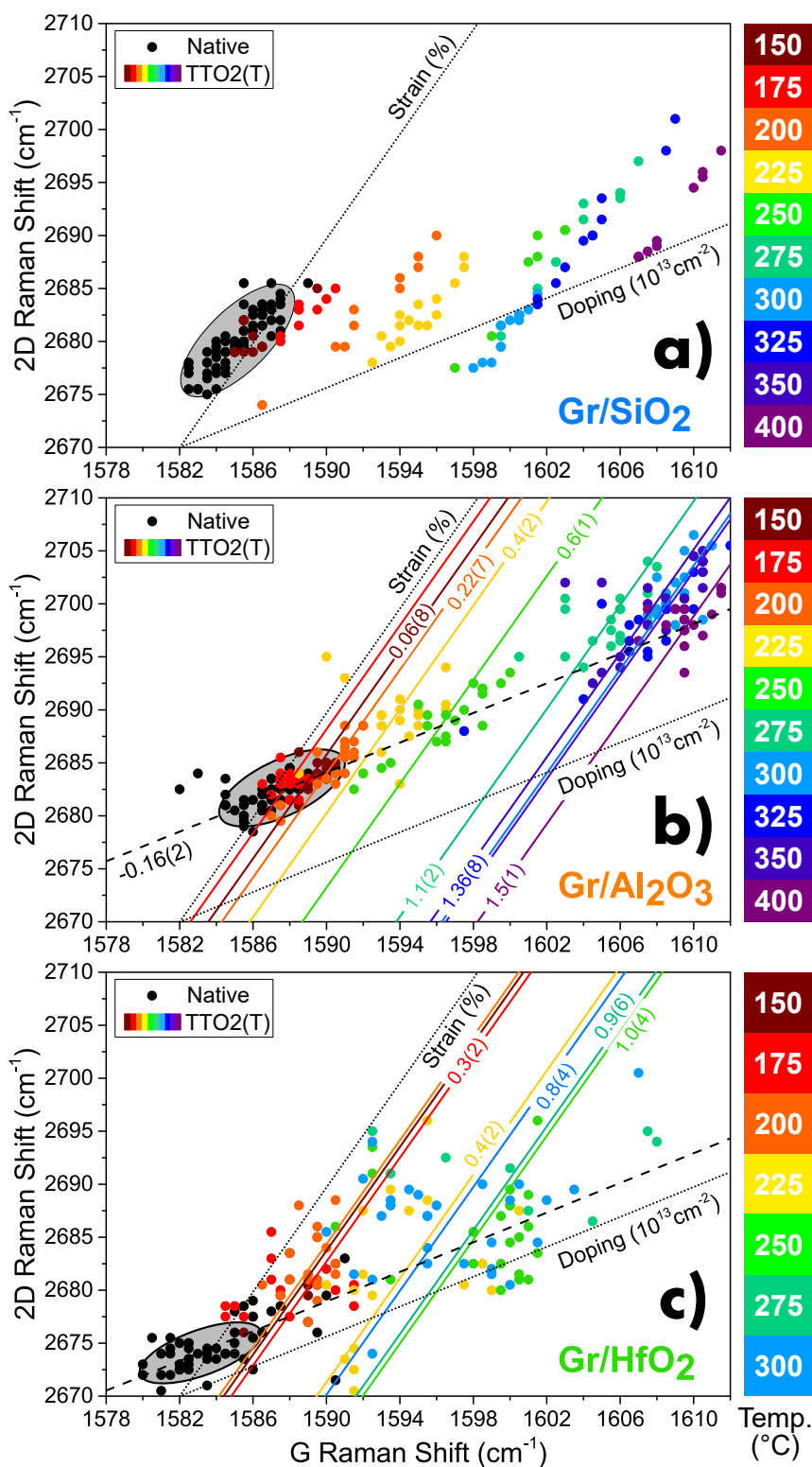


Figure 69: G-2D correlation map of native (black), and thermally treated samples in oxygen (TTO₂) atmosphere on increasing the treatment temperature (color scale) of (a) Gr/SiO₂, (b) Gr/Al₂O₃, and (c) Gr/HfO₂. Dotted lines represent the reference strain and doping axes. Dashed lines and continuous lines mark the average strain and doping, respectively. The extracted values are also reported. The uncertainty value for their last digit is reported in parenthesis. Adapted from Refs. [151, 211, 212].

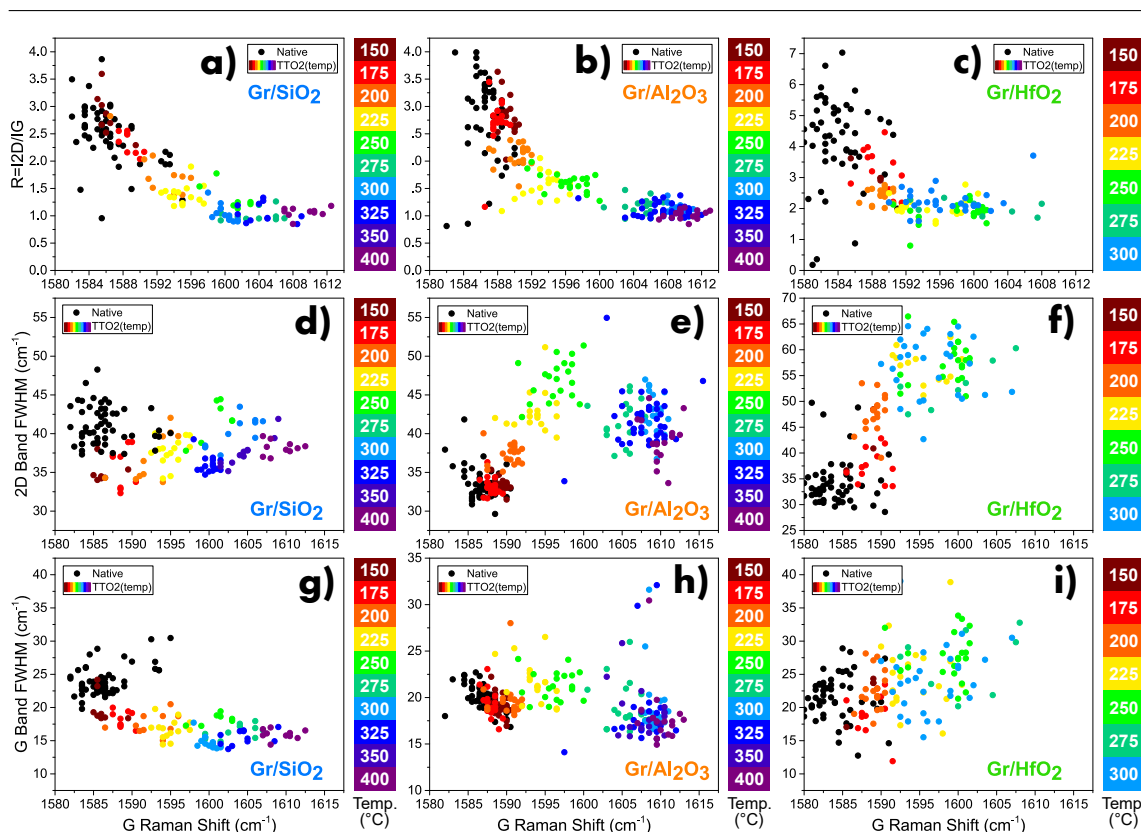


Figure 70: Correlation between (a,b,c) the amplitude ratio R , the FWHM of (d,e,f) 2D and (g,h,i) G bands and the peak position of G band at different treatment temperatures (color scale) for Gr/SiO₂, Gr/Al₂O₃, and Gr/HfO₂. Adapted from Refs. [151, 211, 212].

The values of strain and doping extracted by point clouds at different temperatures shown in Fig. 69 are reported in Fig. 71. Concerning strain (Fig. 71a,b,c), a variegated evolution is observed featuring an overall increase of strain spread, but no particular trend. In particular, the average strain of treated Gr/SiO₂ features equal or lower value with respect to the native sample, whereas the Gr/Al₂O₃ and the Gr/HfO₂ show a slight progressive increase. Besides, a well defined trend is found for the doping evolution (Fig. 71d,e,f), more evident in the case of the samples Gr/SiO₂ and Gr/Al₂O₃ than in the case of Gr/HfO₂ because of the larger spread of values of the latter sample. In fact, the doping increases with the temperature by featuring a sigmoidal trend characterized by a threshold temperature and by a saturation level. The latter is different for the three samples: $1.75(9) \times 10^{13} \text{cm}^{-2}$ for Gr/SiO₂, $1.54(9) \times 10^{13} \text{cm}^{-2}$ for Gr/Al₂O₃, and $0.9(4) \times 10^{13} \text{cm}^{-2}$ for Gr/HfO₂. These values can also be expressed in terms of number of charge carriers per unit of C atoms as equal to 0.45(3)%, 0.39(3)%, and 0.24(9)%, for Gr/SiO₂, Gr/Al₂O₃, and Gr/HfO₂, respectively. Such values indicate the introduction of dopant charges in the range 2000–5000 ppm and testify the large capability to dope graphene by thermal treatments in O₂ which is comparable to heavy doping of typical semiconductors (above 100 ppm). In addition, a decrease of doping occurs at the higher temperatures ($T > 250^\circ\text{C}$) for Gr/HfO₂ only [211].

As previously discussed in Chp. 2, the features of doping obtained by thermal treatment in O₂ atmosphere can be variously related to the support substrate. Some works have already found different results on varying the substrate [149] and, in some cases, the doping was characterized by a spatial heterogeneity [155]. In those studies, it is proposed that doping arises from the diffusion of

O_2 molecules in the interstitial space between graphene and substrate where the process which induces the doping takes place. Therefore, according to this picture, doping is not only *affected* but even *defined* by the substrate and its surface properties. By following this interpretation, the different behaviors above reported are ascribed to the different used substrates, and in particular, to the reaction sites present on their surface. The three curves reported in Fig. 71d,e,f can thereby be interpreted as a cumulative contribution to the doping provided by the fraction of the reaction sites whose activation temperature is below to the treatment temperature. Thus, for each system, we can obtain the distribution in temperature of the reaction sites N_{RS} by means of the

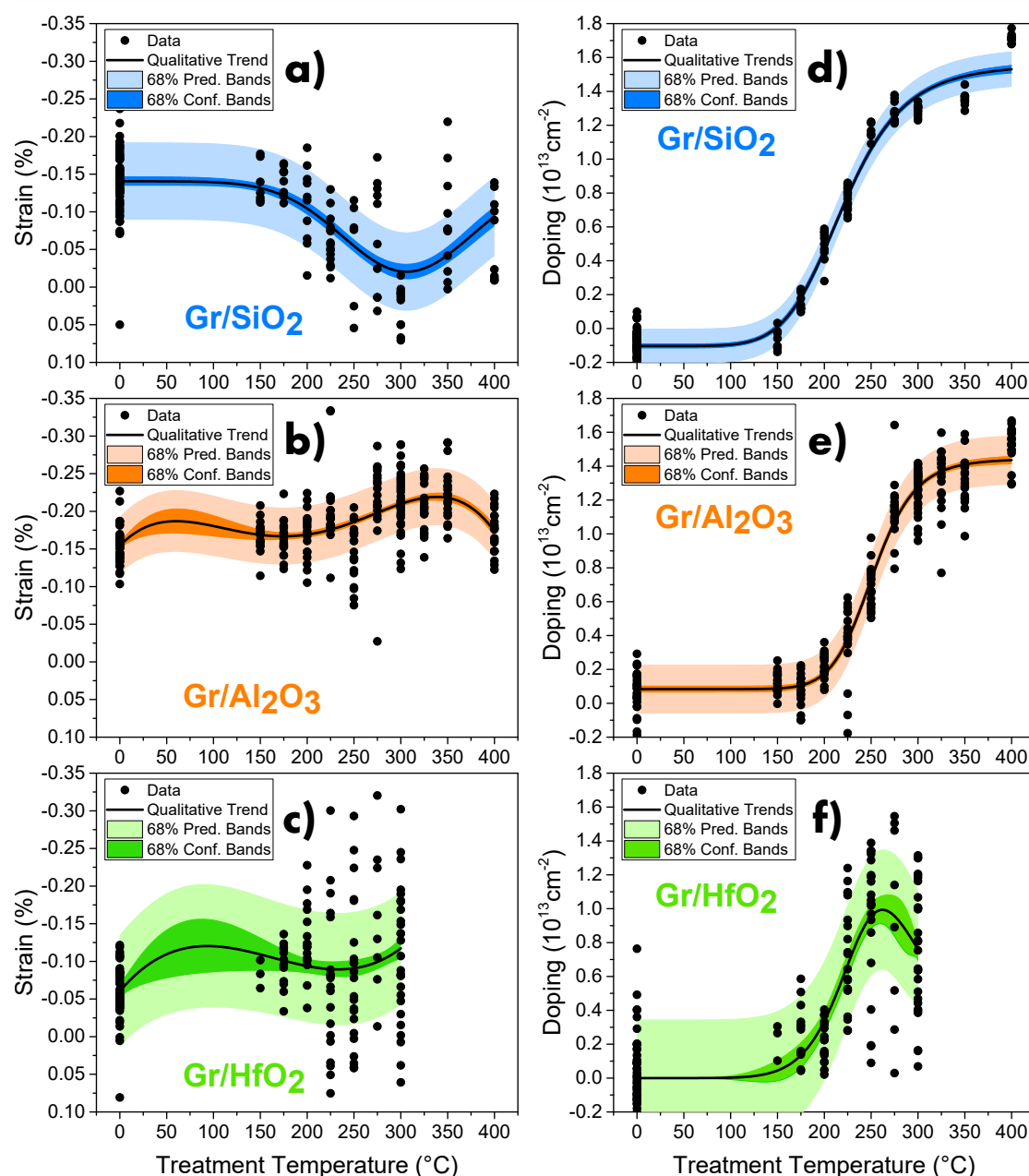


Figure 71: Extracted strain and doping values on varying temperature for (a,d) Gr/SiO₂, (b,e) Gr/Al₂O₃, and (c,f) Gr/HfO₂, respectively. For both strain and doping, representative fit curves mark the trend of the temperature effect. Their uncertainty is reported by the prediction and confidence bands at one standard deviation by the polynomial (strain) and the Logistic or BiHill (doping) curves provided by Origin (OriginLab, Northampton, MA) function library. Adapted from Refs. [151, 211].

mathematical derivative with respect to the temperature of doping curves $N_{RS} \propto \partial D / \partial T$. These distributions are reported in Fig. 72 and are characterized by a maximum population and a temperature distribution. The parameters which are estimated by the mean position and the FWHM of the reported curves are: $(210 \pm 50)^\circ\text{C}$ for Gr/SiO₂, $(250 \pm 40)^\circ\text{C}$ for Gr/Al₂O₃, and $(220 \pm 30)^\circ\text{C}$ for Gr/HfO₂, respectively. In particular, the distributions are constituted by positive and negative terms where the first ones describe the proper temperature distribution of reaction sites and the negative terms describe the potential loss of doping. The latter contributions are found for the Gr/HfO₂ only, because of the net decrease of doping found for this sample (see Fig. 71f). Moreover, the integral of the positive contribution returns the maximum doping obtainable for a given sample, which corresponds to the group of data at the maximum doping of Fig. 71d,e,f. According to this model, by performing the doping thermal treatment at a given temperature, all the reaction sites placed below this value of temperature in the distribution are ready to react and contribute to the observed doping. In the case of Gr/HfO₂, a temperature which includes the negative contributions of the distribution will cause a net decrease of doping. The treatment temperature which yields the maximum doping is thereby $T \approx 250^\circ\text{C}$ for Gr/HfO₂, and the highest possible temperature for Gr/SiO₂ and Gr/Al₂O₃. As shown in Fig. 72, for both these two samples the distribution reaches null values near $T \approx 400^\circ\text{C}$, and therefore higher temperatures are not required. However, in the temperature range between 325 and 400°C it is found experimentally that the treatment is somewhat destructive since some portions of graphene disappear. This effect was found of particular relevance for Gr/HfO₂ for which graphene is entirely lost already at 325°C [211].

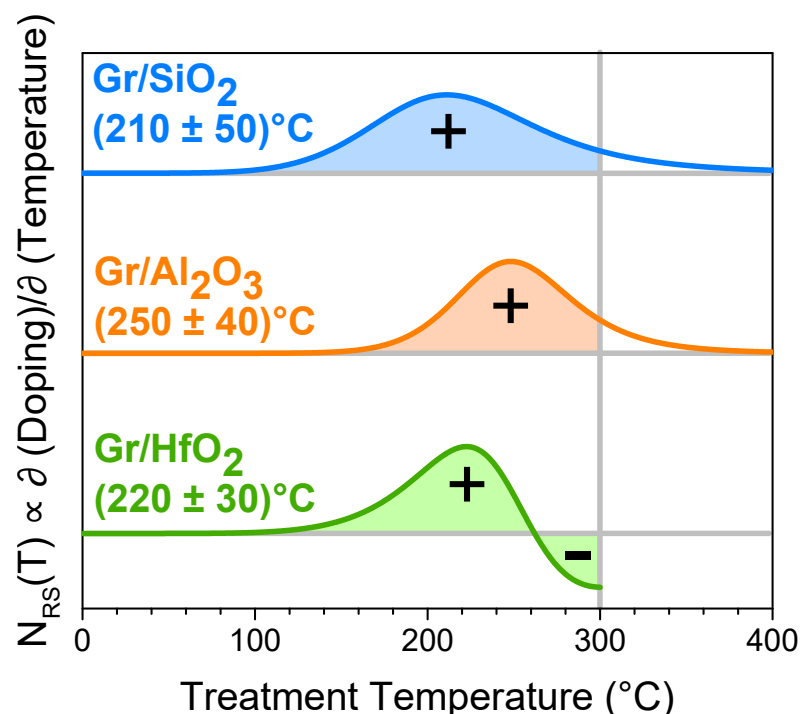


Figure 72: Comparison of the reaction sites distribution N_{RS} for Gr/SiO₂ (azure), Gr/Al₂O₃ (orange), and Gr/HfO₂ (green). The maximum population and the FWHM of the distributions are reported in parenthesis. The positive (+) or negative (-) contribution to doping is highlighted. For a given temperature (for example, 300°C), all the sites activated at lower temperature (colored areas) contribute to the final doping value. Adapted from Ref. [211].

It is important to note that the width of distributions reported in Fig. 72, by ranging from 60 to 100°C, is too large to be ascribed to a mere uncertainty on the threshold temperature of Fig. 71. On the contrary, we suggest that this feature is related to the heterogeneity of doping process. As discussed in Chp. 3, since the charge transfer between graphene and small molecules requires chemisorption between these two species, we suggest a graphene-O₂ adsorption site as the most probable reaction site of doping process and many factors can influence its reactivity. For example, the adsorption of O₂ can occur on both pristine and defected graphene, and different activation and bond energies are expected. The latter quantity directly affects the rate of post-adsorption processes involving the dissociation of O₂, thus influencing the resulting doping. Moreover, a further contribution due to the molecules located between graphene and substrate, or even due to the moieties of substrate surface can be guessed.

Finally, we note that the maximum doping features a close relation with the water affinity of the substrates. In fact, as shown in Fig. 73, the maximum doping of the Gr/substrate system decreases with the increase of contact angle of the bare substrate, that is: the more hydrophilic the substrate, the higher the maximum doping [211]. This result is consistent with the doping arising from oxygen reduction reactions discussed in Chp. 2, for which the presence of water is necessary. As previously mentioned, the water affinity of surface is driven by the surface chemical groups, and for oxides it is attributed to hydroxyl groups. According to this picture, the probable different concentration and steric configuration of these groups can be the cause of the different water affinity found in the three substrates. Consequently, a consequent different amount of water on the surface of the substrates would justify a different doping for the three samples [211].

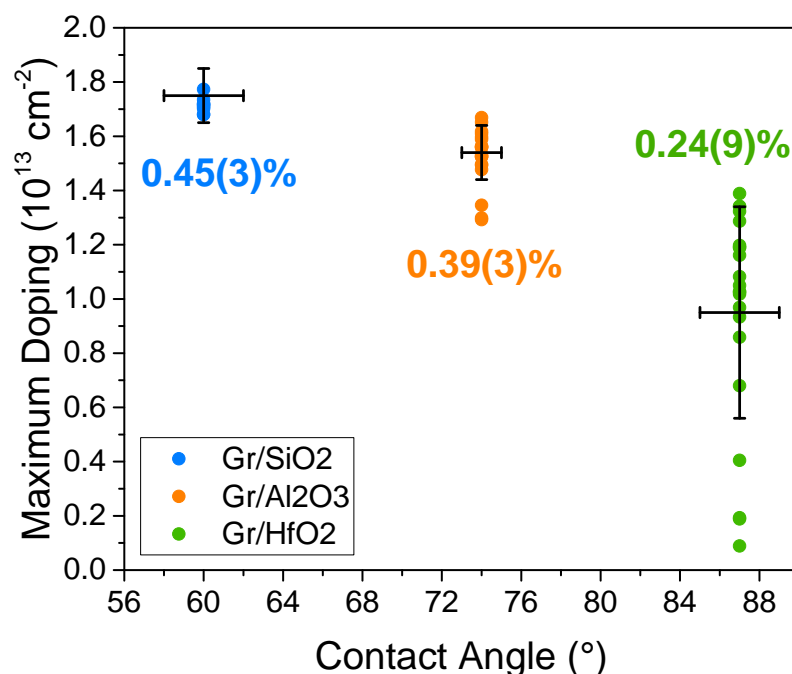


Figure 73: Dependence of maximum available doping on the degree of hydrophilicity of the substrate, as measured by wetting contact angle before the transfer of Gr. Mean values and their uncertainty are reported by error bars. For each sample, the percentage of doped C atoms is also reported. Data at temperature equal to 400°C for Gr/SiO₂, Gr/Al₂O₃, and 250°C for Gr/HfO₂ have been used. Adapted from Ref. [211].

DOPING VS TIME

The time evolution of doping was studied to deepen its dynamic aspects. The kinetics of O_2 doping process reported in Fig. 74 was investigated in the range 5–125 minutes by performing successive thermal treatments at 300°C , and evaluating *ex-situ* the doping as a function of total treatment time. In the case of Gr/SiO_2 and $\text{Gr}/\text{Al}_2\text{O}_3$, a quite homogeneous increase of doping is observed with the increase of exposure time to the gas, up to the reaching of saturation level

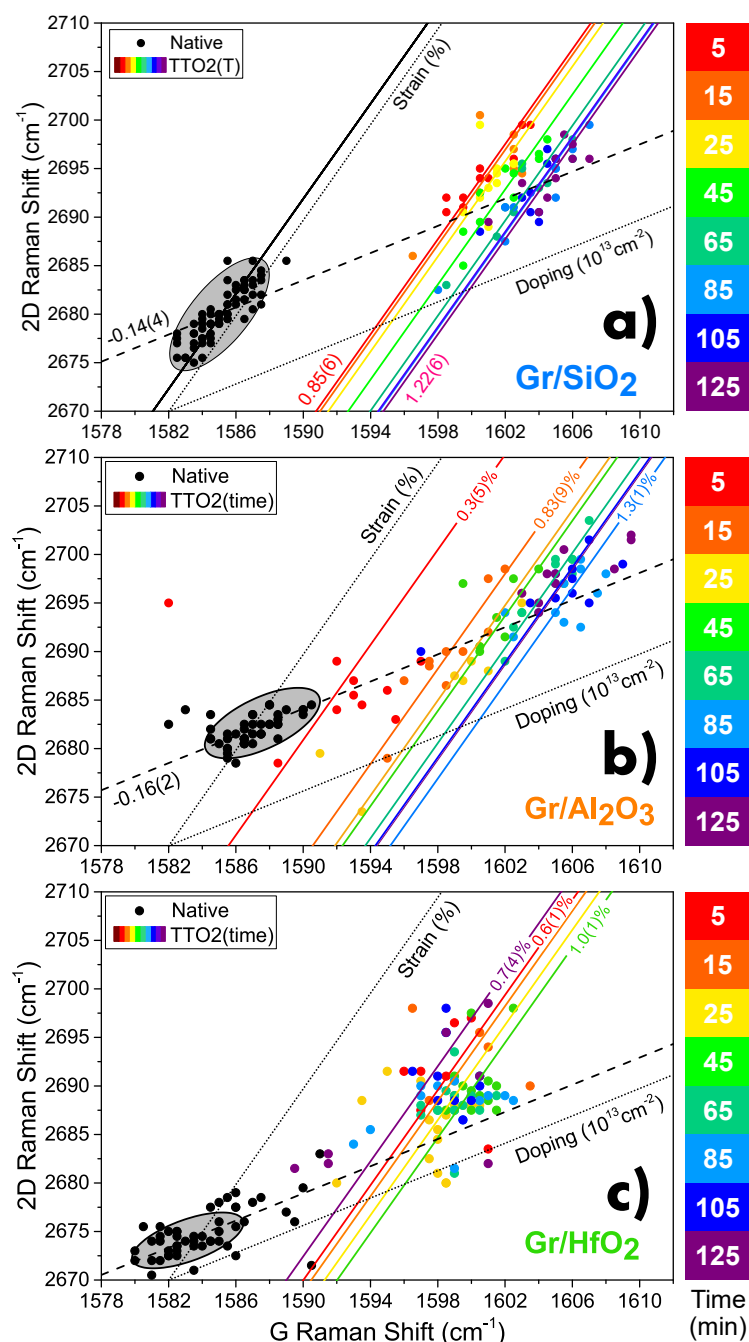


Figure 74: G-2D correlation map of native (black), and thermally treated samples in oxygen (TTO₂) atmosphere on increasing the treatment time (color scale) of (a) Gr/SiO_2 , (b) $\text{Gr}/\text{Al}_2\text{O}_3$, and (c) Gr/HfO_2 . Dotted lines represent the reference strain and doping axes. Dashed lines and continuous lines mark the average strain and doping, respectively. For the latter, the extracted values are also reported. The uncertainty value for their last digit is reported in parenthesis. Adapted from Refs. [211, 212].

which is supposed to be related to the temperature value. By contrast, in the case of Gr/HfO₂ the evolution is more complicated, strongly heterogeneous, and non-monotonous [211] despite, as reported in Fig. 75, the amplitude ratio R, and the Γ_{2D} and Γ_G FWHMs experience a similar evolution with time as that observed in the dependence of doping on temperature: the reduction of R and Γ_G and the increase of Γ_{2D} with the increase of doping. It is worth to mention that, since the doping occurs very fast in the first time-step, the fine observation of the evolution at intermediate doping values is prevented by the lack of measurements due to the experimental time resolution of set-up [211].

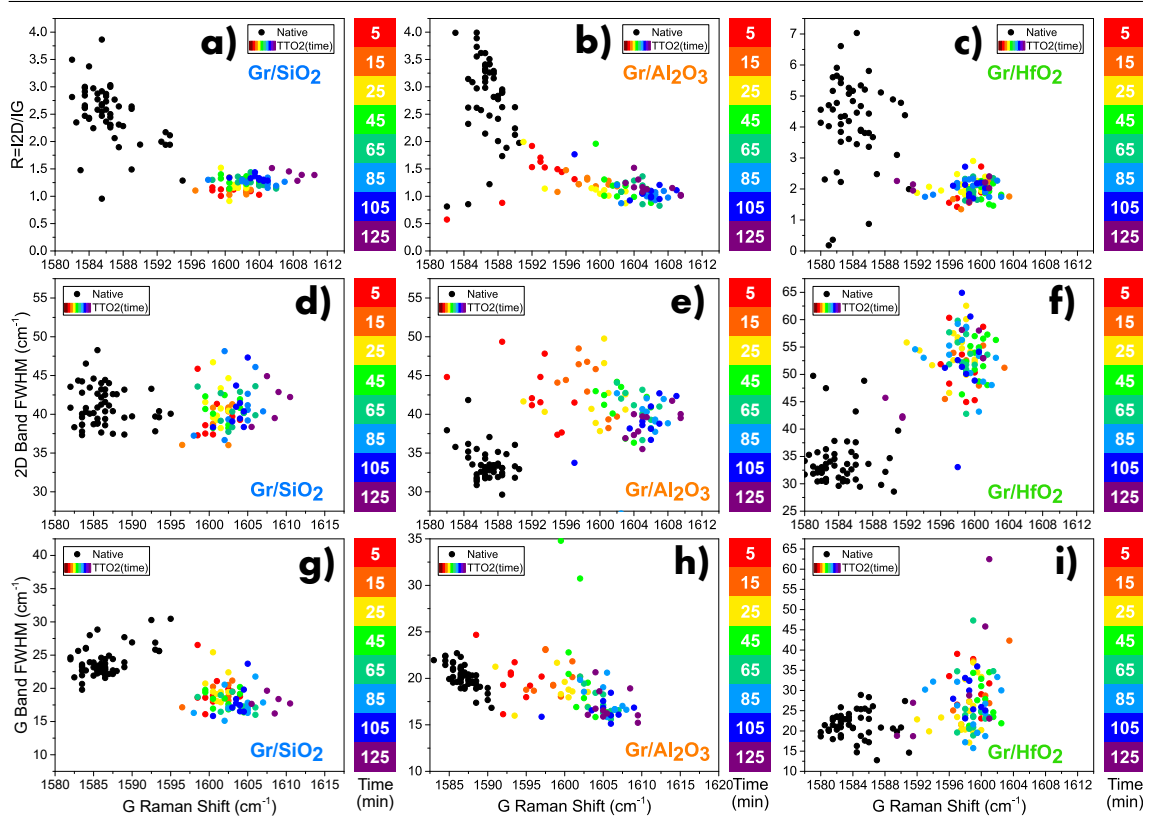


Figure 75: Correlation between (a,b,c) the amplitude ratio R, the FWHM of (d,e,f) 2D and (g,h,i) G bands and the peak position of G band at different treatment time (color scale) for Gr/SiO₂, Gr/Al₂O₃, and Gr/HfO₂. Adapted from Refs. [211, 212].

The strain levels extracted from the different point clouds of Fig. 74 are reported in Fig. 76, where different modification induced in the three samples are highlighted. Concerning Gr/SiO₂, it experiences a first rapid increase of compressive strain which relaxes to the native value with the increase of treatment time (Fig. 76a). On the other hand, a progressive increase of compressive strain is found for both Gr/Al₂O₃ and Gr/HfO₂ (Fig. 76b,c), more pronounced in the latter case since Gr/HfO₂ features a lower native strain than Gr/Al₂O₃. However, these trends are merely qualitative, since no systematic evolution is found.

Concerning the doping, the kinetics of doping is first investigated in Gr/SiO₂ and Gr/Al₂O₃ samples, since they feature a more homogeneous evolution. As discussed in Chp. 2, the observed time kinetics of doping must be interpreted by evaluating which kinetics law better describes their trends [175, 176]. To this aim, both diffusion models (Crank, Weber-Morris, Bangham, Fick)

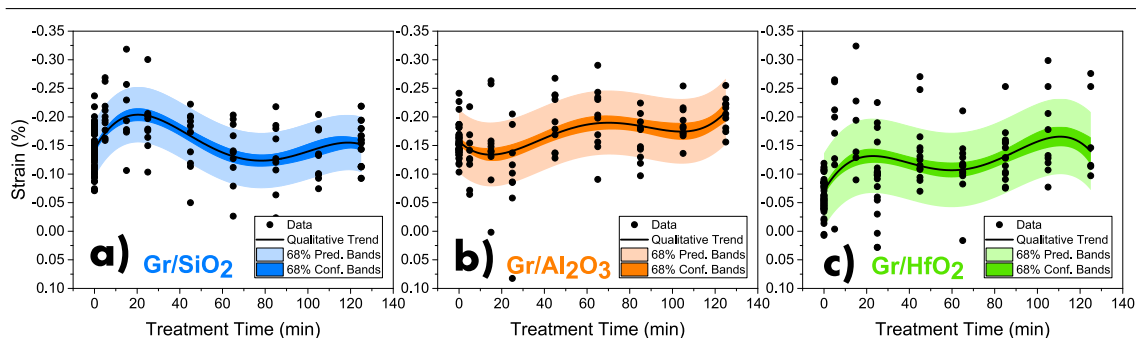


Figure 76: Extracted strain values on varying temperature for (a) Gr/SiO₂, (b) Gr/Al₂O₃, and (c) Gr/HfO₂, respectively. The trend of the time effect on strain is marked by a representative fit curve, whose uncertainty is reported by the prediction and confidence bands at one standard deviation by the polynomial curves. Adapted from Refs. [211].

and adsorption models (Pseudo n -th, Langmuir, Elovich) are used to fit the doping trends. As first step, the *Root Mean Square Error* (RMSE) of each model reported in Fig. 77 is determined and compared to the others so as to evaluate which kinetics model better adapt the experimental data. In particular, Bangham, Langmuir, and Elovich models feature the lowest RMSE, whereas the other models can be discarded because of the higher value.

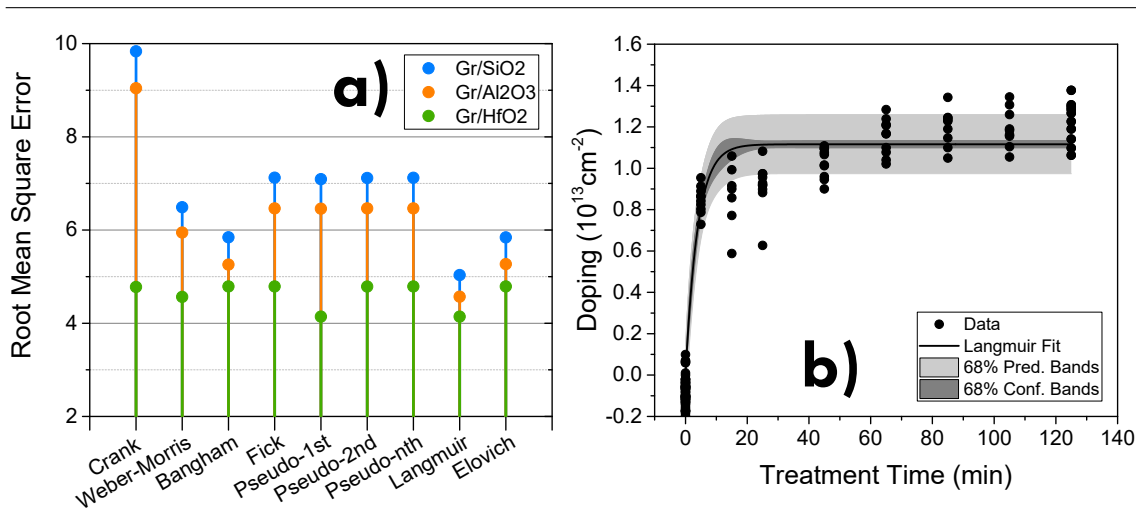


Figure 77: (a) Root Mean Square Error of the kinetics models used for the fitting of time kinetics of doping of Gr/SiO₂, Gr/Al₂O₃, and Gr/HfO₂. (b) Langmuir fit of doping vs temperature curve for Gr/SiO₂. Adapted from Ref. [211].

As second step, the three remaining fitting are compared in order to evaluate the fit quality on the total data set. In particular, Langmuir model can be discarded since it is not able to fit the data at long times (Fig. 77b), whereas both Bangham and Elovich models reasonably well fit the data set, even in the case of Gr/Al₂O₃ and Gr/HfO₂ (Fig. 78). For the latter, a linear contribution $D = cst$ is added in order to describe the kinetic of doping loss, and the ϑ parameter is imposed equal to the value found for Gr/SiO₂ because of fitting esigences in the case of Bangham model [211]. However, since it features a lower uncertainty on the fit parameters (Tab. 2), Bangham model should be preferred to Elovich model. This evaluation is also corroborated by a statistical *F-test*, where Bangham model is suggested as the best fit for both Gr/SiO₂ and Gr/Al₂O₃. Accordingly, the time kinetics of doping is suggested to be limited by a diffusion process ascribable to the

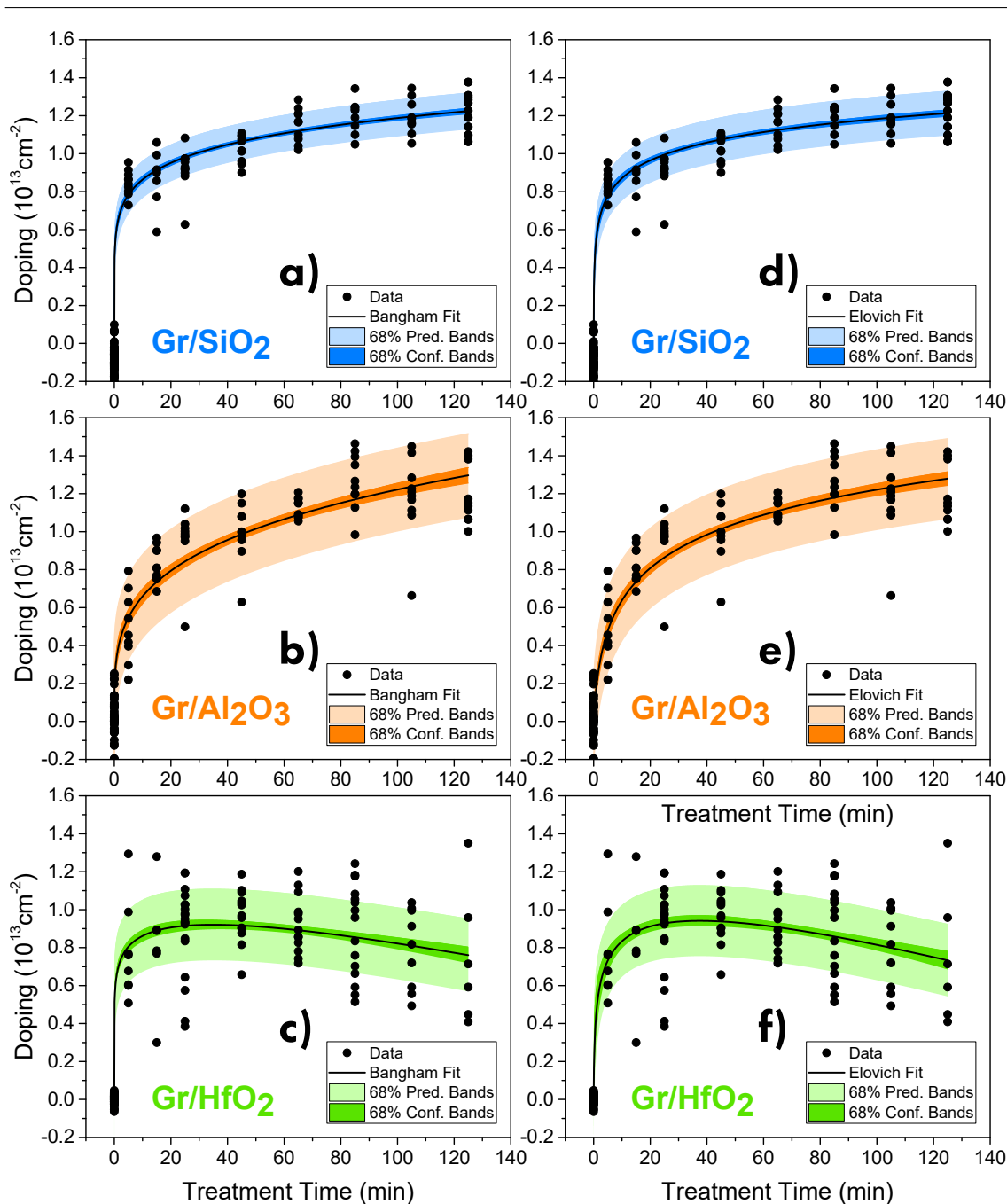


Figure 78: Comparison between (a,b,c) Bangham and (d,e,f) Elovich models in the fit of doping time kinetics of Gr/SiO₂, Gr/Al₂O₃, and Gr/HfO₂, respectively. Their uncertainty is reported by the prediction and confidence bands at one standard deviation by the fit curves. Adapted from Refs. [211].

diffusion of O₂ molecules from the gas phase towards the adsorption sites in the interstitial space between graphene and substrate [211]. Concerning the parameters reported in Tab. 2, Gr/SiO₂ features an higher k and a lower ϑ compared to Gr/Al₂O₃, thus indicating a faster kinetics. In particular, by comparing the half time for the three curves, half of doping is induced in less than 1 minute in Gr/SiO₂ and Gr/HfO₂, whereas at least 9 minutes are required for Gr/Al₂O₃. Moreover, concerning Gr/HfO₂ the rate constant of doping loss s is found two orders of magnitude lower than the rate constant of doping increase k . Therefore, if the increase of doping completes its dynamic in the range of 2 hours, the doping loss is expected to remove all the doping not before

than 6 hours [211]. Further comparison and comments among the different substrates effects will be reported in the following sections, after deepening other experimental aspects.

	ELOVICH MODEL			BANGHAM MODEL			HALF TIME
	k (min ⁻¹)	ϑ	s (min ⁻¹)	α (min ⁻¹)	β	s (min ⁻¹)	$t_{1/2}$ (min)
Gr/SiO ₂	16(9)	7.4(5)	–	0.72(3)	0.13(1)	–	<1
Gr/Al ₂ O ₃	0.3(3)	3.8(4)	–	0.36(5)	0.27(3)	–	~9
Gr/HfO ₂	2(2)	5(2)	-0.005(1)	0.67(3)	0.13(1)	-0.004(6)	<1

Table 2: Fit parameters obtained for the doping time kinetics analysis by using Elovich and Bangham models. For Gr/HfO₂ only, an additional linear loss term $D = cst$ is included. For Bangham model, the same ϑ parameter obtained for Gr/SiO₂ is imposed to Gr/HfO₂ for fit convergence. Half time for Bangham kinetics is also reported.

5.1.4 HYDROXYLATED VS METHYLATED SiO₂

In order to corroborate the hypothesis of a fundamental influence of the substrate surface water affinity on graphene doping by O₂, two substrates characterized by completely different surface groups are compared. In particular, a SiO₂/Si wafer with the usual hydroxylated surface (Si–OH) is used as hydrophilic substrate by taking as reference the results previously discussed for the Gr/SiO₂ sample. On the other hand, a similar SiO₂/Si wafer whose surface has been treated so as to substitute the hydroxyl groups with methyl groups (Si–CH₃) is used as hydrophobic substrate. In fact, such a substitution increases the contact angle of the substrate from the value of 60(2)° up to 83(1)°, thus indicating the hydrophobic character of the methylated surface of SiO₂. Accordingly, as depicted in Fig. 79, the presence of a water buffer layer between graphene and substrate is expected for hydroxylated silica (h-SiO₂), because of its hydrophilic surface, whereas its presence can be considered negligible for methylated silica (m-SiO₂) because of its hydrophobic nature.

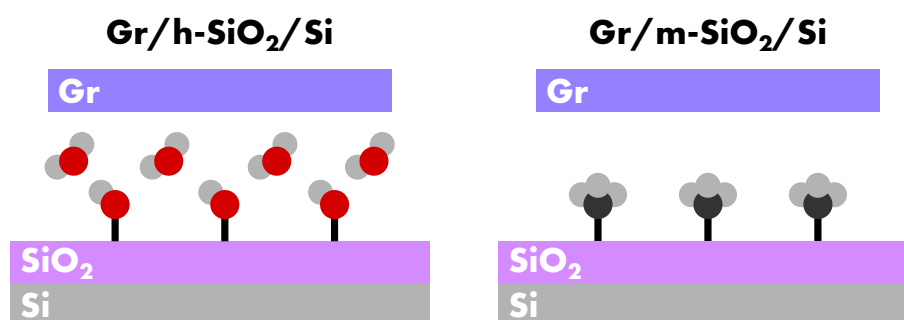


Figure 79: Scheme of layer stacking for graphene transferred onto the hydroxylated silica (h-SiO₂) or onto the methylated silica (m-SiO₂). The presence of water buffer layer for the first sample is also shown.

The comparison of doping and strain values for Gr/h-SiO₂ (data already reported in the previous section) and Gr/m-SiO₂ is shown in Fig. 80. Concerning doping, both the native samples fall in the region of negligible doping, whereas concerning strain, Gr/m-SiO₂ features a narrower distribution value compared to the Gr/h-SiO₂. This result is not surprising, since the methylation of the substrate acts a precise modification of surface, and the reduction of morphological disorder of the latter (which in the native h-SiO₂ is casually determined by the thermal growth process of the oxide) is expected. Most importantly, the two samples experience a different evolution as

effect of treatment in O_2 . In fact, in spite of an analogous evolution of its spectroscopic features (Fig. 80a), the m-SiO₂ is characterized by only $0.4(2) \times 10^{13} \text{ cm}^{-2}$ induced charge carrier concentration, that is one third of the doping occurring in h-SiO₂ in the same conditions (Fig. 80b). Therefore, the doping arising from the thermal treatment strongly depends on the water affinity of the substrate, and the lack of interstitial water dramatically reduces it. However, since a small amount of doping is induced, one has to admit the presence of some water on the substrate surface, probably ascribable to an incomplete methylation of the latter.

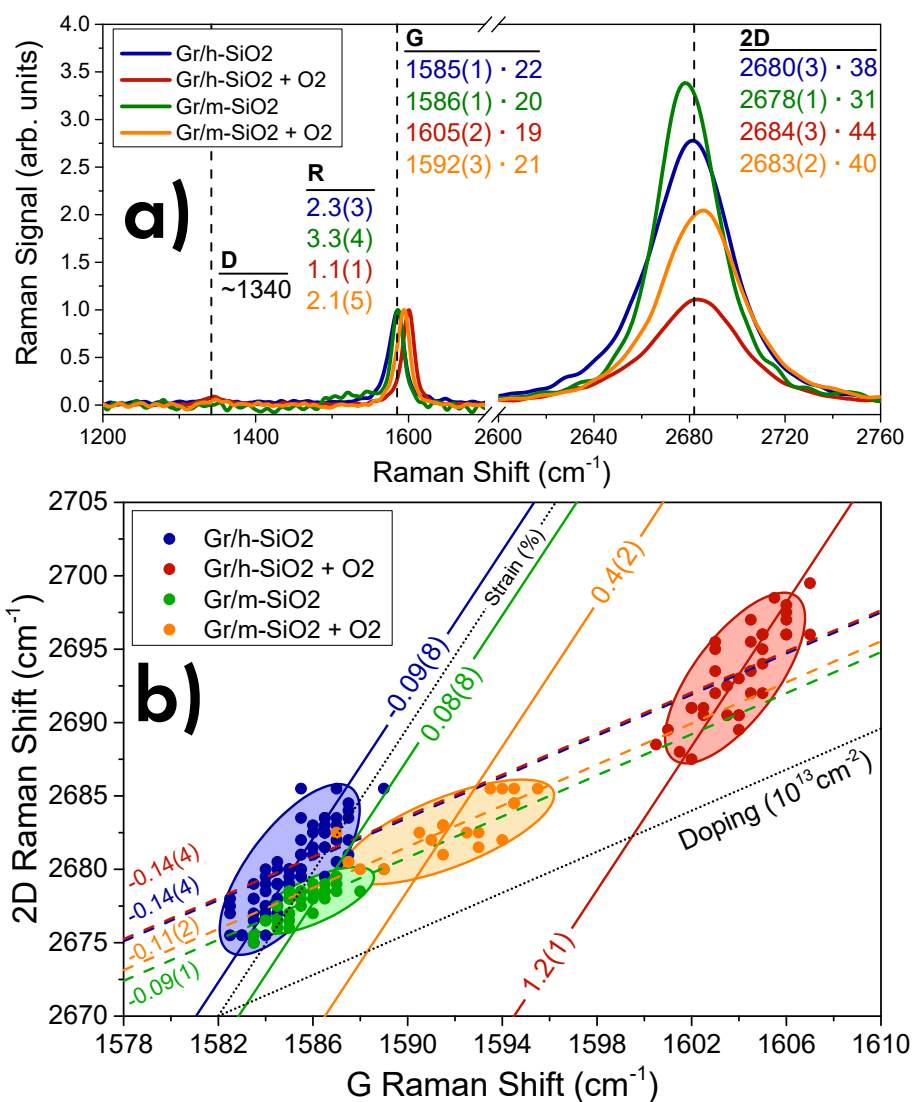


Figure 80: (a) Raman spectra normalized at G peak amplitude of native and thermally treated in O_2 (+ O_2) samples of Gr/h-SiO₂ and Gr/m-SiO₂. Dashed lines mark the peak position of D, G, and 2D bands for the Gr/h-SiO₂ native sample. For each sample, amplitude ratio R, peak positions and FWHM are reported. (b) G-2D correlation map of the same samples. Dotted lines represent the reference strain and doping axes. Dashed lines and continuous lines mark the average strain and doping, respectively. The extracted values are also reported. The uncertainty value for their last digit is reported in parenthesis.

More information can be obtained from the temperature and time dependence of doping, by performing on the Gr/m-SiO₂ the same kind of experiments discussed in the previous section: series of doping treatments at fixed duration (2 hours) and O_2 pressure (2 bar) on increasing the temperature in the range 150–400°C (Fig. 81a), and another series of doping treatments at fixed

temperature (300°C) and O₂ pressure (2 bar) on increasing the treatment durance (Fig. 81b). In both cases the doping increases, similarly to the data reported in the previous experiments. As shown in Fig. 82a, even in the case of Gr/m-SiO₂ the doping levels extracted from the G-2D map reported in Fig. 81a feature a sigmoidal trend on increasing of temperature similar to the other substrate previously discussed (see Fig. 72), and is clearly remarkable the lower saturation level of doping of Gr/m-SiO₂ compared to Gr/h-SiO₂. Moreover, the temperature distribution of reaction sites obtained from the mathematical derivative of the doping curve indicates that Gr/m-SiO₂ significantly differs from the distribution of Gr/h-SiO₂. In particular, since the lower total doping, the distribution of Gr/m-SiO₂ features a minor total area compared to that of Gr/h-SiO₂, and in addition, its peak is placed at lower temperature (185 ± 45)°C because the reaction sites at the highest temperatures (estimated almost two third of the total) are missing (Fig. 82b). Finally,

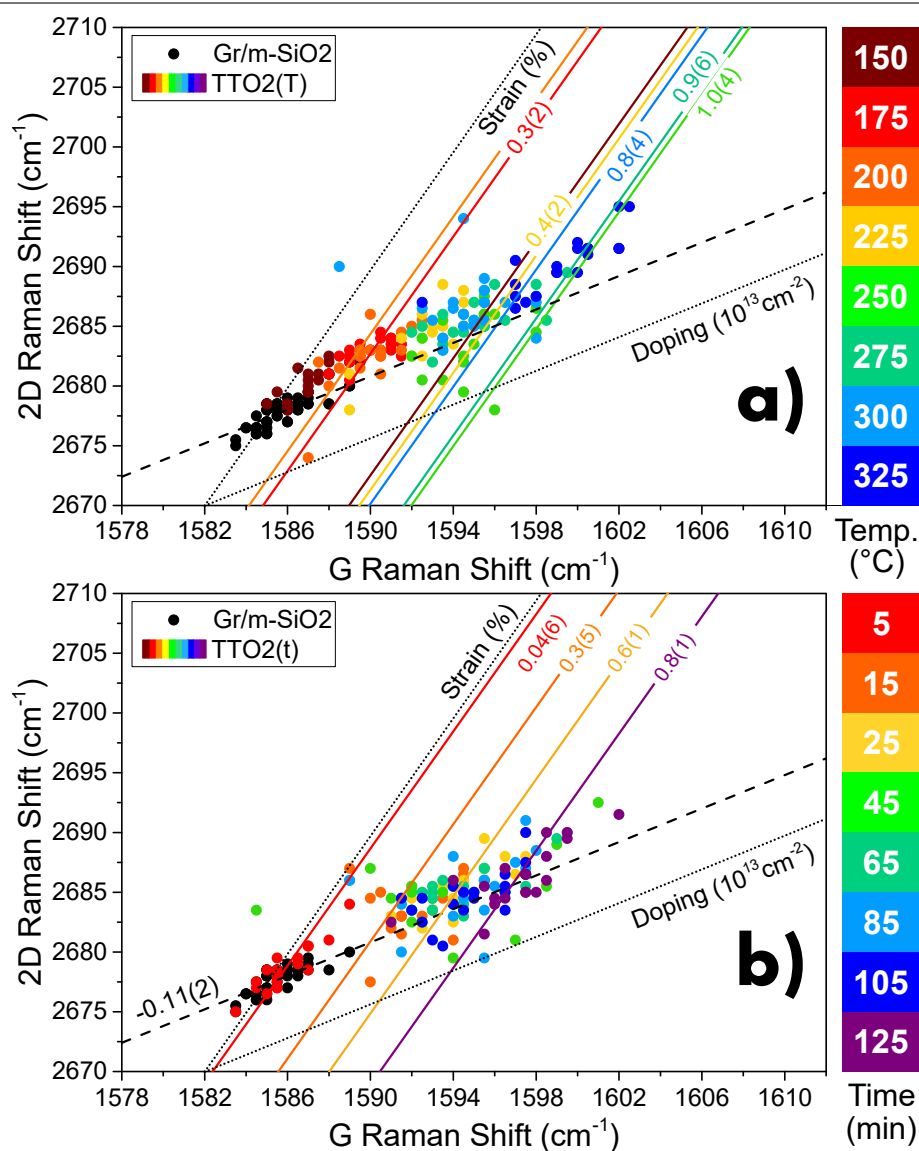


Figure 81: G-2D correlation map of native (black), and treated Gr/m-SiO₂ in oxygen (TTO₂) atmosphere on increasing of (a) temperature and (b) time (color scale). Dotted lines represent the reference strain and doping axes. Dashed lines and continuous lines mark the average strain and doping, respectively. The extracted values are also reported. The uncertainty value for their last digit is reported in parenthesis.

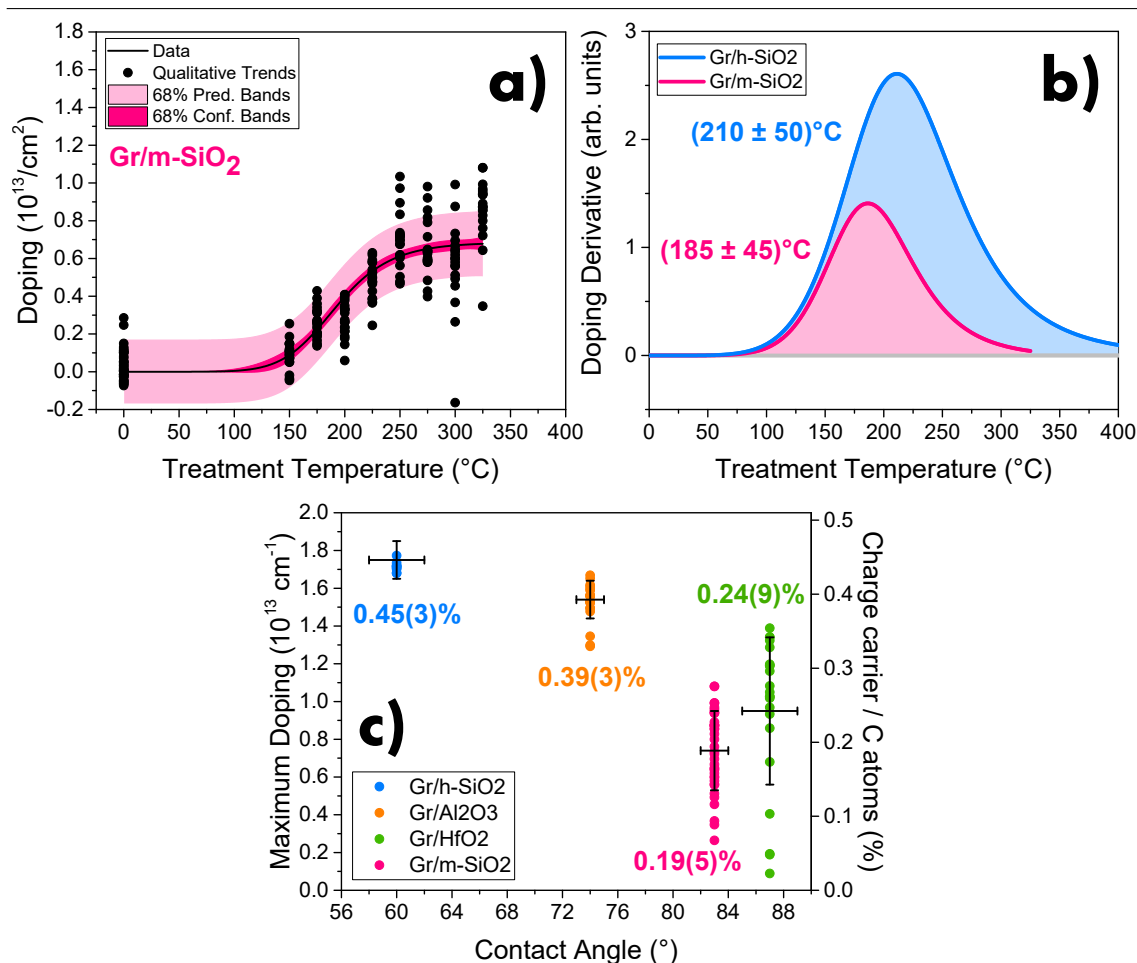


Figure 82: (a) Extracted doping values on varying temperature for Gr/m-SiO₂. A Logistic fit marks the trend of the temperature effect. Its uncertainty is reported by the prediction and confidence bands at one standard deviation by the fit curve. (b) Reaction sites distribution (N_{RS}) of Gr/h-SiO₂ (azure), Gr/m-SiO₂ (pink). (c) Dependence of maximum available doping on the degree of hydrophilicity of the substrate, as measured by wetting contact angle before the transfer of Gr. Mean values and their uncertainty are reported by error bars. For each sample, the percentage of doped C atoms is also reported. Data at temperature equal to 400 $^{\circ}\text{C}$ for Gr/h-SiO₂ and Gr/Al₂O₃, 325 $^{\circ}\text{C}$ for Gr/m-SiO₂ and 250 $^{\circ}\text{C}$ for Gr/HfO₂ have been used. Adapted from Ref. [211].

as reported in Fig. 82c, the maximum doping attainable in Gr/m-SiO₂ is in full accordance with the trend reported in Fig. 73, thus confirming that the water affinity of substrate surface is closely related to the doping capability. Therefore, such capability can be reinterpreted as a property characterizing not only graphene, but the entire system graphene-substrate where a key role is played by the buffer layer between them.

Concerning the dependence on treatment time, Gr/m-SiO₂ features an unexpected delay in the activation of the doping treatment contrarily to the other samples previously discussed. In fact, as reported in Fig. 83, the first effects of doping are found after 15 minutes of treatment, whereas no doping is induced before. Then, a progressive increase of doping is found, which can be described by a Bangham model accordingly to evaluation of doping kinetics reported in Sec. 5.1.3. To this aim, the data of the first time step (5 minutes) are considered as starting point of the kinetic by including a time delay term of 5 minutes the Bangham model. As reported in Tab. 3, the obtained fit parameters are strongly affected by the substrate modification, and they show that the substrate induces a slowing down the doping increase. However, it is worth to note

that since the doping explores a range of values comparable to the spread for the single doping level ($D(t)/\Delta D \sim 1$), the reliability of the Bangham fit for Gr/m-SiO₂ is severely limited, contrary to what previously reported for Gr/h-SiO₂. Nevertheless, the severe influence of the substrate water affinity on the capability of doping by O₂ can be confirmed.

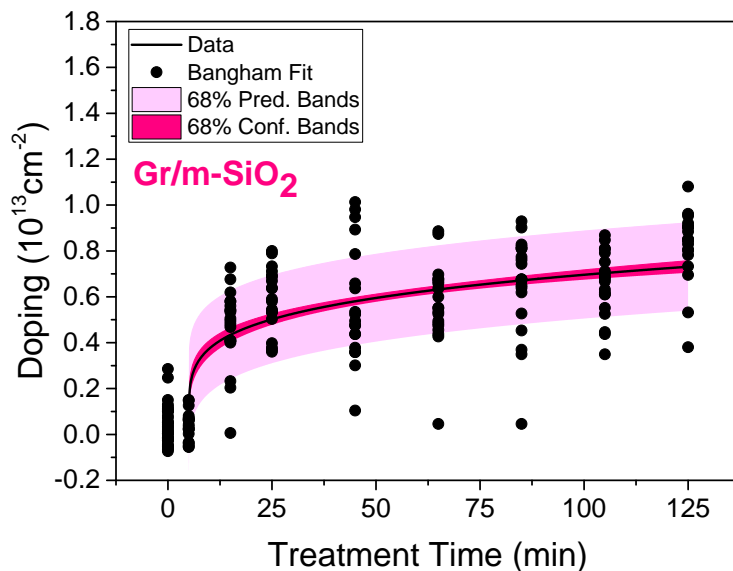


Figure 83: Modification of doping level of Gr/m-SiO₂ as effect of O₂ treatment on increasing the treatment time. The overall trend is evaluated by the Bangham kinetic, whose uncertainty is reported by the prediction and confidence bands at one standard deviation by the fit curve. Adapted from Refs. [211].

	BANGHAM MODEL	
	k (min ⁻¹)	ϑ
Gr/h-SiO ₂	0.72(3)	0.13(1)
Gr/m-SiO ₂	0.27(4)	0.21(4)

Table 3: Fit parameters obtained for the doping time kinetics analysis by using the Bangham model for Gr/h-SiO₂ (already reported in Tab. 2) and Gr/m-SiO₂.

5.1.5 FOLDED GRAPHENE

As shown in Fig. 84, some portion of graphene transferred onto HfO₂ is found in a folded configuration, which can probably be ascribed to the transfer process as already noted for the cracks of graphene. Despite the presence of folded graphene is not peculiar of Gr/HfO₂ – it is abundantly found even in Gr/SiO₂ and Gr/Al₂O₃, as shown in Fig. 61 – it strongly affected the study of this sample. In fact, as already discussed, the thickness and the dielectric constant of the oxide layer in HfO₂/Si induce a very low interference pathway of incident light, thus inducing two effects: the absence of optical contrast between graphene and substrate, and the reduction of the Raman signal of Gr [97]. Accordingly, the acquisition of Gr/HfO₂ Raman signal required the use of pseudo-confocal optic configuration, thus involving the investigation of a rectangular

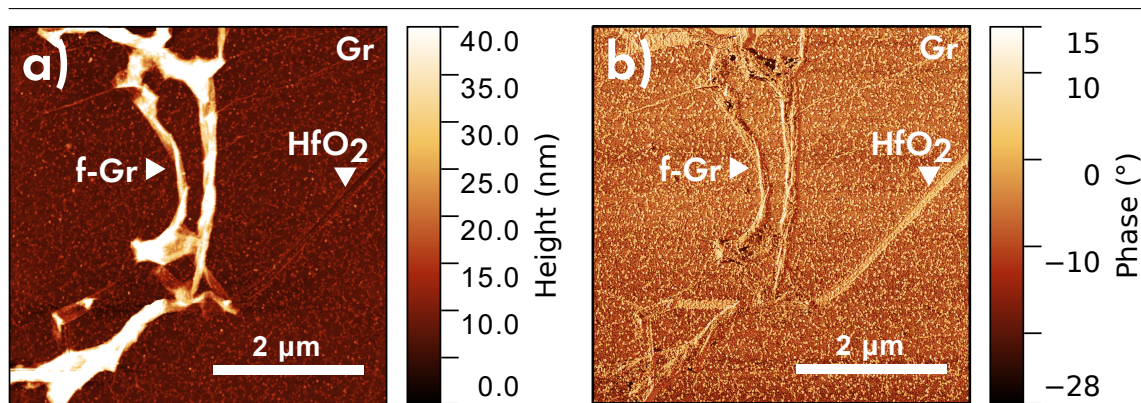


Figure 84: (a) Morphological, and (b) phase AFM images of Gr/HfO₂. Regions of flat graphene (Gr), folded graphene (f-Gr), and the underlying HfO₂ surface are highlighted by labels. Adapted from Ref. [211].

spatial region of $4 \times 15 \mu\text{m}^2$ contrary to the case of Gr/SiO₂ and Gr/Al₂O₃ where the confocal configuration involved a circular region of about $4 \mu\text{m}$ of diameter. Therefore, whether it is possible to avoid the region of folded graphene by using the confocal configuration, the same is not possible in pseudo-confocal configuration. The inclusion of such regions is easily distinguishable by means of the Raman investigation. In fact, the Raman spectrum of folded graphene features a conspicuous blueshift of 2D peak frequency which is related to the modification of Fermi velocity v_F characterizing graphene sheets in a non-AB stacking [71], as reported in Fig. 85a. In this way it is possible to distinguish folded graphene both from single-layer graphene, to which the shift is referred, and from two-layer graphene, which does not feature any shift but rather the inversion of R parameter. The folded graphene is more distinguishable by means of the G-2D map reported in Fig. 85b, where the presence of two different clusters is clearly shown. In particular, the point-cloud of folded graphene is vertically shifted with respect to unfolded graphene, as effect of 2D band blueshift only [211]. Herein, by assuming that f-Gr/HfO₂ is characterized by the same strain of bare Gr/HfO₂, a reduction of Fermi velocity is estimated equal to $\Delta v_F = -3\%$ [71, 223].

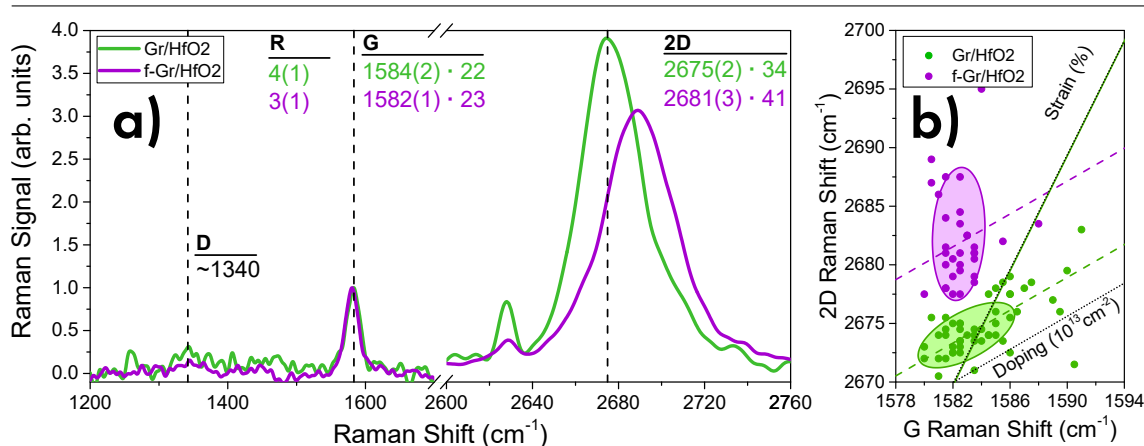


Figure 85: (a) Raman spectra normalized at G peak amplitude of unfolded (Gr) and folded (f-Gr) Gr/HfO₂. Dashed lines mark the peak position of D, G, and 2D bands for Gr/HfO₂ sample. For each sample, amplitude ratio R, peak positions and FWHM are reported. (b) G-2D correlation of the same samples. Qualitative ellipses highlight the four point clouds. Dotted lines mark strain and doping axes. For each cloud, dashed lines and continuous lines mark the average strain and doping, respectively. The uncertainty of the reported values is expressed in terms of one standard deviation, the latter arising from a sampling constituted by 20–50 measurements. Adapted from Ref. [211].

The presence of folded graphene was exploited to discriminate two phases of graphene: bare graphene (simply Gr), which is in contact both with the overlying atmosphere and with the underlying substrate, and folded graphene (f-Gr) which is in contact only with the atmosphere or with other graphene sheet. Therefore, by taking into account the previous discussion about the substrate effect, the doping occurrence in folded graphene is not trivial. The Raman spectra of f-Gr/HfO₂ thermally treated in O₂ atmosphere are reported in Fig. 86a, where the low signal does not allow a deepen discussion. As usual, the G-2D correlation map reported in Fig. 86b provides more information about the samples. In this figure, the point cloud of unfolded graphene are reproduced from Fig. 67. Since all data are acquired on the same sample, the attribution to a specific phase of graphene is given by using the strain axis as discriminant feature. In fact, the points at the left of this axis (beyond the range of uncertainty related to the doping) cannot prescind from the Fermi velocity reduction, thus unambiguously indicating the presence of folded

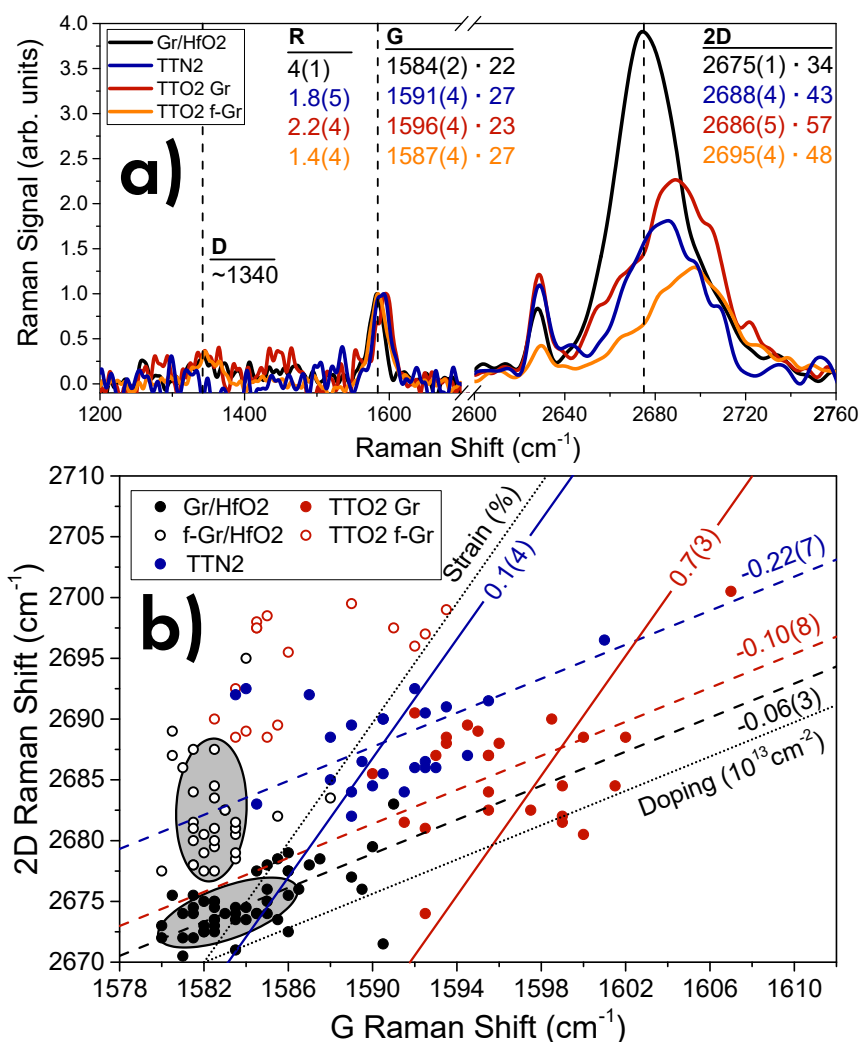


Figure 86: (a) Raman spectra normalized at G peak amplitude of native (black line), thermally treated in O₂ (TTO₂), and thermally treated in N₂ (TTN₂) bare graphene (Gr) and folded graphene (f-Gr) onto HfO₂. Dashed lines mark the peak position of D, G, and 2D bands for unfolded Gr/HfO₂ native sample. The mean values of amplitude ratio R, peak positions and FWHM are reported. The uncertainty value for their last digit is reported in parenthesis. (b) G-2D correlation of the same samples. Dotted lines represent the reference strain and doping axes. Dashed lines and continuous lines mark the average strain and doping, respectively. Adapted from Ref. [211].

graphene. Besides, for the points at the right of the strain axis the distinction is not equally easy. Concerning the treatment in N_2 , since the point clouds is placed around the strain axis, the contribution of folded and unfolded graphene cannot be clearly distinguished, except than for those points placed at the extremes of the distribution. Concerning the treatment in O_2 atmosphere, the additional point cloud of folded graphene occupies a region which features risible doping, as indicated by the intersection between the vertical translation of folded graphene and the strain level of unfolded graphene. Therefore, this result suggests that the contact with the substrate is necessary for the occurrence of doping, since the folded graphene does not experience any relevant doping effect [211]. The investigation of the dependence on treatment temperature and time confirm this result. In fact, as shown in Fig. 87, the increase of doping as effect of the increase of treatment temperature (Fig. 87a) or treatment time (Fig. 87b) is found only in the case of unfolded graphene, whereas only the increase of strain is found for folded graphene.

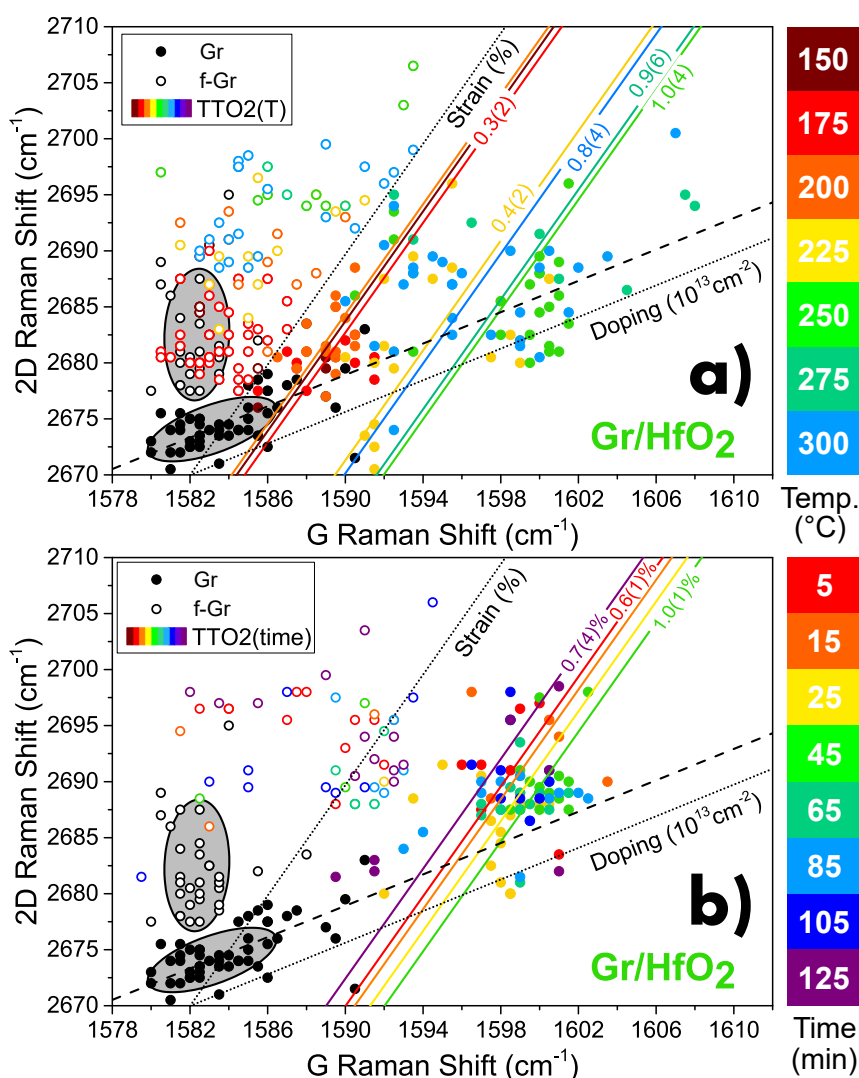


Figure 87: G-2D correlation map of native (black), and thermally treated samples in oxygen (TTO₂) atmosphere of unfolded graphene (full circles) and folded graphene (f-Gr, empty circles) on increasing of (a) temperature and (b) time (color scale). Dotted lines represent the reference strain and doping axes. Dashed lines and continuous lines mark the average strain and doping, respectively. The extracted values are also reported. The uncertainty value for their last digit is reported in parenthesis. Adapted from Ref. [211].

5.1.6 COMPARISON WITH OTHER GASES

The kinetics of doping and strain induced in graphene (considering Gr/SiO₂ only) by means of thermal treatments were also investigated in different atmospheres: vacuum (V), nitrogen (N₂) and carbon dioxide (CO₂). As shown in Fig. 88, the three atmospheres induce different effects. Both treatments in V (Fig. 88a) and N₂ (Fig. 88b) atmospheres cause the largest effect in the first time step (20 minutes), whereas the following steps do not induce further modifications. In both cases, the point clouds show no appreciable doping and the increase of strain, which reaches the values of -0.23(3)% and -0.24(3)% for V and N₂ treatment, respectively. These values of strain are almost equivalent for the two inert atmospheres, and therefore ascribable to a structural modification of graphene induced by the thermal stress experienced during the treatment. On the contrary, the treatment in CO₂ atmosphere (Fig. 88c) shows an evolution dominated by doping. In fact, the doping of graphene suddenly increases before the third step (60 minutes) with minor further increase in the following steps up to a level equal to $0.6(1) \times 10^{13} \text{ cm}^{-2}$, half of the doping induced by O₂. This last result is quite surprising since it is in contrast with previous investigations which found no doping for CO₂ atmosphere (Ref. [149]). Therefore, it can be stated that the doping obtained by means of thermal treatments is not peculiar of O₂, but proper of various oxydizing molecules, such as CO₂ [212].

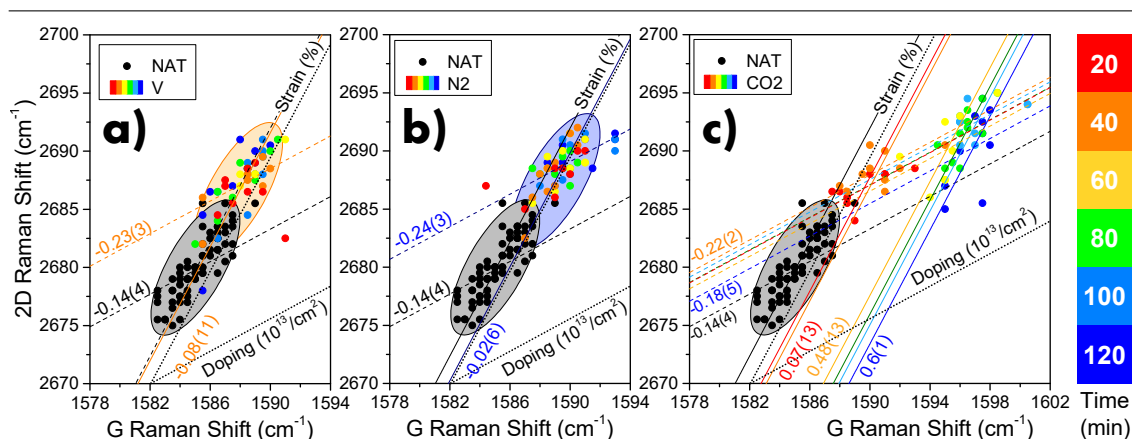


Figure 88: G-2D maps of Raman features of Gr/SiO₂ treated on increasing treatment time (color scale) in various atmospheres: (a) vacuum (V), (b) N₂, and (c) CO₂. For each point cloud the mean value of doping and strain have been found projecting the center of distributions on the doping and strain axes which are defined by two dotted lines. Doping (continuous lines) and strain (dashed lines) levels are marked. The uncertainty value for the last digit is reported in parenthesis. Native cloud (NAT) and its ellipsoidal shape is kept as reference. The same ellipse has been used to highlight the other point clouds. Adapted from Ref. [212].

5.1.7 DOPING REMOVAL BY WATER

As discussed in Chp. 2, it is well known in literature that the doping induced by thermal treatment in O₂ atmosphere fades as effect of the successive exposure to ambient air, whereas graphene keeps doped if it is preserved in vacuum [149, 150, 155]. The contrast to doping performed by the water has thereby been deepened by clarifying two aspects: the evaluation of the time kinetics of doping fading induced by ambient air, and the evaluation of the physical parameters by which better modulate the removal of doping.

Concerning fading, the effect induced by ambient air was investigated by monitoring the doping level of two previously doped samples of Gr/SiO₂ and Gr/Al₂O₃. The evolution of doping is reported in Fig. 89, where the decrease of doping with the increase of exposure time is clearly recognizable for both samples, and it is fundamentally affected by the specific substrate. In fact, the fading occurs homogeneously in Gr/SiO₂ (Fig. 89a), whereas a more heterogeneous evolution occurs in Gr/Al₂O₃ (Fig. 89b). In particular, as reported in Fig. 90, the doping of Gr/SiO₂ fades through a first rapid decrease of $0.4 \times 10^{13} \text{ cm}^{-2}$ occurring in 24 hours, and through a successive slow decrease of $0.2 \times 10^{13} \text{ cm}^{-2}$ occurring in 20 days where the doping seems to approach a level of stability (Fig. 90a) [212]. Concerning strain, no systematic modification is found during the fading process, thus suggesting that the structural modification induced by thermal treatment keeps stable even if the doping is removed [212].

The trend of fading curves can be evaluated by the same procedure used for the evaluation of doping kinetics. In this case, by comparing Langmuir and Bangham models only (see the discussion in Sec. 5.1.3) the latter features the best fit, accordingly to the F-test between the two models. The obtained parameters for the fading kinetic in Gr/SiO₂ are reported in Tab. 4. By contrast, the

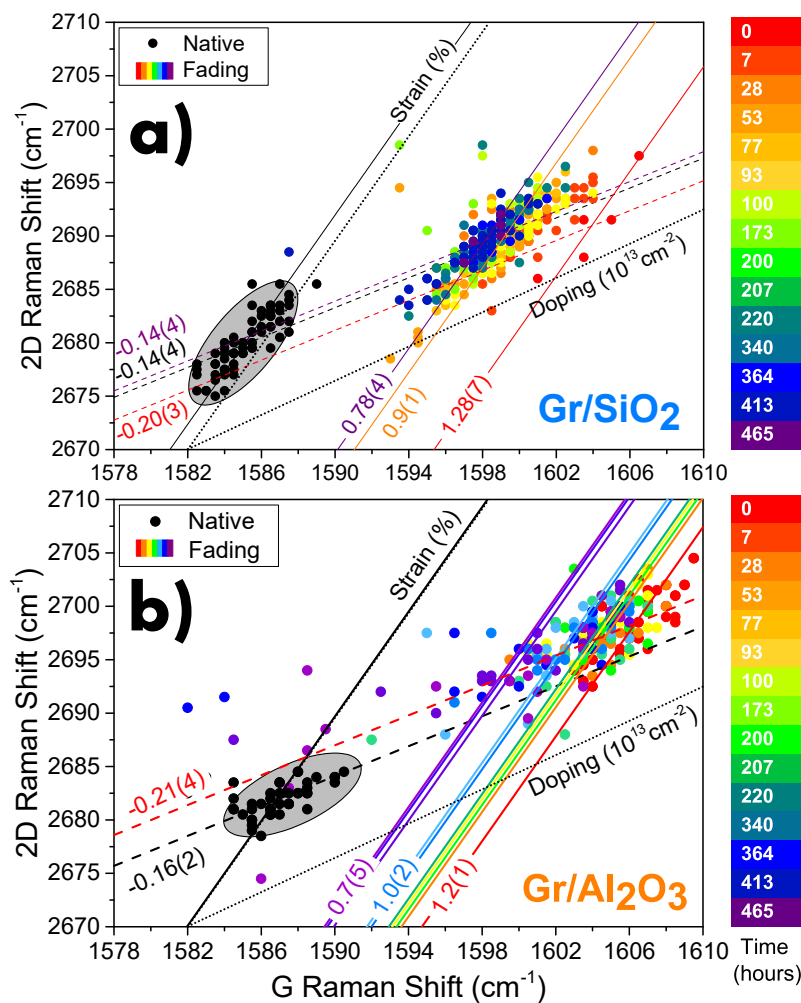


Figure 89: G-2D map of (a) Gr/SiO₂ and (b) Gr/Al₂O₃ doped by O₂ and successively exposed to ambient air. The color scale marks the temporal steps of monitoring. The dashed lines and the continuous ones mark the projections on strain and doping axes, respectively. The uncertainty value for the last digit is reported in parenthesis. Native cloud and its ellipsoidal shape are kept as reference. Adapted from Ref. [212].

more heterogeneous fading in Gr/Al₂O₃ sample for long times can be distinguished in two different dynamics. In fact, large portions of the sample feature a slow fading and a stability level as in the case of Gr/SiO₂ but with a lower rate. On the other hand, a few measurements indicate the presence of an alternative faster fading which almost linearly goes down to the undoped level (Fig. 90b,c). The comparison of two half-lives time for the three fading curves allows to evaluate the different stability of doping. In particular, doping is more stable in Gr/SiO₂ where it endures much more than in Gr/Al₂O₃, even by considering the fraction of measurement which features the display the slowest decay. Therefore, the substrate strongly concerns the stability of doping.

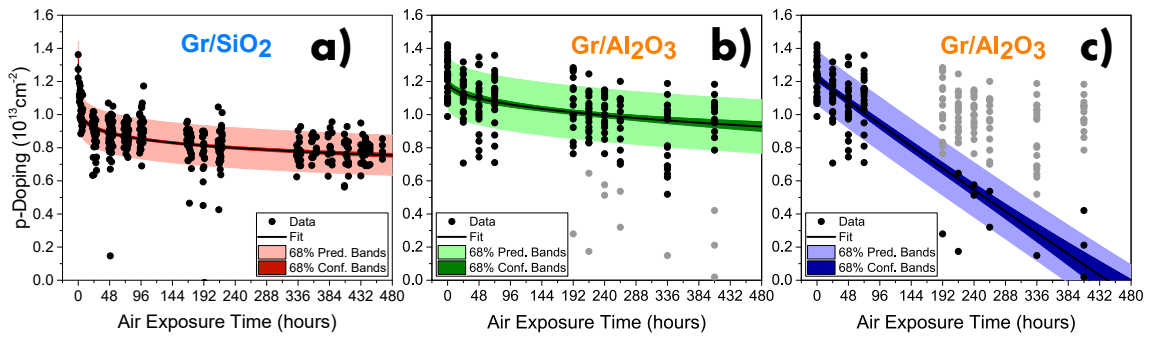


Figure 90: Evolution of doping fading in ambient atmosphere of (a) Gr/SiO₂ and Gr/Al₂O₃ where the (b) slow and (c) fast fading are separately evaluated. Fit uncertainty is reported by the prediction and confidence bands at one standard deviation by the fit curve (black lines). Adapted from Ref. [212].

Sample	k (min ⁻¹)	ϑ	D_M (10 ¹³ cm ⁻²)	$t_{1/4}$ (h)
Gr/SiO ₂	0.26(6)	0.12(2)	1.30(7)	114
Gr/Al ₂ O ₃ SLOW	0.03(2)	0.4(1)	1.21(3)	52
Gr/Al ₂ O ₃ FAST	0.004(2)	0.9(1)	1.22(3)	6

Table 4: Fit parameters obtained for the doping fading kinetics analysis by using Bangham decay $D = D_0(1 - kt^\vartheta)$ where k the rate constant, ϑ the Bangham parameter, and D_0 is the initial doping) and two half-lives time $t_{1/4}$.

To investigate the modulation of fading, two dedoping experiments were compared by using controlled conditions of temperature and pressure in an atmosphere composed by only water vapor (H₂O). The first experiment consists in a series of sequential treatments at high temperature (15°C) and at low pressure of H₂O (< 2 bar). The second one was performed at low temperature (~50°C) and at high pressure of H₂O (> 2 bar). As reported in Fig. 91, in the case of low H₂O pressure the doping is progressively reduced down to $D = 0.02(6) \times 10^{13} \text{ cm}^{-2}$ by accumulating the successive treatments of different time, thus revealing that in this condition the dedoping process can be gradually tuned until completion in 2 hours. On the other hand, in the treatment at high H₂O pressure the complete removal of doping occurs within only 10 minutes. Therefore, the pressure of water, and not its temperature, is the leading parameter of dedoping, since the different values of k do not derive from the temperature but from the different concentration of H₂O set in the two experiments [212]. It is important to note that the two procedures induce different strain in the dedoped samples. In fact, the experiment at low pressure increases the compressive strain, as expected because of the high treatment temperature and for an inert atmosphere. On the other hand, the experiment at high pressure does not induce a strain significantly different both from the doped and the native samples, because of the low treatment temperature.

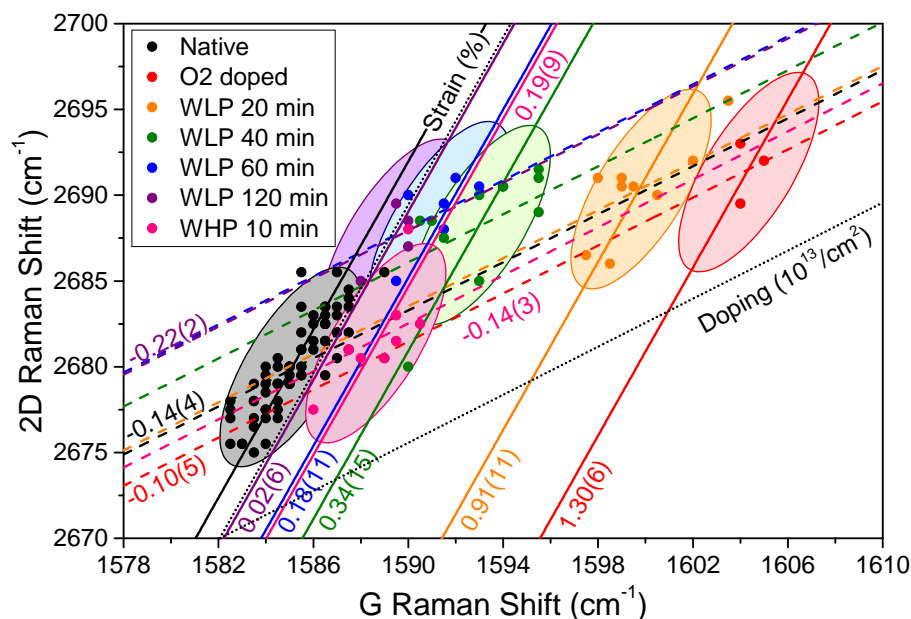


Figure 91: G-2D map of dedoping process performed on Gr/SiO₂ previously doped by standard O₂ treatment. The various steps of the dedoping at low H₂O pressure (< 2 bar) and high temperature (150°C) (WLP) are compared to the single step dedoping at high H₂O pressure (> 2 bar) and low temperature (~ 50°C) (WHP). The dashed lines and the continuous ones mark the projection on strain and doping axes, respectively. Native cloud and its ellipsoidal shape are kept as reference for all the other ones. The same ellipse has been used to highlight the other point clouds. The uncertainty value for the last digit is reported in parenthesis. Adapted from Ref. [212].

5.1.8 STRAIN MODIFICATION

On the basis of the discussion reported in Sec. 5.1.6, the effects on the strain of Gr/SiO₂ induced by thermal treatments can be grouped in two categories: an increase up to a final value in the case of inert atmosphere, and a variable evolution in the case of reacting atmosphere, characterized by an increase of strain at low doping values and a recovery of the initial strain at high doping values. In both cases, the main impact of the thermal treatment is to induce and fix the value of strain reached, both temporarily and definitively. However, even the dynamic features of the thermal treatments have a significant influence on the strain induced in graphene. In fact, as reported in Fig. 92a, a different strain is found in graphene subjected to different stages of room temperature recovery performed at the end of thermal treatments: a fast cooling completed within 60 seconds, and a slow cooling completed in about 6 hours. In particular, as shown in Fig. 92b, in the case of N₂, H₂O and O₂, a slow cooling induces a relaxation of graphene structure, which features a lower strain compared to the same treatments ended by fast cooling. The only exception to this behavior is for vacuum treatment which is not affected by a cooling rate [212]. Therefore, these results suggest a fundamental role of the gas phase in the modulation of graphene strain during the cooling stage, which allows the relaxation of graphene structure regardless the occurrence of doping. Besides, this relaxation is prevented either the gas phase is missing (vacuum conditions) or there is not enough time for the structure rearrangement. Furthermore, in the case of O₂ treatment with slow cooling, graphene reaches a strain lower than the native sample, thus indicating that the structural interaction between graphene and substrate (determined by the adaptation

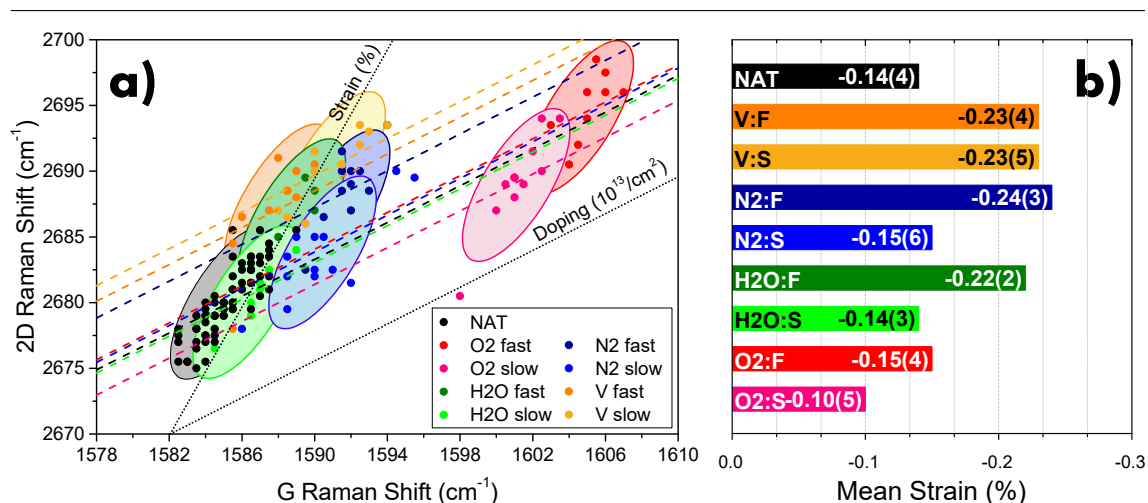


Figure 92: (a) G-2D map of Gr/SiO₂ thermally treated in different gases for 2 hours at 300°C with fast (F) and slow (S) cooling to room temperature. Native cloud (NAT) and its ellipsoidal shape are kept as reference for all the other ones. The same ellipse has been used to highlight the other set of points. (b) Bar graph of strain for the various treatments reported in the previous panel. For both panels, the uncertainty value for the last digit is reported in parenthesis. Adapted from Ref. [212].

of graphene on the morphology of the substrate) can be softened by an opportune thermal treatment [212]. This interpretation is strengthened by the AFM images reported in Fig. 93, which report the morphology of Gr/SiO₂ thermally treated in N₂ and subjected to fast (Fig. 93a) and slow cooling (Fig. 93b). As suggested by the reported section profiles, the cooling rate affects the roughness of graphene, which is equal to 0.49(3) nm and 0.36(8) nm in the case of fast and slow cooling, respectively, thus indicating a trend correlated to the different strain previously reported. In fact, both the roughness evaluated by AFM and the strain evaluated by Raman spectroscopy can be used as an estimation of the corrugation of graphene sheet [94, 214, 215]. In this case both these quantities indicate a low corrugation as a consequence of slow cooling, and a high corrugation for the fast cooling, thus corroborating the relation between the dynamic of the cooling rate and the relaxation of the graphene structure [212].

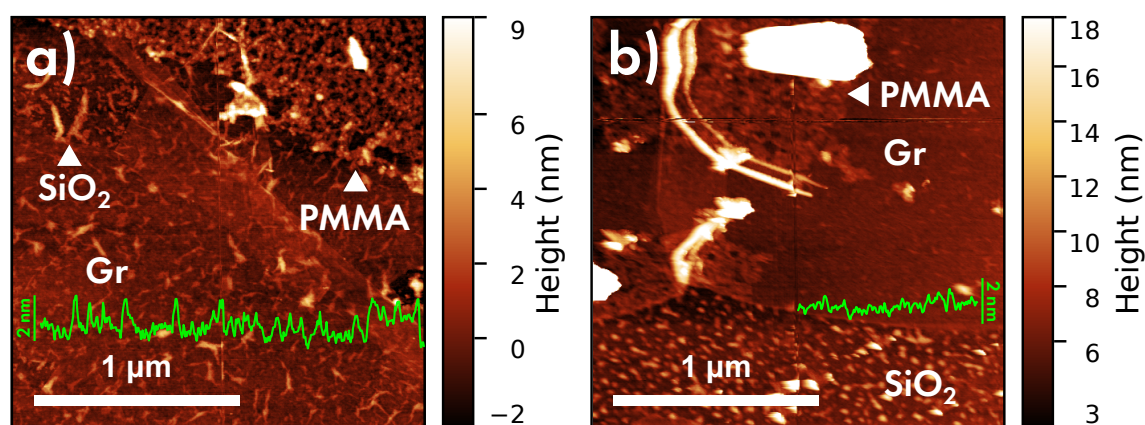


Figure 93: AFM morphological images of Gr/SiO₂ thermally treated in N₂ and subjected to (a) fast and (b) slow cooling. Two representative section profiles are shown by the green continuous lines. The labels highlight the surfaces of silica (SiO₂), polymer clusters (PMMA) and graphene (Gr). Adapted from Ref. [212].

5.1.9 MODEL FOR GRAPHENE-MOLECULES INTERACTION

On the basis of the reported data, the following model for the interaction between graphene and small molecules by thermal treatments can be here drawn up.

The substitution of the support substrate has revealed the fundamental role of this element in the doping process. Therefore, the doping capability cannot be considered a feature of graphene only, but of the entire system constituted by the graphene/substrate stack. Most importantly, the temperature distributions of reaction sites is found fundamentally affected by the substrate water affinity (and drastically reduced for an almost hydrophobic substrate). Accordingly, we state that the presence of the hydroxyl groups of the substrate and the consequent water buffer layer between substrate and graphene is mandatory for the doping of graphene by O_2 . In particular, by considering the chemical species involved in thermal treatments, we state that the doping of graphene obtained by O_2 is related to the reduction reaction (thermally activated) between the gas phase oxygen and the water buffer layer between graphene and substrate depicted in Fig. 94. In this process, graphene intervenes by providing the charges required for the reaction, thus remaining under-charged and thereby p-doped. This result is corroborated by the influence of the substrate on the doping kinetics, strengthening the hypothesis concerning the occurrence of the doping reaction in the interstitial space between graphene and substrate. In this case, the kinetics model which better describes the doping increase with time is the Bangham model, that is a diffusion model. This result suggests that the fast reaction between oxygen and water is preceded by a slower diffusion process which we identify with the oxygen diffusion between graphene and substrate. According to this picture, the evolution of graphene structure indicated by Γ_{2D} on increasing the doping can be interpreted as mark of the modification of the way in which graphene lies onto the substrate due to modification of the buffer layer between them.

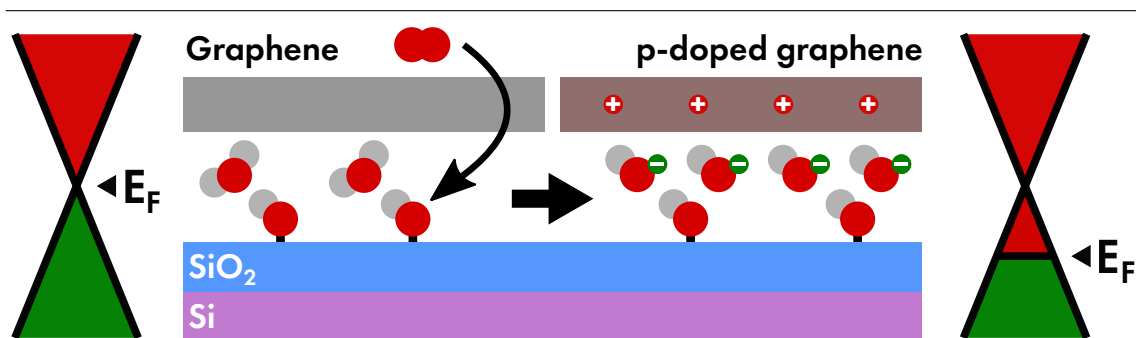


Figure 94: Oxygen reduction reaction involving the water buffer layer located between substrate and graphene. For the completion of the reaction, graphene cedes some electrons, thus getting p-doped.

Beyond the dependence on the thermodynamic treatment parameters, the two main sources of diversity in the outcomes of thermal treatment were the specific atmosphere of treatment, and the support substrate on which graphene is transferred. As depicted in Fig. 95, the various atmospheres explored in this Thesis can be grouped in two categories:

INERT as in the case of V and N_2 , where the modification of graphene is almost completely dominated by strain, with very risible doping effect.

REAGENT specifically oxidizing agents such as O_2 and CO_2 , where doping is the main effect to which a certain part of strain evolution is related. In addition, H_2O can be included to this category as reducing agent because of its capability of dedoping on increasing the pressure, the time of exposure, but with no significant intervention of temperature.

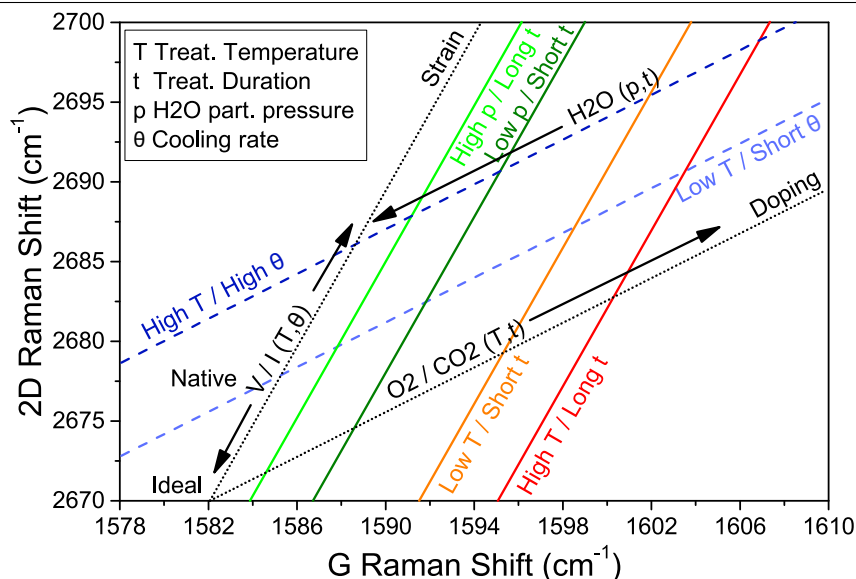


Figure 95: Model of the evolution of strain and doping occurring in thermally treated graphene in relation to the different atmospheres (inert (I) or vacuum (V), or reagent molecules) and leading parameters. The arrows indicate the increase or decrease in doping or strain. Colored lines indicate the different levels of strain (dashed lines) and doping (continuous lines) obtainable in different parametrical conditions. The axis position is calibrated for the excitation energy of 2.33 eV. Adapted from Ref. [212].

Besides, the effects of treatment parameters on strain and doping are schematized as follows:

DOPING the dependence on temperature and time has revealed that doping increases with both these two parameters up to a saturation level. In the case of temperature this level, namely the maximum doping obtainable for a given sample, is reached through a sigmoidal increase. This curve is interpreted as cumulative contribution of an increasing amount of reaction sites activated at ever higher temperature. The temperature distribution of these sites is evaluated from the mathematical derivative of the doping vs temperature curve. Concerning the dependence on time, the Bangham model is the kinetics model which better describes the doping increase. This result suggests that the kinetics of doping is limited by a diffusion process, probably ascribable to the diffusion of doping molecules in the interstitial space between graphene and substrate. Since a similar kinetic is found valid for the dedoping process performed by H_2O molecules, a similar diffusion mechanism should be considered. Such findings suggest that the doping of graphene is kept stable up to the post-treatment products of the interstitial space below it are not modified by other molecules.

STRAIN whether considered alone, it appears in the very early stages of the thermal treatments, and increases up to a level which is determined by the treatment temperature, so that the higher the temperature and the higher the strain. However, the temperature induced strain can be totally removed by an opportune cooling rate according to a mechanism conceptually similar to a glass transition depicted in Fig. 96. In fact, if the temperature of

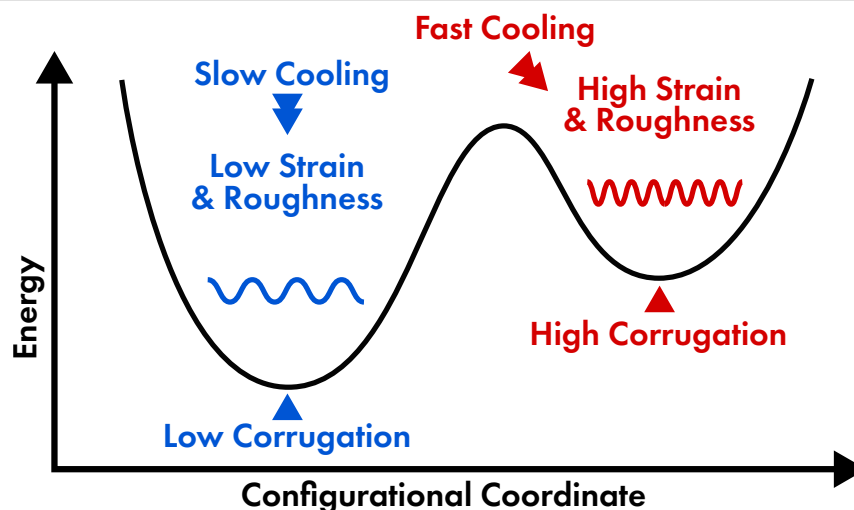


Figure 96: Representative scheme of the intervention of cooling rate in the modification of graphene strain by thermal treatment. In particular, the fast cooling freezes graphene in a configuration at high corrugation, whereas a slow cooling allows it to relax towards a lower corrugation.

graphene is suddenly quenched, its structure keeps *frozen* in an energetic configuration characterized by an high corrugation, the latter evaluated by the physical quantities of strain and roughness. On the other hand, a slow cooling allows a complete relaxation of graphene structure and graphene will feature a configuration at low corrugation characterized by lower strain and roughness values. Since this effect is not found for vacuum treatment, such data suggest that the gas atmosphere plays the key role of thermal capacitor which allows the slow decrease of graphene temperature.

Finally, a grouping of the three main samples investigated, namely Gr/SiO₂, Gr/Al₂O₃, Gr/HfO₂, based on the observed features in this thesis is reported in Fig. 97. Herein, from a merely *quantitative* point of view, Gr/HfO₂ strongly differs from the other two samples, since it features the lowest maximum doping as effect of its hydrophobic surface (similar to the case of methylated SiO₂). Nevertheless, from a more important *qualitative* point of view, is actually Gr/Al₂O₃ that features a peculiar behavior characterized by a minor feasibility to doping. In fact, the doping of Gr/Al₂O₃ features the lowest reaction rate and its temperature distribution of reaction sites is placed at high temperature, whereas the doping of the other two samples feature a faster rate and occurs even at lower temperature.

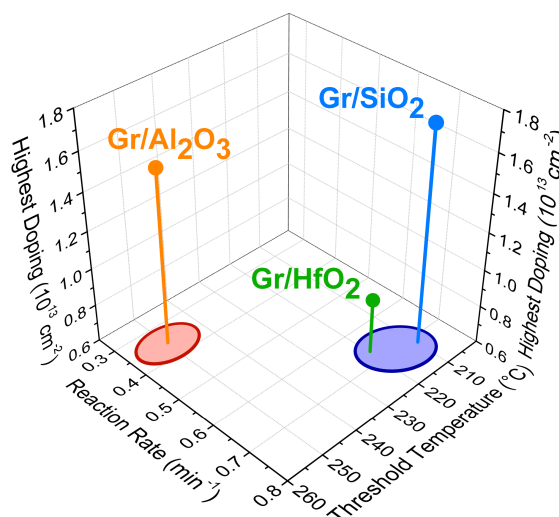


Figure 97: Mean values of highest doping available, reaction rate, and threshold temperature for Gr/SiO₂ (azure), Gr/Al₂O₃ (orange), and Gr/HfO₂ (green). The proposed grouping based on the feasibility of doping is reported by red and blue ellipses. Adapted from Ref. [211].

5.2 INTERACTION WITH NANOPARTICLES

5.2.1 CHARACTERIZATION OF DEPOSITED CDS

As discussed in Chp. 4, a graphene-CDs composite (CDs/Gr) was fabricated by depositing CDs onto graphene by means of the simple drop-casting technique. Such composite system is shown by the optical microscopy images reported in Fig. 98, where graphene with CDs deposited on it is clearly distinguishable from the bare graphene (Fig. 98a) by the presence of a light blue halo spread onto the surface (Fig. 98b). The presence of CDs can also be proven by Atomic Force Microscopy, by which it is possible to compare the flat profile surface of bare graphene (Fig. 98c) and that of CDs/Gr (Fig. 98d), thus noticing the presence of single spherical nanometric objects onto the surface of graphene [213]. A more detailed morphological characterization of CD deposition is reported in Fig. 99, where the spread of CDs is compared between three different surfaces: ultraflat mica (Fig. 99a), graphene (Fig. 99b), and SiO₂ (Fig. 99c), these two latter belonging to

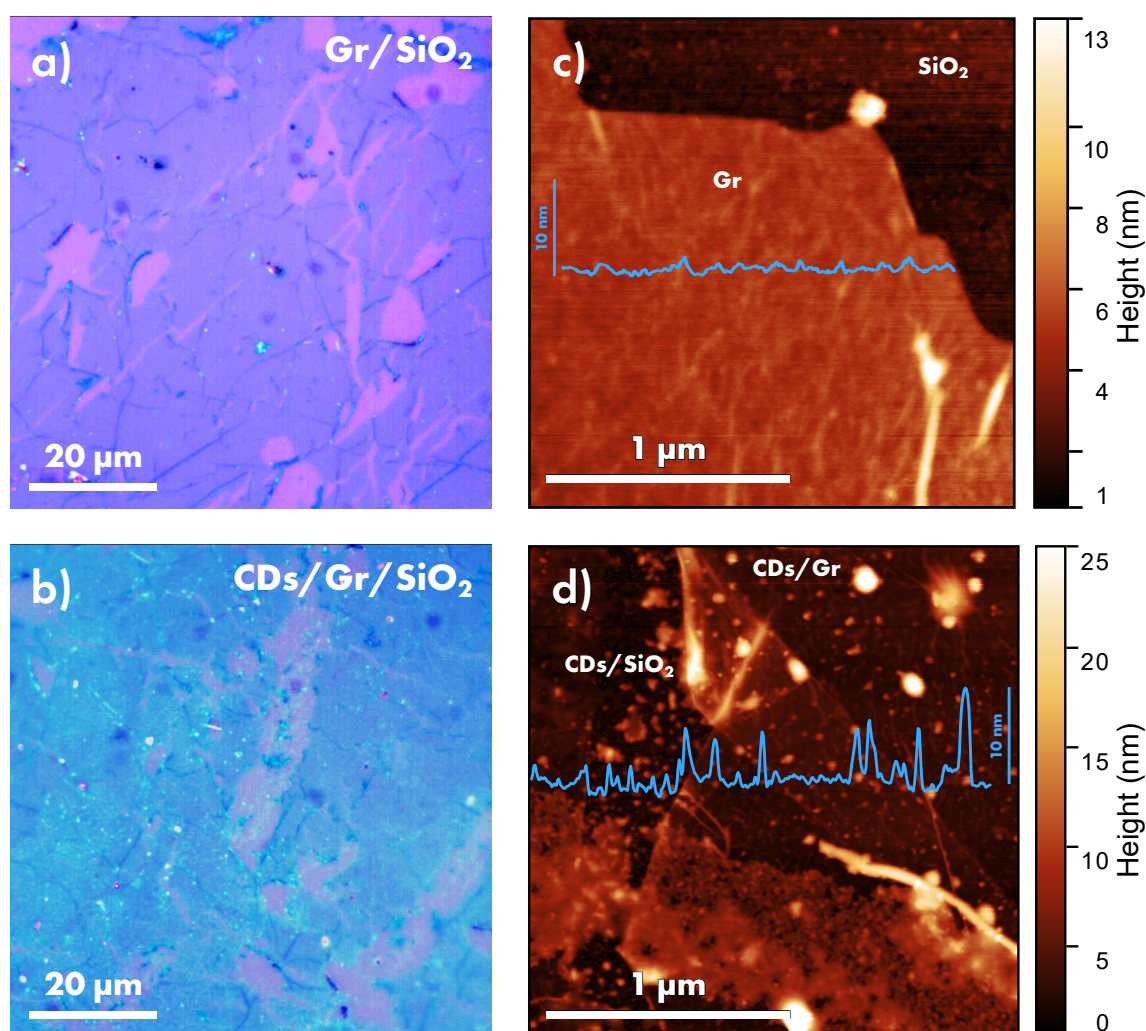


Figure 98: Images obtained by (a,b) optical microscopy, and by (c,d) atomic force microscopy of Gr/SiO₂ and CDs/Gr/SiO₂, respectively. In panel (d), the CDs deposited on SiO₂ (CDs/SiO₂) and CDs deposited on graphene (CDs/Gr) can be distinguished. In addition, in panels (c,d) representative profile is reported (blue line) on the corresponding trace line.

a Gr/SiO₂ sample. The comparison of the three images reveal a different spatial concentration of CDs on mica with respect to CDs on Gr/SiO₂, where the nanoparticles fall both on graphene and on SiO₂ with no relevant influence of local water affinity of the substrate. Moreover, the substrate influence on the spread of CDs can be characterized by comparing the size distribution of the nanoparticles shown in Fig. 99d,e,f. In particular, all the distributions feature an asymmetric shape due to the abundance of counts near to the inferior limit of diameter, namely zero. Despite similar trends are found in every deposition, the distribution extracted from CDs on mica

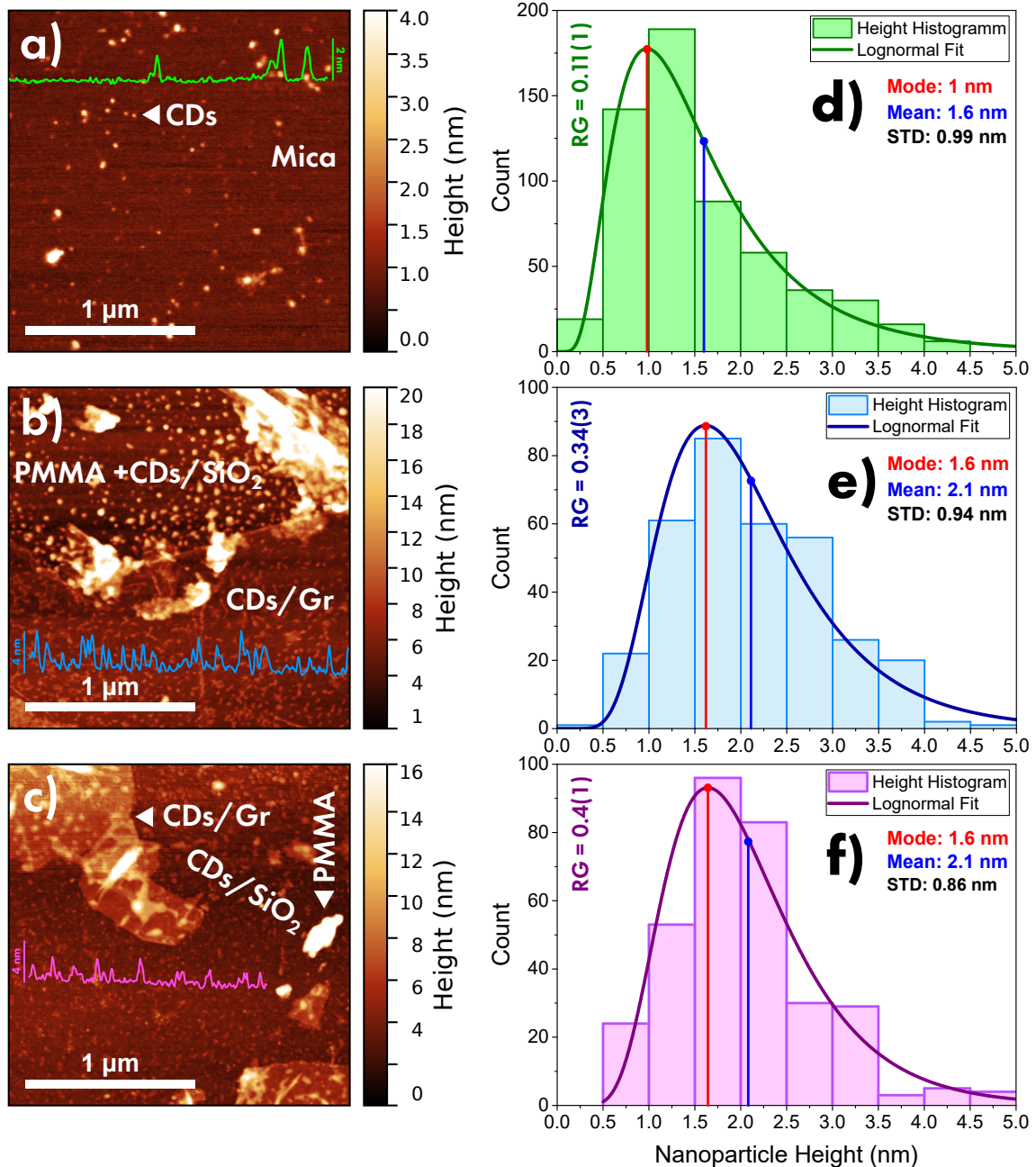


Figure 99: AFM morphological images of CDs deposited onto (a) ultraflat mica, (b) graphene (Gr), and (c) SiO₂, these two latter belonging to a Gr/SiO₂ sample. A representative section profile is shown for each panel. The labels highlight the spread of CDs onto the different surfaces, and the incidental presence of polymer clusters (PMMA). Size distribution of CDs deposited onto (d) ultraflat mica, (e) graphene (Gr), and (f) SiO₂. The values of substrate roughness (RG) is also reported. Adapted from Ref. [213].

can be identified as the most reliable description of deposited CDs (Fig. 99d): a mode equal to 1 nm, a mean equal to 1.6 nm and a standard deviation equal to 0.99 nm and a rapid decrease of counts with the increase of size up to the complete vanishing at about 4.5 nm. As reported in Fig. 99,e,f, the distributions extracted on the other two substrates report a different shape featuring a slight higher characteristic size of CDs: a mode equal to 1.6 nm, a mean equal to 2.1 nm and a standard deviation equal to 0.94 and 0.86 for graphene and SiO₂, respectively. Nevertheless, such a difference can be ascribed to the different recognizability of the smallest CDs due to the different roughness of the three substrates. In fact, mica surface features the lowest surface roughness equal to 0.11(1) nm, whereas the larger roughness of 0.4(1) nm for SiO₂ and 0.34(3) nm for graphene prevents the counting of the smallest fraction of CDs. Therefore, the distributions can be considered mutually compatible, with an extraction method independent on the single substrate. Once the reliability of these analysis is established, it is important to note that it has returned a characteristic size of CDs between 1 and 5 nm, whereas a distribution between 4 and 8 nm is expected from previous investigation [191]. However, such a discrepancy can be explained by considering the formation of clusters and the presence of PMMA residues (for graphene and SiO₂ only), that is two structures that cannot be distinguished by large single CDs. Accordingly, the necessary discarding of structures larger than 5 nm in the count of CDs induces the unintended loss of all this part of the CD size-distribution [213].

5.2.2 EMISSION OF CDs IN SOLID-PHASE

Two liquid solutions of CDs are compared for the deposition procedure in order to evaluate the dependence of the morphological and spectroscopic properties of deposited CDs on a specific solvent: CDs dispersed in water (CDH₂O) and CDs dispersed in ethanol (CDEtOH). As shown in Fig. 100, because of the properties of the solvent, these two dispersions of CDs feature a completely different deposition. In particular, whether a drop of CDH₂O keeps a defined shape during

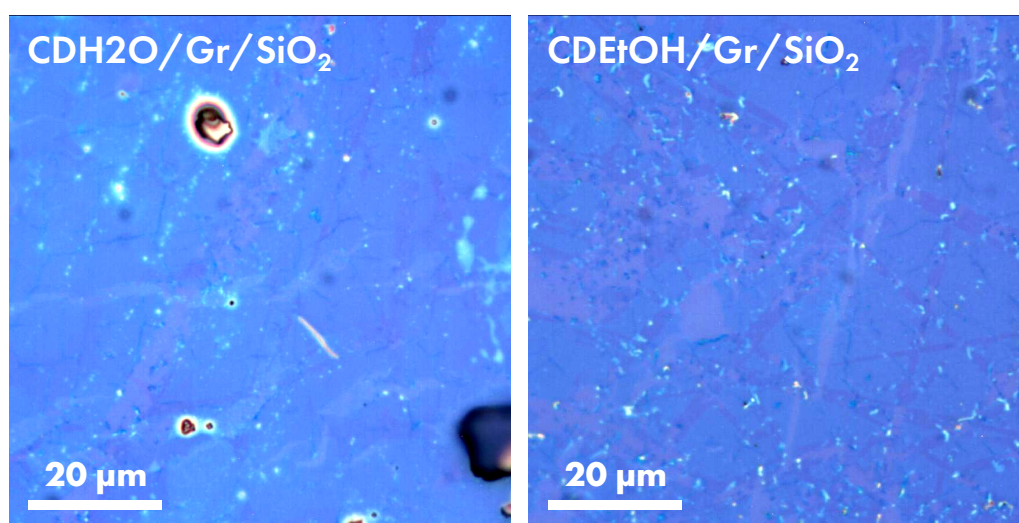


Figure 100: Optical microscopy images of (a) CDH₂O and (b) CDEtOH deposited on Gr/SiO₂ by drop-casting. Adapted from Ref. [213].

the slow solvent evaporation, a drop of CDEtOH involves a large surface of Gr/SiO₂ sample and the ethanol rapidly evaporates. Accordingly, the halo which attests the presence of CDH₂O onto Gr/SiO₂ (Fig. 100a) is more dense compared to the case of CDEtOH (Fig. 100b). However, by considering small regions of some micrometers, a similar morphology can be locally found in region of few μm² [213].

The emission spectrum excited at 2.33 eV (532 nm) of CDs deposited onto a SiO₂/Si substrate is reported in Fig. 101. In particular, as specified in Chp. 4, the PL measurements were carried out by the micro-Raman equipment, and therefore the obtained spectra contain both Raman and photoluminescence signals. For both CDH₂O and CDEtOH, beneath the narrow vibrational contribution of the Raman spectrum of silicon, a single much broader emission band is found, peaked at 2.1 eV and featuring a FWHM 0.3 eV, with no significant differences between the emission spectra of the two samples, thus indicating that the deposited CDs preserve the emission capability of the liquid dispersed CDs, and they show a compatible emission property. Therefore, the same emission mechanism is supposed to subsist for solid phase and liquid phase CDs.

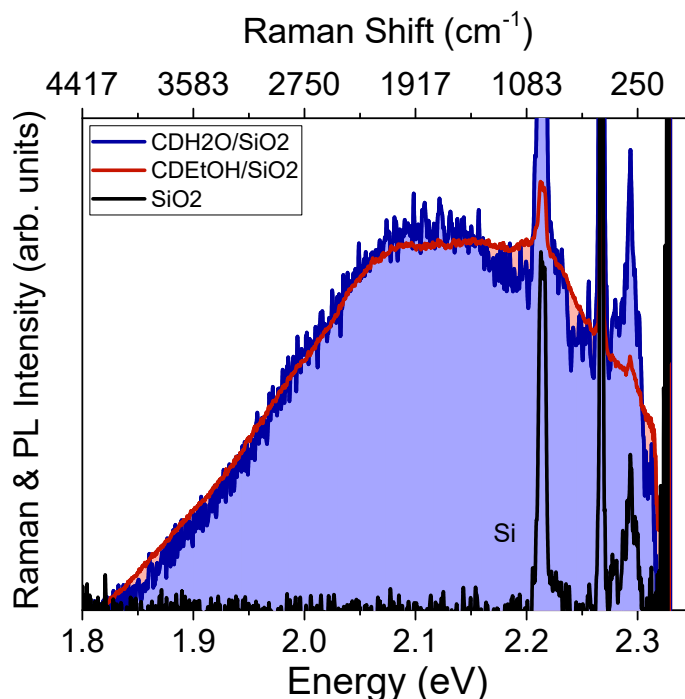


Figure 101: μ -PL of CDH₂O (blue) and CDEtOH (red) dispersed on SiO₂, compared to the Raman signal of the latter (black) acquired without CDs.

In order to explore the resistance of CDs to the temperature, the CDH₂O and CDEtOH deposited on SiO₂ were exposed to thermal treatment in the temperature range of 50–300°C, and both in vacuum or oxygen atmospheres. As shown in Fig. 102, the emission of both CDEtOH and CDH₂O features the same evolution both in vacuum or oxygen atmospheres. In particular, as shown in (Fig. 102) the spectra keep their typical single band in the entire temperature range, but a progressive slight (<0.1 eV) redshift of the CD emission peak is found with the increase in treatment temperature. These results indicate an irreversible modification of CD surface states as effect of thermal treatment, marked by the lowering of their energy and consequently of the

emission energy. Moreover, the negligible influence of the type of atmosphere indicates that this alteration is related to pure thermal effects. However, the most important result is that emission capability of CDs is still preserved in the entire temperature range, thus enabling the implementation of CDs in composite systems for which the exposure to high temperature is required, both in synthesis, processing or in operational contexts [213].

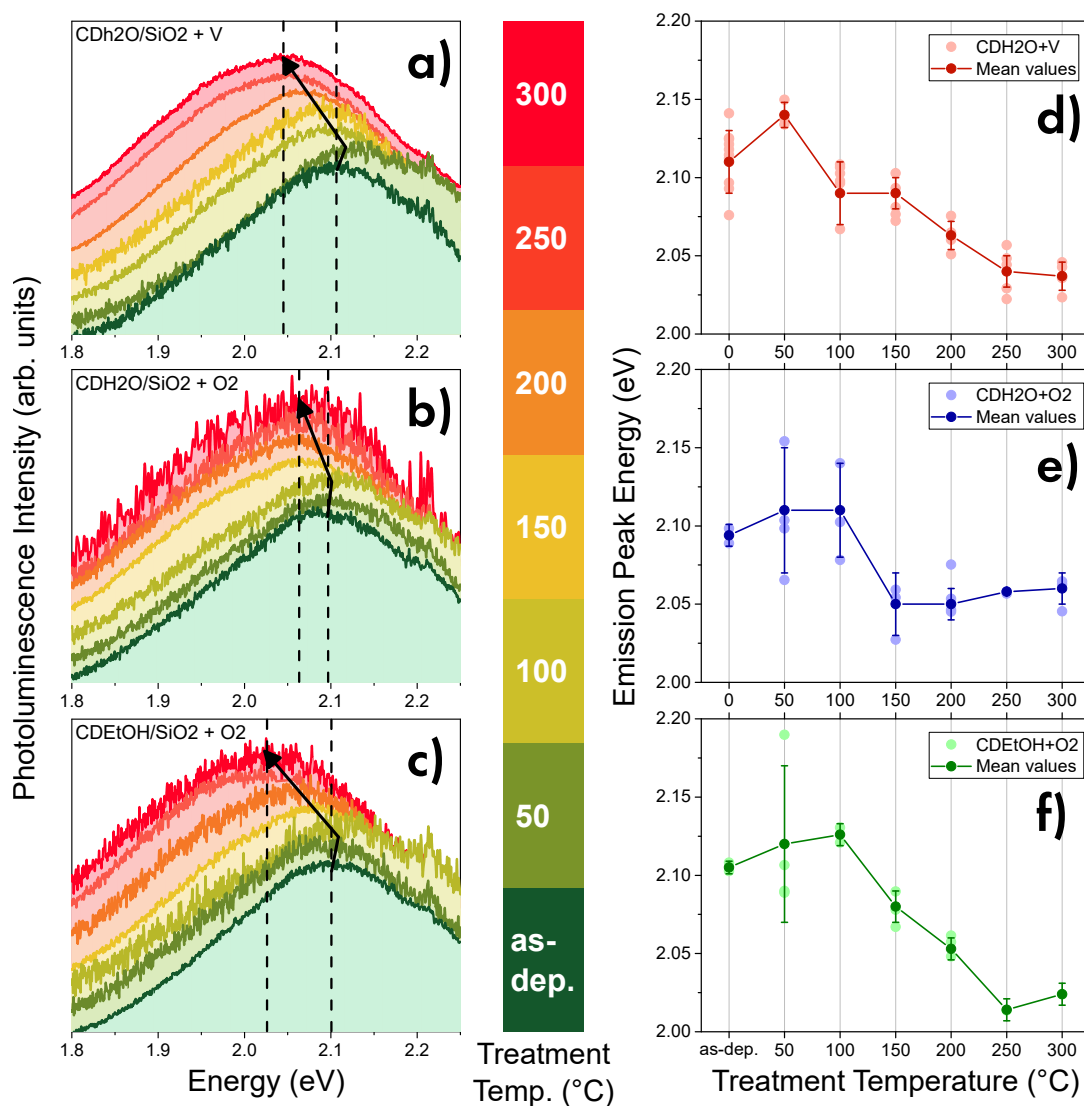


Figure 102: μ -PL of CDs/SiO₂ exposed to thermal treatments in controlled atmosphere for (a) CDH₂O in vacuum atmosphere, and for (b) CDH₂O and (c) CDEtOH in oxygen atmosphere. The evolution of the emission is displayed in color scale with the increase in treatment temperature and highlighted by the black arrows. The respective shift of the emission peak is shown in panels (d,e,f). Adapted from Ref. [213].

5.2.3 CDs-GRAPHENE INTERACTION

The spectroscopic investigation of the interaction between CDs and graphene is conducted by comparing the regions in which the CDs are in contact with graphene (CDs/Gr) with CDs in contact with the SiO₂/Si substrate (CDs/SiO₂) as reference configuration for the nanoparticles, and uncovered Gr/SiO₂ as reference configuration for graphene. In particular, two kinds of graphene

are coupled to CDs: native undoped graphene (Gr), and p-doped graphene (p-Gr) obtained by using a standard thermal treatment in O₂ atmosphere, as discussed in Sec. 5.1.

Concerning the nanoparticles, the emission spectra of CDs deposited on Gr/SiO₂ and p-Gr/SiO₂ are shown in Fig. 103. There the emission of contiguous regions of CDs/Gr and CDs/SiO₂ is compared, and the presence of graphene is assured by the characteristic G and 2D bands. In particular, the emission of CDs in contact with graphene is systematically reduced with respect to the emission of those in contact with SiO₂, independently of the doping level of graphene. Therefore, this result suggests the opening of a non-radiative relaxation channel for photoexcited CDs deposited on Gr, which reduces the emission efficiency.

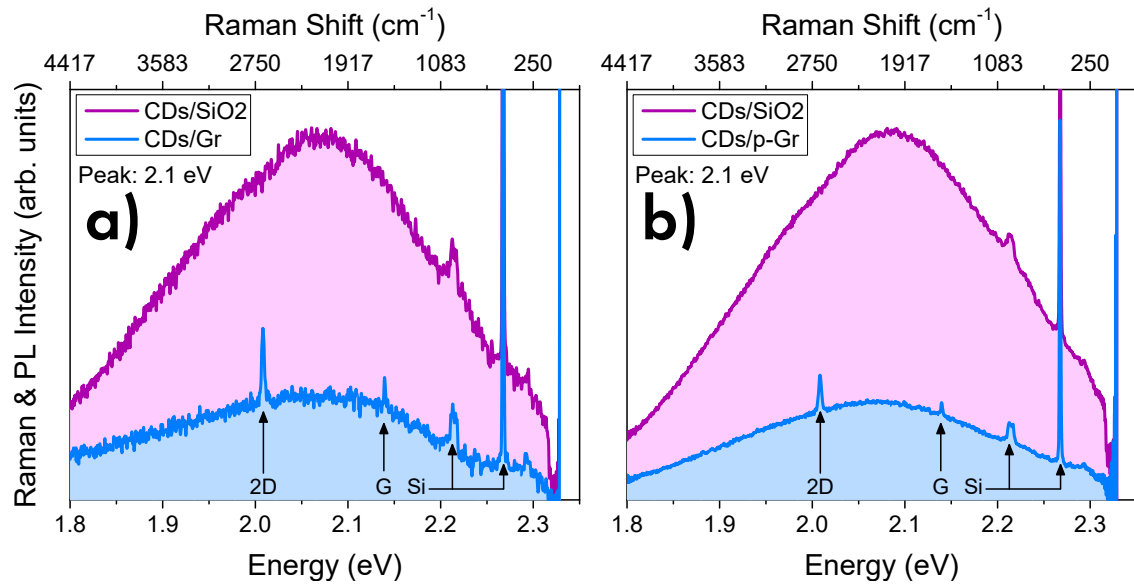


Figure 103: μ -PL excited at 532 nm of CDs deposited on contiguous regions of graphene and SiO₂ of (a) Gr/SiO₂ and (b) p-Gr/SiO₂ samples. Raman signals of Gr and silicon are marked by arrows. The energy axis is reported both in terms of absolute value (bottom), and relative value (Raman Shift, top) to the laser energy. Adapted from Ref. [224].

On the other hand, the influence of CDs on graphene electronic structure can be evaluated by the G-2D map extracted from the Raman spectrum, especially for what concerns the doping of graphene which gives information about the population of graphene electronic states. Concerning undoped graphene, the map shown in Fig. 104a indicates that some modification of graphene occurs as effect of the deposition of CDs. In fact, despite the point clouds are quite overlapped, the CD strongly affects the shape and the center of the point cloud, that is the spread and mean value of strain and doping. In particular, the deposition of CDs slightly increases the compressive strain of graphene, which achieves a narrower distribution along the value -0.16(2)%, probably due to the deformation of graphene structure caused by the weight of nanoparticles. Besides, also the doping is modified by the CD deposition, but no quantitative estimation of the Fermi energy shift can be performed since the point clouds of graphene both with and without CDs fall in a region where the relation between doping and Raman signal is non-linear and with low effects. These modifications can be attributed to CDs, since the effect of the bare solvent reported in Fig. 104b is very different: the strain results larger in absolute value and opposite in sign, whereas the doping modification is qualitatively of minor entity.

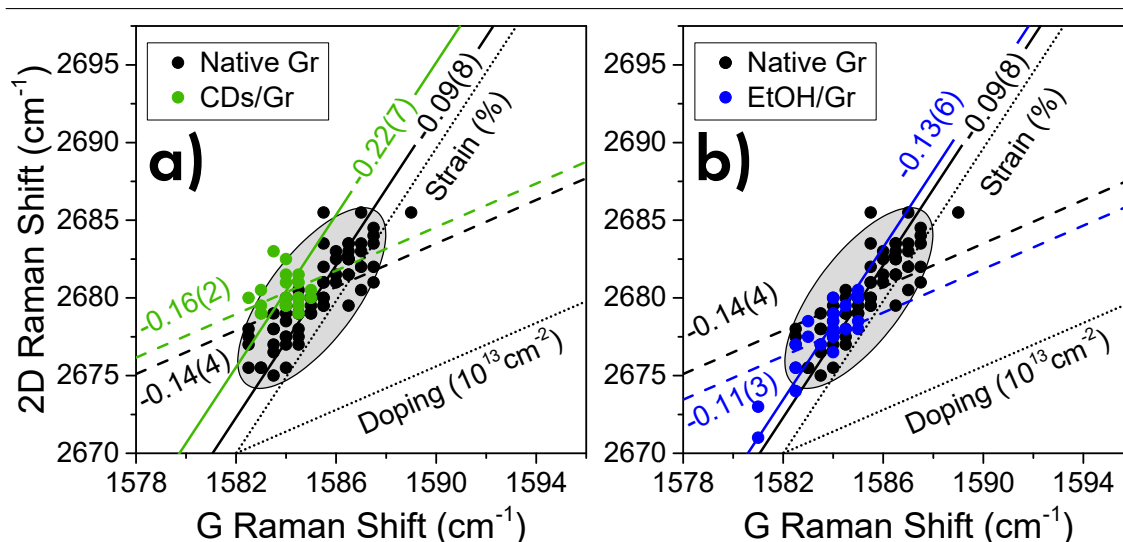


Figure 104: G-2D correlation map at 532 nm laser excitation of (a) CDs/Gr(green) (b) EtOH/Gr, compared to native Gr data (black). Adapted from Ref. [224].

Concerning p-doped Gr, the influence of CDs on graphene evaluated by G-2d map of p-doped graphene both with and without CDs deposited was investigated by using two different laser excitations: the green laser at 532 nm (2.33 eV) used until now, and a further red laser at 633 nm (1.96 eV). The typical Raman spectra of graphene acquired by using these two lasers are shown in Fig. 105. It must be stressed that the Raman signal of graphene is strongly dependent on the

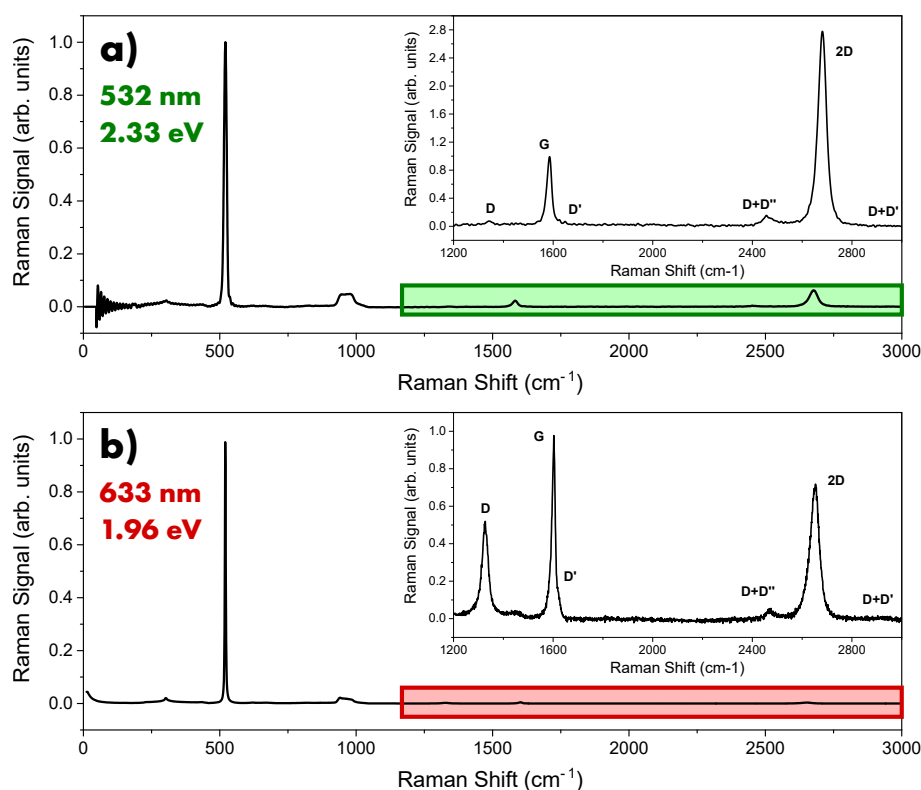


Figure 105: Raman spectrum of Gr/SiO₂/Si acquired by using laser at (a) 532 nm (2.33 eV) and (b) 633 nm (1.96 eV). In both panels, the spectral range between 1200–3000 cm⁻¹ containing the main bands of Gr is shown in the inset. Adapted from Ref. [224].

energy of the used laser, accordingly to the discussion in the Chp. 1. In particular, the intensity ratio between G band (taken as reference) and other bands strongly changes, since the spectra acquired by 633 nm features a significant quenching of 2D band and enhancement of D and D' bands. In addition, whether the G peak frequency does not vary significantly, 2D band features a large redshift equal to about 40 cm^{-1} . Therefore, a large variation in the position of G-2D map is induced for this wavelength, as shown in Fig. 106. In spite of this, the difference between p-doped and undoped graphene is still clearly distinguishable.

Concerning measurements taken at 532 nm (Fig. 106a), the point cloud of bare p-Gr strongly differs from that of CDs/p-Gr, since the latter features a much broader doping value distribution and occupies almost every intermediate doping value between the levels of p-Gr and undoped graphene. Here, an increase of Fermi energy at least equal to 0.2 eV is estimated by the Raman analysis, corresponding up to $5 \times 10^{12}\text{ cm}^{-2}$ transferred electrons. On the other hand, the measurements taken at 633 nm give a completely different result (Fig. 106b), with no significant difference between the graphene sample with and without CDs on it. Similarly to the case of undoped graphene, this effect can be attributed to CDs deposited onto graphene since it is significantly different from the effect of the bare solvent reported in Fig. 106c,d.

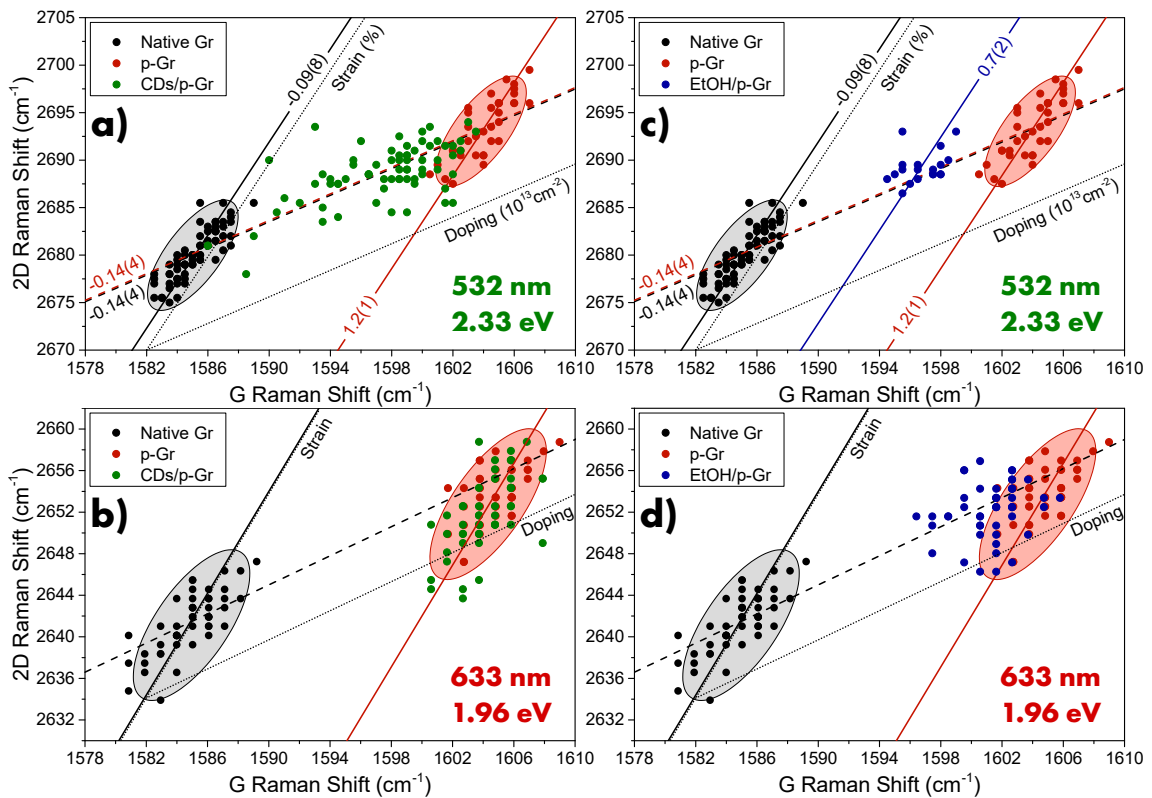


Figure 106: G-2D correlation map at (a) 532 nm and (b) 633 nm laser excitation of p-doped Gr (red dots), p-doped CDs/Gr (green dots), native Gr (black dots). The effect of solvent is shown in panels (c,d). Adapted from Ref. [224].

5.2.4 MODEL FOR GRAPHENE-NANOPARTICLES INTERACTION

The experimental information above reported allows to elaborate the model for the interaction subsisting between graphene and CDs deposited on it based on a photoinduced electron transfer, as described in the following.

As described in Chp. 2, the accepted model for the photocycle of the used CDs involves the extraction of an electron from their core towards their surface states, as effect of photoexcitation. Thence, the following recombination between the surface electron and the hole kept in the core gives rise to the observed fluorescence [193]. Such a mechanism is of fundamental importance for the spectroscopic behavior of CDs, since the exposure at the CD surface of the promoted electron is at the basis of the different charge transfer mechanisms between optically active nanoparticles and their environment. Therefore, from this point of view the crucial feature for an interaction is the capability of graphene to accept or donate charges from/to the CDs. This aspect is clarified by the energy levels scheme shown in Fig. 107, where the energy levels of CDs and graphene are aligned with respect to the vacuum energy $E_v = 0$ eV. Concerning graphene, its electronic structure is characterized by the Fermi level which discriminates empty or occupied states depending on whether they are placed above or below this level, respectively. The energy difference between Fermi and vacuum levels corresponds to the work function ϕ_{Gr} . Concerning

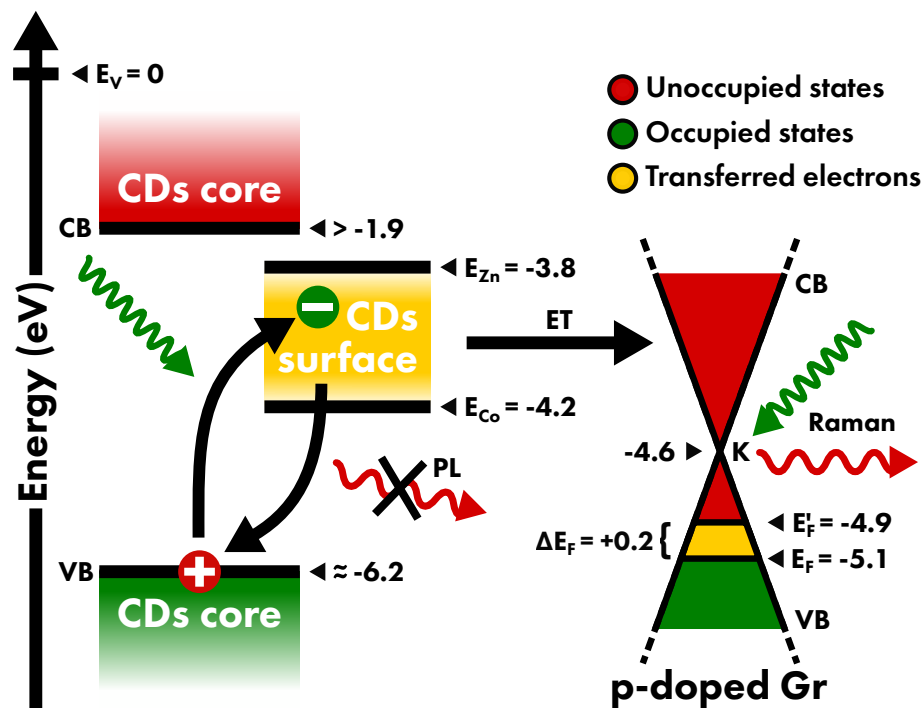


Figure 107: Energy levels scheme of CD core electronic bands, CD surface states, and of Gr electronic bands at K point (Dirac cones) relative to the energy of the vacuum level. The elements of the CDs-Gr interaction described in the proposed model are reported. The laser light (green arrows) is absorbed by CDs and scattered by Gr, thus generating CD PL and Gr Raman signals (red arrows), respectively. In CDs, electrons are promoted from core valence band (VB) to surface states, which energy distribution is between the energies of zinc and cobalt ions. From the surface states the electron migrates towards the conduction band (CB) of Gr (ET). Finally after an ultrafast relaxation towards lower energy states, the states in the VB are populated, as attested by the increase of Fermi energy revealed by Raman signal. Adapted from Ref. [224].

native graphene, since it has no relevant charge doping, its Fermi level can be assumed near to the K point of graphene band structure, and therefore $\varphi_{\text{Gr}} = -4.6$ eV [36]. Besides, in the case of p-doped Gr by thermal treatment in O_2 , the increase of $1.2(1) \times 10^{13} \text{cm}^{-2}$ charge carriers implies a lowering of Fermi energy by about $\Delta E_{\text{F}} = -0.5$ eV [225–227], thus obtaining a work function equal to $\varphi_{\text{p-Gr}} = -5.1$ eV. Concerning the CDs, no direct measurement for the electron affinity of $\beta\text{-C}_3\text{N}_4$ core of CDs is known. However, the alignment of the electronic structure of CDs can be drawn on the basis of their spectroscopic features. The energy position of the surface states is limited to the range between -4.2 eV and -3.8 eV accordingly to the emission quenching of CDs induced by metal ions [228]. In fact, this effect has been related to the redox potential which measures the tendency of a chemical species to accept electrons. The extreme conditions are given by zinc and cobalt ions, since the emission of these CDs is enhanced by the interaction with Zn^{2+} ions, whereas the CD emission is quenched by Co^{2+} [224, 228]. The energy position of the excited state of CDs labeled E_{CDs} is thereby assumed between those of the acceptor level of these two ions quantified by their redox potentials. In terms of energy, the redox potentials of zinc and cobalt equal to $V_{\text{Zn}^{2+}} = -0.76$ V and $V_{\text{Co}^{2+}} = -0.28$ V, respectively, correspond to the energies $E_{\text{Zn}^{2+}} = -3.8$ eV and $E_{\text{Co}^{2+}} = -4.2$ eV. Besides, the valence band of CD core can be placed about 2 eV below the surface state by considering the lack of light absorption at energy below this threshold, whereas the band gap of CD core is guessed be equal to about 4 eV from the absorption properties of CDs [191].

In this picture, the fundamental quantity to consider is the energy difference between the surface states of CDs and the Fermi level of graphene, and in particular its sign. According to the above discussion, after its preliminary promotion from the core of CDs to their surface states, an electron can actually migrate towards the unoccupied states of graphene, thanks to a close contact between these molecular orbitals. Most importantly, since $E_{\text{CDs}} - \varphi_{\text{Gr}} > 0$, the migration occurs spontaneously because the decrease of energy for the transferred electrons. The non-radiative recombination channel revealed for CDs on graphene can thereby be assigned to this transfer, which does not depend on the doping of graphene here compared compatibly with the spectra reported in Fig. 103. For the transferred electrons in graphene an ultra-fast relaxation is expected, and their accumulation in the valence band of graphene determines the increase of Fermi energy indicated by the decrease of p-doping shown in Fig. 106a. Finally, the lack of modification in Raman measurement acquired by 1.96 eV laser confirms the key role of the photoexcitation of CDs in the suggested electron transfer process. In fact, under such a light stimulation, CDs keep unexcited, and no electron are exposed to their surface. The charge transfer from CDs to graphene is thereby inhibited by two key factors. First, the electron in the valence band of CD core are spatially separated from the graphene states by the surface states of CDs, which act as potential barrier. Second, the energy of these electron is well below (~ 1 eV) the Fermi level of graphene, and therefore an electron transfer from CDs towards Gr would require an optical transition between their states.

6 | CONCLUSIONS

THE intended purpose of this Thesis is the study of the fundamental phenomena at the basis of two different charge transfer processes subsisting between graphene and small molecules and carbon nanoparticles, respectively. The reported data have successfully met this target, and the information extracted from the performed experiments is of interest both for basic scientific questions and for their possible impact for applications based on nanomaterials.

Concerning the interaction with small molecules, the research here reported has substantially expanded the information about this process. Thermal treatments in a controlled atmosphere are found to be able to dope graphene by using a selective atmosphere of oxidizing molecules (such as oxygen and carbon dioxide), whereas previous investigations in literature reported a positive outcome only for oxygen. Besides, the strain induced by thermal treatment is found to be constituted by two contributes: the first one, related to the doping process and found only for intermediate doping values; the second one, related to the coupling with the substrate and modifiable by tuning the cooling rate in the final stage of the treatment.

The study concerning the reaction kinetics and the comparison of the experimental evidences observed for various substrates has allowed the identification of the mechanism at the basis of the doping process of graphene by gas molecules, that is a charge transfer process between the 2D material and the interacting molecules. In particular, water affinity of substrate has been identified as the key factor for the capability of doping for the entire graphene/substrate stack. In fact, substrates of different surface water affinity have shown a different capability to doping, which drastically decreases in the case of a hydrophobic surface. On the other hand, the study of the time kinetics of doping indicates the presence of a diffusion stage in the doping process. This result suggests that oxygen molecules diffuse in the interlayer between graphene and substrate before to undergo a reaction in specific sites that determines the doping in graphene. In particular, we suggest that a oxygen reduction reaction is the microscopic mechanism at the basis of the doping process wherein oxygen reacts with the water buffer layer between graphene and substrate. In this process, graphene provides the electrons required for the reduction reaction, thus resulting under-charged and p-doped. In addition, the substrate is found to affect the distribution temperature of reaction sites, that is the statistical distribution of the activation temperature of the oxygen reduction reaction, and the stability of doping to the following exposure to ambient atmosphere. In the latter process, a prominent role of H_2O molecules in gas phase has been highlighted, by revealing a dedoping effect strongly affected by the concentration of these molecules rather than to temperature.

Concerning the interaction with nanoparticles, CDs have proven to be a feasible optical counterpart of graphene in a optoelectronic system. In fact, our results indicates the presence of a photoinduced electron transfer from photoexcited CDs towards graphene. Despite such kind of interaction was already known in literature for various systems, our results posses a significant

relevance. In fact, the graphene-nanoparticle interaction has been investigated in a solid phase composite, thus ensuring a direct transfer potentiality of this result in the design of optoelectronic devices based on nanomaterials. Furthermore, the concurrent use of graphene and CDs guarantees a wide range of applications basing on carbon based materials only by limiting environment impact and cost efforts. First, both graphene and CDs have proven to be largely biocompatible and non-toxic nanoparticles, and therefore such nano-composite is a promising candidate for the substitution of other nanomaterials which are typically used for similar scopes (such as heavy metal or metal-chalcogenide nanoparticles) although their high toxicity. In addition, CDs are very cheap in comparison to other emitting nanoparticles, and their application will produce a consistent decrease of costs. For example, a graphene-CDs composite can find a useful application in nano-sized photovoltaic devices, by taking advantage from the excellent energy conversion of CDs and from the significant transport properties of graphene.

Despite the content of this Thesis gives a consistent advancement in the comprehension of the interaction between graphene and other species at the microscopic scale, several questions are still open. Concerning the interaction with molecules, various issues are not characterized yet, but a plethora of experimental techniques could provide information on them. For example, X-ray photoelectron spectroscopy could provide a finer identification of reaction sites on the substrate surface, and fundamental issues of their interaction with graphene could be investigated by theoretical investigation, such as density functional theory. Besides, by focusing on the properties of graphene, a proper design of the support substrate could allow the investigation of doping process by other techniques able to evaluate the Fermi energy of graphene, such as optical absorption in NIR-visible, electron paramagnetic resonance spectroscopy and angle resolved photoemission spectroscopy. Furthermore, the evolution of the electric properties of graphene subjected to this doping process are unexplored yet, whereas THz spectroscopy and electrical measurement could add this piece to the puzzle. Concerning the interaction with nanoparticles, optical absorption and electrical measurements would give useful information in this case too, the first one by providing an evaluation of graphene Fermi energy with no photoexcitation of CDs, and the second one by evaluating the actual photocurrent obtainable in graphene. In both cases, the investigation could take advantage from the spatial control of the sample morphology, attained for example by a patterned substrate (with both hydrophilic and hydrophobic surface regions) and by a controlled deposition of CDs (inkjet or spin coating are two possibilities). Furthermore, the interaction between CDs and graphene could also be investigated by considering different types of graphene and CDs. In the first case, reduced graphene oxide could be used in order to investigate the CDs-graphene composite in liquid phase. On the other hand, different kinds of CDs could be used. In fact, a different core structure and surface functionalization imply significant variation both in the intrinsic emission mechanism of CDs and, especially, in the interaction with the surrounding species.

BIBLIOGRAPHY

- [1] K. S. Novoselov, A. K. Geim, S. V. Morozov, D. Jiang, Y. Zhang, S. V. Dubonos, I. V. Grigorieva, *et al.*, “Electric field effect in atomically thin carbon films”, *Science*, **306** (5696), 666–669, 2004.
- [2] A. K. Geim and K. S. Novoselov, “The rise of graphene”, *Nat. Mater.*, **6** (3), 183–191, 2007.
- [3] F. Bonaccorso, Z. Sun, T. Hasan, and A. C. Ferrari, “Graphene photonics and optoelectronics”, *Nat. Photonics*, **4** (9), 611, 2010.
- [4] M. J. Allen, V. C. Tung, and R. B. Kaner, “Honeycomb carbon: A review of graphene”, *Chem. Rev.*, **110** (1), 132–145, 2009.
- [5] E. P. Randviir, D. A. Brownson, and C. E. Banks, “A decade of graphene research: Production, applications and outlook”, *Mater. Today*, **17** (9), 426–432, 2014.
- [6] S.-B. Kim, J.-Y. Park, C.-S. Kim, K. Okuyama, S.-E. Lee, H.-D. Jang, and T.-O. Kim, “Effects of graphene in dye-sensitized solar cells based on nitrogen-doped TiO₂ composite”, *J. Phys. Chem. C*, **119** (29), 16552–16559, 2015.
- [7] F. Schwierz, “Graphene transistors”, *Nat. Nanotechnol.*, **5** (7), 487–496, 2010.
- [8] S. Bae, H. Kim, Y. Lee, X. Xu, J.-S. Park, Y. Zheng, J. Balakrishnan, T. Lei, H. R. Kim, Y. I. Song, *et al.*, “Roll-to-roll production of 30-inch graphene films for transparent electrodes”, *Nat. Nanotechnol.*, **5** (8), 574, 2010.
- [9] K. Patel and P. K. Tyagi, “P-type multilayer graphene as a highly efficient transparent conducting electrode in silicon heterojunction solar cells”, *Carbon*, **116**, 744–752, 2017.
- [10] F. Giannazzo, G. Greco, F. Roccaforte, and S. Sonde, “Vertical transistors based on 2d materials: Status and prospects”, *Crystals*, **8** (2), 70, 2018.
- [11] F. Giannazzo, G. Fisichella, G. Greco, A. La Magna, F. Roccaforte, B. Pécz, *et al.*, “Graphene integration with nitride semiconductors for high power and high frequency electronics”, *Phys. Status Solidi (A)*, **214** (4), 2017.
- [12] A. Zubair, A. Nourbakhsh, J.-Y. Hong, M. Qi, Y. Song, D. Jena, *et al.*, “Hot electron transistor with van der Waals base-collector heterojunction and high-performance GaN emitter”, *Nano Lett.*, **17** (5), 3089–3096, 2017.
- [13] C. Mannequin, A. Delamoreanu, L. Latu-Romain, V. Jousseau, H. Grampeix, S. David, C. Rabot, A. Zenasni, C. Vallee, and P. Gonon, “Graphene-HfO₂-based resistive ram memories”, *Microelectron. Eng.*, **161**, 82–86, 2016.
- [14] E. Fitzer, K.-H. Kochling, H. P. Boehm, and H. Marsh, “Recommended terminology for the description of carbon as a solid (IUPAC Recommendations 1995)”, *Pure Appl. Chem.*, **67** (3), 473–506, 1995.
- [15] J. Jeevanandam, A. Barhoum, Y. S. Chan, A. Dufresne, and M. K. Danquah, “Review on nanoparticles and nanostructured materials: History, sources, toxicity and regulations”, *Beilstein J. Nanotechnol.*, **9** (1), 1050–1074, 2018.
- [16] V. Pokropivny and V. Skorokhod, “Classification of nanostructures by dimensionality and concept of surface forms engineering in nanomaterial science”, *Mater. Sci. Eng. C*, **27** (5-8), 990–993, 2007.
- [17] N. Kumar and S. Kumbhat, *Carbon-Based Nanomaterials*, 1st ed. John Wiley and Sons, 2016.

- [18] S. Nasir, M. Hussein, Z. Zainal, and N. Yusof, “Carbon-based nanomaterials/allotropes: A glimpse of their synthesis, properties and some applications”, *Materials*, **11** (2), 295, 2018.
- [19] E. Roduner, “Size matters: Why nanomaterials are different”, *Chem. Soc. Rev.*, **35** (7), 583–592, 2006.
- [20] N. R. Pace, “The universal nature of biochemistry”, *Proc. Natl. Acad. Sci. USA*, **98** (3), 805–808, 2001.
- [21] E. A. Belenkov and V. A. Greshnyakov, “Classification schemes for carbon phases and nanostructures”, *New Carbon Mater.*, **28** (4), 273–282, 2013.
- [22] R. Heimann, S. Evsyukov, and Y Koga, “Carbon allotropes: A suggested classification scheme based on valence orbital hybridization”, *Carbon*, **35** (10-11), 1654–1658, 1997.
- [23] M. Grundmann, *Physics of Semiconductors*, 1st ed. Springer International Publishing, 2006.
- [24] T. W. G. Solomons and C. B. Fryhle, *Organic Chemistry*, 10th ed. John Wiley and Sons, 2009.
- [25] B. H. Bransden and C. J. Joachain, *Physics of Atoms and Molecules*, 2nd ed. Pearson Education, 2003.
- [26] J Poater, M Duran, and M Sola, “Analysis of electronic delocalization in buckminsterfullerene (C₆₀)”, *Int. J. Quantum Chem.*, **98** (4), 361–366, 2004.
- [27] I. A. Popov, K. V. Bozhenko, and A. I. Boldyrev, “Is graphene aromatic?”, *Nano Res.*, **5** (2), 117–123, 2012.
- [28] J. Kroes, A Fasolino, and M. Katsnelson, “Density functional based simulations of proton permeation of graphene and hexagonal boron nitride”, *Phys. Chem. Chem. Phys.*, **19** (8), 5813–5817, 2017.
- [29] B. Bhushan, *Springer handbook of nanotechnology*. Springer, 2017, ch. 3.
- [30] E. Kogan and V. Nazarov, “Symmetry classification of energy bands in graphene”, *Phys. Rev. B*, **85** (11), 115418, 2012.
- [31] W. van Haeringen and H. G. Junginger, “Symmetry classification of energy bands in graphene”, *Sol. Stat. Commun.*, **7**, 1723–1725, 1996.
- [32] P. R. Wallace, “The band theory of graphite”, *Phys. Rev.*, **71** (9), 622, 1947.
- [33] R. Saito, G. Dresselhaus, and M. Dresselhaus, *Physical properties of carbon nanotubes*. World scientific, 1998.
- [34] A. H. Castro Neto, F Guinea, N. M. R. Peres, K. S. Novoselov, and A. K. Geim, “The electronic properties of graphene”, *Mod. Phys.*, **81**, 109, 2009.
- [35] C. Kittel, *Introduction to Solid State Physics*. Wiley, 2004.
- [36] Y.-J. Yu, Y. Zhao, S. Ryu, L. E. Brus, K. S. Kim, and P. Kim, “Tuning the graphene work function by electric field effect”, *Nano Lett.*, **9** (10), 3430–3434, 2009.
- [37] C. N. R. Rao and A. K. Sood, *Graphene: synthesis, properties, and phenomena*. John Wiley & Sons, 2013.
- [38] K. S. Novoselov, A. Geim, S. V. Morozov, D. Jiang, M. I. Katsnelson, I. V. Grigorieva, S. V. Dubonos, and F. A. A., “Two-dimensional gas of massless dirac fermions in graphene”, *Nature*, **438** (7065), 197, 2005.
- [39] S. J. Blundell and K. M. Blundell, *Concepts in thermal physics*. Oxford University Press, 2006.
- [40] C. Bena and S. A. Kivelson, “Quasiparticle scattering and local density of states in graphite”, *Phys. Rev. B*, **72** (12), 125432, 2005.
- [41] K. F. Mak, L. Ju, F. Wang, and T. F. Heinz, “Optical spectroscopy of graphene: From the far infrared to the ultraviolet”, *Solid State Commun.*, **152** (15), 1341–1349, 2012.

- [42] T. Ando, Y. Zheng, and H. Suzuura, “Dynamical conductivity and zero-mode anomaly in honeycomb lattices”, *J. Phys. Soc. Jpn.*, **71** (5), 1318–1324, 2002.
- [43] R. R. Nair, P. Blake, A. N. Grigorenko, K. S. Novoselov, T. J. Booth, T. Stauber, N. M. R. Peres, and A. K. Geim, “Fine structure constant defines visual transparency of graphene”, *Science*, **320** (5881), 1308–1308, 2008.
- [44] J. Kim, S. C. Lim, S. J. Chae, I. Maeng, Y. Choi, S. Cha, Y. H. Lee, and H. Choi, “Ultrafast zero balance of the oscillator-strength sum rule in graphene”, *Sci. Rep.*, **3**, 2663, 2013.
- [45] J. Horng, C.-F. Chen, B. Geng, C. Girit, Y. Zhang, Z. Hao, H. A. Bechtel, M. Martin, A. Zettl, M. F. Crommie, et al., “Drude conductivity of dirac fermions in graphene”, *Phys. Rev. B*, **83** (16), 165113, 2011.
- [46] S. Adhikari, D. J. Perello, C. Biswas, A. Ghosh, N. Van Luan, J. Park, F. Yao, S. V. Rotkin, and Y. H. Lee, “Determining the fermi level by absorption quenching of monolayer graphene by charge transfer doping”, *Nanoscale*, **8** (44), 18710–18717, 2016.
- [47] L. Ju, B. Geng, J. Horng, C. Girit, M. Martin, Z. Hao, H. A. Bechtel, X. Liang, A. Zettl, Y. R. Shen, et al., “Graphene plasmonics for tunable terahertz metamaterials”, *Nat. Nanotechnol.*, **6** (10), 630, 2011.
- [48] Y. Yang, G. Kolesov, L. Kocia, and E. J. Heller, “Reassessing graphene absorption and emission spectroscopy”, *Nano Lett.*, **17** (10), 6077–6082, 2017.
- [49] A. Jorio, M. Dresselhaus, R. Saito, and G. F. Dresselhaus, *Raman spectroscopy in graphene related systems*, 1st ed. John Wiley & Sons, 2010.
- [50] P. Avouris, T. F. Heinz, and T. Low, *2D Materials: Properties and Devices*. Cambridge University Press, 2017.
- [51] P. Venezuela, M. Lazzeri, and F. Mauri, “Theory of double-resonant Raman spectra in graphene: Intensity and line shape of defect-induced and two-phonon bands”, *Phys. Rev. B*, **84** (3), 035433, 2011.
- [52] W. Diery, E. A. Moujaes, and R. Nunes, “Nature of localized phonon modes of tilt grain boundaries in graphene”, *Carbon*, **140**, 250–258, 2018.
- [53] M. Lazzeri and F. Mauri, “Nonadiabatic kohn anomaly in a doped graphene monolayer”, *Phys. Rev. Lett.*, **97** (26), 266407, 2006.
- [54] S. Piscanec, M. Lazzeri, F. Mauri, A. C. Ferrari, and J. Robertson, “Kohn anomalies and electron-phonon interactions in graphite”, *Phys. Rev. Lett.*, **93** (18), 185503, 2004.
- [55] I. Milošević, N. Kepčija, E. Dobardžić, M. Damnjanović, M. Mohr, J. Maultzsch, and C. Thomsen, “Kohn anomaly in graphene”, *Mater. Sci. Eng. B*, **176** (6), 510–511, 2011.
- [56] A. C. Ferrari and D. M. Basko, “Raman spectroscopy as a versatile tool for studying the properties of graphene”, *Nat. Nanotechnol.*, **8** (4), 235, 2013.
- [57] D. L. Mafra, G. Samsonidze, L. M. Malard, D. C. Elias, J. C. Brant, F. Plentz, E. S. Alves, and M. A. Pimenta, “Determination of LA and TO phonon dispersion relations of graphene near the dirac point by double resonance Raman scattering”, *Phys. Rev. B*, **76** (23), 233407, 2007.
- [58] S. D. Costa, A. Righi, C. Fantini, Y. Hao, C. Magnuson, L. Colombo, R. S. Ruoff, and M. A. Pimenta, “Resonant Raman spectroscopy of graphene grown on copper substrates”, *Solid State Commun.*, **152** (15), 1317–1320, 2012.
- [59] A. A. Balandin, S. Ghosh, W. Bao, I. Calizo, D. Teweldebrhan, F. Miao, and C. N. Lau, “Superior thermal conductivity of single-layer graphene”, *Nano Lett.*, **8** (3), 902–907, 2008.

- [60] H. Malekpour and A. A. Balandin, “Raman-based technique for measuring thermal conductivity of graphene and related materials”, *Journal of Raman Spectroscopy*, **49** (1), 106–120, 2018.
- [61] J. Judek, A. P. Gertych, M. Świniarski, A. Łapińska, A. Dużyńska, and M. Zdrojek, “High accuracy determination of the thermal properties of supported 2d materials”, *Scientific reports*, **5**, 12422, 2015.
- [62] W. Cai, A. L. Moore, Y. Zhu, X. Li, S. Chen, L. Shi, and R. S. Ruoff, “Thermal transport in suspended and supported monolayer graphene grown by chemical vapor deposition”, *Nano Lett.*, **10** (5), 1645–1651, 2010.
- [63] S. Chen, A. L. Moore, W. Cai, J. W. Suk, J. An, C. Mishra, C. Amos, C. W. Magnuson, J. Kang, L. Shi, et al., “Raman measurements of thermal transport in suspended monolayer graphene of variable sizes in vacuum and gaseous environments”, *ACS nano*, **5** (1), 321–328, 2010.
- [64] J. H. Seol, I. Jo, A. L. Moore, L. Lindsay, Z. H. Aitken, M. T. Pettes, X. Li, Z. Yao, R. Huang, D. Broido, et al., “Two-dimensional phonon transport in supported graphene”, *Science*, **328** (5975), 213–216, 2010.
- [65] Z. H. Ni, H. M. Wang, J. Kasim, H. M. Fan, T. Yu, Y. H. Wu, Y. P. Feng, and Z. X. Shen, “Graphene thickness determination using reflection and contrast spectroscopy”, *Nano Lett.*, **7** (9), 2758–2763, 2007.
- [66] M. Bayle, N. Reckinger, A. Felten, P. Landois, O. Lancry, B. Dutertre, J.-F. Colomer, A.-A. Zahab, L. Henrard, J.-L. Sauvajol, et al., “Determining the number of layers in few-layer graphene by combining Raman spectroscopy and optical contrast”, *J. Raman Spectrosc.*, **49** (1), 36–45, 2018.
- [67] L. M. Malard, M. H. D. Guimaraes, D. L. Mafrá, A. Jorio, et al., “Group-theory analysis of electrons and phonons in n-layer graphene systems”, *Phys. Rev. B*, **79** (12), 125426, 2009.
- [68] M. Begliarbekov, O. Sul, S. Kalliakos, E.-H. Yang, and S. Strauf, “Determination of edge purity in bilayer graphene using micro-Raman spectroscopy”, *Appl. Phys. Lett.*, **97** (3), 031908, 2010.
- [69] M. S. Dresselhaus, A. Jorio, and R. Saito, “Characterizing graphene, graphite, and carbon nanotubes by Raman spectroscopy”, *Annu. Rev. Condens. Matter Phys.*, **1** (1), 89–108, 2010.
- [70] L. M. Malard, M. A. A. Pimenta, G. Dresselhaus, and M. S. Dresselhaus, “Raman spectroscopy in graphene”, *Phys. Rep.*, **473** (5-6), 51–87, 2009.
- [71] Z. Ni, Y. Wang, T. Yu, Y. You, and Z. Shen, “Reduction of fermi velocity in folded graphene observed by resonance Raman spectroscopy”, *Phys. Rev. B*, **77** (23), 235403, 2008.
- [72] F. Mehmood, R. Pachter, W. Lu, and J. J. Boeckl, “Adsorption and diffusion of oxygen on single-layer graphene with topological defects”, *J. Phys. Chem. C*, **117** (20), 10366–10374, 2013.
- [73] Q. Yu, L. A. Jauregui, W. Wu, R. Colby, J. Tian, Z. Su, H. Cao, Z. Liu, D. Pandey, D. Wei, et al., “Control and characterization of individual grains and grain boundaries in graphene grown by chemical vapour deposition”, *Nat. Mater.*, **10** (6), 443, 2011.
- [74] M. A. Bissett, W. Izumida, R. Saito, and H. Ago, “Effect of domain boundaries on the Raman spectra of mechanically strained graphene”, *ACS Nano*, **6** (11), 10229–10238, 2012.
- [75] L. Zhang and Z. Xia, “Mechanisms of oxygen reduction reaction on nitrogen-doped graphene for fuel cells”, *J. Phys. Chem. C*, **115** (22), 11170–11176, 2011.
- [76] L. Qu, Y. Liu, J.-B. Baek, and L. Dai, “Nitrogen-doped graphene as efficient metal-free electrocatalyst for oxygen reduction in fuel cells”, *ACS Nano*, **4** (3), 1321–1326, 2010.

- [77] J. T. Robinson, J. S. Burgess, C. E. Junkermeier, S. C. Badescu, T. L. Reinecke, F. K. Perkins, M. K. Zalutdniov, J. W. Baldwin, J. C. Culbertson, P. E. Sheehan, et al., "Properties of fluorinated graphene films", *Nano Lett.*, **10** (8), 3001–3005, 2010.
- [78] H. Liu, Z. Hou, C. Hu, Y. Yang, and Z. Zhu, "Electronic and magnetic properties of fluorinated graphene with different coverage of fluorine", *J. Phys. Chem. C*, **116** (34), 18193–18201, 2012.
- [79] F. Banhart, J. Kotakoski, and A. V. Krasheninnikov, "Structural defects in graphene", *ACS Nano*, **5** (1), 26–41, 2010.
- [80] U. I. Kramm, I. Herrmann-Geppert, J. Behrends, K. Lips, S. Fiechter, and P. Bogdanoff, "On an easy way to prepare metal–nitrogen doped carbon with exclusive presence of MeN₄-type sites active for the orr", *J. Am. Chem. Soc.*, **138** (2), 635–640, 2016.
- [81] M. D. Bhatt, G. Lee, and J. S. Lee, "Density functional theory (DFT) calculations for oxygen reduction reaction mechanisms on metal-, nitrogen-co-doped graphene (M–N₂-g (m = Ti, Cu, Mo, Nb and Ru)) electrocatalysts", *Electrochim. Acta*, **228**, 619–627, 2017.
- [82] M. D. Esrafil, N. Saeidi, and L. Dinparast, "Epoxidation of ethylene over Pt⁺, Pd⁺ and Ni⁺ doped graphene in the presence of N₂O as an oxidant: A comparative DFT study", *New J. Chem.*, **41** (18), 9815–9825, 2017.
- [83] L. Yu, X. Pan, X. Cao, P. Hu, and X. Bao, "Oxygen reduction reaction mechanism on nitrogen-doped graphene: A density functional theory study", *J. Catal.*, **282** (1), 183–190, 2011.
- [84] M. Kaukonen, A. V. Krasheninnikov, E. Kauppinen, and R. M. Nieminen, "Doped graphene as a material for oxygen reduction reaction in hydrogen fuel cells: A computational study", *ACS Catal.*, **3** (2), 159–165, 2013.
- [85] D. Chen, H. Feng, and J. Li, "Graphene oxide: Preparation, functionalization, and electrochemical applications", *Chem. Rev.*, **112** (11), 6027–6053, 2012.
- [86] H. He, J. Klinowski, M. Forster, and A. Lerf, "A new structural model for graphite oxide", *Chem. Phys. Lett.*, **287** (1-2), 53–56, 1998.
- [87] M. M. Lucchese, F. Stavale, E. H. M. Ferreira, C. Vilani, M. V. O. Moutinho, R. B. Capaz, C. A. Achete, and A. Jorio, "Quantifying ion-induced defects and Raman relaxation length in graphene", *Carbon*, **48** (5), 1592–1597, 2010.
- [88] L. G. Cançado, A. Jorio, E. M. Ferreira, F. Stavale, C. A. Achete, R. B. Capaz, M. V. O. Moutinho, A. Lombardo, T. Kulmala, and A. C. Ferrari, "Quantifying defects in graphene via Raman spectroscopy at different excitation energies", *Nano Lett.*, **11** (8), 3190–3196, 2011.
- [89] G. Froehlicher and S. Berciaud, "Raman spectroscopy of electrochemically gated graphene transistors: Geometrical capacitance, electron-phonon, electron-electron, and electron-defect scattering", *Phys. Rev. B*, **91** (20), 205413, 2015.
- [90] A. Eckmann, A. Felten, A. Mishchenko, L. Britnell, R. Krupke, K. S. Novoselov, and C. Casiraghi, "Probing the nature of defects in graphene by Raman spectroscopy", *Nano Lett.*, **12** (8), 3925–3930, 2012.
- [91] Y. You, Z. Ni, T. Yu, and Z. Shen, "Edge chirality determination of graphene by Raman spectroscopy", *Appl. Phys. Lett.*, **93** (16), 163112, 2008.
- [92] C. Casiraghi, A. Hartschuh, H. Qian, S. Piscanec, C. Georgi, A. Fasoli, K. Novoselov, D. Basko, and A. Ferrari, "Raman spectroscopy of graphene edges", *Nano Lett.*, **9** (4), 1433–1441, 2009.
- [93] J. Jiang, R. Pachter, F. Mehmood, A. E. Islam, B. Maruyama, and J. J. Boeckl, "A Raman spectroscopy signature for characterizing defective single-layer graphene: Defect-induced i (D)/i(D') intensity ratio by theoretical analysis", *Carbon*, **90**, 53–62, 2015.

- [94] T. M. G. Mohiuddin, A. Lombardo, R. R. Nair, A. Bonetti, G. Savini, R. Jalil, N. Bonini, D. M. Basko, C. Galiotis, N. Marzari, et al., “Uniaxial strain in graphene by Raman spectroscopy: G peak splitting, Grüneisen parameters, and sample orientation”, *Phys. Rev. B*, **79** (20), 205433, 2009.
- [95] C. Androulidakis, G Tsoukleri, N Koutroumanis, G Gkikas, P Pappas, J Parthenios, K Papagelis, and C Galiotis, “Experimentally derived axial stress–strain relations for two-dimensional materials such as monolayer graphene”, *Carbon*, **81**, 322–328, 2015.
- [96] A. Das, S. Pisana, B. Chakraborty, S. Piscanec, S. K. Saha, U. V. Waghmare, K. S. Novoselov, H. R. Krishnamurthy, A. K. Geim, A. C. Ferrari, et al., “Monitoring dopants by Raman scattering in an electrochemically top-gated graphene transistor”, *Nat. Nanotechnol.*, **3** (4), 210, 2008.
- [97] D. Yoon, H. Moon, Y.-W. Son, J. S. Choi, B. H. Park, Y. H. Cha, Y. D. Kim, and H. Cheong, “Interference effect on Raman spectrum of graphene on SiO₂/Si”, *Phys. Rev. B*, **80** (12), 125422, 2009.
- [98] J.-B. Wu, M.-L. Lin, X. Cong, H.-N. Liu, and P.-H. Tan, “Raman spectroscopy of graphene-based materials and its applications in related devices”, *Chem. Soc. Rev.*, **47** (5), 1822–1873, 2018.
- [99] R. H. Miwa, T. M. Schmidt, W. L. Scopel, and A. Fazzio, “Doping of graphene adsorbed on the a-SiO₂ surface”, *Appl. Phys. Lett.*, **99** (16), 163108, 2011.
- [100] X. F. Fan, W. T. Zheng, V. Chihai, Z. X. Shen, and J.-L. Kuo, “Interaction between graphene and the surface of SiO₂”, *J. Phys.: Condens. Matter*, **24** (30), 305004, 2012.
- [101] W. Gao, P. Xiao, G. Henkelman, K. M. Liechti, and R. Huang, “Interfacial adhesion between graphene and silicon dioxide by density functional theory with van der Waals corrections”, *J. Phys. D: Appl. Phys.*, **47** (25), 255301, 2014.
- [102] J. E. Lee, G. Ahn, J. Shim, Y. S. Lee, and S. Ryu, “Optical separation of mechanical strain from charge doping in graphene”, *Nat. Commun.*, **3**, 1024, 2012.
- [103] G. Ahn, H. R. Kim, T. Y. Ko, K. Choi, K. Watanabe, T. Taniguchi, B. H. Hong, and S. Ryu, “Optical probing of the electronic interaction between graphene and hexagonal boron nitride”, *ACS Nano*, **7** (2), 1533–1541, 2013.
- [104] F. Liang, H. Xu, X. Wu, C. Wang, C. Luo, and J. Zhang, “Raman spectroscopy characterization of two-dimensional materials”, *Chin. Phys. B*, **27** (3), 037802, 2018.
- [105] H Aoki and M. S. Dresselhaus, *Physics of graphene*. Springer Science & Business Media, 2013.
- [106] J.-H. Chen, C. Jang, S. Adam, M. S. Fuhrer, E. D. Williams, and M. Ishigami, “Charged-impurity scattering in graphene”, *Nat. Phys.*, **4** (5), 377, 2008.
- [107] S. Chen, A. L. Moore, W. Cai, J. W. Suk, J. An, C. Mishra, C. Amos, C. W. Magnuson, J. Kang, L. Shi, et al., “Raman measurements of thermal transport in suspended monolayer graphene of variable sizes in vacuum and gaseous environments”, *ACS Nano*, **5** (1), 321–328, 2010.
- [108] Y. Wang, N. Xu, D. Li, and J. Zhu, “Thermal properties of two dimensional layered materials”, *Adv. Funct. Mater.*, **27** (19), 1604134, 2017.
- [109] W. Cai, A. L. Moore, Y. Zhu, X. Li, S. Chen, L. Shi, and R. S. Ruoff, “Thermal transport in suspended and supported monolayer graphene grown by chemical vapor deposition”, *Nano Lett.*, **10** (5), 1645–1651, 2010.
- [110] M. M. Sadeghi, M. T. Pettes, and L. Shi, “Thermal transport in graphene”, *Solid State Commun.*, **152** (15), 1321–1330, 2012.
- [111] H. C. Lee, W.-W. Liu, S.-P. Chai, A. R. Mohamed, A. Aziz, C.-S. Khe, N. M. Hidayah, and U Hashim, “Review of the synthesis, transfer, characterization and growth mechanisms of single and multi-layer graphene”, *RSC Adv.*, **7** (26), 15644–15693, 2017.

- [112] M. Coroş, F. Pogăcean, L. Măgeruşan, C. Socaci, and S. Pruneanu, “A brief overview on synthesis and applications of graphene and graphene-based nanomaterials”, *Frontiers of Materials Science*, **13** (1), 23–32, 2019.
- [113] V. Nicolosi, M. Chhowalla, M. G. Kanatzidis, M. S. Strano, and J. N. Coleman, “Liquid exfoliation of layered materials”, *Science*, **340** (6139), 1226419, 2013.
- [114] A. Hadi, J. Zahirifar, J. Karimi-Sabet, and A. Dastbaz, “Graphene nanosheets preparation using magnetic nanoparticle assisted liquid phase exfoliation of graphite: The coupled effect of ultrasound and wedging nanoparticles”, *Ultrason. Sonochem.*, **44**, 204–214, 2018.
- [115] W. S. Hummers Jr and R. E. Offeman, “Preparation of graphitic oxide”, *J. Am. Chem. Soc.*, **80** (6), 1339–1339, 1958.
- [116] L. Tang, X. Li, R. Ji, K. S. Teng, G. Tai, J. Ye, C. Wei, and S. P. Lau, “Bottom-up synthesis of large-scale graphene oxide nanosheets”, *J. Mater. Chem.*, **22** (12), 5676–5683, 2012.
- [117] Z. Yao, H. Nie, Z. Yang, X. Zhou, Z. Liu, and S. Huang, “Catalyst-free synthesis of iodine-doped graphene via a facile thermal annealing process and its use for electrocatalytic oxygen reduction in an alkaline medium”, *Chem. Commun.*, **48** (7), 1027–1029, 2012.
- [118] S. J. Wang, Y. Geng, Q. Zheng, and J.-K. Kim, “Fabrication of highly conducting and transparent graphene films”, *Carbon*, **48** (6), 1815–1823, 2010.
- [119] C. Mattevi, H. Kim, and M. Chhowalla, “A review of chemical vapour deposition of graphene on copper”, *J. Mater. Chem.*, **21** (10), 3324–3334, 2011.
- [120] J. Zhao, M. Shaygan, J. Eckert, M. Meyyappan, and M. H. Rummeli, “A growth mechanism for free-standing vertical graphene”, *Nano Lett.*, **14** (6), 3064–3071, 2014.
- [121] G. Sahoo, S. Ghosh, S. Polaki, T. Mathews, and M. Kamruddin, “Scalable transfer of vertical graphene nanosheets for flexible supercapacitor applications”, *Nanotechnology*, **28** (41), 415702, 2017.
- [122] H. Wang, E. Gao, P. Liu, D. Zhou, D. Geng, X. Xue, L. Wang, K. Jiang, Z. Xu, and G. Yu, “Facile growth of vertically-aligned graphene nanosheets via thermal CVD: The experimental and theoretical investigations”, *Carbon*, **121**, 1–9, 2017.
- [123] H. Wang, T. Maiyalagan, and X. Wang, “Review on recent progress in nitrogen-doped graphene: Synthesis, characterization, and its potential applications”, *ACS Catal.*, **2** (5), 781–794, 2012.
- [124] J. Prekodravac, Z. Marković, S. Jovanović, M. Budimir, D. Peruško, I. Holclajtner-Antunović, V. Pavlović, Z. Syrgiannis, A. Bonasera, and B. Todorović-Marković, “The effect of annealing temperature and time on synthesis of graphene thin films by rapid thermal annealing”, *Synth. Met.*, **209**, 461–467, 2015.
- [125] D. K. Singh, P. K. Iyer, and P. K. Giri, “Improved chemical synthesis of graphene using a safer solvothermal route”, *Int. J. Nanosci.*, **10** (01N02), 39–42, 2011.
- [126] M. Choucair, P. Thordarson, and J. A. Stride, “Gram-scale production of graphene based on solvothermal synthesis and sonication”, *Nat. Nanotechnol.*, **4** (1), 30, 2009.
- [127] D. Deng, X. Pan, L. Yu, Y. Cui, Y. Jiang, J. Qi, W.-X. Li, Q. Fu, X. Ma, Q. Xue, et al., “Toward N-doped graphene via solvothermal synthesis”, *Chem. Mater.*, **23** (5), 1188–1193, 2011.
- [128] N. Mishra, J. Boeckl, N. Motta, and F. Iacopi, “Graphene growth on silicon carbide: A review”, *physica status solidi (a)*, **213** (9), 2277–2289, 2016.
- [129] C. Berger, Z. Song, X. Li, X. Wu, N. Brown, C. Naud, D. Mayou, T. Li, J. Hass, A. N. Marchenkov, et al., “Electronic confinement and coherence in patterned epitaxial graphene”, *Science*, **312** (5777), 1191–1196, 2006.

- [130] C. Virojanadara, M. Syväjarvi, R. Yakimova, L. Johansson, A. Zakharov, and T. Balasubramanian, "Homogeneous large-area graphene layer growth on 6h-sic (0001)", *Physical Review B*, **78** (24), 245403, 2008.
- [131] K. V. Emtsev, A. Bostwick, K. Horn, J. Jobst, G. L. Kellogg, L. Ley, J. L. McChesney, T. Ohta, S. A. Reshanov, J. Röhrl, et al., "Towards wafer-size graphene layers by atmospheric pressure graphitization of silicon carbide", *Nature materials*, **8** (3), 203, 2009.
- [132] I. Chorkendorff and J. W. Niemantsverdriet, *Concepts of Modern Catalysis and Kinetics*, 1st ed. Wiley-VCH, 2003.
- [133] K. W. Kolasinski, *Surface science: foundations of catalysis and nanoscience*. John Wiley & Sons, 2012.
- [134] D. M. Ruthven, *Principles of adsorption and adsorption processes*. John Wiley & Sons, 1984.
- [135] K. Lingmei, E. Axel, S. R. Talat, and A. D. Peter, "Molecular adsorption on graphene", *J Phys Condens Matter*, **26**, 443001, 2014.
- [136] S. Osella, M. Kiliszek, E. Harputlu, C. G. Unlu, K. Ocakoglu, J. Kargul, and B. Trzaskowski, "Controlling the charge transfer flow at the graphene/pyrene-nitrilotriacetic acid interface", *J. Mater. Chem. C*, **6** (18), 5046–5054, 2018.
- [137] P. K. Srivastava, P. Yadav, V. Rani, and S. Ghosh, "Controlled doping in graphene monolayers by trapping organic molecules at the graphene-substrate interface", *ACS Appl. Mater. Interfaces*, **9** (6), 5375–5381, 2017.
- [138] E. Papirer, *Adsorption on silica surfaces*. CRC Press, 2000, vol. 90.
- [139] D. B. Asay and S. H. Kim, "Evolution of the adsorbed water layer structure on silicon oxide at room temperature", *J. Phys. Chem. B*, **109** (35), 16760–16763, 2005.
- [140] S. B. Cho, S. Lee, and Y.-C. Chung, "Water trapping at the graphene/ Al_2O_3 interface", *Japanese Journal of Applied Physics*, **52** (6S), 06–09, 2013.
- [141] A. M. Schrader, J. I. Monroe, R. Sheil, H. A. Dobbs, T. J. Keller, Y. Li, S. Jain, M. S. Shell, J. N. Israelachvili, and S. Han, "Surface chemical heterogeneity modulates silica surface hydration", *Proc. Natl. Acad. Sci. USA*, **115** (12), 2890–2895, 2018.
- [142] K. Nagashio, T. Yamashita, T. Nishimura, K. Kita, and A. Toriumi, "Electrical transport properties of graphene on SiO_2 with specific surface structures", *J. Appl. Phys.*, **110** (2), 024513, 2011.
- [143] M. Lafkioti, B. Krauss, T. Lohmann, U. Zschieschang, H. Klauk, K. v. Klitzing, and J. H. Smet, "Graphene on a hydrophobic substrate: Doping reduction and hysteresis suppression under ambient conditions", *Nano Lett.*, **10** (4), 1149–1153, 2010.
- [144] J. Pezoldt, C. Hummel, and F. Schwierz, "Graphene field effect transistor improvement by graphene-silicon dioxide interface modification", *Physica E*, **44** (6), 985–988, 2012.
- [145] F. Schedin, A. K. Geim, S. V. Morozov, E. W. Hill, P. Blake, M. I. Katsnelson, and K. S. Novoselov, "Detection of individual gas molecules adsorbed on graphene", *Nat. Mater.*, **6** (9), 652, 2007.
- [146] Z. H. Ni, H. M. Wang, Z. Q. Luo, Y. Y. Wang, T. Yu, Y. H. Wu, and Z. X. Shen, "The effect of vacuum annealing on graphene", *J. Raman Spectrosc.*, **41** (5), 479–483, 2010.
- [147] S. Ryu, L. Liu, S. Berciaud, Y.-J. Yu, H. Liu, P. Kim, G. W. Flynn, and L. E. Brus, "Atmospheric oxygen binding and hole doping in deformed graphene on a SiO_2 substrate", *Nano Lett.*, **10** (12), 4944–4951, 2010.
- [148] Y. Yang and R. Murali, "Binding mechanisms of molecular oxygen and moisture to graphene", *Appl. Phys. Lett.*, **98** (9), 093116, 2011.

- [149] A. Piazza, F. Giannazzo, G. Buscarino, G. Fisichella, A. La Magna, F. Roccaforte, M. Cannas, F. M. Gelardi, B. Pignataro, M. Scopelliti, and S. Agnello, "Substrate and atmosphere influence on oxygen p-doped graphene", *Carbon*, **107**, 696–704, 2016.
- [150] A. Piazza, F. Giannazzo, G. Buscarino, G. Fisichella, A. La Magna, F. Roccaforte, M. Cannas, F. M. Gelardi, and S. Agnello, "Effect of air on oxygen p-doped graphene on SiO₂", *Phys. Status Solidi (A)*, **213** (9), 2341–2344, 2016.
- [151] A. Piazza, F. Giannazzo, G. Buscarino, G. Fisichella, A. La Magna, F. Roccaforte, M. Cannas, F. M. Gelardi, and S. Agnello, "Graphene p-type doping and stability by thermal treatments in molecular oxygen controlled atmosphere", *J. Phys. Chem. C*, **119** (39), 22718–22723, 2015.
- [152] Y. Yamada, K. Murota, R. Fujita, J. Kim, A. Watanabe, M. Nakamura, S. Sato, K. Hata, P. Ercius, J. Ciston, et al., "Subnanometer vacancy defects introduced on graphene by oxygen gas", *J. Am. Chem. Soc.*, **136** (6), 2232–2235, 2014.
- [153] H. Y. Nan, Z. H. Ni, J. Wang, Z. Zafar, Z. X. Shi, and Y. Y. Wang, "The thermal stability of graphene in air investigated by Raman spectroscopy", *J. Raman Spectrosc.*, **44** (7), 1018–1021, 2013.
- [154] S. D. Costa, J. E. Weis, O. Frank, M. Fridrichová, and M. Kalbac, "Monitoring the doping of graphene on SiO₂/Si substrates during the thermal annealing process", *RSC Adv.*, **6** (76), 72859–72864, 2016.
- [155] D. Lee, G. Ahn, and S. Ryu, "Two-dimensional water diffusion at a graphene–silica interface", *J. Am. Chem. Soc.*, **136** (18), 6634–6642, 2014.
- [156] N. Tit, K. Said, N. M. Mahmoud, S. Kouser, and Z. H. Yamani, "Ab-initio investigation of adsorption of CO and CO₂ molecules on graphene: Role of intrinsic defects on gas sensing", *Appl. Surf. Sci.*, **394**, 219–230, 2017.
- [157] F. Mehmood, R. Pachter, W. Lu, and J. J. Boeckl, "Adsorption and diffusion of oxygen on single-layer graphene with topological defects", *J. Phys. Chem. C*, **117** (20), 10366–10374, 2013.
- [158] W. Wang, Y. Zhang, C. Shen, and Y. Chai, "Adsorption of CO molecules on doped graphene: A first-principles study", *AIP Adv.*, **6** (2), 025317, 2016.
- [159] S. Nandhini, A. Rajkamal, B. Saha, and R. Thapa, "First-principles identification of site dependent activity of graphene based electrocatalyst", *Molecular Catalysis*, **432**, 242–249, 2017.
- [160] K. P. Katin, V. S. Prudkovskiy, and M. M. Maslov, "Chemisorption of hydrogen atoms and hydroxyl groups on stretched graphene: A coupled QM/QM study", *Phys. Lett. A*, **381** (33), 2686–2690, 2017.
- [161] T. O. Wehling, A. I. Lichtenstein, and M. I. Katsnelson, "First-principles studies of water adsorption on graphene: The role of the substrate", *Appl. Phys. Lett.*, **93** (20), 202110, 2008.
- [162] J. Dai and J. Yuan, "Physisorption to chemisorption transition of NO₂ on graphene induced by the interplay of SiO₂ substrate and van der Waals forces: A first principles study", *Chem. Phys.*, **405**, 161–166, 2012.
- [163] H. Xu, Y. Chen, J. Zhang, and H. Zhang, "Investigating the mechanism of hysteresis effect in graphene electrical field device fabricated on SiO₂ substrates using Raman spectroscopy", *Small*, **8** (18), 2833–2840, 2012.
- [164] P. K. Srivastava, P. Yadav, V. Rani, and S. Ghosh, "Controlled doping in graphene monolayers by trapping organic molecules at the graphene–substrate interface", *ACS Appl. Mater. Interfaces*, **9** (6), 5375–5381, 2017.
- [165] J. Benson, Q. Xu, P. Wang, Y. Shen, L. Sun, T. Wang, M. Li, and P. Papakonstantinou, "Tuning the catalytic activity of graphene nanosheets for oxygen reduction reaction via size and thickness reduction", *ACS Appl. Mater. Interfaces*, **6** (22), 19726–19736, 2014.

- [166] M. Zhou, H.-L. Wang, and S. Guo, "Towards high-efficiency nanoelectrocatalysts for oxygen reduction through engineering advanced carbon nanomaterials", *Chem. Soc. Rev.*, **45** (5), 1273–1307, 2016.
- [167] C. R. Raj, A. Samanta, S. H. Noh, S. Mondal, T. Okajima, and T. Ohsaka, "Emerging new generation electrocatalysts for the oxygen reduction reaction", *J. Mater. Chem. A*, **4** (29), 11156–11178, 2016.
- [168] R. Lv, H. Wang, H. Yu, and F. Peng, "Controllable preparation of holey graphene and electrocatalytic performance for oxygen reduction reaction", *Electrochim. Acta*, **228**, 203–213, 2017.
- [169] C. Bautista-Flores, R. Y. Sato-Berrú, and D. Mendoza, "Doping graphene by chemical treatments using acid and basic substances", *Journal of Materials Science and Chemical Engineering*, **3** (10), 17–21, 2015.
- [170] M. Zhou, H.-L. Wang, and S. Guo, "Towards high-efficiency nanoelectrocatalysts for oxygen reduction through engineering advanced carbon nanomaterials", *Chem. Soc. Rev.*, **45** (5), 1273–1307, 2016.
- [171] L. Zheng, X. Cheng, Z. Wang, C. Xia, D. Cao, L. Shen, Q. Wang, Y. Yu, and D. Shen, "Reversible n-type doping of graphene by H₂O-based atomic-layer deposition and its doping mechanism", *J. Phys. Chem. C*, **119** (11), 5995–6000, 2015.
- [172] Y. G. Lee, C. G. Kang, C. Cho, Y. Kim, H. J. Hwang, and B. H. Lee, "Quantitative analysis of hysteretic reactions at the interface of graphene and SiO₂ using the short pulse i–v method", *Carbon*, **60**, 453–460, 2013.
- [173] U. Jung, Y. Gon Lee, C. Goo Kang, S. Lee, and B. Hun Lee, "Quantitative analysis of interfacial reactions at a graphene/SiO₂ interface using the discharge current analysis method", *Appl. Phys. Lett.*, **104** (15), 151604, 2014.
- [174] U. Jung, Y. G. Lee, C. G. Kang, S. Lee, J. J. Kim, H. J. Hwang, S. K. Lim, M.-H. Ham, and B. H. Lee, "Quantitatively estimating defects in graphene devices using discharge current analysis method", *Sci. Rep.*, **4**, 4886, 2014.
- [175] C. P. Bergmann and F. M. Machado, *Carbon nanomaterials as adsorbents for environmental and biological applications*. Springer, 2015.
- [176] L. Largette and R. Pasquier, "A review of the kinetics adsorption models and their application to the adsorption of lead by an activated carbon", *Chem. Eng. Res. Des.*, **109**, 495–504, 2016.
- [177] J. Low, S. Cao, J. Yu, and S. Wageh, "Two-dimensional layered composite photocatalysts", *Chem. Commun.*, **50** (74), 10768–10777, 2014.
- [178] K. S. Fernando, S. Sahu, Y. Liu, W. K. Lewis, E. A. Gulians, A. Jafariyan, P. Wang, C. E. Bunker, and Y.-P. Sun, "Carbon quantum dots and applications in photocatalytic energy conversion", *ACS Appl. Mater. Interfaces*, **7** (16), 8363–8376, 2015.
- [179] Z. De Liu, H. X. Zhao, and C. Z. Huang, "Obstruction of photoinduced electron transfer from excited porphyrin to graphene oxide: A fluorescence turn-on sensing platform for iron (III) ions", *PLoS One*, **7** (12), e50367, 2012.
- [180] P. Guarracino, T. Gatti, N. Canever, M. Abdu-Aguye, M. A. Loi, E. Menna, and L. Franco, "Probing photoinduced electron-transfer in graphene–dye hybrid materials for DSSC", *Phys. Chem. Chem. Phys.*, **19** (40), 27716–27724, 2017.
- [181] A. Raja, A. Montoya-Castillo, J. Zultak, X.-X. Zhang, Z. Ye, C. Roquelet, D. A. Chenet, A. M. Van Der Zande, P. Huang, S. Jockusch, et al., "Energy transfer from quantum dots to graphene and ZnO: The role of absorption and screening in two-dimensional materials", *Nano Lett.*, **16** (4), 2328–2333, 2016.

- [182] R. Beura and P Thangadurai, “Structural, optical and photocatalytic properties of graphene-ZnO nanocomposites for varied compositions”, *J. Phys. Chem. Solids*, **102**, 168–177, 2017.
- [183] X. Wu, L. Wen, K. Lv, K. Deng, D. Tang, H. Ye, D. Du, S. Liu, and M. Li, “Fabrication of ZnO/graphene flake-like photocatalyst with enhanced photoreactivity”, *Appl. Surf. Sci.*, **358**, 130–136, 2015.
- [184] J. Qin, X. Zhang, C. Yang, M. Cao, M. Ma, and R. Liu, “ZnO microspheres-reduced graphene oxide nanocomposite for photocatalytic degradation of methylene blue dye”, *Appl. Surf. Sci.*, **392**, 196–203, 2017.
- [185] X. Pan, Y. Zhao, S. Liu, C. L. Korzeniewski, S. Wang, and Z. Fan, “Comparing graphene-TiO₂ nanowire and graphene-TiO₂ nanoparticle composite photocatalysts”, *ACS Appl. Mater. Interfaces*, **4** (8), 3944–3950, 2012.
- [186] L.-L. Tan, W.-J. Ong, S.-P. Chai, and A. R. Mohamed, “Reduced graphene oxide-TiO₂ nanocomposite as a promising visible-light-active photocatalyst for the conversion of carbon dioxide”, *Nanoscale Res. Lett.*, **8** (1), 465, 2013.
- [187] X. Zeng, Z. Wang, N. Meng, D. T. McCarthy, A. Deletic, J.-h. Pan, and X. Zhang, “Highly dispersed TiO₂ nanocrystals and carbon dots on reduced graphene oxide: Ternary nanocomposites for accelerated photocatalytic water disinfection”, *Appl. Catal., B*, **202**, 33–41, 2017.
- [188] Q. Xiang, J. Yu, and M. Jaroniec, “Preparation and enhanced visible-light photocatalytic H₂-production activity of graphene/C₃N₄ composites”, *J. Phys. Chem. C*, **115** (15), 7355–7363, 2011.
- [189] C. A. Ubani, M. A. Ibrahim, M. A. M. Teridi, K. Sopian, J. Ali, and K. T. Chaudhary, “Application of graphene in dye and quantum dots sensitized solar cell”, *Sol. Energy*, **137**, 531–550, 2016.
- [190] A. Sciortino, A. Cannizzo, and F. Messina, “Carbon nanodots: A review—from the current understanding of the fundamental photophysics to the full control of the optical response”, *C*, **4** (4), 67, 2018.
- [191] A. Sciortino, N. Mauro, G. Buscarino, L. Sciortino, R. Popescu, R. Schneider, G. Giammona, D. Gerthsen, M. Cannas, and F. Messina, “β-C₃N₄ nanocrystals: Carbon dots with extraordinary morphological, structural, and optical homogeneity”, *Chem. Mater.*, **30** (5), 1695–1700, 2018.
- [192] F. Messina, L. Sciortino, R. Popescu, A. M. Venezia, A. Sciortino, G. Buscarino, S. Agnello, R. Schneider, D. Gerthsen, M. Cannas, et al., “Fluorescent nitrogen-rich carbon nanodots with an unexpected β-C₃N₄ nanocrystalline structure”, *J. Mater. Chem. C*, **4** (13), 2598–2605, 2016.
- [193] A. Sciortino, E. Marino, B. v. Dam, P. Schall, M. Cannas, and F. Messina, “Solvatochromism unravels the emission mechanism of carbon nanodots”, *J. Phys. Chem. Lett.*, **7** (17), 3419–3423, 2016.
- [194] C. Liu, B. Tang, S. Zhang, M. Zhou, M. Yang, Y. Liu, Z.-L. Zhang, B. Zhang, and D.-W. Pang, “Photoinduced electron transfer mediated by coordination between carboxyl on carbon nanodots and Cu²⁺ quenching photoluminescence”, *J. Phys. Chem. C*, **122** (6), 3662–3668, 2018.
- [195] J. Zong, X. Yang, A. Trinchì, S. Hardin, I. Cole, Y. Zhu, C. Li, T. Muster, and G. Wei, “Carbon dots as fluorescent probes for “off-on” detection of Cu²⁺ and L-cysteine in aqueous solution”, *Biosens. Bioelectron.*, **51**, 330–335, 2014.
- [196] S. Hu, Y. Wang, W. Zhang, Q. Chang, and J. Yang, “Multicolour emission states from charge transfer between carbon dots and surface molecules”, *Materials*, **10** (2), 165, 2017.
- [197] Y.-Q. Dang, S.-Z. Ren, G. Liu, J. Cai, Y. Zhang, and J. Qiu, “Electrochemical and capacitive properties of carbon dots/reduced graphene oxide supercapacitors”, *Nanomaterials*, **6** (11), 212, 2016.
- [198] M. K. Barman, P. Mitra, R. Bera, S. Das, A. Pramanik, and A. Parta, “An efficient charge separation and photocurrent generation in the carbon dot–zinc oxide nanoparticle composite”, *Nanoscale*, **9** (20), 6791–6799, 2017.

- [199] C. N. Banwell, E. M. McCash, et al., *Fundamentals of Molecular Spectroscopy*, 3rd ed. McGraw-Hill, 1983.
- [200] J. R. Ferraro, *Introductory Raman spectroscopy*, 2nd ed. Elsevier, 2003.
- [201] D. A. Long, *The Raman Effect*, 1st ed. Wiley, 2002.
- [202] J. R. Lakowicz, *Principles of fluorescence spectroscopy*, 3rd ed. Springer, 2013.
- [203] B. Valeur, *Molecular fluorescence*, 2012.
- [204] D. J. Griffiths and D. F. Schroeter, *Introduction to quantum mechanics*, 2nd ed. Cambridge University Press, 2004.
- [205] R. García, *Amplitude modulation atomic force microscopy*. John Wiley & Sons, 2011.
- [206] G. Haugstad, *Atomic force microscopy: understanding basic modes and advanced applications*. John Wiley & Sons, 2012.
- [207] 1 Broadway, Cambridge, MA 02142, U.S.A. [Online]. Available: <https://www.graphenea.com/>.
- [208] D. Wei, S. Haque, P. Andrew, J. Kivioja, T. Ryhänen, A. Pesquera, A. Centeno, B. Alonso, A. Chuvilin, and A. Zurutuza, "Ultrathin rechargeable all-solid-state batteries based on monolayer graphene", *J. Mater. Chem.A*, **1** (9), 3177–3181, 2013.
- [209] J. H. Parker, D. W. Feldman, and M. Ashkin, "Raman scattering by silicon and germanium", *Phys. Rev.*, **155**, 712–714, 3 1967.
- [210] P. A. Temple and C. E. Hathaway, "Multiphonon Raman spectrum of silicon", *Phys. Rev. B*, **7**, 3685–3697, 8 1973.
- [211] A. Armano, G. Buscarino, M. Cannas, F. M. Gelardi, F. Giannazzo, E. Schilirò, R. Lo Nigro, and S. Agnello, "Influence of oxide substrates on monolayer graphene doping process by thermal treatments in oxygen", *Carbon*, **149**, 546–555, 2019.
- [212] A. Armano, G. Buscarino, M. Cannas, F. M. Gelardi, F. Giannazzo, E. Schilirò, and S. Agnello, "Monolayer graphene doping and strain dynamics induced by thermal treatments in controlled atmosphere", *Carbon*, **127**, 270–279, 2018.
- [213] A. Armano, G. Buscarino, F. Messina, A. Sciortino, M. Cannas, F. M. Gelardi, F. Giannazzo, E. Schilirò, and S. Agnello, "Photoinduced charge transfer from carbon dots to graphene in solid composite", *Thin Solid Films*, **669**, 620–624, 2019.
- [214] C. H. Lui, L. Liu, K. F. Mak, G. W. Flynn, and T. F. Heinz, "Ultraflat graphene", *Nature*, **462** (72), 339, 2009.
- [215] W. G. Cullen, M. Yamamoto, K. M. Burson, J. Chen, C. Jang, L. Li, M. S. Fuhrer, and E. D. Williams, "High-fidelity conformation of graphene to SiO₂ topographic features", *Phys. Rev. Lett.*, **105** (21), 215504, 2010.
- [216] A. Catena, T. McJunkin, S. Agnello, F. M. Gelardi, S. Wehner, and C. B. Fischer, "Surface morphology and grain analysis of successively industrially grown amorphous hydrogenated carbon films (aC:H) on silicon", *Appl. Surf. Sci.*, **347**, 657–667, 2015.
- [217] A. Catena, S. Agnello, L. M. Rösken, H. Bergen, E. Recktenwald, F. Bernsmann, et al., "Characteristics of industrially manufactured amorphous hydrogenated carbon (ac:H) depositions on high-density polyethylene", *Carbon*, **96**, 661–671, 2016.
- [218] J. Hong, M. K. Park, E. J. Lee, D. Lee, D. S. Hwang, and S. Ryu, "Origin of new broad Raman D and G peaks in annealed graphene", *Sci. Rep.*, **3**, 2700, 2013.

- [219] E Zion, A Butenko, Y Kaganovskii, V Richter, L Wolfson, A Sharoni, et al., “Effect of annealing on Raman spectra of monolayer graphene samples gradually disordered by ion irradiation”, *J. Appl. Phys.*, **121** (11), 114301, 2017.
- [220] Y. Ahn, J. Kim, S. Ganorkar, Y.-H. Kim, and S.-I. Kim, “Thermal annealing of graphene to remove polymer residues”, *Materials Express*, **6** (1), 69–76, 2016.
- [221] C. Gong, H. C. Floresca, D. Hinojos, S. McDonnell, X. Qin, Y. Hao, S. Jandhyala, G. Mordi, J. Kim, L. Colombo, et al., “Rapid selective etching of pmma residues from transferred graphene by carbon dioxide”, *J. Phys. Chem. C*, **117** (44), 23000–23008, 2013.
- [222] A. Pirkle, J. Chan, A. Venugopal, D. Hinojos, C. W. Magnuson, S. McDonnell, et al., “The effect of chemical residues on the physical and electrical properties of chemical vapor deposited graphene transferred to SiO₂”, *Appl. Phys. Lett.*, **99** (12), 122108, 2011.
- [223] R. Zhou, S. Yasuda, H. Minamimoto, and K. Murakoshi, “Sensitive Raman probe of electronic interactions between monolayer graphene and substrate under electrochemical potential control”, *ACS Omega*, **3** (2), 2322–2328, 2018.
- [224] A. Armano, G. Buscarino, F. Messina, A. Sciortino, M. Cannas, F. M. Gelardi, F. Giannazzo, E. Schilirò, and S. Agnello, “Dynamic modification of fermi energy in single layer graphene by photoinduced electron transfer from carbon dots”, *Submitted*,
- [225] A. Das, B Chakraborty, S Piscanec, S Pisana, A. Sood, and A. Ferrari, “Phonon renormalization in doped bilayer graphene”, *Phys. Rev. B*, **79** (15), 155417, 2009.
- [226] R. Larciprete, S. Ulstrup, P. Lacovig, M. Dalmiglio, M. Bianchi, F. Mazzola, L. Hornekær, F. Orlando, A. Baraldi, P. Hofmann, et al., “Oxygen switching of the epitaxial graphene–metal interaction”, *ACS Nano*, **6** (11), 9551–9558, 2012.
- [227] T. Fang, A. Konar, H. Xing, and D. Jena, “Carrier statistics and quantum capacitance of graphene sheets and ribbons”, *Appl. Phys. Lett.*, **91** (9), 092109, 2007.
- [228] A. Sciortino, A Madonia, M. Gazzetto, L. Sciortino, E. J. Rohwer, T. Feurer, F. Gelardi, M Cannas, A. Cannizzo, and F. Messina, “The interaction of photoexcited carbon nanodots with metal ions disclosed down to the femtosecond scale”, *Nanoscale*, **9** (33), 11902–11911, 2017.

CURRICULUM VITÆ

ANGELO ARMANO

PLACE AND DATE OF BIRTH	Cefalù 20 July 1991
ADDRESS	Contrada Santuzza s.n.c., 90013 Castelbuono (PA), Italia
PHONE	+39 3387292096
EMAIL	Work: angelo.armano@unipa.it Personal: angeloarmano.lupo815@gmail.com

EDUCATION

OCTOBER 2016	Master of Science Degree PHYSICS, CURRICULUM IN MATTER PHYSICS UNIVERSITÀ DEGLI STUDI DI PALERMO Via Archirafi 36, 90123 Palermo, Italia Thesis: <i>Graphene doping and stress by thermal treatments in controlled atmosphere</i> Score: 110/110 CUM LAUDE
OCTOBER 2014	Bachelor of Science Degree PHYSICAL SCIENCES UNIVERSITÀ DEGLI STUDI DI PALERMO Via Archirafi 36, 90123 Palermo, Italia Thesis: <i>Spin Glasses</i> Score: 107/110

SCHOOLS & SEMINARIES

SCHOOLS | 2

JUNE 2018	<i>Training School on Spectroscopy Methods for the Characterization of Carbon-Related Materials</i> (COST Action 15107) UNIVERSITÄT WIEN · FAKULTÄT FÜR PHYSIK Wien · Österreich
FEBRUARY 2016	<i>Memristive Phenomena - From Fundamental Physics to Neuromorphic Computing</i> FORSCHUNGSZENTRUM JÜLICH · 47TH IFF SPRING SCHOOL Jülich · Deutschland

SEMINARIES | 12 (112 TOTAL HOURS)

MAY 2018	<i>Funzionalizzazione Chimica di nanoforme di carbonio</i> UNIVERSITÀ DEGLI STUDI DI PALERMO Prof. F. Giacalone
APRIL 2018	<i>Lectures on Electrochemistry</i> UNIVERSITÀ DEGLI STUDI DI CATANIA Prof. Y. Shacham-Diamand
APRIL 2018	<i>Big-Data Processing Techniques for Materials Chemistry</i> UNIVERSITÀ DEGLI STUDI DI CATANIA Prof. N. Tuccitto
APRIL 2018	<i>La progettazione su fondi H2o2o</i> UNIVERSITÀ DEGLI STUDI DI PALERMO Dr. B. Mourenza (APRE)

FEBRUARY 2017	<i>Tensors, piezoelectrics and their applications</i> SCUOLA SUPERIORE DI CATANIA Prof. A. Bartasyte
FEBRUARY 2017	<i>Lanthanides: useful probes for modern applications</i> SCUOLA SUPERIORE DI CATANIA Prof. A. Speghini
FEBRUARY 2017	<i>Using chemistry to deposit thin functional materials. Applications in nanoscience and energy</i> SCUOLA SUPERIORE DI CATANIA Prof. D. Muñoz Rojaz
JANUARY 2017	<i>Spettroscopia di assorbimento dei raggi X nello studio dei materiali. Concetti di base ed analisi di dati sperimentali</i> UNIVERSITÀ DEGLI STUDI DI PALERMO Prof. F. Giannici
JANUARY 2017	<i>Metodi elettrochimici per la deposizione e caratterizzazione di semiconduttori per celle solari</i> UNIVERSITÀ DEGLI STUDI DI PALERMO Prof. R. Inguanta
JANUARY 2017	<i>Spettroscopia computazionale</i> UNIVERSITÀ DEGLI STUDI DI PALERMO Prof. F. Ferrante
JANUARY 2017	<i>Spettroscopia Raman e μ-Raman: applicazioni allo studio dei materiali</i> UNIVERSITÀ DEGLI STUDI DI PALERMO Prof. S. Agnello
JANUARY 2017	<i>Spettroscopia di emissione risolta in tempo. Applicazioni allo studio dei materiali</i> UNIVERSITÀ DEGLI STUDI DI PALERMO Prof. M. Cannas

PUBLICATIONS

PUBLISHED | 6

APRIL 2019	<i>Influence of oxide substrates on monolayer graphene doping process by thermal treatments in oxygen</i> CARBON 149 546–555 (2019) A. Armano, G. Buscarino, M. Cannas, F. M. Gelardi, F. Giannazzo, E. Schilirò, R. Lo Nigro, and S. Agnello
APRIL 2019	<i>Seed-Layer-Free Atomic Layer Deposition of Highly Uniform Al₂O₃ Thin Films onto Monolayer Epitaxial Graphene on Silicon Carbide</i> ADVANCED MATERIAL INTERFACES 6 (10) 1900097 (2019) E. Schilirò, R. Lo Nigro, F. Roccaforte, I. Deretzis, A. La Magna, A. Armano, S. Agnello, B. Pecz, I. G. Ivanov, R. Yakimova, and F. Giannazzo
JANUARY 2019	<i>Carbon Dots Dispersed on Graphene/SiO₂/Si: A Morphological Study</i> PHYSICA STATUS SOLIDI A 216 (3) 1800559 (2019) G. Faggio, A. Gnisci, G. Messina, N. Lisi, A. Capasso, G. H. Lee, A. Armano, A. Sciortino, F. Messina, M. Cannas, F. M. Gelardi, E. Schilirò, F. Giannazzo, and S. Agnello
JANUARY 2019	<i>Graphene-SiO₂ Interaction from Composites to Doping</i> PHYSICA STATUS SOLIDI A 216 (3) 1800540 (2019) A. Armano, G. Buscarino, M. Cannas, F. M. Gelardi, F. Giannazzo, E. Schilirò, R. Lo Nigro, and S. Agnello

- NOVEMBER 2018 | *Photoinduced charge transfer from Carbon Dots to Graphene in solid composite*
 THIN SOLID FILMS | **669** 620–624 (2019)
 A. Armano, G. Buscarino, F. Messina, A. Sciortino, M. Cannas, F. M. Gelardi, F. Giannazzo, E. Schilirò, and S. Agnello
- NOVEMBER 2017 | *Monolayer graphene doping and strain dynamics induced by thermal treatments in controlled atmosphere*
 CARBON | **127** 270–279 (2018)
 A. Armano, G. Buscarino, M. Cannas, F. M. Gelardi, F. Giannazzo, E. Schilirò, and S. Agnello

UNDER REVISION | 2

- JULY 2019 | *Dynamic Modification of Fermi Energy in Single Layer Graphene by Photoinduced Electron Transfer from Carbon Dots*
 Submitted to: J. PHYS. CHEM. C | ? ?–? (20??)
 A. Armano, G. Buscarino, F. Messina, A. Sciortino, M. Cannas, F. M. Gelardi, F. Giannazzo, E. Schilirò, and S. Agnello
- AUGUST 2019 | *Two-Dimensional Carbon: a Review of Electronic and Optical Properties, Raman Features, and Synthesis Methods of Graphene*
 Submitted to: C | ? ?–? (20??)
 A. Armano and S. Agnello

CONFERENCE CONTRIBUTIONS**ORAL PRESENTATIONS | 4**

- JUNE 2019 | *Substrate-dependent molecular doping of supported graphene by charge transfer process*
 NANOTECH FRANCE 2019 | Paris · France
 A. Armano, G. Buscarino, M. Cannas, F. M. Gelardi, F. Giannazzo, E. Schilirò, R. Lo Nigro, and S. Agnello
- MAY 2019 | *Substrate-dependent doping process of monolayer graphene by thermal treatments in oxygen*
 E-MRS SPRING MEETING 2019 | Nice · France
 A. Armano, G. Buscarino, M. Cannas, F. M. Gelardi, F. Giannazzo, E. Schilirò, R. Lo Nigro, and S. Agnello
- JUNE 2018 | *Doping and strain effects of Graphene induced by thermal treatments in controlled atmosphere*
 E-MRS SPRING MEETING 2018 | Strasbourg · France
 A. Armano, G. Buscarino, M. Cannas, F. M. Gelardi, F. Giannazzo, E. Schilirò, and S. Agnello

- JUNE | *Charge-transfer between Graphene and Carbon nanodots or small molecules*
 2018 | E-MRS SPRING MEETING 2018 | Strasbourg · France
 A. Armano, G. Buscarino, A. Sciortino, F. Messina, M. Cannas, F. M. Gelardi, F. Giannazzo,
 E. Schilirò, and S. Agnello

POSTER PRESENTATIONS | 1

- MAY | *Micro-photoluminescence analysis of carbon dots-graphene composites*
 2019 | E-MRS SPRING MEETING 2019 | Nice · France
 G. Faggio, G. Messina, N. Lisi, T. Dikonimos, A. Capasso, F. Giannazzo, E. Schilirò,
 A. Armano, G. Buscarino, A. Sciortino, F. Messina, M. Cannas, F. M. Gelardi, and
 S. Agnello

CO-AUTHORED CONTRIBUTIONS | 5

- SEPTEMBER | *Graphene Doping by Oxygen Adsorption Driven by Substrate Interaction*
 2019 | E-MRS FALL MEETING 2019 | Warsaw · Poland
 A. Armano, G. M. Lo Piccolo, F. Bruno, G. Buscarino, M. Cannas, F. M. Gelardi,
 F. Giannazzo, E. Schilirò, and S. Agnello
- JUNE | *High-k substrate effect on the thermal doping of graphene by oxygen*
 2019 | NANOINNOVATION 2019 | Rome · Italy
 A. Armano, G. Buscarino, M. Cannas, F. M. Gelardi, F. Giannazzo, E. Schilirò, R. Lo Nigro,
 and S. Agnello
- JULY | *Charge-transfer processes between Graphene and simple molecules or carbon*
 2018 | *nanodots*
 CARBON 2018 | Madrid · Spain
 A. Armano, G. Buscarino, F. Messina, A. Sciortino, M. Cannas, F. M. Gelardi, F. Giannazzo,
 E. Schilirò, and S. Agnello
- JUNE | *Graphene–SiO₂ interaction from composites to doping*
 2018 | SiO₂ 2018 | Bari · Italy
 A. Armano, G. Buscarino, M. Cannas, F. M. Gelardi, F. Giannazzo, E. Schilirò, R. Lo Nigro,
 and S. Agnello
- JUNE | *Carbon dots dispersed on graphene/SiO₂/Si: a morphological study*
 2018 | SiO₂ 2018 | Bari · Italy
 G. Faggio, A. Gnisi, G. Messina, N. Lisi, A. Capasso, A. Armano, A. Sciortino, F. Messina,
 M. Cannas, F. M. Gelardi, E. Schilirò, F. Giannazzo, S. Agnello

PROPOSALS | 1

- FEBRUARY | *First Principle Investigation of Silica-Supported Graphene Electronic Structure*
 2019 | CINECA - Italian SuperComputing Resource Allocation(ISCRA) | Proposal Class · C
 G. M. Lo Piccolo, A. Armano, F. Bruno, and S. Agnello